Kinase-mediated regulation of CryAB in muscle: from NUAK-dependent signaling to extracellular vesicle–driven amyloid secretion

by

Ziwei Zhao

B.S., Inner Mongolia Medical University, 2016
M.S., Emporia State University, 2020

AN ABSTRACT OF DISSERTATION

submitted in partial fulfillment of the requirements for the degree

DOCTOR OF PHILOSOPHY

Department of Biochemistry and Molecular Biophysics
College of Arts and Sciences

KANSAS STATE UNIVERSITY
Manhattan, Kansas

2025

Abstract

This thesis examines the role of NUAK kinase and CryAB in muscle proteostasis, addressing two key questions: (1) how does NUAK activity prevent protein aggregation, and (2) how do pathogenic CryAB alleles perturb proteostasis and promote amyloidogenesis?

NUAK is a member of the AMP-activated protein kinase (AMPK) family, a conserved group of serine/threonine kinases with broad regulatory functions. To define the requirement for NUAK catalytic activity, I introduced point mutations at residues essential for phosphotransfer activity. Three independent loss-of-function alleles abolished enzymatic activity, leading to aberrant protein accumulation and progressive muscle degeneration, thereby establishing NUAK kinase activity as indispensable for muscle integrity. A prior yeast two-hybrid screen identified a physical interaction between NUAK and CryAB. To test whether CryAB is a direct substrate, I overexpressed NUAK, which enriched for phosphorylated CryAB species. Mass spectrometry of HA-tagged CryAB purified from muscle tissue identified serines 68 and 70 as phosphorylation targets. Alanine substitutions at these positions eliminated the modification, confirming NUAK-dependent regulation of CryAB through site-specific phosphorylation.

The second half of this work delineates how CryAB pathogenic mutations perturb proteostasis and promote inclusion formation. Mutational analyses revealed two phenotypic classes: conventional aggregates and distinct inclusion-like structures. CryAB aggregates colocalized with canonical protein quality control markers including ubiquitin, p62/SQSTM1, and Bag3, consistent with impaired proteostasis. In contrast, CryAB inclusions were characterized by a unique association with desmin, extracellular vesicle (EV)-associated proteins (Rab27, CD81, Alix, TSG101), and localized preferentially at fiber peripheries. Transmission electron microscopy and Congo red staining confirmed that these inclusions are amyloidogenic. Preliminary genetic

perturbations demonstrated that depletion of EV biogenesis components in CryAB mutant flies reduced both the size and abundance of amyloid inclusions, implicating EV pathways in their assembly.

Collectively, these findings define NUAK as a critical kinase that maintains muscle proteostasis through phosphorylation of CryAB and establish that pathogenic CryAB mutations induce amyloidogenic inclusions whose formation is modulated by extracellular vesicle pathways. This work uncovers new mechanisms linking kinase signaling, molecular chaperones, and vesicle biology to amyloid pathology in muscle disease.

Kinase-mediated regulation of CryAB in muscle: from NUAK-dependent signaling to extracellular vesicle–driven amyloid secretion

by

Ziwei Zhao

B.S., Inner Mongolia Medical University, 2016
M.S., Emporia State University, 2020

A DISSERTATION

submitted in partial fulfillment of the requirements for the degree

DOCTOR OF PHILOSOPHY

Department of Biochemistry and Molecular Biophysics
College of Arts and Sciences

KANSAS STATE UNIVERSITY
Manhattan, Kansas

2025

Approved by:
Major Professor
Erika R. Geisbrecht

Copyright

Abstract

This thesis examines the role of NUAK kinase and CryAB in muscle proteostasis, addressing two key questions: (1) how does NUAK activity prevent protein aggregation, and (2) how do pathogenic CryAB alleles perturb proteostasis and promote amyloidogenesis?

NUAK is a member of the AMP-activated protein kinase (AMPK) family, a conserved group of serine/threonine kinases with broad regulatory functions. To define the requirement for NUAK catalytic activity, I introduced point mutations at residues essential for phosphotransfer activity. Three independent loss-of-function alleles abolished enzymatic activity, leading to aberrant protein accumulation and progressive muscle degeneration, thereby establishing NUAK kinase activity as indispensable for muscle integrity. A prior yeast two-hybrid screen identified a physical interaction between NUAK and CryAB. To test whether CryAB is a direct substrate, I overexpressed NUAK, which enriched for phosphorylated CryAB species. Mass spectrometry of HA-tagged CryAB purified from muscle tissue identified serines 68 and 70 as phosphorylation targets. Alanine substitutions at these positions eliminated the modification, confirming NUAK-dependent regulation of CryAB through site-specific phosphorylation.

The second half of this work delineates how CryAB pathogenic mutations perturb proteostasis and promote inclusion formation. Mutational analyses revealed two phenotypic classes: conventional aggregates and distinct inclusion-like structures. CryAB aggregates colocalized with canonical protein quality control markers including ubiquitin, p62/SQSTM1, and Bag3, consistent with impaired proteostasis. In contrast, CryAB inclusions were characterized by a unique association with desmin, extracellular vesicle (EV)-associated proteins (Rab27, CD81, Alix, TSG101), and localized preferentially at fiber peripheries. Transmission electron microscopy and Congo red staining confirmed that these inclusions are amyloidogenic. Preliminary genetic

perturbations demonstrated that depletion of EV biogenesis components in CryAB mutant flies reduced both the size and abundance of amyloid inclusions, implicating EV pathways in their assembly.

Collectively, these findings define NUAK as a critical kinase that maintains muscle proteostasis through phosphorylation of CryAB and establish that pathogenic CryAB mutations induce amyloidogenic inclusions whose formation is modulated by extracellular vesicle pathways. This work uncovers new mechanisms linking kinase signaling, molecular chaperones, and vesicle biology to amyloid pathology in muscle disease.

Table of Contents

List of Figures

List of Tables

Acknowledgements

I am deeply grateful to **Dr. Erika Geisbrecht** for her guidance and support during the past five years of my PhD journey. When I first joined the laboratory, I was uncertain, lacking confidence, and new to research. Erika's constant encouragement and patient teaching helped me grow into an independent scientist. She celebrated my small successes, guided me through failures by helping identify problems, and inspired me to keep moving forward. She encouraged me to present my work with confidence, carefully helping me refine my posters and slides again and again. With her support, I was able to attend international conferences in Italy, where I was honored to receive the Best Talk Award, and I experienced the excitement of publishing my first research article, with our fluorescence microscope image featured on the cover. These milestones built my confidence and strengthened my passion for science. Erika has been not only my doctoral advisor but also like family to me in a foreign country, and I will always be grateful for her kindness and mentorship.

I would also like to thank my committee members, **Dr. Timothy Durrett, Dr. Michael Kanost, and Dr. Jocelyn McDonald**, for their invaluable support. When Erika and I were unsure how to describe the CryAB ring phenotype, Dr. McDonald suggested the term "CryAB inclusion," which has become central to my work. Dr. Kanost provided important opportunities for academic exchange by organizing insect meetings every semester, which broadened my scientific knowledge and allowed me to hear diverse perspectives. Dr. Durrett has been very supportive in my career development, writing recommendation letters that helped me secure scholarships. I am truly grateful for your guidance, encouragement, and generosity.

Special thanks go to **David Brooks**, who patiently taught me many experimental techniques and helped me learn from mistakes in my early days. I still remember following him

around the lab with my notebook, carefully recording every detail he shared. I am also thankful to **Yungui Guo, Jared Ridder and Dylan Feist** for their friendship and for making my time in the lab both productive and enjoyable. My sincere thanks go to **Mr. Dave Manning** for his technical support, and to our department chair, **Dr. Michal Zolkiewski**, for providing financial support that allowed me to travel for research.

To all of you who have supported me along the way—thank you. Your guidance, encouragement, and kindness have not only shaped my research but also made this journey truly meaningful.

Dedication

This work is dedicated with love to my parents, **Suxia Wang** and **Zhongmin Zhao**, and to my little sister **Zi'ai Zhao**, who has always cared for me. Your unwavering financial and emotional support made my PhD journey possible. To my boyfriend, **Dr. Huiquan Duan**, as well as my pets, **Fupo** and **Xiaomao**, whose love, joy, and constant presence gave me the courage and happiness I needed along the way.

Chapter 1 - Myofibrillar Myopathy and *Drosophila*

1.1 Basic structure of Muscle

When you read this work, your eyes shift across the page, your eyelids blink, and your fingers turn the paper. Each of these actions, though seemingly effortless, depends on the coordinated activity of muscle. Skeletal muscle is fundamental to human life. It generates movement, enables breathing, supports posture, and contributes to thermoregulation and energy balance. In addition to these mechanical roles, muscle acts as an endocrine organ through the secretion of myokines, serves as the body's largest reservoir of amino acids, and plays a central role in glucose and lipid metabolism [1, 2]. Maintaining muscle integrity is therefore essential not only for locomotion but also for systemic physiological stability. In humans, skeletal muscle represents 40–50% of total body weight, a proportion comparable to that observed in model organisms such as mice, *Drosophila melanogaster*, and zebrafish [1-5]. Muscle is also a major protein reservoir: it contains approximately 50–75% of total body protein in humans, 25–50% in mice, and 40–50% during the larval stages of *Drosophila* [3, 5, 6]. Given its scale and metabolic contribution, any disruption of muscle function—whether due to disease, injury, or aging—has profound consequences for health and survival.

Structurally, skeletal muscle consists of long, multinucleated fibers formed during development through the fusion of myoblasts. These fibers are densely packed with myofibrils, which are organized into repeating contractile units called sarcomeres. The sarcomere is the fundamental structural and functional unit of contraction. Its highly ordered arrangement produces the characteristic striated appearance of skeletal muscle. Sarcomeres are defined by Z-discs at either end, from which thin filaments of actin extend. These filaments, together with regulatory proteins such as tropomyosin and the troponin complex, form the I band region. Thick filaments

composed primarily of myosin occupy the A band, with the M line at the center. The H zone surrounds the M line and contains only thick filaments. This intricate architecture allows sarcomeres to convert molecular interactions into the force necessary for muscle contraction **(Figure 1.1)** [1, 2].

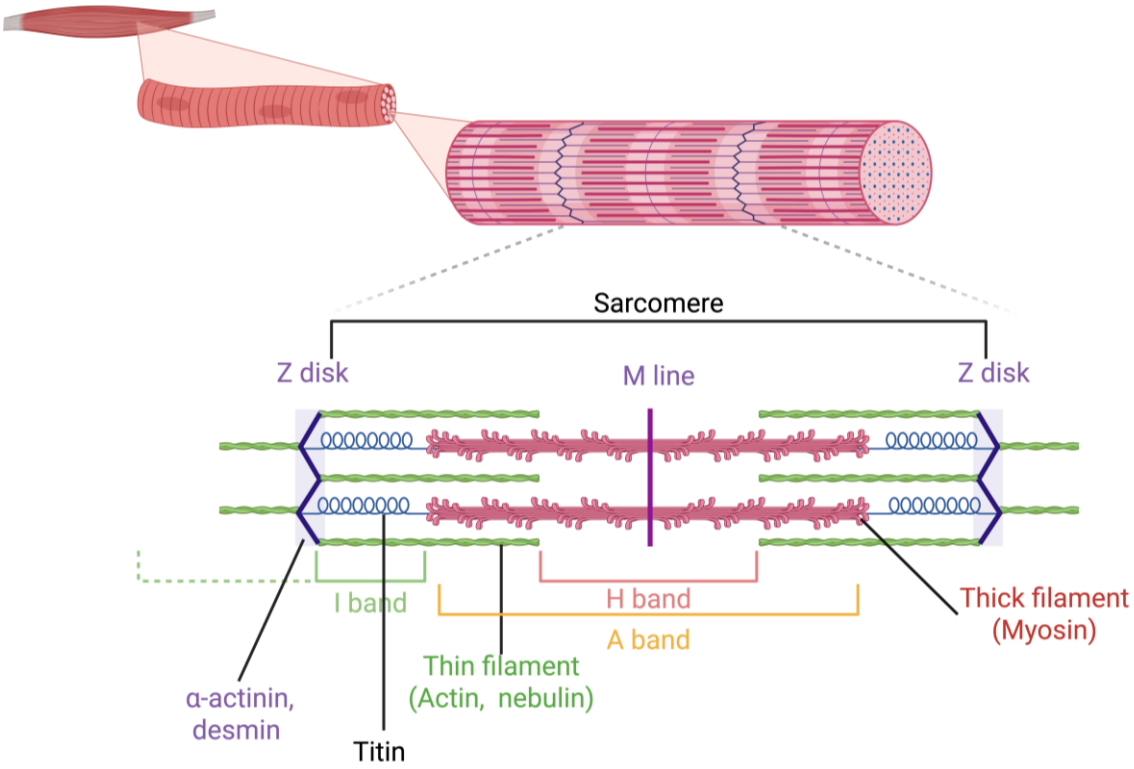

Figure 1.1 Basic muscle structure.
A skeletal muscle is organized hierarchically. The whole muscle is composed of bundles of fascicles, each fascicle contains multiple muscle fibers (cells). Muscle fibers contain myofibrils, which are made up of repeating sarcomeres, the fundamental contractile units. Thin filaments (actin) are anchored to the Z-lines, while thick filaments (myosin) are positioned in the center. Key regions include the I band, A band, H band and the M line.

The ordered interactions between actin and myosin filaments, powered by ATP hydrolysis and regulated by calcium signaling, drive the contraction-relaxation cycles of muscle. In mammalian, key structural proteins such as titin, nebulin, α-actinin, and desmin maintain the alignment and elasticity of sarcomeres, ensuring the force generated by contraction is transmitted

uniformly across the fiber [7-10]. This intricate architecture allows skeletal muscle to withstand repeated mechanical stress while maintaining both strength and flexibility.

During development, skeletal muscle plays a critical role not only as a structural component of the musculoskeletal system but also as a signaling hub that influences the formation and maturation of other tissues. Myogenesis, the process by which muscle tissue forms, begins early in embryogenesis and involves the tightly regulated proliferation, migration, and differentiation of mesoderm-derived precursor cells known as myoblasts. These cells undergo a complex series of gene expression changes, guided by key transcription factors such as MyoD, Myf5, and myogenin, ultimately leading to their fusion into multinucleated myotubes that mature into functional muscle fibers **(Figure 1.2)** [11-13]. Defects in muscle development can result in congenital myopathies, impaired movement, and systemic developmental delays [14-16]. Furthermore, proper sarcomere assembly during this time is essential, as errors in the initial organization of contractile structures often have long-lasting consequences, predisposing muscle tissue to instability and disease later in life [17, 18]. Thus, skeletal muscle is not only essential for adult physiology, but also for orchestrating the complex morphogenetic events that shape the organism during early life.

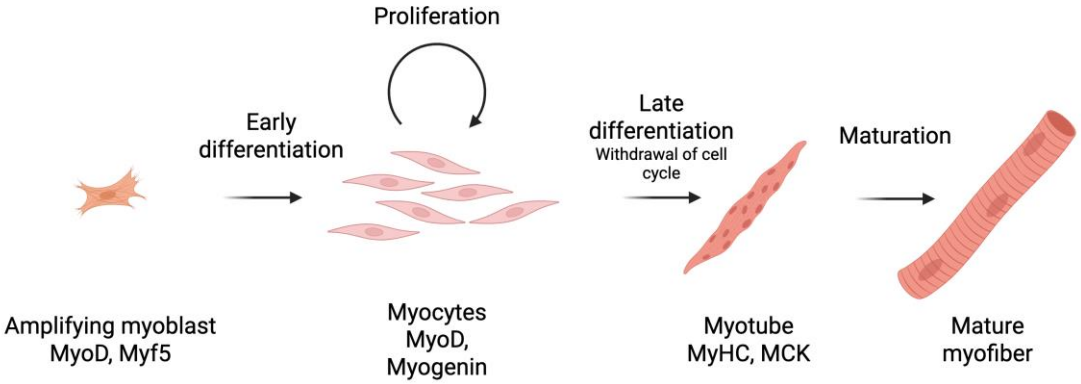

Figure 1.2 Myoblast Fusion and Key Regulatory Factors in Myogenesis.

During skeletal muscle development, mononucleated myoblasts align and fuse to form elongated, multinucleated myotubes. This process is tightly controlled by myogenic regulatory factors (MRFs), including MyoD, Myf5, myogenin, MyHC and MCK.

1.2 Protein quality control

Proteins, once translated from mRNAs, must fold correctly to function properly. Misfolding can occur due to translation errors, cellular stress, or genetic mutations, leading to loss of function and potential toxicity. To maintain intracellular health, cells employ protein quality control (PQC) systems: molecular chaperones, the ubiquitin–proteasome system, and autophagy [19, 20].

Molecular chaperones are essential for maintaining protein quality within the cell. They detect misfolded proteins and either assist in restoring their proper shape or direct them for degradation [21]. Among these chaperones, heat shock proteins (Hsps) are the most extensively studied. Hsps are rapidly induced under stress conditions such as heat, oxidative damage, or exposure to toxic agents. They are categorized mainly by molecular weight: larger ATP-dependent Hsps (including Hsp70, Hsp90, Hsp60, and Hsp40) and smaller ATP-independent proteins known as small heat shock proteins (sHsps) [22-25]. One example of an sHsp is αB-crystallin (CryAB or HSPB5), which has a molecular weight of approximately 20 kDa (more details in Chapter 1-1.9) [26, 27]. Despite belonging to the same family, Hsps perform distinct cellular functions. Large Hsps like Hsp70 and Hsp90 act as "foldases." They use ATP hydrolysis to unfold misfolded proteins, allowing them another chance to fold correctly into their functional state [28, 29]. By contrast, sHsps act as "holdases." Rather than refolding proteins, they bind to misfolded species, keeping them in a soluble state and preventing toxic aggregation. These bound proteins are then directed to degradation pathways for removal **(Figure 1.3)** [30].

Protein degradation is primarily carried out through two interconnected systems: the ubiquitin–proteasome pathway and the autophagy–lysosome pathway. In the ubiquitin–proteasome system, proteins targeted for removal are tagged with ubiquitin molecules through the action of E1, E2, and E3 ligases. These ubiquitinated proteins are then degraded by the 20S proteasome **(Figure 1.3)** [31, 32]. However, when misfolded proteins accumulate and form aggregates, they can inhibit this pathway [33]. This limitation highlights the need for additional mechanisms to maintain protein balance.

Autophagy provides this complementary safeguard. The term, derived from the Greek for "self-eating," refers to a conserved cellular process in plants, yeast, and mammals. Autophagy sequesters damaged proteins, organelles, or other cellular components into double-membrane vesicles called autophagosomes [34, 35]. These vesicles subsequently fuse with lysosomes, where their contents are degraded and recycled. This process not only clears harmful material but also helps sustain cellular energy balance under stress. The formation of autophagosomes is orchestrated by the ATG (autophagy-related) protein family [36, 37]. These proteins regulate steps such as initiation, cargo recognition, and vesicle expansion. Many ATG proteins are recycled after completing their roles, ensuring efficiency. A central marker of autophagosome biogenesis is ATG8, a ubiquitin-like protein that conjugates to phosphatidylethanolamine (PE) on the autophagosomal membrane, enabling its growth and closure [37, 38]. In mammalian cells, the LC3 proteins, homologs of ATG8, also bind to PE and are widely used as markers of autophagosome formation [39, 40]. In addition, adaptor proteins such as Ref(2)p (alternative name: p62) link misfolded protein aggregates to the autophagy machinery and are themselves degraded in the process, serving as indicators of autophagic turnover **(Figure 1.3)** [41, 42].

Together, molecular chaperones, the ubiquitin–proteasome system and the autophagy–lysosome pathways form the backbone of cellular protein quality control. Their coordinated activity is vital for preventing the toxic buildup of misfolded proteins. When these systems are disrupted, protein aggregates accumulate, contributing to the development of muscle diseases and other disorders linked to impaired proteostasis.

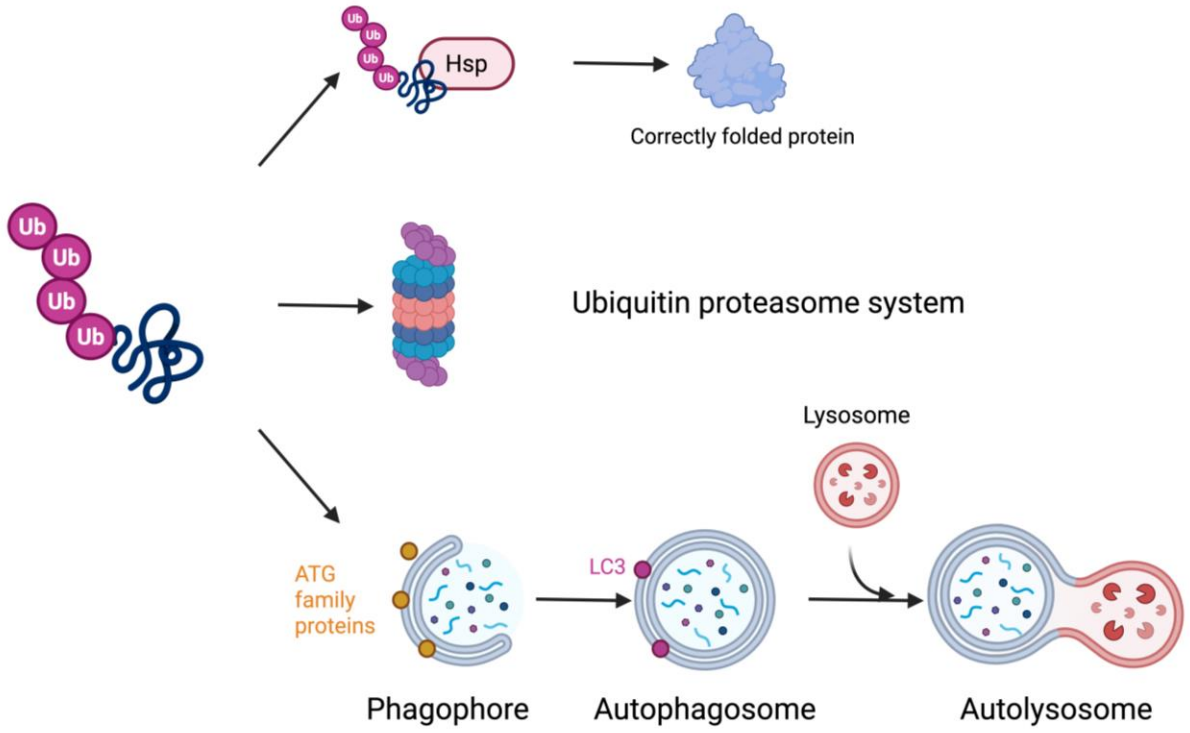

Figure 1.3 Protein Quality Control Pathways: Chaperones, the Ubiquitin–Proteasome System, and Autophagy

This schematic illustrates the major cellular pathways responsible for maintaining protein homeostasis (proteostasis). Molecular chaperones assist in protein folding, prevent aggregation, and facilitate refolding of misfolded proteins. Proteins that fail to attain their native conformation are often targeted for degradation by the ubiquitin–proteasome system (UPS), which selectively tags substrates with ubiquitin chains for proteasomal breakdown. Larger protein aggregates or damaged organelles that cannot be handled by the UPS are eliminated through autophagy, where cytoplasmic material is sequestered into autophagosomes and delivered to lysosomes for degradation. Together, these interconnected quality control systems preserve cellular function and protect against proteotoxic stress.

1.3 Myofibrillar Myopathy

Maintaining the structural and functional integrity of muscle requires not only the proper assembly of sarcomeres during development but also lifelong protein quality control. Because skeletal muscle cells are post-mitotic, they do not readily divide to replace damaged fibers. Preserving protein quality is therefore essential for muscle health and performance. Declining muscle function is a hallmark of aging, but even in younger individuals, muscle fibers are constantly exposed to mechanical strain and high metabolic demands [43, 44]. These stresses make them particularly vulnerable to protein damage and misfolding. To counteract this, muscle cells rely on robust proteostasis systems that monitor, refold, or eliminate misfolded proteins. When these mechanisms are compromised—whether by genetic mutations or overwhelming stress—misfolded proteins can accumulate and form toxic aggregates, disrupting sarcomere structure and impairing muscle function [45]. Disrupted proteostasis is a central feature of several muscle diseases, including Duchenne muscular dystrophy (DMD), sarcopenia, and amyotrophic lateral sclerosis (ALS) [46-50]. DMD, for example, is an X-linked disorder affecting roughly one in every 5,000 boys [46]. Symptoms typically appear between ages three and five, with progressive muscle weakness leading to severe disability and death from cardiopulmonary complications in the second decade of life. These conditions illustrate how muscle integrity is directly tied to quality of life and survival.

Myofibrillar myopathies (MFMs) represent another major group of protein aggregate diseases, first recognized as a distinct category in 1996 [51]. MFMs are defined by disorganization of myofibrils combined with the accumulation of insoluble protein aggregates. Clinically, they are marked by progressive muscle weakness, which often begins in distal muscles and worsens with

age. Some patients also develop early-onset cataracts, typically in their 40s, while severe genetic variants can result in life-threatening outcomes in infancy [52, 53].

Genetic studies have linked MFMs to mutations in multiple genes, most of which encode Z-line associated structural proteins [53]. At least 12 causative proteins have been identified in patients, including desmin [54-56], CryAB [57, 58], myotilin (MYOT) [53], LDB3 (ZASP) [59, 60], filamin C [61, 62], BAG3 [52], FHL1 [63], titin [64], DNAJB6 [65], and HSPB8 [66]. However, this list is likely incomplete. Advances in genetic testing have improved diagnostic precision, but the high cost and limited availability of sequencing remain barriers. Muscle biopsy can provide insights, yet variability in lesions and overlap with other myopathies complicate interpretation. The absence of disease-specific patient registries further limits systematic data collection and research progress. As a result, understanding of MFMs remains partial, and no targeted or effective therapies are currently available.

1.4 Advantages of *Drosophila melanogaster* as a genetic model

Drosophila melanogaster is a powerful *in vivo* model for investigating the genetic mechanisms underlying muscle diseases. Approximately 75% of human disease-related genes have functional counterparts in flies, making them highly relevant for translational research. Their short life cycle—about 10 days from embryo to adult—enables rapid generation of experimental data. Flies are inexpensive to maintain, require minimal laboratory space, and thrive under standard culture conditions [67]. In addition, the *Drosophila* research community has built extensive genetic resources, including mutant and transgenic lines readily available through repositories such as the Bloomington *Drosophila* Stock Center (https://bdsc.indiana.edu/) and FlyBase (https://flybase.org/).

When compared with mammalian models such as mice, *Drosophila* differs in lifespan, body size, and muscle architecture. Nevertheless, it remains a valuable system for muscle research because of its conserved processes of myogenesis, functional parallels in muscle degeneration, and shared molecular components of muscle structure [68-70]. Insights generated from fly studies frequently inform mammalian systems, and conversely, discoveries in mammals can be modeled and tested in flies.

During embryogenesis, *Drosophila* muscle development follows a well-defined sequence: myoblast fusion begins at stage 12-14, myotubes form by stages 15-16, and mature myotubes are established by the end (stage 16-17) of embryogenesis. Each stage progresses within about an hour, providing a rapid developmental timeline **(Figure 1.4, upper image)**. Genetic manipulation in flies allows straightforward functional analysis of genes involved in these steps. Because embryos are transparent, live imaging can capture dynamic processes such as myoblast fusion in real time, offering valuable insights into muscle development [68, 71].

In the larval stage, each abdominal hemisegment contains 30 well-defined muscles. The third instar larva (L3), with its larger body size compared to earlier stages, is commonly used for structural studies **(Figure 1.4, middle image)** [72, 73]. During metamorphosis, larval muscles are remodeled, and new fibers are synthesized in the pupal stage. Severe muscle defects often lead to contraction failure in pupae, producing lethal phenotypes that prevent flies from reaching adulthood. In adults, the indirect flight muscles (IFMs) are the largest and most widely studied, owing to their structural similarity to mammalian skeletal muscle, including clearly defined Z-lines and M-lines **(Figure 1.4, bottom image)**. Additional thoracic muscles, such as the dorsal longitudinal muscles (DLMs) and dorsal ventral muscles (DVMs), also provide accessible models for structural and functional analyses [73-75]. Muscle performance can be assessed at multiple

stages: crawling assays and muscle contraction tests in larvae, and flight, climbing, and jumping assays in adults. Advanced microscopy, coupled with specific molecular labeling, enables detailed analysis of muscle architecture and protein localization.

Genetic tools further enhance the utility of *Drosophila* as a model. The GAL4–UAS system allows precise spatial and temporal control of gene expression **(Figure 1.4)** [76]. For muscle-specific studies, drivers such as *Mef2*-Gal4 are commonly used, while additional lines such as *C57*-Gal4 or *G7*-Gal4 provide temporal regulation [77, 78]. CRISPR–Cas technology now permits precise endogenous editing of genes of interest, further expanding experimental possibilities [79]. In our laboratory, *Drosophila* serves as a versatile model to study genetic muscle diseases, offering detailed insights into muscle development, structure, degeneration, and aging-related decline.

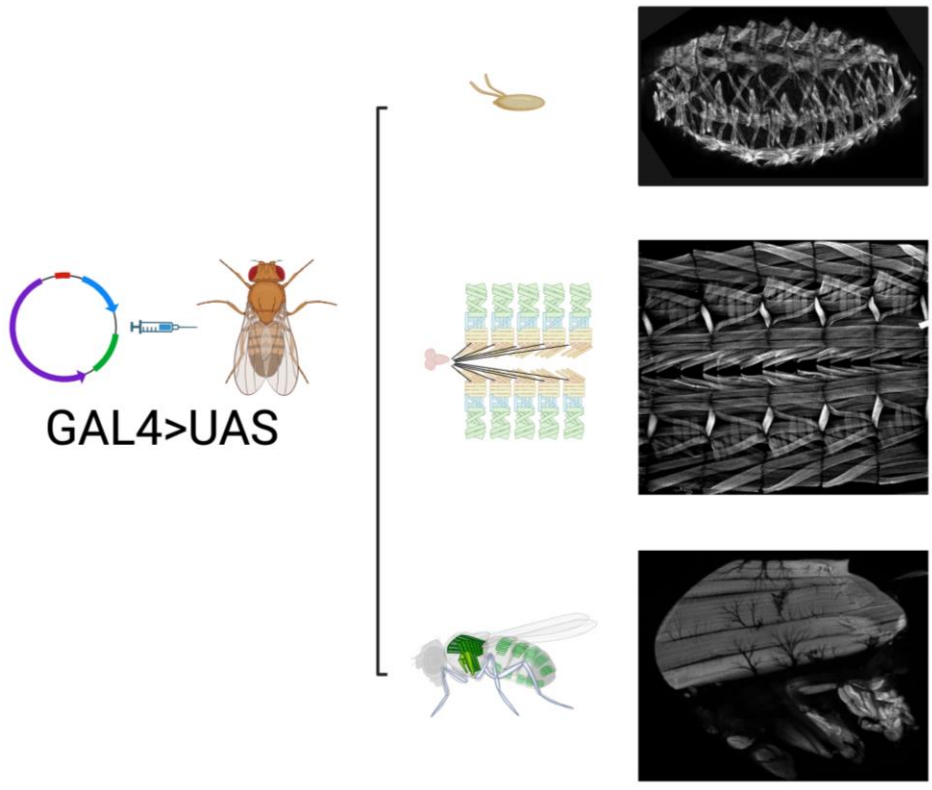

Figure 1.4 Drosophila Muscle as a Model for Genetic Muscle Diseases

This schematic outlines the application of immunohistochemical staining in Drosophila melanogaster muscle as a model to investigate genetic muscle diseases. The workflow illustrates

the key stages of muscle staining, enabling visualization of muscle fibers, sarcomeric organization, and cellular architecture. The use of the Gal4-UAS system facilitates targeted gene expression in muscle tissues, providing a versatile platform to study muscle development, structure, and disease-associated alterations. This approach highlights how *Drosophila* serves as a powerful genetic model for dissecting the molecular mechanisms underlying muscle pathology.

1.5 NUAK Proteins and Cytoskeletal Regulation in Muscle Disease

AMPK and the AMPK-Related Kinase Family

Skeletal muscle is one of the most metabolically active tissues in the human body, relying primarily on adenosine triphosphate (ATP) for energy. During exercise, ATP is rapidly consumed, increasing the cellular ratio of adenosine monophosphate (AMP) to ATP. This shift activates a kinases known as AMP-activated protein kinases (AMPKs), which act as central regulators of energy homeostasis [80, 81]. Closely related to AMPK is the AMPK-related kinase (ARK) family, which shares a highly conserved catalytic α-domain across species. Unlike AMPK, ARKs generally lack the β and γ regulatory subunits and thus do not directly sense cellular AMP/ATP ratios [82]. Instead, they function as serine/threonine kinases activated by phosphorylation. The ARK family consists of 12 members, including NUAK1, NUAK2, BRSK1, BRSK2, QIK, QSK, SIK, MARK1–4, and MELK, all of which, along with AMPKα1 and AMPKα2, can be phosphorylated by the upstream kinase LKB1 *in vitro* **(Figure 1.5)** [83-85]. Phosphorylation sites of serine and threonine were highly conserved in ARK family proteins (Light yellow box of phosphorylation peptide and green box labelled conserved serine and threonine residues in **figure 1.5**). In this manuscript, we primarily discuss NUAK proteins.

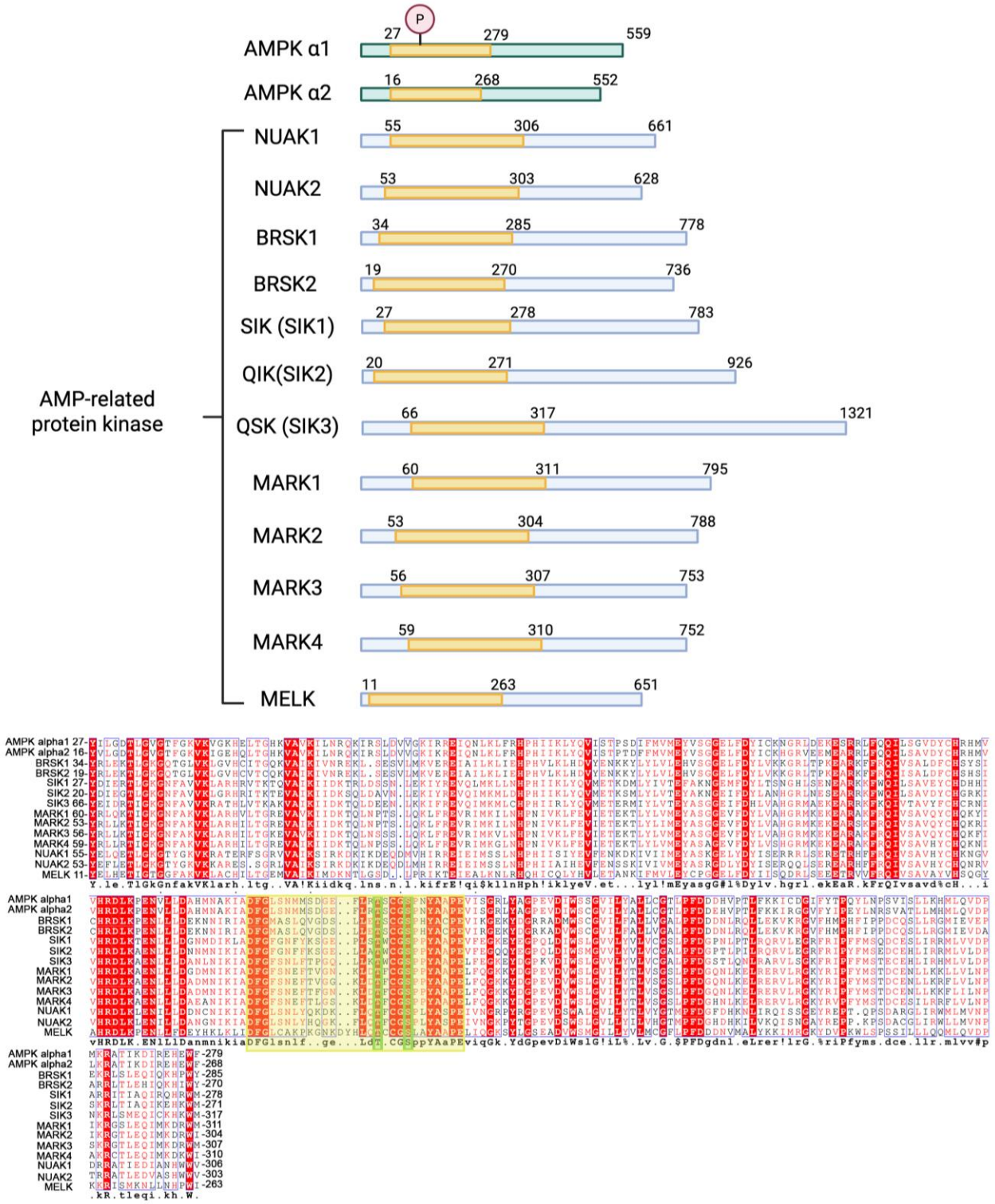

Figure 1.5 AMPK-related protein kinase and kinase domain alignment

The schematic illustrates the protein length and conserved kinase domain (yellow) of AMPK-related protein kinases. The top panel depicts the overall domain organization of each family member, highlighting the conserved kinase domain within variable protein lengths. The lower

panel shows sequence alignment of the kinase domains, emphasizing conserved motifs and serine/threonine residue (green box) shared across the AMPK-related kinase family.

In mammals, the NUAK subfamily consists of two isoforms: NUAK1 (also known as ARK5) and NUAK2 (also known as SNARK). NUAK1 shows high RNA expression in the cerebral cortex, skin, heart, and skeletal muscle, while NUAK2 is expressed at lower levels in heart and skeletal muscle (The human protein: https://www.proteinatlas.org/). This differential expression pattern suggests that the two isoforms may serve distinct physiological roles.

The distribution of NUAK isoforms varies across model organisms [86]. Mice, for example, possess two isoforms, whereas *C. elegans* and *Drosophila melanogaster* each contain only one. Zebrafish, by contrast, express three isoforms. The presence of a single NUAK ortholog in *C. elegans* and *Drosophila* makes these organisms particularly useful for genetic studies, as they simplify *in vivo* functional analyses **(Figure 1.6 A)**. Comparative sequence studies demonstrate that the NUAK kinase domain is highly conserved across species, underscoring its evolutionary and functional importance. For instance, human NUAK1 kinase domain shares 99% identity with mouse NUAK1 and 62–66% identity with orthologs in *Drosophila*, *C. elegans*, and zebrafish **(Figure 1.6 B)**. NUAK2 exhibits similarly high levels of conservation. Beyond the kinase domain, the C-terminal region contains a conserved GILK motif responsible for binding protein phosphatase PP1β (see Chapter 1.7) [87]. Interestingly, this GILK motif is absent in *C. elegans* and *Drosophila*, suggesting that the C-terminal domain is more dynamic and may engage with different binding partners depending on the species **(Figure 1.6 A, green box)**. Overall, the strong evolutionary conservation of the kinase domain highlights the fundamental role of NUAK proteins, while variation in the C-terminal region suggests adaptability to species-specific cellular contexts. These features make NUAK an attractive focus for studying conserved and divergent mechanisms

of muscle biology and disease.

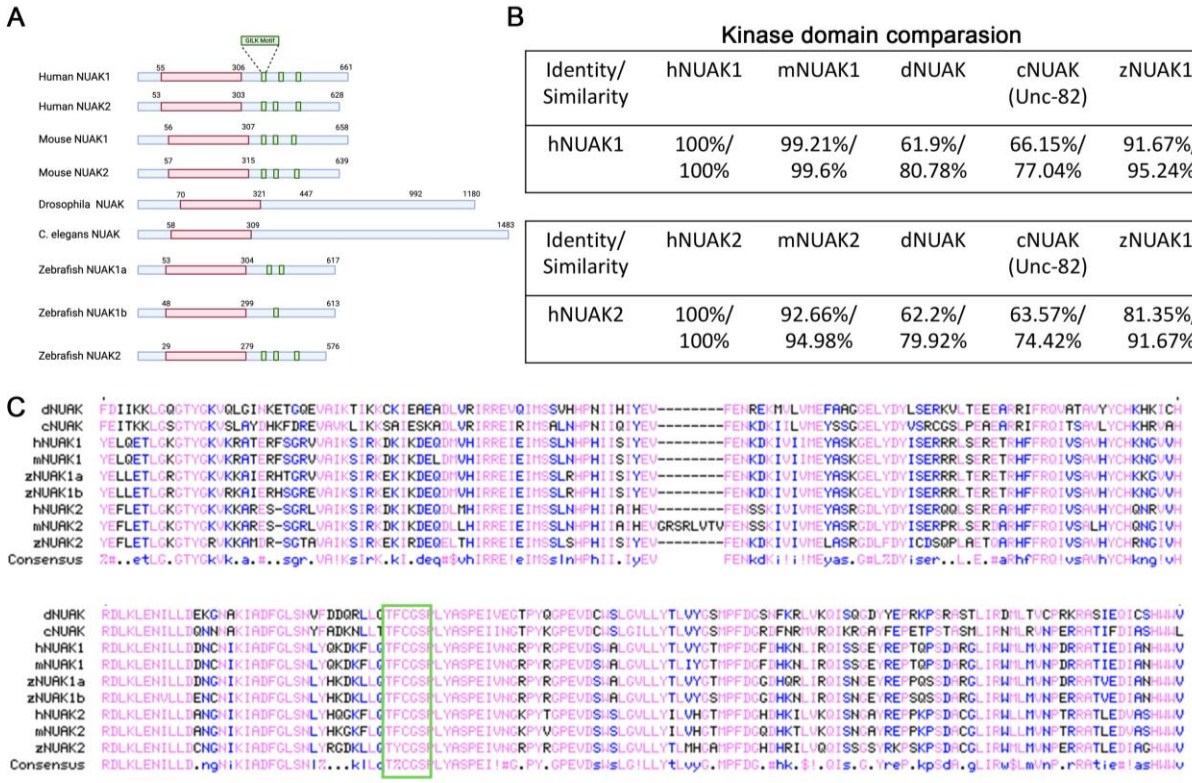

Figure 1.6 Conservation of NUAK Proteins and Kinase Domains Across Species

(A) Schematic representation of NUAK proteins from different species, illustrating variability in total protein length but conservation of the kinase domain and the GILK motif, which mediates binding to the phosphatase PP1β.
(B) Comparative analysis of NUAK kinase domains across species, highlighting the high degree of sequence similarity and identity within the catalytic core.
(C) Multiple sequence alignment of NUAK kinase domains from representative species, showing conserved phospho-regulatory peptides. Key threonine and serine residues critical for kinase regulation are boxed in green, underscoring their evolutionary conservation.

Structural Features of NUAK Proteins

Despite advances in structural biology, full-length NUAK protein structures remain unresolved. NUAK proteins in *Drosophila* and *C. elegans* have notably longer C-terminal domains than their human counterparts **(Figure 1.6 A)**. AlphaFold predictions reveal high-confidence models for the kinase domains (blue color) of human NUAK1 (AlphaFold ID:AF-O60285-F1), mouse NUAK1 (AF-Q641K5-F1), and *Drosophila* NUAK (AF-Q7KSS0-F1), while the N- and C-

terminal regions appear largely disordered **(Figure 1.7 A)**. The functions of these disordered regions and their interactions with partner proteins remain important open questions. In the kinase domain sequencing alignment, which clearly see the conserved serine and threonine residues **(Figure 1.6 C, green box)** cross the species. The conserved threonine phosphorylation residue in the predicted NUAK structure is conserved in these three species **(Figure 1.7 B, green labeled residue)**.

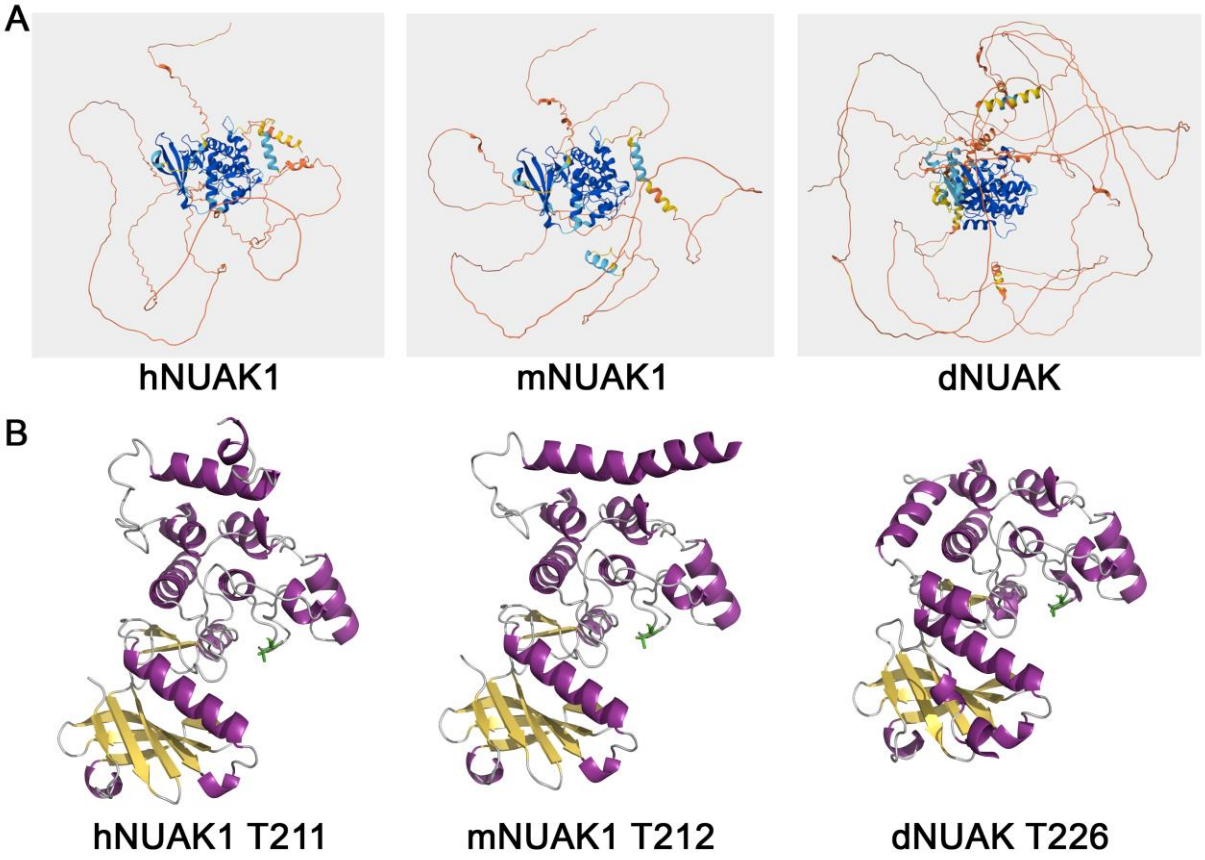

Figure 1.7 AlphaFold-predicted structures of NUAK kinases across species reveal conserved activation loop threonine residues

(A) Predicted three-dimensional structures of NUAK proteins from human (hNUAK1), mouse (mNUAK1), and *Drosophila melanogaster* (dNUAK) generated by AlphaFold. The core kinase domains are shown, highlighting structural conservation across species.
(B) Detailed view of the activation loop in each NUAK structure. The conserved threonine residues critical for phosphorylation and activation are indicated: Thr211 in hNUAK1, Thr212 in

mNUAK1, and Thr226 in dNUAK. These residues occupy equivalent positions within the activation loop, underscoring evolutionary conservation of NUAK regulatory mechanisms.

1.6 NUAK is critical for development

NUAK kinases play essential roles in mammalian embryonic development, particularly in cytoskeletal organization. Loss-of-function mutations can cause severe congenital disorders [88]. In mice, NUAK1 deletion results in incomplete ventral body wall closure, a condition known as omphalocele, leading to embryonic lethality [89]. This phenotype suggests a role for NUAK1 in actomyosin contractility and epithelial sheet closure. NUAK1/NUAK2 double knockout mice exhibit neural tube defects such as exencephaly, facial clefting, and spina bifida [90]. Normally, phosphorylated myosin light chain 2 (MLC2), F-actin, and cortactin are enriched at the apical surface of neuroepithelial cells during neural tube closure, supported by stable microtubules. In double mutants, these cytoskeletal components are mislocalized, and microtubule stability is reduced [90].

Human genetic studies further support NUAK function in development. In one case, multiple fetuses from the same family presented with anencephaly due to NUAK2 mutations [89]. Neural progenitor cells derived from these patients exhibited loss of apical NUAK2 localization, reduced MLC2 phosphorylation [90], enlarged neuroepithelial cells, and diminished nuclear YAP, indicating impaired Hippo-YAP signaling—a pathway critical for organ size control and cell proliferation (more detail see chapter 1.8) [91].

Together, findings highlight NUAK kinases as regulators of cytoskeletal dynamics. Their functions span embryonic morphogenesis, tissue homeostasis, and cytoskeletal integrity—processes that are disrupted in both developmental disorders.

1.7 NUAK Kinases and Cytoskeletal Regulation

NUAK kinases are frequently amplified in several cancers, including adenocarcinomas, uterine corpus endometrial carcinoma, and melanoma (TCGA). These kinases participate in multiple signaling pathways that regulate cytoskeletal dynamics, cell polarity, and motility [86, 88]. Proteomic analysis in HEK293 cells identified NUAK1 interaction partners within the myosin phosphatase complex (MCLP), which consists of the catalytic subunit protein phosphatase 1 (PP1), the myosin phosphatase target subunit 1 (MYPT1), and a small regulatory subunit (M20). MCLP normally dephosphorylates myosin light chain (MLC), inactivating myosin and reducing contractility **(Figure 1.8, normal condition)** [92]. In contrast, myosin light chain kinase phosphorylates MLC to activate it. NUAK1, once phosphorylated by the upstream kinase LKB1, binds PP1 through conserved Gly-Ile-Leu-Lys (GILK) motifs and phosphorylates MYPT1 at S445, S472, and S910. These modifications promote MYPT1 binding to 14-3-3 proteins, inhibit MCLP activity, and sustain MLC phosphorylation—enhancing myosin activity and cell contractility **(Figure 1.8, NUAK overexpression)** [87].

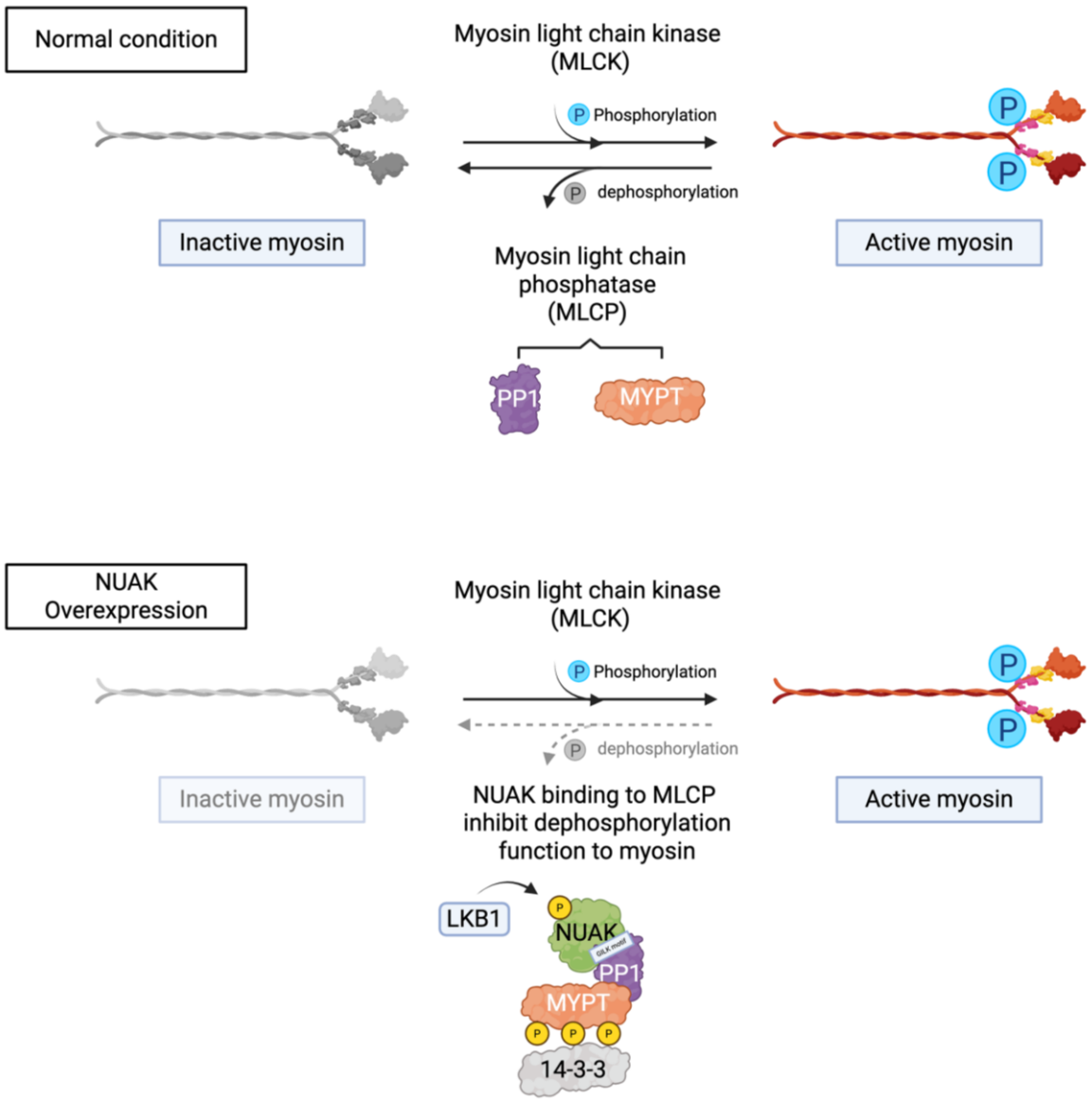

Figure 1.8 NUAK-Mediated Regulation of Myosin Activation Through Inhibition of MLCP

Schematic illustrating the role of NUAK in modulating myosin activity. Under normal conditions (top), myosin activity is dynamically regulated by phosphorylation via myosin light chain kinase (MLCK) and dephosphorylation via myosin light chain phosphatase (MLCP), composed of PP1 and MYPT, maintaining a balance between inactive and active myosin. In contrast, during NUAK overexpression (bottom), LKB1 activates NUAK, which binds to the MLCP complex. This interaction, stabilized by MYPT phosphorylation and 14-3-3 binding, inhibits MLCP-mediated dephosphorylation of myosin. As a result, phosphorylation by MLCK dominates, leading to sustained myosin activation.

In the same year, the actin-binding protein MPRIP (myosin phosphatase Rho-interacting protein) as a binding partner of NUAK2. MPRIP normally interacts with MLC through its N-terminal domain to promote MLC dephosphorylation, leading to actin fiber disassembly. NUAK2 binding to MPRIP via its C-terminal region increases MLC phosphorylation, promoting stress fiber formation and cell adhesion [91]. Together, NUAK1 and NUAK2 enhance MLC activation, supporting cytoskeletal organization and force generation.

From nematodes to mammals, NUAK kinases emerge as guardians of muscle architecture, ensuring that myosin filaments remain precisely aligned during growth and stress. A genetic screen in *Caenorhabditis elegans* identified NUAK (UNC-82) as essential for body wall muscle contraction during embryonic development. They further showed that while early cytoskeletal patterning and initial filament assembly occur normally in UNC-82 mutants, defects in thick filament structure progressively worsen during embryonic elongation and growth [93, 94]. Recent research in 2024 demonstrated that UNC-82 plays a selective role in myosin isoform utilization during thick filament assembly in striated muscle. Specifically, they found that UNC-82 is required for myosin A, but not myosin B, to properly assemble and function within the thick filament arms, revealing an isoform-specific regulatory mechanism. Loss of UNC-82 disrupted myosin A incorporation and organization, leading to structural and functional defects, while myosin B assembly remained largely unaffected [95]. These findings highlight how NUAK kinases contribute not only to general myosin filament stability, as previously shown, but also to the fine-tuned isoform-specific regulation of contractile apparatus assembly in muscle. This work demonstrates that UNC-82 is not required for filament initiation but is essential for stabilizing and preserving filament organization under the mechanical demands of muscle development.

In mice, global *Nuak1* knockout is embryonic lethal [89]. Muscle-specific knockdown resulted in no obvious muscle structural abnormalities, functional redundancy with NUAK2 or other AMPK-related kinases. However, muscle-specific *Nuak1*-deficient mice were smaller in adulthood, even on a high-fat diet, implicating NUAK1 in skeletal muscle glucose metabolism via negative regulation of insulin signaling [96].

In 2020, it was demonstrated that NUAK plays a critical role in maintaining muscle integrity in *Drosophila* by working with the BAG3 ortholog Starvin (Stv) and molecular chaperones such as Hsp70 to regulate chaperone-assisted selective autophagy (CASA)**.** *Drosophila* lacking NUAK show severe muscle degeneration, impaired contraction, and the buildup of insoluble protein aggregates containing Filamin and CryAB, accompanied by autophagy markers like ubiquitin, Ref(2)p/p62, and Atg8a. The study shows that NUAK physically associates with Stv, CryAB, and Filamin, phosphorylates Filamin, and requires its kinase activity for normal function, suggesting phosphorylation is a key step in marking cytoskeletal proteins for degradation. In the absence of NUAK, aggregates accumulate but fail to be cleared by lysosomes, indicating a block in autophagic protein turnover. Genetic interactions further confirm that NUAK and Stv act together in this pathway, with *Stv* overexpression able to partially rescue *NUAK* loss **(Figure 1.9)** [97]. Collectively, the work identifies NUAK as an essential regulator that links kinase signaling to selective autophagy in muscle, highlighting its potential relevance to human myopathies and other protein-aggregation diseases.

Although NUAK's contribution to cytoskeletal organization is now well established, its precise kinase-dependent functions in muscle remain incompletely understood. This gap forms the rationale for the first project of this thesis (Chapter 2).

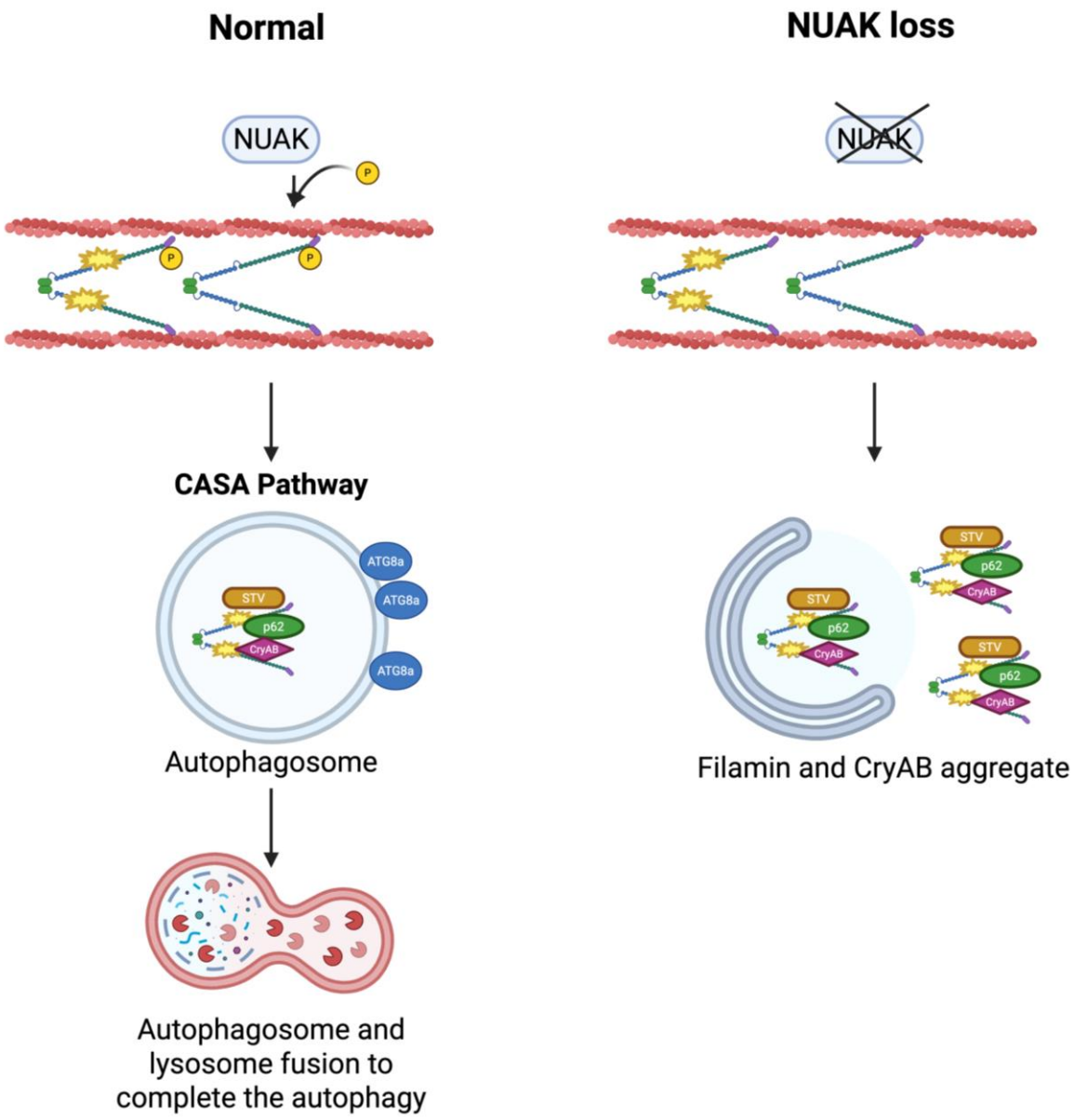

Figure 1.9 NUAK–Starvin/BAG3 Cooperation in Autophagic Protein Turnover

Schematic summarizing the functional interaction between *Drosophila* NUAK and Starvin (BAG3 ortholog) in the regulation of autophagic protein turnover. NUAK works together with Starvin/BAG3 to promote the clearance of protein aggregates (damaged filamin) through the autophagy pathway. This cooperative mechanism highlights a conserved role for NUAK and BAG3-family proteins in maintaining proteostasis, particularly in muscle tissue, by ensuring efficient removal of damaged or misfolded proteins.

1.8 Additional functions of NUAK

PI3K/AKT Signaling Pathway

The PI3K/AKT signaling pathway, often dysregulated in cancer, is a central regulator of cell growth, survival, and proliferation. Cancer cells can adapt remarkably well to nutrient-poor environments. In pancreatic cancer cells, NUAK1 is phosphorylated at serine 600 by AKT (protein kinase B), a serine/threonine kinase [98]. Activated NUAK1 subsequently phosphorylates the tumor suppressor ATM (ataxia-telangiectasia mutated), which increases the phosphorylated form of p53, enhancing cell survival through PI3K/AKT-mediated DNA repair mechanisms [99]. In addition to promoting survival, activated NUAK1 stimulates matrix metalloproteinases MMP2 and MMP9, which degrade the extracellular matrix, thereby facilitating cancer cell invasion [100, 101]. In 2006, a novel NUAK1 phosphorylation site, threonine 211, was identified. This site is phosphorylated by nuclear Dbf2-related kinase 2 (NDR2, also known as STK38L), linking NUAK1 to PI3K-associated signaling events **(Figure 1.10)** [102].

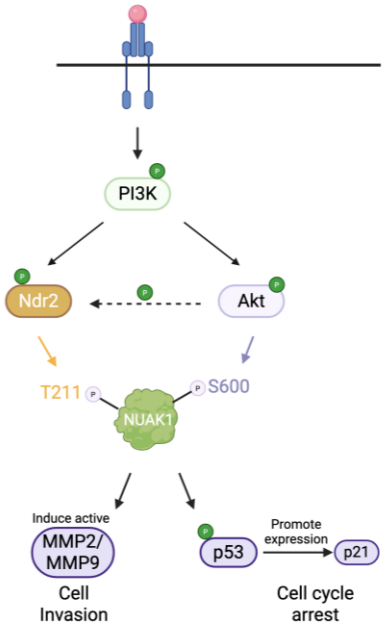

Figure 1.10 Integration of NUAK1 into the Insulin/PI3K Signaling Pathway

Schematic representation of NUAK1 regulation within the insulin signaling pathway. Insulin receptor activation stimulates PI3K, which signals through downstream kinases Ndr2 and Akt. Ndr2 phosphorylates NUAK1 at threonine 211 (T211), while Akt phosphorylates NUAK1 at serine 600 (S600), leading to NUAK1 activation. Activated NUAK1 mediates two major cellular

outcomes: (1) induction of MMP2/MMP9 activity to promote cell invasion, and (2) stabilization of p53, which upregulates p21 expression and drives cell cycle arrest. This highlights NUAK1 as a key effector of insulin/PI3K signaling, linking metabolic cues to pathways that control both cell proliferation and invasive behavior.

Hippo Signaling Pathway

The Hippo pathway regulates organ size, cell proliferation, apoptosis, and tissue regeneration, functioning as a tumor suppressor by inhibiting proliferation and promoting cell death [103]. NUAK1 phosphorylates large tumor suppressor kinase 1 (LATS1) at serine 464, activating YAP/TAZ-mediated protein degradation in the cytoplasm [104]. Overexpression of NUAK1 reduces LATS1 protein levels through this degradation pathway **(Figure 1.11 Hippo "ON")**. When Hippo signaling is inactive, unphosphorylated YAP/TAZ translocate to the nucleus, where they activate transcription of target genes, including NUAK itself. NUAK expression is also influenced by the TGF-β signaling pathway, indicating cross-talk between these regulatory systems **(Figure 1.11 Hippo "OFF")** [91, 105].

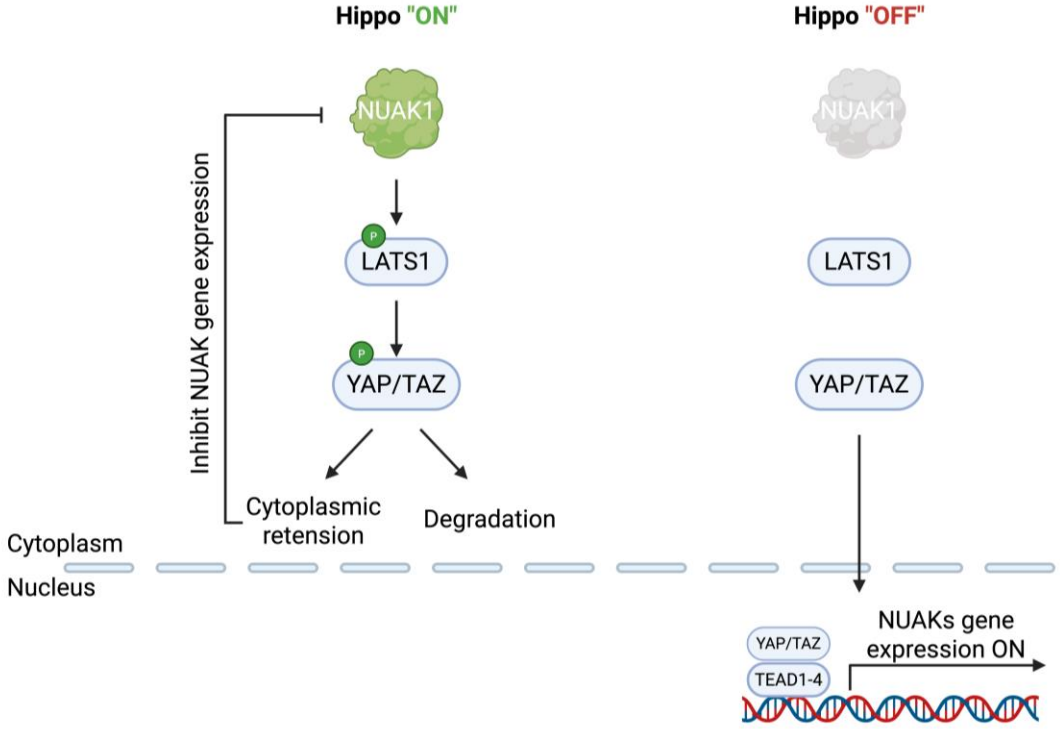

Figure 1.11 Regulation of NUAK1 by the Hippo Pathway

Schematic representation of NUAK1 regulation through the Hippo signaling pathway. When Hippo is "ON," NUAK1 promotes phosphorylation of LATS1 and YAP/TAZ, leading to YAP/TAZ cytoplasmic retention and degradation, thereby suppressing NUAK gene expression. In contrast, when Hippo is "OFF," YAP/TAZ remain unphosphorylated, translocate into the nucleus, and interact with TEAD transcription factors (TEAD1–4) to activate NUAK gene expression. This highlights the reciprocal regulation between NUAK1 and Hippo signaling in controlling cell fate through transcriptional programs.

Regulation of NUAK Expression by TGF-β Signaling

TGF-β signaling affects embryonic development and continues to play roles throughout the lifespan of multicellular organisms [106]. It interacts with various intracellular signaling pathways; however, here we focus on how TGF-β signaling induces the expression of hNUAK genes, which were discovered in mammalian cancer cell lines such as lung and liver fibroblasts. [105]. The TGF-β signaling pathway is known to modulate NUAK transcription. The TGF-β signaling pathway is triggered by the heterotrimer of ligand, TGF-β receptor II (TβRII), and phosphorylated TGF-β receptor I (TβRI) [107, 108]. The traditional downstream proteins small mother against decapentaplegic (SMAD) 2 and 3 can be phosphorylated, recruiting SMAD4 to form heterotrimer complexes [108, 109]. This SMAD2-SMAD3-SMAD4 complex has the ability to translocate into the nucleus and activate the NUAK2 gene transcription **(Figure 1.12)** [105, 110]. NUAK2 also participate the Hippo pathway (described above) to control the NUAK1 expression level to form feedback loop [91]. NUAK2 as an upstream protein of LATS 1/2 protein, which can through phosphorylation to activate LATS 1/2 and then further stimulate the HIPPO signaling pathway to enhance the NUAKs expression which controlled by the HIPPO effectors YAP1 and TAZ **(Figure 1.11 and 1.12)** [91, 104, 105, 110].

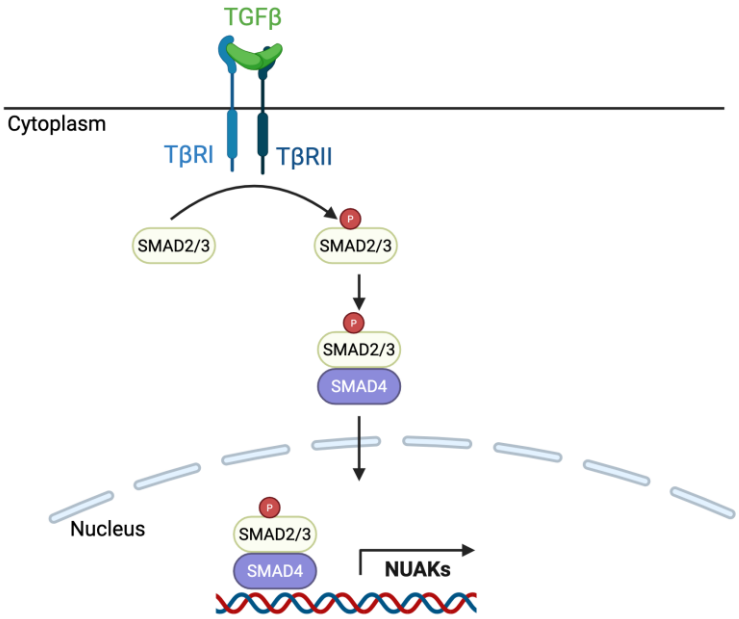

Figure 1.12 TGF-β/SMAD Signaling Regulates NUAK2 Gene Expression

Schematic representation of NUAK regulation by the TGF-β signaling pathway. Binding of TGF-β to its receptor complex (TβRI and TβRII) induces phosphorylation of receptor-regulated SMADs (SMAD2/3). Activated SMAD2/3 form a complex with SMAD4 and translocate into the nucleus, where they bind to target gene promoters. This transcriptional complex drives NUAK2 gene expression, linking extracellular TGF-β signals to the regulation of NUAK2 kinases and downstream cellular responses.

PLK1 Signaling Pathway

NUAK1 and polo-like kinase 1 (PLK1) are connected through a feedback loop that governs both activation and degradation [111]. In 2014, Banerjee et al. reported that cyclin-dependent kinase (CDK) phosphorylates NUAK1 at serine 445, a site outside its kinase domain. This modification enables PLK1 binding, which in turn phosphorylates NUAK1 at serines 476 and 480 within a conserved ESGYYS motif. These phosphorylations recruit the SCF-βTRCP E3 ubiquitin

ligase complex, targeting NUAK1 for degradation [111].

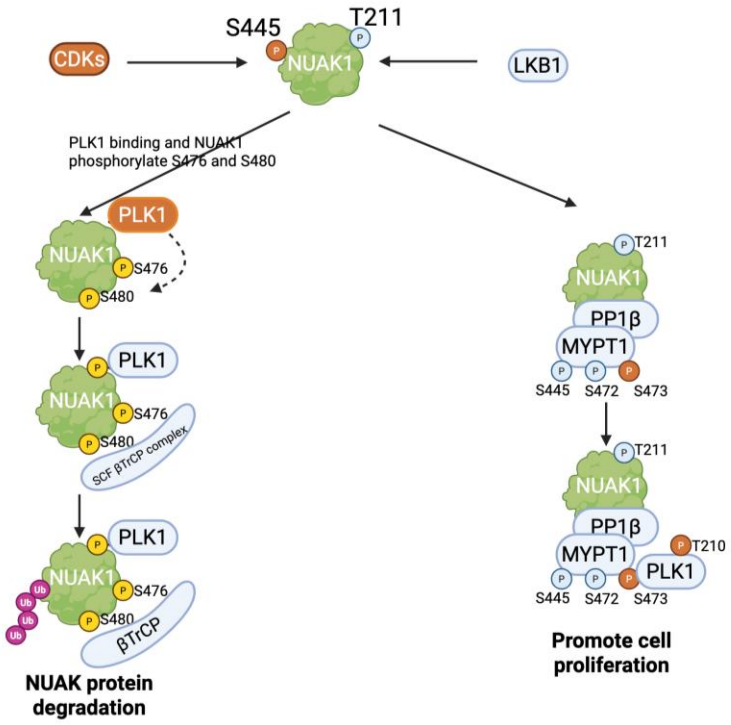

Figure 1.13 Dual Regulation of NUAK1 by PLK1: Balancing Protein Degradation and Cell Proliferation

Schematic representation of NUAK1 regulation by PLK1 through distinct phosphorylation-dependent pathways. On the left, CDKs phosphorylate NUAK1 at S445, facilitating PLK1 binding and subsequent phosphorylation at S476 and S480. This modification recruits the SCF–βTrCP ubiquitin ligase complex, leading to ubiquitination and NUAK1 protein degradation. On the right, LKB1 phosphorylates NUAK1 at T211, enabling interaction with PP1β and MYPT1. This complex supports additional phosphorylation events (S445, S472, S473) and recruitment of PLK1 at T210, which collectively stabilize NUAK1 and promote cell proliferation. Together, these pathways highlight the dual role of PLK1 in either targeting NUAK1 for proteasomal degradation or supporting its function in growth signaling.

NUAK1 can also regulate PLK1 activity via the LKB1–NUAK1–PP1β–MYPT1 pathway [87]. PLK1 activation is promoted by MYPT1 phosphorylation at serine 473, facilitating the G2/M transition in the cell cycle [111]. PP1 dephosphorylates PLK1, inactivating it. NUAK1 activation of PP1β–MYPT1 indirectly maintains PLK1 activity, supporting cell cycle progression and proliferation **(Figure 1.13)** [112].

NUAK in Neurodegenerative Diseases

NUAK kinases may also contribute to the pathology of neurodegenerative disorders such as Alzheimer's and Parkinson's diseases, both of which involve accumulation of misfolded proteins in the brain [113]. In a *Drosophila* genetic screen, NUAK was shown to phosphorylate Tau at serine 356, stabilizing the protein [114]. In mouse models, loss of NUAK function alleviated tauopathy-related pathology, suggesting NUAK inhibition as a potential therapeutic strategy in neurodegenerative disease [113].

1.9 *α-Crystallin B* related-Myofibrillar myopathy

Cellular stress refers to changes in the intracellular environment that threaten cell health [115]. Such stress can arise during normal development or in pathological conditions, triggered by factors such as heat, nutrient deprivation, pH fluctuations, or ultraviolet radiation [116]. To survive and adapt, cells activate a protective network of proteins known as heat shock proteins (HSPs) [22, 116]. These molecular chaperones are critical for maintaining protein homeostasis by binding misfolded or unfolded proteins, facilitating their refolding, or targeting them for degradation.

In humans, the heat shock protein family includes five major conserved groups—HSP110, HSP90, HSP70, HSP60, and DNAJ (HSP40)—alongside ten small heat shock proteins (sHSPs; HSPB1–HSPB10)[25]. Many sHSPs are abundantly expressed in the heart and skeletal muscle, reflecting their specialized role in maintaining structural and functional integrity in contractile tissues[117, 118].

Table 1.1 Small heat shock protein (HSPB) family members and their tissue-specific expression

Name	Synonymous name	Tissue specificity
HSPB1	HSP27, HSP28, SRP27	Ubiquitous
HSPB2	MKBP	Cardiac, skeletal muscle
HSPB3	HSP 17, HSP27, HSPL27	Cardiac, skeletal muscle
HSPB4	CRYAA, CRYA1	Eye lens
HSPB5	CRYAB, CRYA2	Ubiquitous, mainly in eye lens and muscle
HSPB6	HSP20	Ubiquitous, mainly in smooth and cardiac muscle
HSPB7	CVHSP	Skeletal and cardiac muscle
HSPB8	CRYAC, E2IG1, HSP22	Ubiquitous, mainly in brain, muscle
HSPB9	CT51	Testis
HSPB10	ODF1, ODFP	Testis

One of the most studied sHSPs is HSPB5, also known as α-Crystallin B (CryAB), first identified in the eye lens [119]. CryAB is essential for lens transparency, and mutations in this protein are linked to cataracts [120]. However, its high expression in skeletal and cardiac muscle also associates CryAB dysfunction with myofibrillar myopathies (MFMs), inclusion body myositis and cardiomyopathies [27, 121]. Clinically, CryAB-related disorders present a broad spectrum. While many cases manifest later in life with progressive muscle weakness, stiffness, cataracts [57, 122, 123]. Notably, autosomal dominant infantile hypertonic muscular dystrophy can present within the first year of life, often leading to early mortality due to diaphragmatic weakness and respiratory failure, sometimes requiring mechanical ventilation [53, 124, 125].

Since the first pathogenic CryAB mutation was reported in 1998, at least 18 variants have been identified in patients [57]. These mutations span different regions of the protein: N-terminal domain: R11H [126], P20S [127], S21A (S21AfsX24) [125], R56W [128], R69C [129]. α-Crystallin domain (ACD): D109H (A or G mutation) [123, 124, 130], S115fsX128 [125], R120G [57], R123W [131], D140N [132]. C-terminal domain: R151X [58], G154S [133], L155fsX163 [58], R157H [134], A171T [135] (Figure 1.14 A and B). These mutations are clinically heterogeneous, producing variable disease onset, severity, and tissue involvement **(Figure 1.14 B)**. Muscle biopsy samples from affected individuals typically reveal disorganized myofibrillar structures and electron-dense, granular protein aggregates—hallmarks of impaired chaperone function and disrupted cytoskeletal integrity[58, 136].

CryAB Protein Structure

Human α-Crystallin B (CryAB; HSPB5) is a 17.5 kDa small heat shock protein composed of a highly flexible N-terminal domain, a conserved central α-crystallin domain (ACD), and a flexible C-terminal domain [123]. While the complete structure of human CryAB was resolved in 2010 (PDB:2KLR) **(Figure 1.15 A)** [137]. The ACD adopts a characteristic β-sandwich structure consisting of six antiparallel β-strands (β3, β4, β5, β6+7, β8, β9) and mediates CryAB dimerization and oligomerization **(Figure 1.15 B)** [137, 138].

A

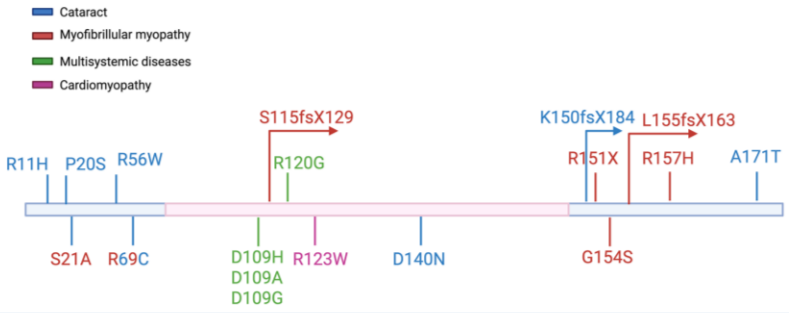

B

Mutation	Cataracts	Myofibrillar myopathy	Cardiomyopathy	Respiratory failure	Dysphonia/ dysarthria	Ref.
R11H	√	x	x	x	x	Chen et al. 2009
P20S	√	x	x	x	x	Liu et al., 2006a
S21AfsX24	x	√	x	√	x	Del Bigio et al., 2010
R56W	√	x	x	x	x	Safieh et al., 2009
R69C	√	x	x	x	x	Sun et al., 2011
D109H	√	√	x	√	√	Sacconi et al., 2012
D109A	√	√	√	x	x	Fichna et al., 2017
D109G	x	√	√	x	x	Brodehl et al., 2017
S115fsX129	x	√	x	√	x	Forrest et al., 2011
R120G	√	√	√	x	√	Vicart et al., 1998
R123W (Non-clinical report)	-	-	√	-	-	Chou et al., 2023
D140N	√	x	x	x	x	Liu et al., 2006b
K150fsX184	√	x	x	x	x	Berry et al., 2001
R151X	x	√	x	x	x	Selcen et al., 2003
G154S	x	√	√	x	x	Pilotto et al., 2006
L155fsX163	x	√	x	√	√	Selcen et al., 2003
R157H	x	x	√	x	x	Inagaki et al., 2006
A171T	√	x	x	x	x	Devi et al., 2008

Figure 1.14 Disease-associated mutations in HSPB8 and their clinical manifestations

(A)Schematic representation and summary table of reported mutations in the small heat shock protein HSPB8. The top panel shows the location of identified missense and nonsense mutations along the HSPB8 protein sequence, color-coded by associated pathology: cataract (blue), myofibrillar myopathy (red), multisystemic diseases (green), and cardiomyopathy (purple). (B)The table summarizes the clinical consequences of each mutation, including cataracts, myofibrillar myopathy, cardiomyopathy, respiratory failure, and dysphagia/dysarthria, with corresponding literature references. This highlights the diverse and tissue-specific disease outcomes caused by HSPB8 dysfunction.

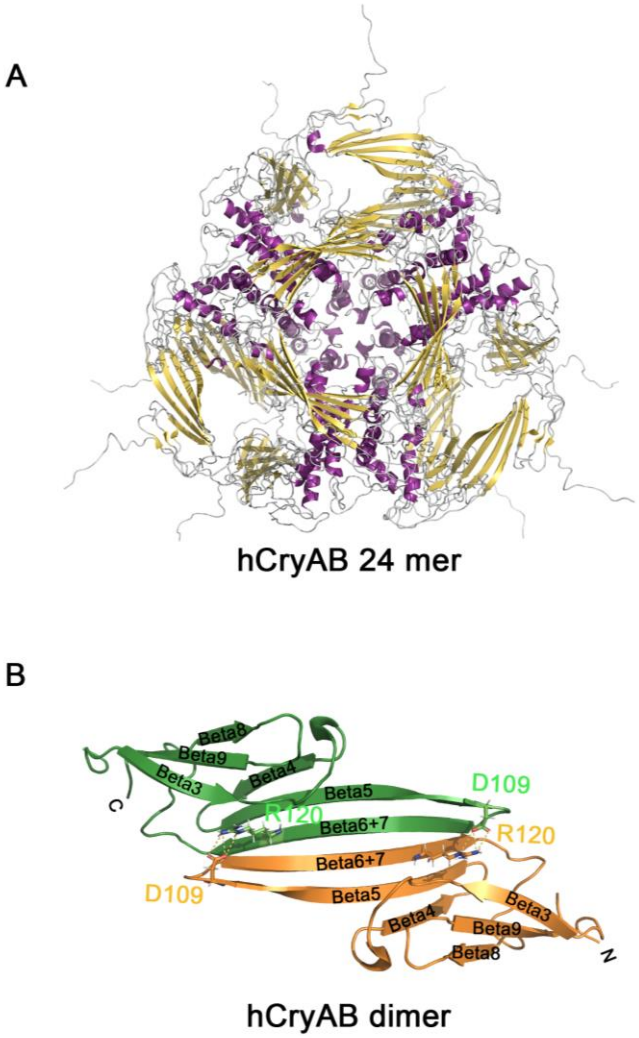

Figure 1.15 Structural Organization of Human αB-Crystallin (hCryAB) Oligomer and Dimer

(A) Structural representation of the human αB-crystallin (hCryAB) 24-mer, showing the oligomeric assembly characteristic of the small heat shock protein family. The arrangement highlights β-strand interactions forming the core architecture.
(B) Structural view of the hCryAB dimer, the fundamental building block of the oligomer. Key β-strands (β3–β9) are labeled, along with critical residues D109 and R120 that mediate dimer stabilization through electrostatic interactions. This structural organization underlies the dynamic assembly of higher-order oligomers and contributes to the chaperone function of hCryAB.

Within the ACD, the β6+7 strand contains two key residues—Asp109 (negatively charged) and Arg120 (positively charged)—that form a salt bridge and ionic interaction between adjacent monomers, with Tyr122 contributing additional stabilization [123]. Mutations at these sites, such

as D109A, D109H, or R120G, disrupt this interface, leading to loss of hydrogen bonding, altered β-sheet conformation, and impaired chaperone activity **(Figure 1.15 B)** [123, 139]. Molecular dynamics simulations and biochemical assays show that D109 mutations reduce protein refolding capacity, degradation efficiency, and cell survival under heat stress, while promoting oligomerization and amyloid fibril formation *in vitro* [139]. This highlights the central role of the ACD in maintaining CryAB chaperone function and preventing pathogenic aggregation.

The N-terminal domain (residues 1–65) contains α-helices (α1, α2) and β-strands (β1, β2) important for higher-order oligomer assembly and client protein binding [137]. The C-terminal domain in mammalian system contains a conserved IXI (Ile-X-Ile) motif that forms a hydrophobic groove for substrate interaction [140]. Recent findings suggest that IXI-like motifs also exist in the N-terminal domain, with AXA (Ala-X-Ala) substitutions altering chaperone activity and promoting dynamic fibril formation *in vitro* [141]. While the IXI motif is not conserved in *Drosophila*, the C-terminal residue Arg157 is highly conserved across species. Mutation R157H, associated with myofibrillar myopathy, reduces oligomerization and fibril formation *in vitro* while enhancing chaperone activity, likely by increasing the proportion of functional dimers [134, 142].

Mammalian Transcriptional Regulation

CryAB expression in non-ocular tissues is governed by cis-regulatory elements upstream of its promoter. Five main elements—αBE1 (-420/-396), αBE4 (-394/-369), αBE2 (-360/-327), αBE3 (-320/-302), and the muscle regulatory factor (MRF) site (-300/-270)—coordinate tissue-specific transcription **(Figure 1.16)** [143]. αBE1 binds the glucocorticoid receptor (GR) and is essential for broad CryAB expression during development, except in the lens and cornea [144]. αBE4 contains a reverse CArG box (5'-GG(A/T)$_6$CC-3'), part of the serum response element,

which recruits a transcriptional complex including NFAT, Nished, and STAT3 [145]. The MRF site contains an E-box motif that binds myogenic transcription factors such as MyoD and myogenin, driving CryAB expression in skeletal muscle and adult heart [143, 146, 147]. However, full transcriptional activity requires cooperation between MRF and other upstream elements. αBE2 and αBE3 remain less characterized. The CryAB promoter contains two TATA boxes, with the -76/-69 element predominantly driving lens-specific expression compared to muscle and heart [148].

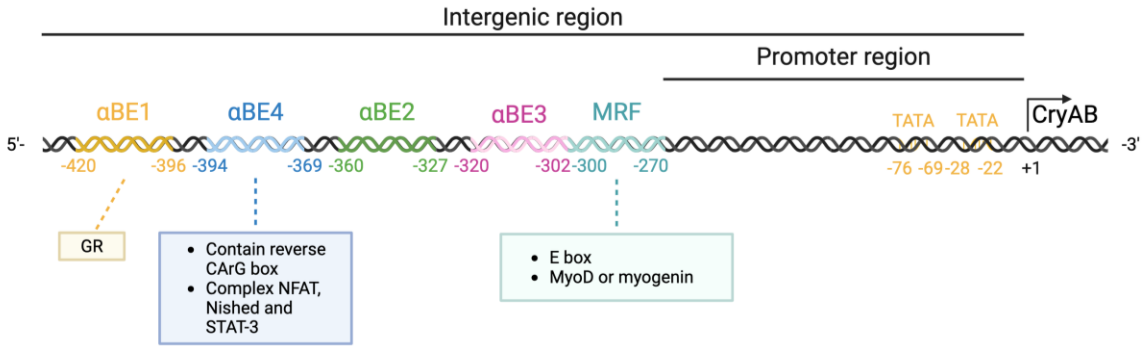

Figure 1.16 Regulatory Elements in the Mammalian CryAB Promoter

Schematic representation of the mammalian *CryAB* transcriptional regulatory region, including both intergenic and promoter elements. Upstream enhancer elements (αBE1–αBE4 and αBE3) and the MRF binding site coordinate transcriptional control. αBE1 interacts with the glucocorticoid receptor (GR), while αBE4 contains a reverse CArG box and binding motifs for NFAT, Nished, and STAT3. The MRF site harbors an E-box recognized by MyoD or myogenin, linking *CryAB* expression to myogenic regulation. The proximal promoter contains multiple TATA boxes that drive transcription initiation at the *CryAB* start site (+1). Collectively, these elements integrate signaling and transcription factor inputs to regulate tissue-specific and stress-responsive *CryAB* expression.

Post-Translational modification: Phosphorylation

Phosphorylation of serine residues is the most studied post-translational modification of CryAB [138]. In bovine lens, six serine residues (S19, S21, S43, S45, S53, S59) have been identified as potential phosphorylation sites [149]. Among these, S45 and S59 are well-characterized targets of p44/42 MAP kinase and MAPKAP kinase 2, respectively [150].

Phosphomimetic substitutions (e.g., S to E) at S19, S45, and S59 destabilize CryAB, increase subunit exchange dynamics, and shift oligomer populations [151]. Triple phosphomimetic mutations (S19E/S45E/S59E) reduce chaperone activity for lactate dehydrogenase and luciferase but enhance protection of other substrates such as citrate synthase, malate dehydrogenase, catalase, p53, and β-crystallin [138, 151-155]. These findings suggest substrate-specific effects of CryAB phosphorylation. However, the precise structural changes that alter chaperone activity and oligomerization following phosphorylation remain unknown.

CryAB's Cellular Function and related diseases

Apoptosis

Apoptosis, or programmed cell death, is a tightly regulated process essential for maintaining tissue homeostasis [156-158]. It can be activated by two main pathways: the extrinsic pathway, triggered by external signals, and the intrinsic pathway, initiated by intracellular stress [156, 158]. Both converge on the activation of cysteine proteases known as caspases, the central executioners of apoptosis. The intrinsic, or mitochondrial, pathway is particularly important in stress response s[157]. Under cellular stress, the mitochondrial outer membrane becomes permeable (MOMP), allowing proteins such as cytochrome c to leak into the cytoplasm. Cytochrome c, together with other mitochondrial proteins, promotes the activation of caspases, leading to cell death [158]. CryAB, a small heat shock protein and molecular chaperone, plays a protective role in stressed cells [115, 116, 150, 159]. Its anti-apoptotic function was demonstrated by Mao and colleagues in 2004. CryAB can directly bind pro-apoptotic proteins, including Bax and Bcl-xS, preventing their translocation to mitochondria and thereby inhibiting caspase activation [160, 161]. Through this mechanism, CryAB effectively suppresses apoptosis. However,

mutations in CryAB compromise this protective role. For example, the R120G mutation reduces CryAB's binding affinity for Bax and Bcl-xS, weakening its ability to block apoptosis [160]. CryAB also interacts with p53, a key tumor suppressor responsible for maintaining genomic stability. By modulating p53 activity, CryAB further contributes to the balance between survival and programmed cell death [162, 163].

Neuron diseases

Altered expression of CryAB has been reported in several neurodegenerative disorders, including Alzheimer's disease, Parkinson's disease, multiple sclerosis, and amyotrophic lateral sclerosis [164-167]. In most cases, CryAB levels are elevated within affected brain regions, suggesting a compensatory response to cellular stress [164]. Research on CryAB in neurological conditions has largely centered on its role in protein quality control, reflecting its function as a molecular chaperone [134, 167]. However, recent studies also highlight its involvement in neuroinflammation [168]. In a mouse model of multiple sclerosis, CryAB demonstrated not only anti-apoptotic activity but also anti-inflammatory effects, reducing the production of inflammatory cytokines. Consistently, CryAB has been detected in the cerebrospinal fluid of both mouse models and human patients with multiple sclerosis [168, 169].

Therapeutic administration of CryAB protein in mouse model further supports its protective role. In a mouse model of stroke, injection of CryAB within 12 hours reduced infarct volume and suppressed inflammatory cytokine levels [166, 169]. Mass spectrometry of CryAB-binding proteins from human and mouse plasma revealed associations with more than 70 pro-inflammatory mediators, including acute-phase proteins, complement components, and clotting factors. Importantly, CryAB administration lowered the concentrations of innate immune proteins

such as complement factors C3 and C5, thereby limiting complement activation and dampening neuroinflammation [168]. However, CryAB is a double-edged sword. Whether it can enter the clinical treatment of patients after stroke is still a long way to go.

Heart diseases

The first disease-associated mutation in αB-crystallin (CryAB), R120G, was identified in cardiomyopathy and has since been a focus of extensive research [170]. Mutations in CryAB are primarily linked to desmin-related cardiomyopathy and hypertrophic cardiomyopathy (HCM), and less frequently to dilated cardiomyopathy (DCM) and restrictive cardiomyopathy (RCM) [130, 131, 134, 139, 142, 170, 171]. Despite this progress, most studies on CryAB in heart disease have concentrated on protein aggregation, with less emphasis on dissecting the underlying molecular mechanisms.

Desmin, an intermediate filament protein, is critical for maintaining muscle structure by connecting Z-disks across myofibrils [51, 57]. CryAB associates with desmin *in vitro* and contributes to amyloid-like fiber formation, although the precise binding structure remains unknown [170, 172, 173]. Mutations in desmin further influence this interaction: the I451M mutation shows reduced binding affinity for CryAB compared with the R454W mutation [173]. These findings highlight how distinct desmin mutations may differentially shape the pathological consequences of CryAB–desmin interactions in cardiomyopathy.

In 2001, transgenic mouse models expressing CryAB R120G provided key insights into disease pathology [170]. These animals exhibited severe myofibrillar disruption, protein aggregation, and aggregates co-localizing with desmin [170, 172]. Similar studies of R120G and D109A mutations revealed increased autophagic vesicle accumulation and higher levels of insoluble proteins, as confirmed by histological and ultrastructural analyses [124, 170].

Subsequent work identified BAG3, a proteostasis regulator, as a binding partner of mutant CryAB [174]. BAG3 overexpression reduced protein aggregation in muscle cells, suggesting a protective role in CryAB-related proteotoxic stress.

Drosophila models have provided complementary evidence. Knockdown of CryAB in fly muscle resulted in thin L3 muscle fibers, irregular Z-lines, and disorganized actin filaments [175]. Expression of GFP-tagged CryAB or CryAB-R120G in these models revealed abnormal sarcomere organization, with the R120G mutation producing more severe phenotypes. Targeted expression of mutant CryAB in cardiac tissue further impaired heart performance, closely paralleling human cardiomyopathy phenotypes [175].

Together, these studies underscore the pathological importance of CryAB mutations in cardiac disease, particularly through mechanisms involving protein aggregation and cytoskeletal disruption. However, the precise molecular pathways linking CryAB dysfunction to cardiomyopathy progression remain unresolved, leaving critical gaps in our understanding of how these mutations drive disease.

1.10 Amyloid fiber formation and diseases

Protein misfolding and aggregation are central to many degenerative diseases [176]. While most research in this area focuses on neurodegenerative disorders—such as Alzheimer's disease, Parkinson's disease, and amyotrophic lateral sclerosis (ALS)—muscle diseases, including CryAB-related myopathies, also display pathological protein aggregation [123, 177]. In neurodegeneration, hallmark proteins such as amyloid-β, Tau, α-synuclein, and huntingtin form insoluble fibrillar deposits known as amyloid plaques [177-179]. Similar amyloid-like deposits

have been observed in the muscle tissue of CryAB-related myopathies, though evidence remains limited.

Amyloid fibril formation can occur through several mechanisms: 1) Self-association of monomers. 2) Aggregation of conformationally altered proteins. 3) Nucleation-dependent pathways. 4) Nucleation-independent pathways. 5) Aggregation via chemical modifications or degradation. The nucleation-dependent pathway is the most common and involves a lag phase (nucleation), a rapid elongation phase (fibril growth and fragmentation), and a stationary phase (mature fibril accumulation) [177, 180, 181]. CryAB, under physiological conditions, acts as a molecular chaperone; however, under pathological stress or mutation, it can misfold and enter amyloidogenic pathways—particularly mechanisms 1, 2, 3, and 5.

Mutations such as R120G and D109A destabilize CryAB's structure, exposing hydrophobic residues that promote aggregation [123, 139]. These misfolded species serve as seeds for nucleation-dependent fibrillogenesis. Chemical modifications—including oxidation, phosphorylation, and truncation—further exacerbate aggregation, particularly in aged or stressed cells. *In vitro*, both wild-type CryAB and its R120G mutant can form amyloid fibrils , though wild-type CryAB generally maintains dynamic oligomers with chaperone activity [182]. Stress can shift this balance toward monomer release and misfolding. In parallel, desmin mutants have been shown to form amyloid fibrils that physically interact with CryAB oligomers [183].

In vivo, CryAB aggregates frequently co-localize with desmin and ubiquitin, indicating impaired proteostasis involving both the ubiquitin-proteasome system and autophagy [184]. Notably, desmin amino acids 117–348 form a core amyloidogenic region, explaining its strong pathological synergy with CryAB mutations in disrupting cardiac function [173]. Different CryAB mutations associate with distinct cardiomyopathy subtypes—including restrictive, hypertrophic,

and dilated forms—in animal models [185]. However, clear evidence of bona fide amyloid fibrils in CryAB-related diseases *in vivo* is still lacking, and the amyloid characteristics of CryAB aggregates in muscle remain poorly defined.

1.11 Multi-vesicular bodies and extracellular vesicles related to the amyloid pathogenic propagation.

Extracellular vehicles (EVs) are membrane-bound particles that mediate intercellular communication by transporting proteins, lipids, and nucleic acids between cells [186-188]. They are classified primarily by size: exosomes (30–150 nm), microvesicles (100–1,000 nm), apoptotic bodies (100–5,000 nm), and oncosomes (up to 10 μm). EVs originate either from the endosomal pathway—forming multivesicular bodies (MVBs)—or from plasma membrane budding, before being released into the extracellular space [187, 188]. Beyond normal signaling, EVs also play pathogenic roles by transferring toxic or misfolded proteins to healthy cells. In neurodegenerative diseases, EVs have been shown to transport amyloid species between neurons, contributing to disease spread; such vesicles can even be detected in blood as potential biomarkers [189, 190]. In cardiovascular disease, EV-mediated communication between cardiomyocytes and fibroblasts contributes to cardiac hypertrophy, with EV protein cargo serving as diagnostic markers for hypertrophy or heart failure [191, 192].

Given that CryAB mutations cause cardiomyopathies—including hypertrophic and dilated forms—there is growing interest in their potential relationship with EV biology. However, only limited studies have explored this link. In age-related macular degeneration disease (AMD), studies conducted in 2010 using human polarized retinal pigment epithelium cell noticed CryAB could be secreted through exosome pathway which plays the protection role in adjacent cells [193].

In 2016, one study reported that CryAB phosphorylation negatively regulates exosome release in glioma cells. Single-cell transcriptomics of cardiac exosomes from diseased mouse hearts later revealed an enrichment of stress-related proteins, including CryAB [194]. Nevertheless, EV involvement in CryAB-related muscle diseases remains largely unexplored.

Several factors contribute to this gap: muscle lesions in myopathies are often focal and difficult to capture via biopsy; conventional muscle sampling typically targets longitudinal fiber sections, missing surface pathology; and research focus tends to prioritize upstream nervous system defects over intrinsic muscle pathology. As a result, the relationship between CryAB amyloid pathology and EV-mediated protein transfer in myofibrillar myopathies remains poorly understood, which is the focus of my investigation in Chapter 4.

Characterization of Muscle Driver Expression Patterns:

During the investigation of NUAK protein mutations and their effects on muscle growth and development, various genetic drivers were employed to precisely control the temporal expression of the mutant genes. However, during the manuscript review process, the reviewers requested citations specifying the exact temporal expression patterns of these muscle drivers (*Mef2*-GAL4, *C57*-GAL4 and *G7*-Gal4). At that time, only textual descriptions from early literature—dating back to the 19th century—were available, lacking accompanying visual or quantitative data. To address these data gaps, Chapter 3 presents comprehensive spatiotemporal expression data for the muscle drivers utilized in this study, thereby providing a foundational reference for future research employing these drivers.

1.12 References

1. Lieber, R.L., *Skeletal muscle structure, function, and plasticity*. 2002: Lippincott Williams & Wilkins.
2. Frontera, W.R. and J. Ochala, *Skeletal muscle: a brief review of structure and function.* Calcified tissue international, 2015. **96**(3): p. 183-195.
3. Deshmukh, A.S., et al., *Deep Proteomics of Mouse Skeletal Muscle Enables Quantitation of Protein Isoforms, Metabolic Pathways, and Transcription Factors*[S].* Molecular & Cellular Proteomics, 2015. **14**(4): p. 841-853.
4. Yuan, C., et al., *Potential of Drosophila melanogaster (fruit fly) as a dietary protein source for broilers.* Journal of Animal Science, 2022. **100**(11): p. skac290.
5. Listrat, A., et al., *How muscle structure and composition influence meat and flesh quality.* The scientific world journal, 2016. **2016**(1): p. 3182746.
6. Liu, Z., et al., *The regulation of body and skeletal muscle protein metabolism by hormones and amino acids.* The Journal of nutrition, 2006. **136**(1): p. 212S-217S.
7. Ebashi, S., M. Endo, and I. Ohtsuki, *Control of muscle contraction.* Quarterly reviews of biophysics, 1969. **2**(4): p. 351-384.
8. Bagshaw, C.R., *Muscle contraction*. 1993: Springer Science & Business Media.
9. Geeves, M.A. and K.C. Holmes, *Structural mechanism of muscle contraction.* Annual review of biochemistry, 1999. **68**(1): p. 687-728.
10. Sweeney, H.L. and D.W. Hammers, *Muscle contraction.* Cold Spring Harbor perspectives in biology, 2018. **10**(2): p. a023200.
11. Sabourin, L.A. and M.A. Rudnicki, *The molecular regulation of myogenesis.* Clinical genetics, 2000. **57**(1): p. 16-25.
12. Bentzinger, C.F., Y.X. Wang, and M.A. Rudnicki, *Building muscle: molecular regulation of myogenesis.* Cold Spring Harbor perspectives in biology, 2012. **4**(2): p. a008342.
13. Chal, J. and O. Pourquié, *Making muscle: skeletal myogenesis in vivo and in vitro.* Development, 2017. **144**(12): p. 2104-2122.
14. Grefte, S., et al., *Skeletal muscle development and regeneration.* Stem cells and development, 2007. **16**(5): p. 857-868.
15. Dayanidhi, S. and R.L. Lieber, *Skeletal muscle satellite cells: mediators of muscle growth during development and implications for developmental disorders.* Muscle & nerve, 2014. **50**(5): p. 723-732.
16. Nabeshima, Y., et al., *Myogenin gene disruption results in perinatal lethality because of severe muscle defect.* Nature, 1993. **364**(6437): p. 532-535.
17. Burkholder, T.J. and R.L. Lieber, *Sarcomere length operating range of vertebrate muscles during movement.* Journal of Experimental Biology, 2001. **204**(9): p. 1529-1536.
18. Ertbjerg, P. and E. Puolanne, *Muscle structure, sarcomere length and influences on meat quality: A review.* Meat science, 2017. **132**: p. 139-152.
19. Chen, B., et al., *Cellular strategies of protein quality control.* Cold Spring Harbor perspectives in biology, 2011. **3**(8): p. a004374.
20. Sontag, E.M., R.S. Samant, and J. Frydman, *Mechanisms and functions of spatial protein quality control.* Annual review of biochemistry, 2017. **86**: p. 97-122.
21. Bukau, B., J. Weissman, and A. Horwich, *Molecular chaperones and protein quality control.* Cell, 2006. **125**(3): p. 443-451.

22. Sharp, F.R., S.M. Massa, and R.A. Swanson, *Heat-shock protein protection.* Trends in neurosciences, 1999. **22**(3): p. 97-99.
23. Schlesinger, M.J., *Heat shock proteins: the search for functions.* The Journal of cell biology, 1986. **103**(2): p. 321-325.
24. Lindquist, S. and E.A. Craig, *The heat-shock proteins.* Annual review of genetics, 1988. **22**(1): p. 631-677.
25. Li, Z. and P. Srivastava, *Heat-shock proteins.* Current protocols in immunology, 2003. **58**(1): p. A. 1T. 1-A. 1T. 6.
26. Klemenz, R., et al., *Alpha B-crystallin is a small heat shock protein.* Proceedings of the National Academy of Sciences, 1991. **88**(9): p. 3652-3656.
27. Horwitz, J., *Alpha-crystallin.* Experimental eye research, 2003. **76**(2): p. 145-153.
28. Csermely, P. and C.R. Kahn, *The 90-kDa heat shock protein (hsp-90) possesses an ATP binding site and autophosphorylating activity.* Journal of Biological Chemistry, 1991. **266**(8): p. 4943-4950.
29. Mallouk, Y., et al., *Heat shock protein 70 and ATP as partners in cell homeostasis.* International journal of molecular medicine, 1999. **4**(5): p. 463-537.
30. Mitra, R., et al., *ATP-independent chaperones.* Annual Review of Biophysics, 2022. **51**(1): p. 409-429.
31. Ciechanover, A., *The ubiquitin–proteasome pathway: on protein death and cell life.* The EMBO journal, 1998.
32. Lecker, S.H., A.L. Goldberg, and W.E. Mitch, *Protein degradation by the ubiquitin–proteasome pathway in normal and disease states.* Journal of the American society of nephrology, 2006. **17**(7): p. 1807-1819.
33. Bence, N.F., R.M. Sampat, and R.R. Kopito, *Impairment of the ubiquitin-proteasome system by protein aggregation.* Science, 2001. **292**(5521): p. 1552-1555.
34. Mizushima, N., *Autophagy: process and function.* Genes & development, 2007. **21**(22): p. 2861-2873.
35. Glick, D., S. Barth, and K.F. Macleod, *Autophagy: cellular and molecular mechanisms.* The Journal of pathology, 2010. **221**(1): p. 3-12.
36. Mizushima, N., *The ATG conjugation systems in autophagy.* Current opinion in cell biology, 2020. **63**: p. 1-10.
37. Lee, Y.-K. and J.-A. Lee, *Role of the mammalian ATG8/LC3 family in autophagy: differential and compensatory roles in the spatiotemporal regulation of autophagy.* BMB reports, 2016. **49**(8): p. 424.
38. Shpilka, T., et al., *Atg8: an autophagy-related ubiquitin-like protein family.* Genome biology, 2011. **12**(7): p. 226.
39. Tanida, I., T. Ueno, and E. Kominami, *LC3 and autophagy*, in *Autophagosome and phagosome*. 2008, Springer. p. 77-88.
40. Tanida, I., T. Ueno, and E. Kominami, *LC3 conjugation system in mammalian autophagy.* The international journal of biochemistry & cell biology, 2004. **36**(12): p. 2503-2518.
41. Lamark, T., S. Svenning, and T. Johansen, *Regulation of selective autophagy: the p62/SQSTM1 paradigm.* Essays in biochemistry, 2017. **61**(6): p. 609-624.
42. Bjørkøy, G., et al., *Monitoring autophagic degradation of p62/SQSTM1.* Methods in enzymology, 2009. **452**: p. 181-197.
43. Nair, K.S., *Aging muscle.* The American journal of clinical nutrition, 2005. **81**(5): p. 953-963.

44. Distefano, G. and B.H. Goodpaster, *Effects of exercise and aging on skeletal muscle.* Cold Spring Harbor perspectives in medicine, 2018. **8**(3): p. a029785.
45. Price, S.R. and W.E. Mitch, *Mechanisms stimulating protein degradation to cause muscle atrophy.* Current Opinion in Clinical Nutrition & Metabolic Care, 1998. **1**(1): p. 79-83.
46. Yiu, E.M. and A.J. Kornberg, *Duchenne muscular dystrophy.* J Paediatr Child Health, 2015. **51**(8): p. 759-64.
47. Rennie, M., et al., *Effects of Duchenne muscular dystrophy on muscle protein synthesis.* Nature, 1982. **296**(5853): p. 165-167.
48. Evans, W.J., *Skeletal muscle loss: cachexia, sarcopenia, and inactivity.* The American journal of clinical nutrition, 2010. **91**(4): p. 1123S-1127S.
49. Tan, K.T., S.T.J. Ang, and S.Y. Tsai, *Sarcopenia: tilting the balance of protein homeostasis.* Proteomics, 2020. **20**(5-6): p. 1800411.
50. Loeffler, J.P., et al., *The role of skeletal muscle in amyotrophic lateral sclerosis.* Brain Pathology, 2016. **26**(2): p. 227-236.
51. Nakano, S., et al., *Myofibrillar myopathy with abnormal foci of desmin positivity. I. Light and electron microscopy analysis of 10 cases.* Journal of Neuropathology & Experimental Neurology, 1996. **55**(5): p. 549-562.
52. Selcen, D. and A.G. Engel, *Myofibrillar myopathies.* Handbook of clinical neurology, 2011. **101**: p. 143-154.
53. Selcen, D., K. Ohno, and A.G. Engel, *Myofibrillar myopathy: clinical, morphological and genetic studies in 63 patients.* Brain, 2004. **127**(2): p. 439-451.
54. Goldfarb, L.G., et al., *Missense mutations in desmin associated with familial cardiac and skeletal myopathy.* Nature genetics, 1998. **19**(4): p. 402-403.
55. Muñoz-Mármol, A.M., et al., *A dysfunctional desmin mutation in a patient with severe generalized myopathy.* Proceedings of the National Academy of Sciences, 1998. **95**(19): p. 11312-11317.
56. Dalakas, M.C., et al., *Desmin myopathy, a skeletal myopathy with cardiomyopathy caused by mutations in the desmin gene.* New England Journal of Medicine, 2000. **342**(11): p. 770-780.
57. Vicart, P., et al., *A missense mutation in the αB-crystallin chaperone gene causes a desmin-related myopathy.* Nature genetics, 1998. **20**(1): p. 92-95.
58. Selcen, D. and A.G. Engel, *Myofibrillar myopathy caused by novel dominant negative αB-crystallin mutations.* Annals of Neurology: Official Journal of the American Neurological Association and the Child Neurology Society, 2003. **54**(6): p. 804-810.
59. Selcen, D. and A.G. Engel, *Mutations in ZASP define a novel form of muscular dystrophy in humans.* Annals of neurology, 2005. **57**(2): p. 269-276.
60. Griggs, R., et al., *Zaspopathy in a large classic late-onset distal myopathy family.* Brain, 2007. **130**(6): p. 1477-1484.
61. Vorgerd, M., et al., *A mutation in the dimerization domain of filamin c causes a novel type of autosomal dominant myofibrillar myopathy.* The American Journal of Human Genetics, 2005. **77**(2): p. 297-304.
62. Kley, R.A., et al., *Clinical and morphological phenotype of the filamin myopathy: a study of 31 German patients.* Brain, 2007. **130**(12): p. 3250-3264.
63. Selcen, D., et al., *Reducing bodies and myofibrillar myopathy features in FHL1 muscular dystrophy.* Neurology, 2011. **77**(22): p. 1951-1959.

64. Pfeffer, G., et al., *Titin founder mutation is a common cause of myofibrillar myopathy with early respiratory failure.* Journal of Neurology, Neurosurgery & Psychiatry, 2014. **85**(3): p. 331-338.
65. Harms, M.B., et al., *Exome sequencing reveals DNAJB6 mutations in dominantly-inherited myopathy.* Annals of neurology, 2012. **71**(3): p. 407-416.
66. Dubińska-Magiera, M., et al., *Characterization of Hspb8 in zebrafish.* Cells, 2020. **9**(6): p. 1562.
67. Roberts, D.B., *Drosophila melanogaster: the model organism.* Entomologia experimentalis et applicata, 2006. **121**(2): p. 93-103.
68. Baylies, M.K., M. Bate, and M.R. Gomez, *Myogenesis: a view from Drosophila.* Cell, 1998. **93**(6): p. 921-927.
69. Ruiz-Gómez, M., *Muscle patterning and specification in Drosophila.* Int J Dev Biol, 1998. **42**(3): p. 283-90.
70. Rai, M., U. Nongthomba, and M.D. Grounds, *Skeletal muscle degeneration and regeneration in mice and flies.* Current topics in developmental biology, 2014. **108**: p. 247-281.
71. Rout, P., M. Preußner, and S.F. Önel, *Drosophila melanogaster: a model system to study distinct genetic programs in myoblast fusion.* Cells, 2022. **11**(3): p. 321.
72. Bate, M., *The embryonic development of larval muscles in Drosophila.* Development, 1990. **110**(3): p. 791-804.
73. Weitkunat, M. and F. Schnorrer, *A guide to study Drosophila muscle biology.* Methods, 2014. **68**(1): p. 2-14.
74. Fernandes, J., M. Bate, and K. Vijayraghavan, *Development of the indirect flight muscles of Drosophila.* Development, 1991. **113**(1): p. 67-77.
75. Bothe, I. and M.K. Baylies, *Drosophila myogenesis.* Curr Biol, 2016. **26**(17): p. R786-91.
76. Fischer, J.A., et al., *GAL4 activates transcription in Drosophila.* Nature, 1988. **332**(6167): p. 853-6.
77. Lilly, B., et al., *D-MEF2: a MADS box transcription factor expressed in differentiating mesoderm and muscle cell lineages during Drosophila embryogenesis.* Proc Natl Acad Sci U S A, 1994. **91**(12): p. 5662-6.
78. Zhao, Z. and E.R. Geisbrecht, *Stage-specific modulation of Drosophila gene expression with muscle GAL4 promoters.* Fly, 2025. **19**(1): p. 2447617.
79. Bassett, A.R., et al., *Highly efficient targeted mutagenesis of Drosophila with the CRISPR/Cas9 system.* Cell reports, 2013. **4**(1): p. 220-228.
80. Steinberg, G.R. and B.E. Kemp, *AMPK in health and disease.* Physiological reviews, 2009. **89**(3): p. 1025-1078.
81. Herzig, S. and R.J. Shaw, *AMPK: guardian of metabolism and mitochondrial homeostasis.* Nature reviews Molecular cell biology, 2018. **19**(2): p. 121-135.
82. Bright, N., C. Thornton, and D. Carling, *The regulation and function of mammalian AMPK-related kinases.* Acta physiologica, 2009. **196**(1): p. 15-26.
83. Sakamoto, K., et al., *Activity of LKB1 and AMPK-related kinases in skeletal muscle: effects of contraction, phenformin, and AICAR.* American Journal of Physiology-Endocrinology and Metabolism, 2004. **287**(2): p. E310-E317.
84. Jaleel, M., et al., *The ubiquitin-associated domain of AMPK-related kinases regulates conformation and LKB1-mediated phosphorylation and activation.* Biochemical Journal, 2006. **394**(3): p. 545-555.

85. Hawley, S.A., et al., *Complexes between the LKB1 tumor suppressor, STRADα/β and MO25α/β are upstream kinases in the AMP-activated protein kinase cascade.* Journal of biology, 2003. **2**(4): p. 28.
86. Sun, X., et al., *The regulation and function of the NUAK family.* Journal of molecular endocrinology, 2013. **51**(2): p. R15-R22.
87. Zagórska, A., et al., *New roles for the LKB1-NUAK pathway in controlling myosin phosphatase complexes and cell adhesion.* Science signaling, 2010. **3**(115): p. ra25-ra25.
88. Bennison, S.A., X. Liu, and K. Toyo-Oka, *Nuak kinase signaling in development and disease of the central nervous system.* Cellular signalling, 2022. **100**: p. 110472.
89. Hirano, M., et al., *A new serine/threonine protein kinase, Omphk1, essential to ventral body wall formation.* Developmental dynamics, 2006. **235**(8): p. 2229-2237.
90. Ohmura, T., et al., *Neural tube defects by NUAK1 and NUAK2 double mutation.* Developmental Dynamics, 2012. **241**(8): p. 1350-1364.
91. Bonnard, C., et al., *A loss-of-function NUAK2 mutation in humans causes anencephaly due to impaired Hippo-YAP signaling.* Journal of Experimental Medicine, 2020. **217**(12): p. e20191561.
92. Matsumura, F. and D.J. Hartshorne, *Myosin phosphatase target subunit: Many roles in cell function.* Biochemical and biophysical research communications, 2008. **369**(1): p. 149-156.
93. Hoppe, P.E., et al., *Caenorhabditis elegans unc-82 encodes a serine/threonine kinase important for myosin filament organization in muscle during growth.* Genetics, 2010. **184**(1): p. 79-90.
94. Schiller, N.R., et al., *The role of the UNC-82 protein kinase in organizing myosin filaments in striated muscle of Caenorhabditis elegans.* Genetics, 2017. **205**(3): p. 1195-1213.
95. Schiller, N.R., S.A. Almuhanna, and P.E. Hoppe, *UNC-82/NUAK kinase is required by myosin A, but not myosin B, to assemble and function in the thick filament arms of C. elegans striated muscle.* Cytoskeleton, 2024. **81**(12): p. 753-774.
96. Inazuka, F., et al., *Muscle-specific knock-out of NUAK family SNF1-like kinase 1 (NUAK1) prevents high fat diet-induced glucose intolerance.* Journal of Biological Chemistry, 2012. **287**(20): p. 16379-16389.
97. Brooks, D., et al., *Drosophila NUAK functions with Starvin/BAG3 in autophagic protein turnover.* PLoS Genet, 2020. **16**(4): p. e1008700.
98. Suzuki, A., et al., *Identification of a novel protein kinase mediating Akt survival signaling to the ATM protein.* Journal of Biological Chemistry, 2003. **278**(1): p. 48-53.
99. Hou, X., et al., *A new role of NUAK1: directly phosphorylating p53 and regulating cell proliferation.* Oncogene, 2011. **30**(26): p. 2933-2942.
100. Chen, P., et al., *High NUAK1 expression correlates with poor prognosis and involved in NSCLC cells migration and invasion.* Experimental lung research, 2013. **39**(1): p. 9-17.
101. Xiong, X., et al., *MiR-145 functions as a tumor suppressor targeting NUAK1 in human intrahepatic cholangiocarcinoma.* Biochemical and biophysical research communications, 2015. **465**(2): p. 262-269.
102. Suzuki, A., T. Ogura, and H. Esumi, *NDR2 acts as the upstream kinase of ARK5 during insulin-like growth factor-1 signaling.* Journal of Biological Chemistry, 2006. **281**(20): p. 13915-13921.
103. Ma, S., et al., *The Hippo pathway: biology and pathophysiology.* Annual review of biochemistry, 2019. **88**(1): p. 577-604.

104. Humbert, N., et al., *Regulation of ploidy and senescence by the AMPK-related kinase NUAK1.* The EMBO journal, 2010. **29**(2): p. 376-386.
105. van de Vis, R.A., A. Moustakas, and L.P. van der Heide, *NUAK1 And NUAK2 fine-tune TGF-β signaling.* Cancers, 2021. **13**(13): p. 3377.
106. Tzavlaki, K. and A. Moustakas, *TGF-β Signaling.* Biomolecules, 2020. **10**(3): p. 487.
107. Kang, J.S., C. Liu, and R. Derynck, *New regulatory mechanisms of TGF-β receptor function.* Trends in cell biology, 2009. **19**(8): p. 385-394.
108. Massagué, J. and R.R. Gomis, *The logic of TGFβ signaling.* FEBS letters, 2006. **580**(12): p. 2811-2820.
109. Moustakas, A. and C.-H. Heldin, *The regulation of TGFβ signal transduction.* Development, 2009. **136**(22): p. 3699-3714.
110. Kolliopoulos, C., et al., *Transforming growth factor β (TGFβ) induces NUAK kinase expression to fine-tune its signaling output.* Journal of Biological Chemistry, 2019. **294**(11): p. 4119-4136.
111. Banerjee, S., et al., *Interplay between Polo kinase, LKB1-activated NUAK1 kinase, PP1βMYPT1 phosphatase complex and the SCFβTrCP E3 ubiquitin ligase.* Biochemical Journal, 2014. **461**(2): p. 233-245.
112. Banerjee, S., et al., *Characterization of WZ4003 and HTH-01-015 as selective inhibitors of the LKB1-tumour-suppressor-activated NUAK kinases.* Biochemical Journal, 2014. **457**(1): p. 215-225.
113. Lasagna-Reeves, C.A., et al., *Reduction of Nuak1 decreases tau and reverses phenotypes in a tauopathy mouse model.* Neuron, 2016. **92**(2): p. 407-418.
114. Ando, K., et al., *Tau phosphorylation at Alzheimer's disease-related Ser356 contributes to tau stabilization when PAR-1/MARK activity is elevated.* Biochemical and biophysical research communications, 2016. **478**(2): p. 929-934.
115. Fulda, S., et al., *Cellular stress responses: cell survival and cell death.* International journal of cell biology, 2010. **2010**(1): p. 214074.
116. Hightower, L.E., *Heat shock, stress proteins, chaperones, and proteotoxicity.* Cell, 1991. **66**(2): p. 191-197.
117. Salinthone, S., M. Tyagi, and W.T. Gerthoffer, *Small heat shock proteins in smooth muscle.* Pharmacology & therapeutics, 2008. **119**(1): p. 44-54.
118. Jakob, U., et al., *Small heat shock proteins are molecular chaperones.* Journal of Biological Chemistry, 1993. **268**(3): p. 1517-1520.
119. Spector, A., et al., *cAMP-dependent phosphorylation of bovine lens alpha-crystallin.* Proceedings of the National Academy of Sciences, 1985. **82**(14): p. 4712-4716.
120. Horwitz, J., et al., *Lens α-crystallin: function and structure.* Eye, 1999. **13**(3): p. 403-408.
121. Graw, J., *Genetics of crystallins: cataract and beyond.* Experimental eye research, 2009. **88**(2): p. 173-189.
122. Simon, S., et al., *Myopathy-associated αB-crystallin Mutants.* Journal of Biological Chemistry, 2007. **282**(47): p. 34276-34287.
123. Sacconi, S., et al., *A novel CRYAB mutation resulting in multisystemic disease.* Neuromuscular Disorders, 2012. **22**(1): p. 66-72.
124. Fichna, J.P., et al., *A novel dominant D109A CRYAB mutation in a family with myofibrillar myopathy affects αB-crystallin structure.* BBA clinical, 2017. **7**: p. 1-7.
125. Del Bigio, M.R., et al., *Infantile muscular dystrophy in Canadian aboriginals is an αb-crystallinopathy.* Annals of neurology, 2011. **69**(5): p. 866-871.

126. Chen, Q., et al., *A novel mutation in CRYAB associated with autosomal dominant congenital nuclear cataract in a Chinese family.* Molecular vision, 2009. **15**: p. 1359.
127. Liu, M., et al., *Identification of a CRYAB mutation associated with autosomal dominant posterior polar cataract in a Chinese family.* Investigative ophthalmology & visual science, 2006. **47**(8): p. 3461-3466.
128. Safieh, L.A., A. Khan, and F. Alkuraya, *Identification of a novel CRYAB mutation associated with autosomal recessive juvenile cataract in a Saudi family.* Molecular Vision, 2009. **15**: p. 980.
129. Sun, W., et al., *Mutation analysis of 12 genes in Chinese families with congenital cataracts.* Molecular vision, 2011. **17**: p. 2197.
130. Brodehl, A., et al., *The novel αB-crystallin (CRYAB) mutation p. D109G causes restrictive cardiomyopathy.* Human mutation, 2017. **38**(8): p. 947-952.
131. Chou, C., et al., *A novel αB-crystallin R123W variant drives hypertrophic cardiomyopathy by promoting maladaptive calcium-dependent signal transduction.* Frontiers in Cardiovascular Medicine, 2023. **10**: p. 1223244.
132. Liu, Y., et al., *A novel αB-crystallin mutation associated with autosomal dominant congenital lamellar cataract.* Investigative ophthalmology & visual science, 2006. **47**(3): p. 1069-1075.
133. Reilich, P., et al., *The p. G154S mutation of the alpha-B crystallin gene (CRYAB) causes late-onset distal myopathy.* Neuromuscular Disorders, 2010. **20**(4): p. 255-259.
134. Inagaki, N., et al., *αB-crystallin mutation in dilated cardiomyopathy.* Biochemical and biophysical research communications, 2006. **342**(2): p. 379-386.
135. Devi, R.R., et al., *Crystallin gene mutations in Indian families with inherited pediatric cataract.* Molecular vision, 2008. **14**: p. 1157.
136. Claeys, K.G., et al., *Electron microscopy in myofibrillar myopathies reveals clues to the mutated gene.* Neuromuscular Disorders, 2008. **18**(8): p. 656-666.
137. Jehle, S., et al., *Solid-state NMR and SAXS studies provide a structural basis for the activation of αB-crystallin oligomers.* Nature structural & molecular biology, 2010. **17**(9): p. 1037-1042.
138. Bakthisaran, R., et al., *Phosphorylation of αB-crystallin: Role in stress, aging and pathophysiological conditions.* Biochimica et Biophysica Acta (BBA)-General Subjects, 2016. **1860**(1): p. 167-182.
139. Hafizi, M., et al., *Structural and functional studies of D109A human αB-crystallin contributing to the development of cataract and cardiomyopathy diseases.* PloS one, 2021. **16**(11): p. e0260306.
140. Quinlan, R.A., et al., *Changes in the quaternary structure and function of MjHSP16. 5 attributable to deletion of the IXI motif and introduction of the substitution, R107G, in the α-crystallin domain.* Philosophical Transactions of the Royal Society B: Biological Sciences, 2013. **368**(1617): p. 20120327.
141. McFarland, R., et al., *Dynamic fibrillar assembly of αB-crystallin induced by perturbation of the conserved NT-IXI motif resolved by cryo-EM.* Nature communications, 2024. **15**(1): p. 10336.
142. Nasiri, P., et al., *The biochemical association between R157H mutation in human αB-crystallin and development of cardiomyopathy: Structural and functional analyses of the mutant protein.* Biochimie, 2021. **190**: p. 36-49.

143. Gopal-Srivastava, R., W.T. Kays, and J. Piatigorsky, *Enhancer-independent promoter activity of the mouse αB-crystallin/small heat shock protein gene in the lens and cornea of transgenic mice.* Mechanisms of development, 2000. **92**(2): p. 125-134.
144. Scheier, B., et al., *Glucocorticoids regulate the expression of the stressprotein alpha B-crystallin.* Molecular and cellular endocrinology, 1996. **123**(2): p. 187-198.
145. Manukyan, I., et al., *Cross-talk between calcineurin/NFAT and Jak/STAT signalling induces cardioprotective αB-crystallin gene expression in response to hypertrophic stimuli.* Journal of Cellular and Molecular Medicine, 2010. **14**(6b): p. 1707-1716.
146. Gopal-Srivastava, R. and J. Piatigorsky, *Identification of a lens-specific regulatory region (LSR) of the murine αB-crystallin gene.* Nucleic acids research, 1994. **22**(7): p. 1281-1286.
147. Weintraub, H., S. Hauschka, and S.J. Tapscott, *The MCK enhancer contains a p53 responsive element.* Proceedings of the National Academy of Sciences, 1991. **88**(11): p. 4570-4571.
148. Haynes II, J.I., R. Gopal-Srivastava, and J. Piatigorsky, *αB-crystallin TATA sequence mutations: lens-preference for the proximal TATA box and the distal TATA-like sequence in transgenic mice.* Biochemical and biophysical research communications, 1997. **241**(2): p. 407-413.
149. Kantorow, M. and J. Piatigorsky, *Phosphorylations of αA-and αB-crystallin.* International journal of biological macromolecules, 1998. **22**(3-4): p. 307-314.
150. Ito, H., et al., *Phosphorylation of αB-crystallin in response to various types of stress.* Journal of Biological Chemistry, 1997. **272**(47): p. 29934-29941.
151. Ito, H., et al., *Phosphorylation-induced change of the oligomerization state of αB-crystallin.* Journal of Biological Chemistry, 2001. **276**(7): p. 5346-5352.
152. Ahmad, M.F., et al., *Effect of phosphorylation on αB-crystallin: differences in stability, subunit exchange and chaperone activity of homo and mixed oligomers of αB-crystallin and its phosphorylation-mimicking mutant.* Journal of molecular biology, 2008. **375**(4): p. 1040-1051.
153. Peschek, J., et al., *Regulated structural transitions unleash the chaperone activity of αB-crystallin.* Proceedings of the National Academy of Sciences, 2013. **110**(40): p. E3780-E3789.
154. Koteiche, H.A. and H.S. Mchaourab, *Mechanism of chaperone function in small heat-shock proteins: phosphorylation-induced activation of two-mode binding in αB-crystallin.* Journal of Biological Chemistry, 2003. **278**(12): p. 10361-10367.
155. Ecroyd, H., et al., *Mimicking phosphorylation of αB-crystallin affects its chaperone activity.* Biochemical Journal, 2007. **401**(1): p. 129-141.
156. Reed, J.C., *Mechanisms of apoptosis.* The American journal of pathology, 2000. **157**(5): p. 1415-1430.
157. Häcker, G., *The morphology of apoptosis.* Cell and tissue research, 2000. **301**(1): p. 5-17.
158. Hongmei, Z., *Extrinsic and intrinsic apoptosis signal pathway review*, in *Apoptosis and medicine*. 2012, InTechOpen.
159. Xu, F., et al., *αB-crystallin regulates oxidative stress-induced apoptosis in cardiac H9c2 cells via the PI3K/AKT pathway.* Molecular biology reports, 2013. **40**(3): p. 2517-2526.
160. Mao, Y., et al., *Human αA-and αB-crystallins bind to Bax and Bcl-XS to sequester their translocation during staurosporine-induced apoptosis.* Cell Death & Differentiation, 2004. **11**(5): p. 512-526.

161. Hu, W.-F., et al., *αA-and αB-crystallins interact with caspase-3 and Bax to guard mouse lens development.* Current molecular medicine, 2012. **12**(2): p. 177-187.
162. Liu, S., et al., *As a novel p53 direct target, bidirectional gene HspB2/αB-crystallin regulates the ROS level and Warburg effect.* Biochimica et Biophysica Acta (BBA)-Gene Regulatory Mechanisms, 2014. **1839**(7): p. 592-603.
163. Zhang, J., et al., *Progression of the role of CRYAB in signaling pathways and cancers.* OncoTargets and therapy, 2019: p. 4129-4139.
164. Liu, Y., et al., *Upregulation of alphaB-crystallin expression in the substantia nigra of patients with Parkinson's disease.* Neurobiology of aging, 2015. **36**(4): p. 1686-1691.
165. Link, C.D., et al., *Gene expression analysis in a transgenic Caenorhabditis elegans Alzheimer's disease model.* Neurobiology of aging, 2003. **24**(3): p. 397-413.
166. Steinman, L., *New targets for treatment of multiple sclerosis.* Journal of the neurological sciences, 2008. **274**(1-2): p. 1-4.
167. Marino, M., et al., *Differences in protein quality control correlate with phenotype variability in 2 mouse models of familial amyotrophic lateral sclerosis.* Neurobiology of Aging, 2015. **36**(1): p. 492-504.
168. van Noort, J.M., et al., *αB-crystallin is a target for adaptive immune responses and a trigger of innate responses in preactive multiple sclerosis lesions.* Journal of Neuropathology & Experimental Neurology, 2010. **69**(7): p. 694-703.
169. Quach, Q.L., et al., *CRYAB modulates the activation of CD4+ T cells from relapsing–remitting multiple sclerosis patients.* Multiple Sclerosis Journal, 2013. **19**(14): p. 1867-1877.
170. Wang, X., et al., *Expression of R120G–αB-crystallin causes aberrant desmin and αB-crystallin aggregation and cardiomyopathy in mice.* Circulation research, 2001. **89**(1): p. 84-91.
171. Maloyan, A., et al., *Mitochondrial dysfunction and apoptosis underlie the pathogenic process in α-B-crystallin desmin-related cardiomyopathy.* Circulation, 2005. **112**(22): p. 3451-3461.
172. Sanbe, A., et al., *Desmin-related cardiomyopathy in transgenic mice: a cardiac amyloidosis.* Proceedings of the National Academy of Sciences, 2004. **101**(27): p. 10132-10136.
173. Houck, S.A., et al., *Multiple sites in αB-crystallin modulate its interactions with desmin filaments assembled in vitro.* PloS one, 2011. **6**(11): p. e25859.
174. Hishiya, A., et al., *BAG3 directly interacts with mutated alphaB-crystallin to suppress its aggregation and toxicity.* PloS one, 2011. **6**(3): p. e16828.
175. Wójtowicz, I., et al., *Drosophila small heat shock protein CryAB ensures structural integrity of developing muscles, and proper muscle and heart performance.* Development, 2015. **142**(5): p. 994-1005.
176. Ross, C.A. and M.A. Poirier, *Protein aggregation and neurodegenerative disease.* Nature medicine, 2004. **10**(Suppl 7): p. S10-S17.
177. Benson, M.D., et al., *Amyloid nomenclature 2020: update and recommendations by the International Society of Amyloidosis (ISA) nomenclature committee.* Amyloid, 2020. **27**(4): p. 217-222.
178. Hayashi, H., et al., *A seed for Alzheimer amyloid in the brain.* Journal of Neuroscience, 2004. **24**(20): p. 4894-4902.

179. Rodrigue, K.M., K.M. Kennedy, and D.C. Park, *Beta-amyloid deposition and the aging brain.* Neuropsychology review, 2009. **19**: p. 436-450.
180. Ruschak, A.M. and A.D. Miranker, *Fiber-dependent amyloid formation as catalysis of an existing reaction pathway.* Proceedings of the National Academy of Sciences, 2007. **104**(30): p. 12341-12346.
181. Padrick, S.B. and A.D. Miranker, *Islet amyloid: phase partitioning and secondary nucleation are central to the mechanism of fibrillogenesis.* Biochemistry, 2002. **41**(14): p. 4694-4703.
182. Meehan, S., et al., *Characterisation of amyloid fibril formation by small heat-shock chaperone proteins human αA-, αB-and R120G αB-crystallins.* Journal of molecular biology, 2007. **372**(2): p. 470-484.
183. Sharma, S., et al., *αB-crystallin is a sensor for assembly intermediates and for the subunit topology of desmin intermediate filaments.* Cell Stress Chaperones, 2017. **22**(4): p. 613-626.
184. Wang, X., et al., *αB-crystallin modulates protein aggregation of abnormal desmin.* Circulation research, 2003. **93**(10): p. 998-1005.
185. Dimauro, I., et al., *The role of αB-crystallin in skeletal and cardiac muscle tissues.* Cell Stress and Chaperones, 2018. **23**(4): p. 491-505.
186. Yáñez-Mó, M., et al., *Biological properties of extracellular vesicles and their physiological functions.* Journal of extracellular vesicles, 2015. **4**(1): p. 27066.
187. El Andaloussi, S., et al., *Extracellular vesicles: biology and emerging therapeutic opportunities.* Nature reviews Drug discovery, 2013. **12**(5): p. 347-357.
188. Van der Pol, E., et al., *Classification, functions, and clinical relevance of extracellular vesicles.* Pharmacological reviews, 2012. **64**(3): p. 676-705.
189. Thompson, A.G., et al., *Extracellular vesicles in neurodegenerative disease—pathogenesis to biomarkers.* Nature Reviews Neurology, 2016. **12**(6): p. 346-357.
190. Hill, A.F., *Extracellular vesicles and neurodegenerative diseases.* Journal of Neuroscience, 2019. **39**(47): p. 9269-9273.
191. Boulanger, C.M., et al., *Extracellular vesicles in coronary artery disease.* Nature reviews cardiology, 2017. **14**(5): p. 259-272.
192. Jansen, F., G. Nickenig, and N. Werner, *Extracellular vesicles in cardiovascular disease: potential applications in diagnosis, prognosis, and epidemiology.* Circulation research, 2017. **120**(10): p. 1649-1657.
193. Sreekumar, P.G., et al., *αB crystallin is apically secreted within exosomes by polarized human retinal pigment epithelium and provides neuroprotection to adjacent cells.* PloS one, 2010. **5**(10): p. e12578.
194. Kore, R.A. and E.C. Abraham, *Phosphorylation negatively regulates exosome mediated secretion of cryAB in glioma cells.* Biochimica et Biophysica Acta (BBA)-Molecular Cell Research, 2016. **1863**(2): p. 368-377.

Chapter 2 - Identification of CryAB as a target of NUAK kinase activity in *Drosophila* muscle tissue

This chapter has been published as a journal article in the *Genetics*.

Ziwei Zhao[a], David Brooks[a], Yungui Guo[a], and Erika R. Geisbrecht[a, *]

[a]*Department of Biochemistry and Molecular Biophysics, Kansas State University, Manhattan, KS 66506, USA*

*Corresponding author: geisbrechte@ksu.edu

Keywords: Muscle, NUAK, CryAB, *Drosophila*

2.1 Abstract

Phosphorylation reactions performed by protein kinases are one of the most studied post-translational modifications within cells. Much is understood about conserved residues within protein kinase domains that perform catalysis of the phosphotransfer reaction, yet the identity of the target substrates and downstream biological effects vary widely among cells, tissues, and organisms. Here we characterize key residues essential for NUAK kinase activity in *Drosophila melanogaster* myogenesis and homeostasis. Creation of a *NUAK* kinase-dead mutation using CRISPR/Cas9 results in lethality at the embryo to larval transition, while loss of NUAK catalytic function later in development produces aggregation of the chaperone protein CryAB in muscle tissue. Yeast two-hybrid assays demonstrate a physical interaction between NUAK and CryAB. We further show that a phosphomimetic version of NUAK promotes the phosphorylation of CryAB and this post-translational modification occurs at two previously unidentified phosphosites that are conserved in the primary sequence of human CryAB. Mutation of these serine residues in *D. melanogaster* NUAK abolishes CryAB phosphorylation, thus proving their necessity at the biochemical level. These studies together highlight the importance of kinase activity regulation and provide a platform to further explore muscle tissue proteostasis.

2.2 Introduction

Protein kinases have broad functions in regulating molecular aspects of cell signaling as well as imparting diverse outputs in biological processes. While many substrates of kinase activity have been identified, there are hundreds of kinase-substrate pairs still waiting to be uncovered. Since the deregulation of kinase activity leads to cancer and other diseases, dissecting kinase-

substrate relationships is of great importance for the development of therapeutic targets. However, it is difficult to predict or extrapolate generalized phosphorylation events as many kinases are activated in response to varied extracellular insults and/or have tissue-specific targets.

Multiple approaches, each with their own advantages and limitations, exist to identify and verify protein kinase substrates [1]. Genetic screens can be performed to uncover candidate substrates that mimic and/or modify kinase mutant phenotypes. While genetic methods will identify kinase-substrate pairs that are physiologically or functionally relevant, these experiments must be followed up with biochemical verification. High throughput methods include peptide arrays, phage display, or mass spectrometry (MS)-based phosphoproteomic profiling [2-4]. Alternatively, computational approaches to predict phosphorylation motifs in addition to protein interaction-based screens such as yeast two-hybrid (Y2H) or affinity purification have been successfully utilized to uncover kinase substrates [1]. The gold standard for kinase-substrate verification is the *in vitro* kinase assay, whereby purified kinase is incubated with candidate substrate in the presence of ATP to detect phosphotransfer activity [5, 6]. Ultimately, all of these lines of inquiry are necessary to uncover and validate kinase-substrate pairs.

AMP-activated protein kinase (AMPK) is a phylogenetically conserved serine/threonine (S/T) kinase that senses cellular ATP levels and redirects metabolism based upon energy requirements [7-9]. Twelve additional AMPK-related protein kinases (NUAK1/2, BRSK1/2, QIK, QSK, SIK, MARK1/2/3/4, and MELK) have been identified that share extensive sequence homology with the catalytic kinase domain of AMPK, yet lack the regulatory subunits that mediate energy homeostasis [10, 11]. Phosphorylation of a conserved threonine in the T-loop region in the kinase domain of all AMPK-related protein kinases promotes activation of downstream physiological processes. With the exception of MELK, this phosphorylation can be mediated by

Liver kinase B1 (LKB1) [12, 13] or a handful of other kinases, although this regulation may be protein or context-dependent [10].

Mammalian NUAK1/ARK5 and NUAK2/SNARK can impact cytoskeletal rearrangement, insulin signaling, cell death, and cancer migration and metastasis [11, 14]. Based upon published literature and expression databases (https://www.proteinatlas.org/), both NUAK1 and NUAK2 show overlapping mRNA expression in multiple tissues [11, 14, 15]. However, *NUAK1 mRNA* is more highly enriched in brain and muscle, while *NUAK2 mRNA* is more predominant in the gastrointestinal tract and blood cells. Thus, expression alone does not provide insight into unique or redundant functions of NUAK1 or NUAK2. While TGF-β transcriptionally induces both *NUAK1* and *NUAK2* expression, each has opposing roles on outputs of this signaling pathway [16]. Independent roles for both proteins have been identified in skeletal muscle, whereby NUAK1 suppresses insulin-mediated glucose uptake and NUAK2 regulates contraction-stimulated glucose transport [17, 18]. These biological differences may be mediated by distinct phosphorylation events.

A handful of NUAK1 and/or NUAK2 kinase targets have been uncovered in various cell types, each with diverse downstream consequences. Shared substrates of both NUAK1 and NUAK2 kinase activity include Large tumor suppressor kinase 1 (LATS1) in human embryonic kidney (HEK) 293 cells and the Protein phosphatase 1 (PP1) subunit myosin phosphatase targeting protein (MYPT) in multiple cell types [19-21]. Ataxia telangiectasia-mutated (ATM) and p53 are additional target substrates of NUAK1 upon glucose starvation, among others [22, 23]. Despite this knowledge, many targets of NUAK activity remain to be identified.

Our lab has focused on deciphering biological roles of the *D. melanogaster* ortholog of mammalian NUAK1/2 [24, 25]. Relevant to this manuscript, *NUAK* mutants exhibit progressive

muscle degeneration concomitant with the impairment of autophagy [24]. In this study we further examined candidates that arose from a Y2H screen using NUAK as a bait protein and identified αB-crystallin, or CryAB/l(2)efl. We further show that NUAK kinase activity promotes CryAB phosphorylation and is essential to prevent CryAB accumulation in muscle tissue. Together, these data expand the spectrum of NUAK kinase targets and provide a molecular role for NUAK in the regulation of CryAB function.

2.3 Results

NUAK kinase activity is required throughout muscle development and growth

We previously characterized an ethyl methanesulfonate (EMS)-induced stop codon allele in the *Drosophila NUAK* (*NUAK*^{R829*}) gene for its role in autophagic protein degradation [24]. Since this mutation results in a stop codon that lies outside of the evolutionarily conserved kinase domain **(Figure 2.1 A)**, we sought to evaluate the contribution of NUAK kinase activity. CRISPR/Cas9 techniques were utilized to create a kinase-dead form of NUAK by mutating a conserved lysine residue required for catalytic activity (*NUAK*^{K99R}) [31, 32]. Sanger sequencing of PCR-amplified genomic DNA from heterozygous *NUAK*^{K99R}/+ individuals confirmed the presence of the desired nucleotide alteration (AAA→CGC) that resulted in a lysine to arginine (K→R) mutation in the active site **(Figure 2.1 B)**. This new allele provides an entryway to examine the direct contribution of NUAK kinase activity during *Drosophila* development.

Lethal phase analysis was performed to compare the relative allelic strength of the $NUAK^{R829*}$ or $NUAK^{K99R}$ mutations **(Figure 2.1 C)**. Both *WT* (w^{1118}/w^{1118} or w^{1118}/*Canton-S*) and heterozygous *NUAK* ($NUAK^{R829*}$/+ and $NUAK^{K99R}$/+) controls largely eclosed as adults, with some lethality occurring at the embryonic to L1 transition. The majority of homozygous $NUAK^{R829*}/NUAK^{R829*}$ individuals were lethal at the pupal stage, consistent with our previous characterization [24]. In contrast, approximately 60% of homozygous $NUAK^{K99R}/NUAK^{K99R}$ embryos failed to hatch into L1 larvae and did not survive to pupation. To assess if this embryonic lethality in our kinase-dead embryos may be due to abnormal myogenesis, we analyzed the musculature of stage 16 embryos. The stereotypical muscle pattern present in *WT* embryos **(Figure 2.1 D, left panel)** was largely preserved in $NUAK^{K99R}/NUAK^{K99R}$ embryos **(Figure 2.1 E, left panel)**, while occasionally we observed muscles that were narrower in width in mutant embryos (asterisks, inset). With no obvious defects in myoblast fusion or muscle patterning, we next assessed sarcomere formation. Analysis of *WT* L1 larvae soon after hatching revealed a regular spacing of sarcomeres marked by sls-GFP **(Figure 2.1 D, right panel)**. $NUAK^{K99R}/NUAK^{K99R}$ L1 larvae also showed relatively normal sarcomeres, but a higher prevalence of thinner muscles than observed in mutant embryos of the same genotype **(Figure 2.1 E, asterisks, inset)**. Embryonic muscles marked by sls-GFP showed no obvious difference in contractile ability in live imaging experiments (Supplementary videos do not provide in this thesis). These data together argue that during embryogenesis, muscle development largely proceeds as normal, with minor contributions

of NUAK to the final width of individual muscles.

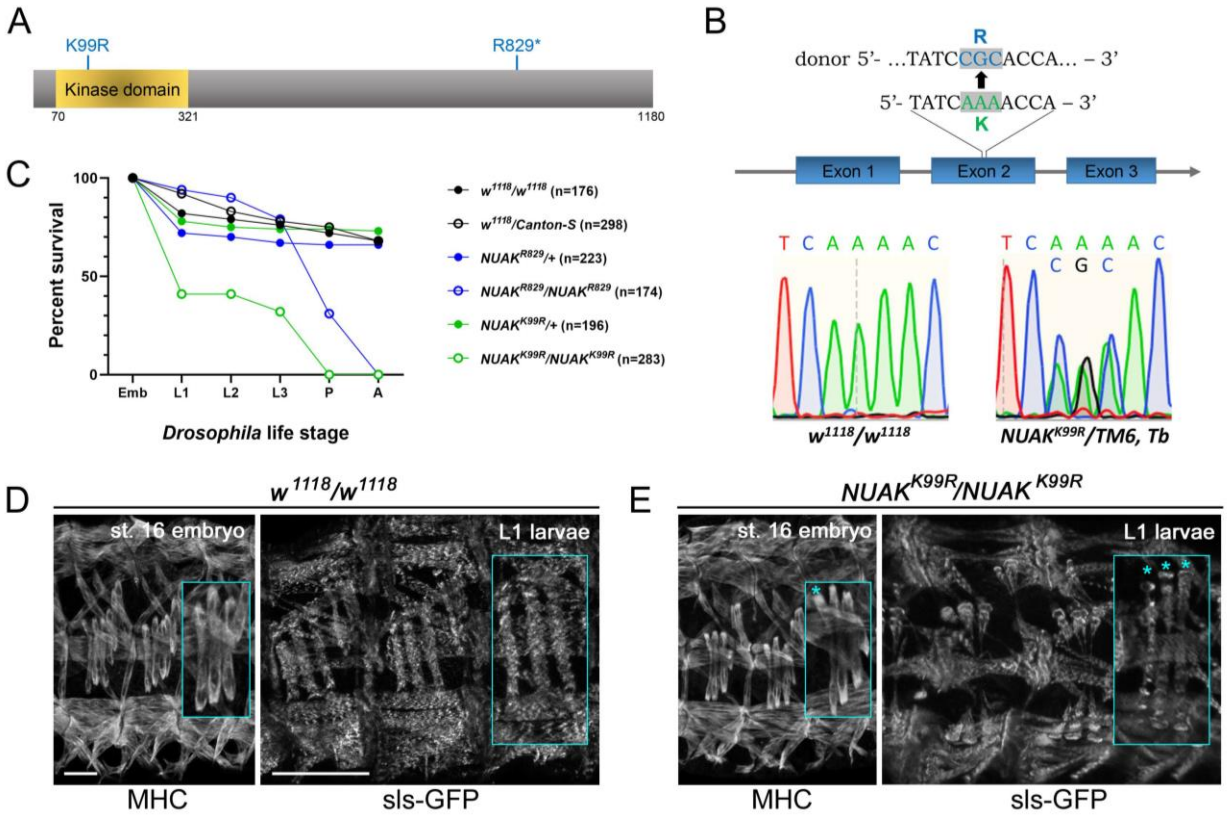

Figure 2.1 A kinase-dead mutation in NUAK causes early lethality.

(A) Schematic of the *D. melanogaster* NUAK protein isoform PD showing the conserved kinase domain spanning AA 70-321. The location of the K99R and R829* alleles are shown. (B) Sequence verification of the K→R change at residue 99 in $NUAK^{K99R}$/+ flies. Top panel shows WT and donor sequences. Sanger sequencing chromatogram of *WT* or $NUAK^{K99R}$/+ flies verify the desired nucleotide change. (C) Lethal phase of *NUAK* mutants. Either *WT* or *NUAK* heterozygous controls largely survive until adulthood. Homozygous $NUAK^{R829*}/NUAK^{R829*}$ individuals are lethal at the pupal stage, while more than 50% of the $NUAK^{K99R}$/ $NUAK^{K99R}$ mutants die at the embryo/L1 transition. *Drosophila* life cycle stage abbreviations - Emb, Embryo; L1, 1st larval stage; L2, 2nd larval stage; L3, 3rd larval stage; P, pupal stage; A, adult. (D,E) Stage 16 embryos stained with anti-MHC (left panel) or L1 muscles marked with sls-GFP (right panel). The third set of lateral transvserse muscles is enlarged in each panel (inset). (D) Three hemisegments of the *WT* embryonic musculature adopt a stereotypical organization. This muscle pattern is preserved in L1 muscles and sarcomeres are marked by sls-GFP labeled Z-discs. (E) Embryos homozygous mutant for the $NUAK^{K99R}$ allele exhibit an overall normal muscle pattern, although some muscles appear thinner. This thinning phenotype is exacerbated in L1 muscles. Emb scale bar, 20 µm. L1 scale bar, 50 µm.

Since most homozygous $NUAK^{K99R}/NUAK^{K99R}$ larvae do not survive until the L3 stage for the analysis of muscle morphology, we leveraged the spatial and temporal control of the Gal4/UAS

system to assess the impact of mutations that alter kinase activity. Three independent amino acid changes were generated within the kinase domain: (1) K99R within subdomain II; (2) E197K within subdomain VIb; and (3) T226A in the T-loop region of the kinase domain **(Figure 2.2 A)**. The glutamic acid at position 197 was mutated to mimic a missense mutation that disrupted muscle architecture in *C. elegans unc-82* mutants [33]. Finally, the conserved threonine located within the T-loop of NUAK was altered to an alanine (T226A) to abolish phosphorylation by upstream kinases [11, 34].

We first tested whether overexpression of each mutation on its own caused dominant effects by monitoring pupal length as a proxy for muscle contraction [24, 35]. During the larval to pupal transition, shortening of the body wall muscles ensures a stereotypical pupal case axial ratio (length/width) of ~3 for *WT* **(Figure 2.2 B)**. Under control of the *Mef2* promoter, expression of two irrelevant UAS lines (*Mef2>GFP RNAi* or *Mef2>lacZ*) exhibited normal muscle contraction. In contrast, *Mef2>NUAK RNAi* individuals showed an increased axial ratio in the range of 4.6-5.9 and thus served as a positive control [24]. Myofiber expression of transgenes that abolish key residues required for NUAK catalytic activity (*Mef2>NUAK K99R*, *Mef2>NUAK E197K*) or activation of kinase activity (*Mef2>NUAK T226A)* each showed a range of pupal case lengths that were increased compared to controls, indicating defective muscle contraction.

To examine if these mutant transgenes also cause morphological defects similar to those we previously described for *NUAK RNAi* [24], we examined the distribution of F-actin in L3 muscles. Indeed, expression of *NUAK K99R*, *NUAK E197K*, or *NUAK T226A* using *Mef2*-Gal4 in a *WT* background caused a range of sarcomere abnormalities, including thinning muscles and/or a loss of sarcomere patterning **(Figure 2.2 C)**. The average percentage of muscles that exhibited morphological abnormalities in *Mef2>NUAK K99R* or *Mef2>NUAK E197K* L3 larvae was greater

than 80%, with a penetrance similar to *Mef2>NUAK RNAi* **(Figure 2.2 D)**. Expression of the *NUAK T226A* transgene exhibited milder defects, whereby approximately 40% of muscles showed aberrant muscle morphology. Similar results were obtained for dominant overexpression of kinase mutations using the muscle driver *C57*-Gal4 **(Appendix Figure D.1 A-D)**.

Since *Mef2* turns on transgene expression at embryonic stage 12 and remains elevated in muscle tissue throughout larval development [36], we next utilized the post-embryonic muscle *G7*-Gal4 driver to assess if NUAK kinase activity is required in contractile larval muscles. Few abnormalities were observed in *G7>NUAK RNAi* muscles, likely due to the relatively late temporal expression of the *G7* driver in knocking down *NUAK mRNA* compared to *Mef2* **(Figures 2.2 C, D)**. Both *G7>NUAK K99R* or *G7>NUAK E197K* showed extensive muscle phenotypes, while those observed with expression of the *NUAK T226A* were weaker. Post-embryonic expression of the *G7* promoter was confirmed with a UAS-based *mCherry::NLS* (*mCh::NLS*) construct. *Mef2> mCh::NLS* was apparent in all muscles by the end of myogenesis in stage 16 embryos, while *G7> mCh::NLS* was undetectable **(Figure 2. 2E)**. These data together confirm that key residues in the kinase domain of NUAK are essential to maintain normal muscle structure during larval muscle growth and/or contraction.

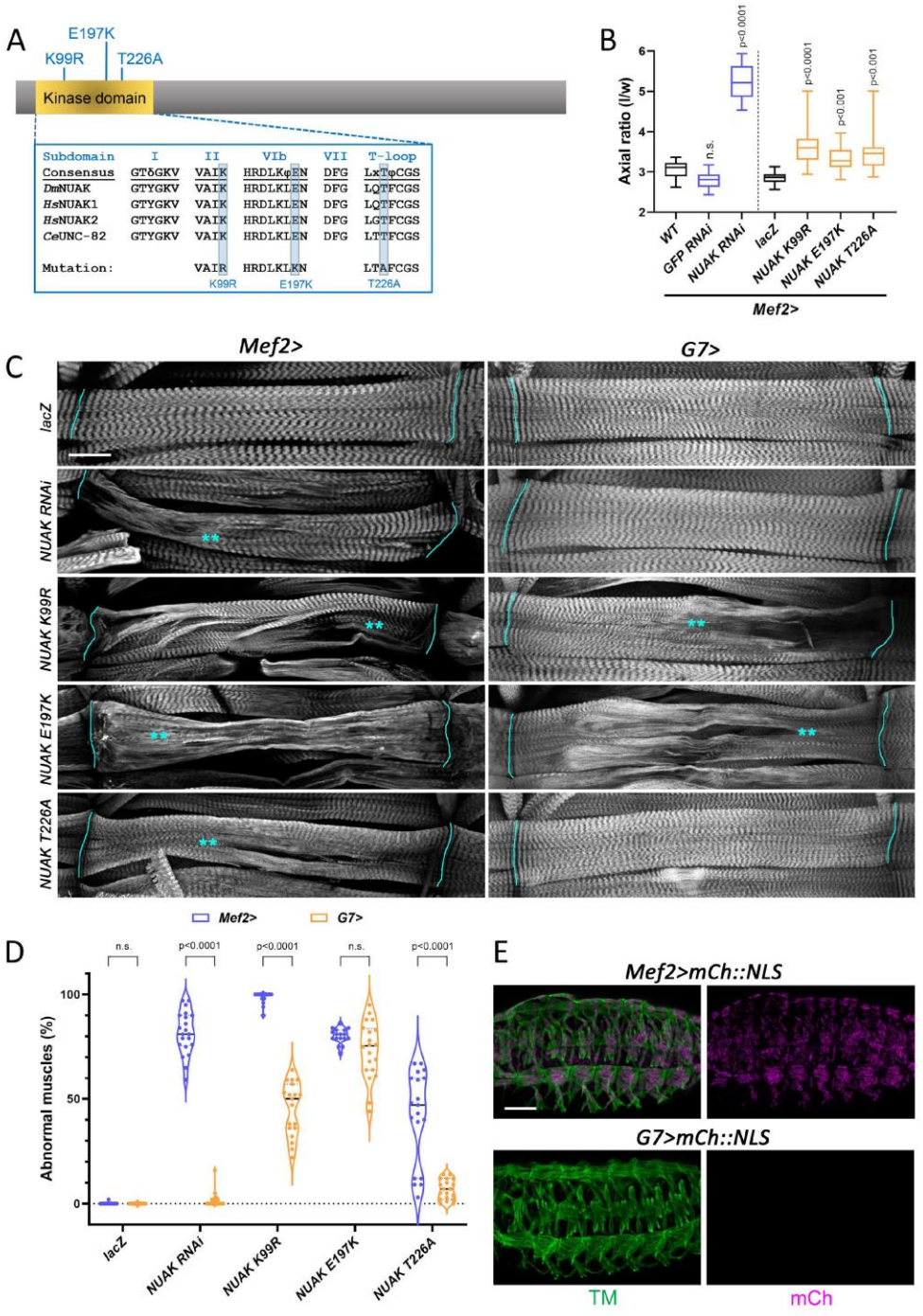

Figure 2.2 Kinase activity is essential to maintain the architecture of contractile muscles.

(A) Schematic of the NUAK protein showing the location of UAS-based kinase domain mutations. (B) Box and whisker plot quantifying the relative amount of muscle contraction at the L3 to pupal transition. Control pupae (*WT*, *Mef2>GFP RNAi*, or *Mef2>lacZ*) exhibit a standard axial ratio (length to width ratio) consistent with normal muscle contraction. RNAi knockdown of NUAK or

expression of individual kinase domain mutations (K99R, E197K, or T226A) in a *WT* background under control of the *Mef2* promoter significantly impairs muscle contraction, resulting in increased axial ratios. N≥20 for each genotype. (C) Representative maximum intensity projections of L3 larval muscles stained with phalloidin to visualize F-actin. UAS-based constructs expressing either *NUAK RNAi* or NUAK kinase domain mutations with *Mef2*-Gal4 or *G7*-Gal4. Cyan lines indicate muscle attachment sites and asterisks are located next to regions that show abnormal F-actin morphology. Scale bar, 25 μm. (D) Violin plot with individual data points showing the percentage of muscles in panel C exhibiting abnormal muscle morphology. (E) Maximum intensity projections of *Mef2>mCh::NLS* (top panels) or *G7 mCh::NLS* (bottom panels) embryos stained with anti-Tropomyosin (TM) confirm that the *G7* promoter is not expressed during embryogenesis. Scale bar, 50 μm.

NUAK promotes CryAB phosphorylation

We previously conducted a Y2H screen with full-length NUAK and identified physical interactions between NUAK-Filamin and NUAK-Stv [24]. Two additional proteins that emerged as high confidence interacting proteins were Paramyosin (Prm) and l(2)efl/CryAB. In *C. elegans*, Prm genetically interacts with the NUAK ortholog Unc-82 [37]. Clones containing the smallest region of either Prm (AA589-671) or CryAB (AA79-154) that physically associated with NUAK were verified in a 1 by 1 interaction assays. The previously published SMAD-SMURF interaction was used as a positive control [30]. Empty bait vector with Prm or CryAB yielded no yeast growth, while an interaction between NUAK-Prm or NUAK-CryAB could be reproduced in 3 independent biological replicates **(Figure 2.3 A)**.

We next tested if a disruption in NUAK function altered the distribution of CryAB or Prm in muscle tissue. CryAB is detected at the Z-disc and largely excluded from other regions that are enriched for F-actin in *Mef2>lacZ* control muscles **(Figure 2.3 B)** [38]. In both *Mef2>NUAK RNAi* [24] or *Mef2>NUAK* kinase mutants, larger areas that lack F-actin instead accumulate CryAB in an abnormal pattern. The specificity of the CryAB antibody was confirmed with immunostaining and Western blotting of *CryAB RNAi* muscles **(Appendix Figure D.2)**. In contrast, immunostaining for Prm did not reveal similar results. In *NUAK RNAi* or upon expression of

NUAK kinase domain mutations, areas of muscle tissue without F-actin also lacked Prm **(Appendix Figure D.3)**. Thus, while NUAK physically interacts with both proteins, the subcellular fate of CryAB or Prm is different when NUAK function is compromised.

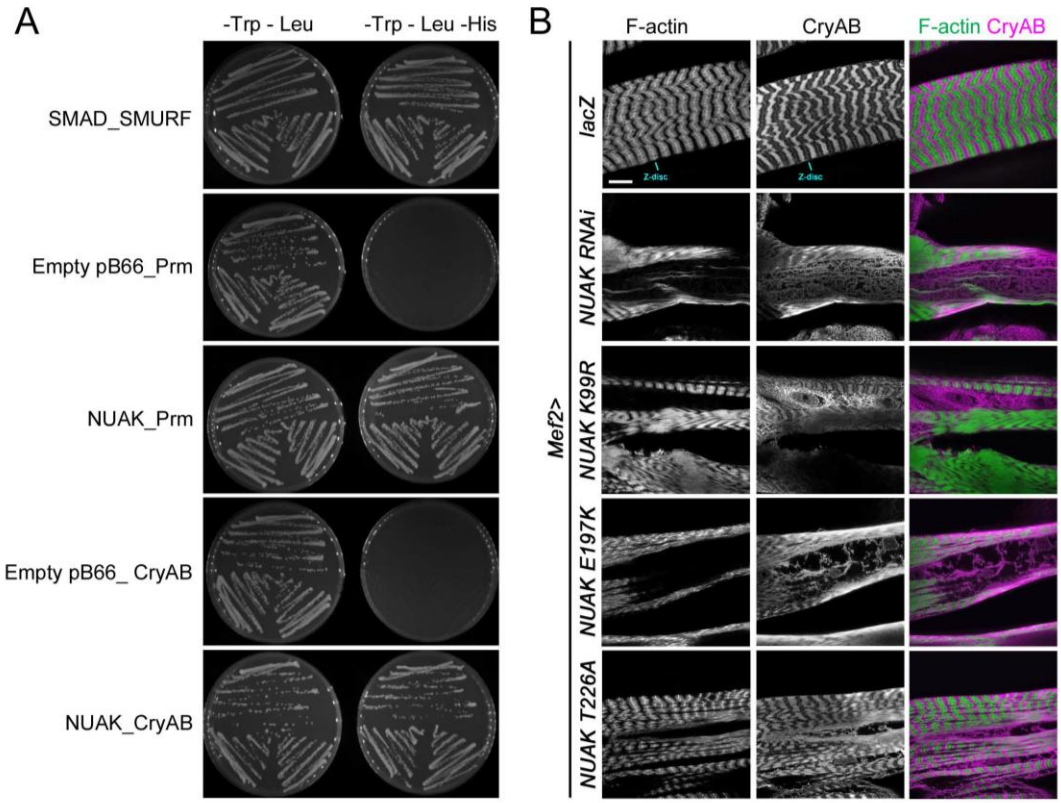

Figure 2.3 CryAB physically interacts with NUAK and accumulates abnormally in NUAK mutant muscles.

(A) Y2H experiments test for an interaction between bait and prey proteins. Yeast growth on media lacking Trp and Leu verify the presence of the bait and prey plasmids. Colony growth on selective media plates (-Trp –Leu –His) indicate a physical interaction between SMAD_SMURF (positive control), NUAK_Prm, and NUAK_CryAB. No growth was observed for the empty bait vector with Prm or CryAB. Three independently transformed yeast clones were tested for each bait-prey pair. (B) L3 larval muscles stained with phalloidin to visualize F-actin or an antibody raised against CryAB. F-actin and CryAB overlap at the Z-disc and can be observed in complementary patterns in control *Mef2>lacZ* muscles. Muscle expression of *NUAK RNAi* or *NUAK* kinase domain mutations (*K99R*, *E197K*, or *T226A*) all show abnormal accumulation of CryAB in regions that lack F-actin. Scale bar, 50 µm.

The necessity of NUAK kinase activity obviates the question of whether CryAB could be a target substrate. To examine if phosphorylation could be detected, we first overexpressed NUAK in muscle tissue and assessed the migration pattern of CryAB by Western blotting. Slower migrating bands suggestive of a post-translational modification (PTM) were apparent for CryAB upon overexpression of full-length NUAK (NUAK FL) **(Figure 2.4 A)**. These putative phospho-CryAB bands were either reduced in intensity or not present after induction of *NUAK RNAi* or upon dominant expression of kinase-dead (*NUAK K99R*) or inactivated (*NUAK T226A*) NUAK proteins. Next we treated lysates derived from muscles overexpressing NUAK with λ-phosphatase and observed the disappearance of higher migrating bands corresponding to phosphorylated CryAB species **(Figure 2.4 B)**, thus proving that NUAK influences CryAB phosphorylation.

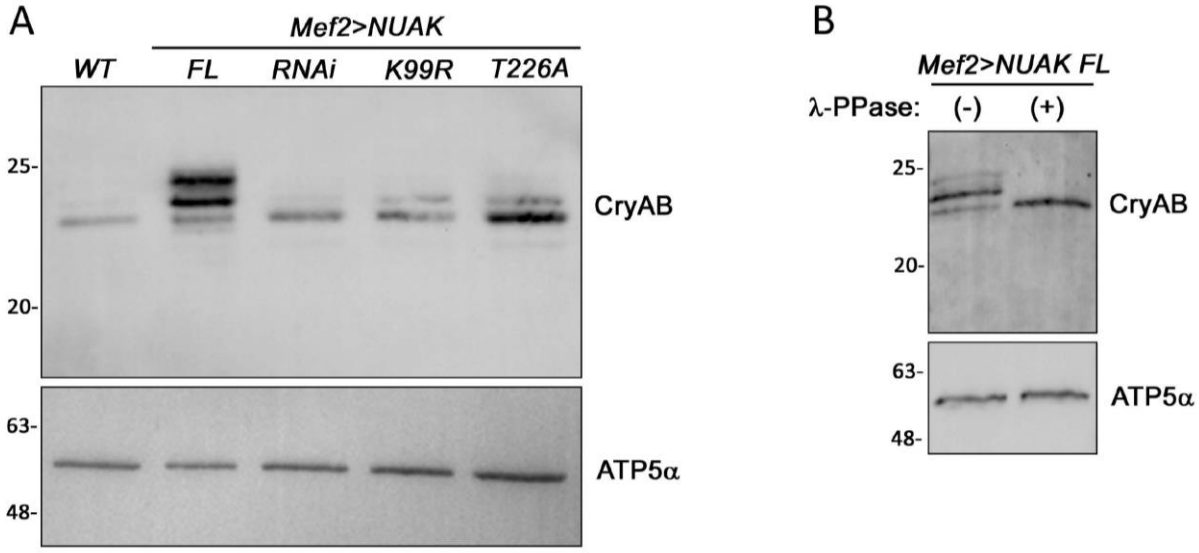

Figure 2.4 NUAK promotes CryAB phosphorylation.

(A) Western blot showing the migration pattern of CryAB bands in the indicated genotypes. Overexpression of *NUAK FL* result in higher migrating forms of CryAB. Knockdown of NUAK protein using RNAi or dominant expression of *NUAK K99R* or *NUAK T226A* reduces the amount of slower migrating CryAB bands. (B) The multiple bands observed upon *Mef2>NUAK FL* expression collapse into a single band upon λ-PPase treatment. ATP5α is used as a loading control.

Since the T226A mutation in NUAK abolished phosphorylation of CryAB, we tested if changing this threonine to a glutamic acid (T226E) could functionally mimic NUAK activation. First we tested the specificity of the threonine mutation using a phospho-specific antibody generated against the corresponding threonine (T211) residue in a synthetic human ARK5 peptide. Seven of the eight amino acids, in addition to T211/T226, are conserved between HsARK5, HsSNARK, DsNUAK **(Figure 2.5 A)**. This NUAK phospho-specific antibody (pNUAK) did not detect endogenous protein in control *lacZ* muscle lysates, but effectively recognized elevated levels of K99R, E197K **(Figure 2.5 B)**, or NUAK FL **(Appendix Figure D.4)** driven by *Mef2*-Gal4. As expected, the T226A or T226E mutations failed to be recognized by the pT211 Ab **(Figure 2.5 B)**, but expression of each produced different outcomes. Consistent with Figure 4A, T226A lysates reduced CryAB phosphorylation, while expression of T226E mimicked phosphorylation events on CryAB similar to that of FL overexpression **(Figure 2.5 C)**.

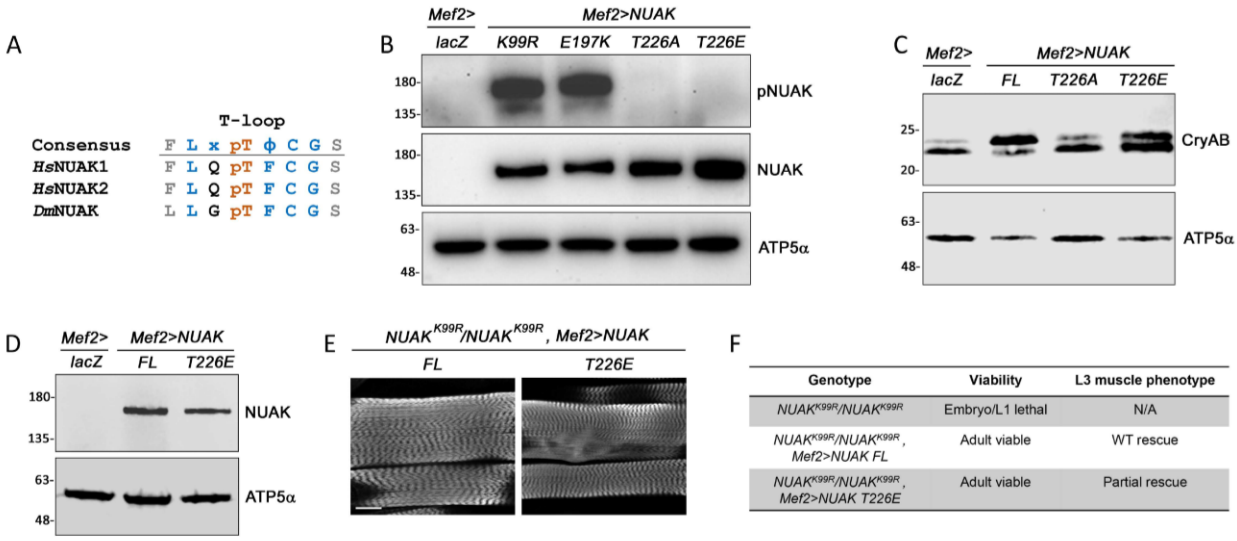

Figure 2.5 Phosphomimetic NUAK T226E rescues NUAK K99R mutant phenotypes.

(A) Location of the pT residue in the conserved T-loop region of HsNUAK1/ARK5, HsNUAK2/SNARK, and DsNUAK. (B) Confirmation of the *T226A* or *T226E* mutation by Western blotting. The pNUAK Ab, raised against HsNUAK1, recognizes overexpressed *NUAK K99R* and *NUAK E197K*, but not mutation of the *T226* residue. (C) Phosphomimetic *T226E* is sufficient for CryAB phosphorylation and *T226A* reduced this modification. *NUAK FL* was used

as a positive control. (D-F) Rescue of $NUAK^{K99R}/NUAK^{K99R}$ mutants with muscle expression of *NUAK FL* or *NUAK T226E*. (D) Western blotting confirms expression of *NUAK FL* or *NUAK T226E*. ATP5α is used as a loading control. (E) L3 larval muscles stained for F-actin have largely *WT* sarcomeres. Scale bar, 50 μm. (F) Table summarizes lethality and muscle phenotype.

We next tested whether T226E is sufficient to rescue $NUAK^{K99R}/NUAK^{K99R}$ mutants. NUAK FL was used as a positive control since we previously demonstrated that muscle expression of this transgene rescued the generative muscle phenotype in $NUAK^{R829*}/NUAK^{R829*}$ mutants [24]. First we confirmed protein expression of the NUAK FL or T226E transgenes in larval lysates **(Figure 2.5 D)** and then assessed the extent of rescue in L3 muscles. Indeed, *Mef2*-induced expression of NUAK FL or T226E in homozygous $NUAK^{K99R}/NUAK^{K99R}$ muscles was largely normal **(Figure 2.5 E)**. Moreover, this muscle expression produced viable adults **(Figure 2.5 F)**, showing that T226E can functionally rescue aspects of NUAK biology throughout all of muscle development.

Next we took advantage of an HA-tagged version of CryAB to map phosphorylation sites. First we needed to confirm that the 3xHA affinity tag did not interfere with the *in vivo* NUAK-CryAB complex. Therefore, we performed proximity ligation assay (PLA) experiments using a rabbit antibody against NUAK and a mouse antibody that detects the HA tag on the C-terminus of CryAB. *LacZ* control muscles showed an average of ~ 2 puncta/50 μm^2 **(Figure 2.6 A)**. The number of PLA(+) structures representing the NUAK-CryAB complex was increased upon muscle expression of CryAB::3xHA alone and in the presence of NUAK FL overexpression **(Figure 2.6 B)**. Controls for the PLA plus or minus probes only did not produce any signal.

While expression of CryAB::3xHA alone in muscle induced more phosphorylation than controls, this PTM was further enhanced upon co-expression with NUAK **(Figure 2.6 C)**. Hence, this hyper-phosphorylated CryAB was isolated from muscle tissue using anti-HA beads and run

on an SDS-PAGE gel followed by Coomassie staining. Bands corresponding to CryAB were removed, trypsin digested and subjected to mass spectrometry (MS) analysis **(Figure 2.6 D)**. Total CryAB sequence coverage was ~88% after three independent biological replicates. Attempts to improve peptide coverage corresponding to the extreme N- and C-termini with chymotrypsin were not successful. Nevertheless, the trypsin digest experiments revealed two putative phosphorylation sites on serine residues located at amino acids 68 and 70 within the same peptide **(Figures 2.6 E,F)**.

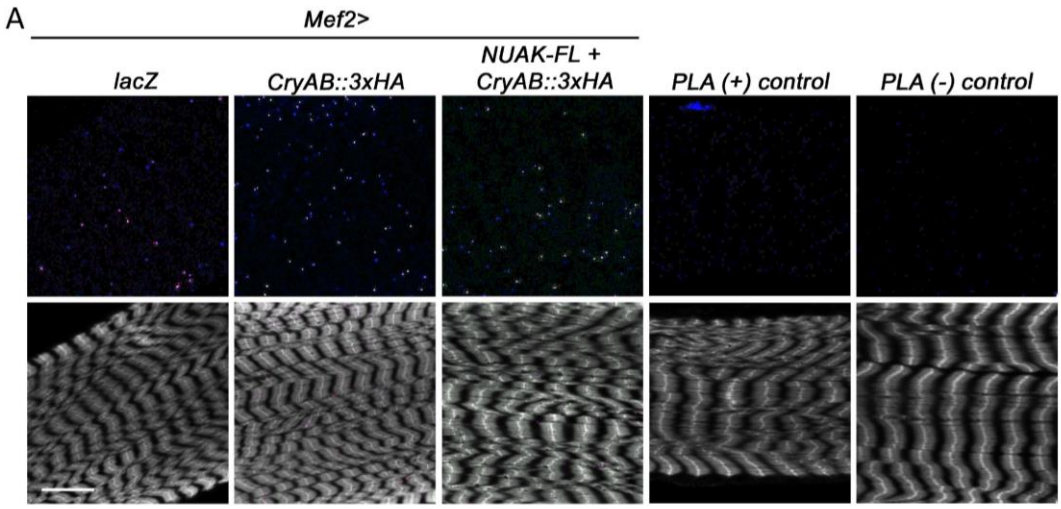

E

Sample #	Sequence coverage	pPeptide sequence	AA position	Ascore	Confidence	# of peptides
Sample 1	78.6%	K.QES#GSTLNIDSEK.F	S68	≥17.0	>95%	2
Sample 2	76.4%	K.QES#GSTLNIDSEK.F	S68	≥17.0	>95%	3
Sample 3	75.6%	K.QES#GSTLNIDSEK.F	S68	≥17.0	>95%	2
Sample 1	78.6%	K.QESGS#TLNIDSEK.F	S70	≥22.9	>99%	2
Sample 2	76.4%	K.QESGS#TLNIDSEK.F	S70	≥22.9	>99%	3
Sample 3	75.6%	K.QESGS#TLNIDSEK.F	S70	≥22.9	>99%	2

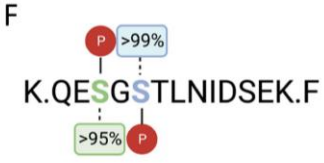

Figure 2.6 Determination of phosphorylation sites on CryAB isolated from muscle.

(A,B) Either endogenous or overexpressed NUAK can form a complex with CryAB as assayed by PLA experiments. (A) Maximum intensity projections of L3 muscle tissue (F-actin labeled in grey) to visualize the NUAK-CryAB complex (magenta). Scale bar, 25 μm. (B) Scatter plot showing an increase in the number of PLA(+) puncta/50 μm^2 for tagged CryAB with and without NUAK compared to *Mef2>lacZ* or PLA controls. One-way ANOVA was performed and the indicated p-values are in comparison to *lacZ*. N=10. (C) Western blots confirming that the 3xHA-tagged version of CryAB is phosphorylated in muscle tissue. Bands corresponding to phosphorylated CryAB can be visualized with either anti-CryAB (left panel) or anti-HA (right panel) upon expression of *Mef2>CryAB::3xHA* alone or with *NUAK FL* expression. (D) Strategy depicting expression and isolation of CryAB for phosphorylation site identification by MS. (E) Table with summary of phospho-MS experiments. Three independent biological replicates were analyzed with total peptide coverage of CryAB ranging from 75.6 - 78.6%. Serines corresponding to amino acid residues 68 and 70 were both found to be phosphorylated with confidence values >95%. (F) Summary of CryAB phosphosites.

Each monomer of CryAB has three distinct regions: a conserved α-crystallin domain (ACD) that is comprised of eight anti-parallel beta strands flanked by an unstructured N-terminal region (NTR) and a shorter C-terminal region (CTR) [39, 40]. The general location of these two phosphoresidues are conserved in human CryAB, with *Drosophila* S68 or S70 corresponding to human T63 or S66, respectively **(Figure 2.7 A)**. The location of these phospho-S/T residues were mapped onto the *Drosophila* or human CryAB Alphafold protein structures. S68 lies in a small loop region that preceeds the first β-sheet of the ACD and S70 is the first AA of this β-sheet **(Figure 2.7 B)**. To assess if serine 68 and/or serine 70 are indeed phosphorylated by NUAK, we mutated each of these residues to either alanine (to prevent phosphorylation) or glutamic acid (phospho-mimic). Overall protein levels of CryAB were increased upon expression of WT or phospho-mutant versions of CryAB compared to lacZ control lysates **(Figure 2.7 C)**. Slower migrating, or phosphorylated forms of CryAB, were reduced upon expression of S68A or S70A and completely abolished in the S68A/S70A double mutant. Phosphorylated versions of CryAB were present upon expression of S68E or S70E, with the latter showing multiple bands. Together,

these data demonstrate that S68 and S70 are both targeted for phosphorylation and the S70E phospho-mimetic induces hyperphosphorylation.

To test if human NUAK1 or human NUAK2 function similar to its *D. melanogaster* counterpart, we generated transgenic flies expressing either full-length (hNUAK1 or hNUAK2) or kinase-dead (hNUAK1 K84R or hNUAK2 K81R) versions of each protein and expressed them in larval muscle tissue. Expression of only hNUAK1 K84R showed phenotypes similar to expression of *D. melanogaster NUAK RNAi* or the dominant NUAK transgenes (K99R, E197K, T226A), whereby the prevalent phenotype was muscle degeneration and CryAB accumulation **(Figure 2.7 D)**. These data suggest that there may be shared features between human NUAK1 and fly NUAK that affect cellular processes and possibly even common substrates, at least in muscle tissue.

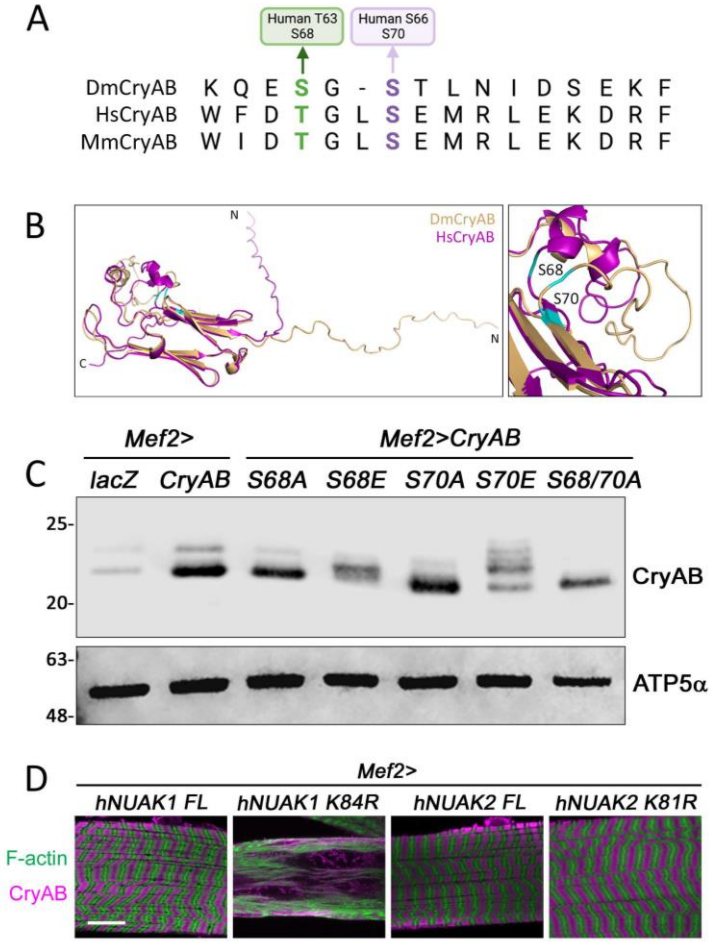

Figure 2.7 Functionalconfirmation of CryAB phosphosites.

(A) Alignment of CryAB sequences from *D. melanogaster* (Dm), human (Hs) or mouse (Mm) showing conservation of either S and/or T residues that can be modified, at least on *D. melanogaster* CryAB. (B) An overlay of the ribbon diagrams for DmCryAB (gold) and HsCryAB (magenta). The location of S68 and S70 are shown in cyan. (C) Western blot for CryAB protein upon mutation of S68 and/or S70. No phosphorylation is observed in the S68/S70A double mutation. ATP5α is used as a loading control. (D) L3 muscles stained for F-actin or anti-CryAB. Overexpression of kinase-dead hNUAK1 (*Mef2>hNUAK1 K84R*), but not hNUAK2 (*Mef2>hNUAK2 K81R*), disrupts muscle morphology and causes CryAB accumulation. Scale bar, 20 μm

2.4 Discussion

In this manuscript we show that the catalytic activity of NUAK is essential for viability and to prevent muscle degeneration. We verify a physical interaction between NUAK and CryAB and further demonstrate that NUAK promotes the phosphorylation of CryAB at S68 and S70. Since mutations in human FLNC, BAG3, or CRYAB are causative for protein aggregate diseases [41-44], our molecular analysis confirms the functional importance of phosphorylation in the prevention of abnormal protein accumulation in muscle tissue.

How do NUAK kinase-dead mutations inhibit phosphorylation? Since dominant expression of these kinase variants produce phenotypes in the presence of endogenous protein, NUAK may limit phosphotransfer activity via three mechanisms. First, since the NUAK UAS-expression constructs drive higher levels of expression than seen for endogenous NUAK, stable interactions between NUAK and CryAB could favor the inactive kinase over the active endogenous one - thereby reducing CryAB phosphorylation. Second, if dimerization of NUAK is required for kinase activity, interactions between endogenous NUAK and its kinase-dead counterpart could titrate out kinase activity of WT NUAK. In addition, or alternatively, substrate proteins may initially interact with the catalytic pocket of kinase-dead NUAK, but remain in the

active site for longer than usual if the protein cannot be released. This would effectively limit the amount substrate available for cellular functions.

Multiple studies have shown that a loss of AMPK-related kinase activation in the T-loop reduces catalytic activity [8, 10, 11, 34]. While we also observed a reduction in NUAK function upon expression of T226A, the percentage of muscle abnormalities were less severe compared to K99R or E197K. Maybe the phosphate appended to T226 is somewhat stable on the pool of endogenous NUAK and can outcompete the ectopic NUAK T226A protein for substrate phosphorylation. It is also possible that additional amino acids aside from T226 are regulated by phosphorylation. In addition to the T-loop residue in human NUAK1, amino acid 600 is also phosphorylated by Akt [22]. *D. melanogaster* lacks this conserved Akt phosphosite, but may have others yet to be determined. An additional unknown is the identity of the upstream kinase(s) that phosphorylate(s) NUAK in response to muscle contraction and/or increased mechanical tension.

Multiple pieces of evidence provide support for NUAK-mediated phosphorylation of CryAB. First, a physical interaction between NUAK and CryAB was identified by Y2H. Overexpression of WT or activated NUAK (T226E) increase the pool of phosphorylated CryAB, while kinase-dead (K99R, E197K) or inactivated (T226A) NUAK reduced this modification. Due to the inability to purify full-length *D. melanogaster* NUAK, we have been unable to show that CryAB phosphorylation is directly mediated by NUAK. It is possible that NUAK phosphorylates an intermediate kinase that in turn acts on CryAB. Purified p44/42 mitogen-activated protein kinase (MAPK) and mitogen-activated protein kinase-activated protein-2 (MAPKAP kinase-2) can phosphorylate S45 and S59 in human CryAB [45]. Phosphorylation of CryAB S59 is also increased during C2C12 differentiation, in C2C12 cells subjected to electrical pulse stimulation (EPS), and in resistance exercise-loading in human skeletal muscle [46-48]. Inhibition of

NUAK1/ARK5 kinase activity using the NUAK1-specific inhibitor WZ4003 in C2C12 cells shows a reduction in phospho-S59 levels **(Appendix Figure D.5)**. While more experiments need to be done to confirm a direct relationship between the phosphorylation of CryAB by mammalian NUAK1, these data suggest a possible conservation of the NUAK-CryAB signaling axis.

Even though hCryAB is ubiquitously expressed, dominant or recessive mutations identified in multiple patients can result in multisystem disorders characterized by cardiomyopathies, cataracts, or skeletal myopathies [39, 49]. The correlation between individual molecular mutations, disease onset and variable expressivity is not well understood at the tissue or organismal level. Chaperone functions for CryAB are largely thought to prevent the abnormal accumulation of cellular proteins. While specific binding partners of CryAB, such as Desmin, have been verified [46, 50], the promiscuous nature of CryAB in other contexts have made it difficult to pinpoint its molecular function. In our hands, incubation of larval lysates with *CryAB::3xHA* in pulldown experiments produced hundreds of proteins in experimental versus control experiments. This suggests that interactions of CryAB with other proteins may be tightly regulated in intact cells, but this contextual specificity is lost outside of the normal cellular environment.

Numerous studies demonstrate that the oligomerization state of mammalian CryAB/HSPB5 is crucial for the regulation of chaperone activity [39, 40, 49]. Monomeric CryAB assembles into dimers via interactions between antiparallel beta strands located within the ACD [51-53]. Intermolecular contacts in the CTR of three CryAB dimers form a hexameric unit which can form higher order multimers (12-mer or 24-mer) largely mediated by the NTR [54-56]. It is proposed that the equilibrium between smaller and larger oligomeric CryAB complexes determine client substrate interactions. Multimeric species may act as storage forms of CryAB, whereas

smaller oligomers exhibit chaperone activity since potential substrate binding sites within the NTR, ACD, or CTR are exposed for protein interactions.

Phosphorylation alters the distribution of CryAB towards lower oligomeric species [40, 57]. In particular, mimicking phosphorylation events on three known serine residues in mammalian CryAB (S19D/S45D/S59D) reduces the mean diameter of CryAB complexes and decreases stability as assessed by urea denaturation experiments [58]. Generally, aging, stress, or disease increases the relative pool of phosphorylated CryAB. Both aged muscle tissue and eye lenses with cataracts have increased levels of phosphorylated CryAB that partition into the insoluble fraction [59-62]. Heat stress or oxidative stress produce a similar phenomenon in various cell types including neurons [40]. As of yet there is no clear consensus on the biological implications of CryAB phosphorylation, which have been shown to be beneficial or deleterious, depending on the cellular context. In terms of autophagy, we hypothesize that NUAK may activate CryAB to unfold aggregates to prevent abnormal protein accumulation. Future experiments will focus on clarifying the molecular role of CryAB phosphorylation in muscle tissue.

2.5 Material and methods

Drosophila stocks and husbandry

All stocks were reared at 25 °C on standard cornmeal-molasses-yeast media. w^{1118} was used as the *WT* control with the inclusion of *Canton-S* in Figure 1C. The $NUAK^{R829}$ mutants and sls-GFP insertion ($sls^{ZCL2144}$) were previously published [24, 26]. *Drosophila* stocks obtained from the Bloomington *Drosophila* Stock Center (BDSC) are indicated with BL followed by the stock number. The following Gal4 drivers were used to direct expression in muscle tissue: *Mef2*-Gal4 (BL27390), *c57*-Gal4 (L. Wallrath) and *G7*-Gal4 (M. Baylies). Muscle phenotypes due to

induction of UAS-*NUAK RNAi* (BL31885) and the generation of NUAK transgenes (UAS-*NUAK FL 548*, UAS-*NUAK K99R* and UAS-*NUAK E197K*) were described previously [24]. UAS-*lacZ* (BL3956) was used as a control for Gal4-mediated experiments and UAS-*mCherry.NLS* (BL38424) was utilized to confirm the lack of *G7* expression in embryonic muscles. The UAS-*CryAB-3xHA* stock (F003130) was obtained from the FlyORF project [27] and UAS-*CryAB RNAi* (BL41724) was used to confirm anti-CryAB specificity.

CRISPR/Cas9 NUAK allele

CRISPR-mediated mutagenesis was performed by WellGenetics Inc. using modified methods of Kondo and Ueda [28]. In brief, the gRNA sequences CATCAAGAAGTGCAAGATCG[AGG]/TCATAATCTGCACCTCGCGA[CGG] were cloned into the U6 promoter plasmid separately. The K99R-BacDsRed cassette containing two PBac terminals, 3xP3-DsRed, and two homology arms with the point mutation K99R were cloned into pUC57 Kan as a donor template for repair. NUAK/CG43143 targeting gRNAs and hs-Cas9 were supplied in DNA plasmids, together with a donor plasmid for microinjection into embryos of control strain w^{1118}*; attP40[nos Cas9]/CyO* . F1 flies carrying the 3xP3-DsRed selection marker were further validated by genomic PCR and sequencing for introduction of the K99R point mutation. The DsRed selection marker was excised and we again reconfirmed the K99R mutation using PCR amplification followed by sequencing (Genewiz, South Plainfield, NJ). Primer sequences were forward 5'-ATGGTGATAAGCAAACCCGATGGAGC-3' and reverse 5'-GATCTTGTGCTTGTGACAGTAGTAGA-3'.

Quantitative RT-PCR

RNA was extracted from 10 whole L3 larvae for each genotype using the RNAeasy Mini Kit (Qiagen, Valencia, CA). Following elution from the column, RNA concentrations were measured and single strand complementary DNA (cDNA) was generated from 175 ng of RNA using the SuperScript VILO cDNA Synthesis Kit (Invitrogen, Carlsbad, CA). For each qPCR reaction, the cDNA sample was diluted to 1:25 and mixed with Power UP SYBR Green Master mix and primers (Applied Biosystems, Foster City, CA). *rp49* was the reference gene. Integrated DNA Technologies (IDT) synthesized the following primers: *rp49* forward 5'-GCCCAAGGGTAT CGACAACA-3', *rp49* reverse 5'-GCGCTTGTTCGATCCGTAAC-3'; *NUAK* forward 5'-ATGGTGATAAGCAAACCCGATGGAACG-3', reverse 5'-GATCTTGTGCTTGTGACA GTAGTAGA-3'; and *l(2)efl/CryAB* forward 5'-TTCCACCCTCAACATCGACA, reverse 5'-CATGCTTTCCCTCCACGATG. Three independent biological replicates were processed for each genotype and reactions were run in triplicate using the Quant Studio 3 Applied Biosystem with Quant studio design and analysis software. The average of the triplicates was used to calculate the 2-ΔΔCt values (normalized fold expression). Quantification of mRNA levels between genotypes was performed using the student t-test.

Creation of transgenic flies

NUAK

The QuikChange II XL Site-directed Mutagenesis kit (Agilent Technologies, Santa Clara, CA) was used to introduce the T226A mutation into the *NUAK-RD* cDNA in the pENTR/D-TOPO vector (ThermoFisher Scientific, Waltham, MA). Primers used were forward 5'-GAACCGCAAAAGGCGCCCAGCAGTCGC-3' and reverse 5'-GCGACTGCTGGGCGCCTTTTGCGGTTC-3'. The resulting mutagenized sequence was

recombined into the pTW destination plasmid to generate UAS-*NUAK T226A* using standard Gateway cloning protocols [29]. All other UAS-*NUAK* lines (*DsNUAK T226E*, *HsNUAK1*, *HsNUAK1 K84R*, *HsNUAK2,* and *HsNUAK2 K81R*) were created using gene synthesis by Genscript and subcloned into the pUAST vector using NotI and XbaI restriction sites. Plasmid DNA from all constructs were purified with a Qiagen Maxi Kit (Hilden, Germany), sequence verified, and sent to Rainbow Trangenics for the creation of transgenic flies. The insertions were balanced on their respective chromosomes.

CryAB

cDNA corresponding to the coding region of *CryAB-RC* was synthesized by Genscript and subcloned into the pUASTattB vector using EcoRI/XbaI sites. All phosphosite mutations were performed by Genscript to produce UAS-*CryAB S68A*, UAS-*CryAB S68E,* UAS-*CryAB S70,* UAS-*CryAB S70E,* and UAS-*CryAB S68/70A.* Plasmid DNA was purified using the Qiagen Maxi kit (Hilden, Germany) and sent to Rainbow Trangenics. After generation of transgenic flies at the PhiC31landing site (BL9736-53B2), all lines were balanced over the Cyo,Tb balancer (BL36335).

Visualization of muscle tissue

Embryo immunostaining

Crosses of the desired genotypes were set up in FlyStuff embryo collection cages (#59-105; Genesee Scientific, San Diego, CA) and inverted onto 35 mm petri dishes containing apple juice-agar with fresh yeast paste. The pots were placed in an incubator at a defined temperature (25°C or 31°C) and humidity (60%) where flies were allowed to lay eggs. After 2-3 hours, the collection plate was further staged for ~ 15 hours and a new plate was used to collect the next batch of embryos. Using a wet paintbrush, the embryos were collected into a mesh basket filled with 1x

PBS and rinsed to remove yeast paste. Embryos were dechorionated in freshly diluted 50% bleach and rinsed with a solution of 0.7% NaCl/0.04% Triton X-100 before transferring to small glass vial containing a 1:1 fixative solution of heptane and 4% formaldehyde in PEM (0.1 M Pipes, pH 8.0; 2 mM $MgSO_4$; 1 mM EGTA). The embryos were shaken vigorously for 12 minutes on a platform shaker to ensure penetration of the fixative solution. The bottom layer of fixative was removed and an equal volume of methanol was added. The settled embryos were transferred to a microcentrifuge tube, washed three times with methanol, followed by three washes with PBT. Embryos were blocked in PBT with 5% normal goat serum for 30 min before incubating in mouse anti-Myosin heavy chain (Mhc) (1:100; Susan Abmayr) or rat anti-Tropomyosin (TM) MAC141 (1:50; Babraham Institute, Cambridge, UK) in PBT and 5% normal goat serum at 4°C overnight or at room temperature for 2 hours. Embryos were washed three times for 10 minutes each in PBT and reblocked in PBT with 5% normal goat serum for 30 minutes. Fluorescent anti-mouse Alexa Fluor 488 or anti-rat Alexa Fluor 488 (1:400, ThermoFisher Scientific, Waltham, MA) were added for 1 hour at room temperature. The embryos were again washed three times for 10 minutes each in PBT. After washing, the embryos were mounted onto glass slides, and imaged with a Zeiss 700.

Larval muscle staining

Wandering L3 larvae were heat killed, placed onto a Sylgard plate, pinned near the mouth hooks at the anterior end and the internal organs were removed. The muscle carcasses were fixed in 4% formaldehyde and immunostained using standard immunostaining protocols, with normal goat serum used as a blocking agent in PBT. Tissues were stained with the following primary antibodies: rabbit anti-CryAB DZ33926 (1:200, Boster Bio, Pleasanton, CA) or mouse anti-Prm 5-23 [1:200, Developmental Studies Hybridoma Bank (DSHB)]. Secondary antibodies were used

to detect fluorescence: anti-rabbit or anti-mouse Alexa Fluor 488 or 594 (1:400, Invitrogen, Waltham, MA). Phalloidin 594 was used to label F-actin (1:400, Molecular Probes, Eugene, OR). A Zeiss 700 confocal microscope was used to capture the images.

Live imaging

A small square of biofoil (AB-0718, Thermo Scientific) was cut and placed on the center of a glass slide in preparation for imaging. Using a wet paintbrush, an embryo of the appropriate developmental stage was immersed in halocarbon oil (#27 sigma) before transferring to the biofoil and orienting it properly for imaging. A coverslip was added over the embryo with small pieces of clay at the corners for support. Live imaging was performed with a Zeiss 700 using the following parameters: 20x objective, 1x zoom; time interval: 10 min; total time: 4 hours; laser power: 1.

Image processing

Image processing and analysis was performed using a combination of Zen Black (Zeiss), ImageJ (NIH), and Adobe Photoshop. All images taken at 20x are displayed as maximum intensity projections. Data acquisition at increased magnifications (63x) are presented as single plane images.

Western blotting

Dissected muscle carcasses were placed into 3x SDS sample buffer [188 mM Tris-HCl (pH 6.8), 3% (w/v) SDS, 30% (v/v) glycerol, 0.01% (w/v) bromophenol-blue, and 15% (v/v) β-mercaptoethanol], boiled at 95 °C for 3 min, homogenized, boiled for an additional 10 min at 95 °C, and centrifuged at 20,000 x g for 1 min to pellet debris. The resulting protein samples were separated by sodium dodecyl sulfate polyacrylamide gel electrophoresis (SDS-PAGE) and transferred to the nitrocellulose blotting membrane (pore size 0.45 μm, Cytiva, Marlborough, MA)

using the Trans-Blot® TurboTM Transfer System (Bio-Rad, Hercules, CA). Membranes were probed with the following primary antibodies: rabbit anti-l(2)efl/CryAB DZ33926 (1:1000, Boster Bio, Pleasanton, CA), rabbit anti-NUAK DZ41105 (1:400, Boster Bio, Pleasanton, CA), rabbit anti-pT211 AB-PK737 (1:1000, Kinexus, Vancouver, Canada), mouse anti-ATP5α ab14748 (1:20000, Abcam, Waltham, MA). IRDye 800CW anti-rabbit and IRDye 680RD anti-mouse secondary antibodies (LI-COR Biosciences, Lincoln, NE) were used at 1:10000 and Revert 700 Total Protein Stain (LI-COR Biosciences, Lincoln, NE) or anti-ATP5α was used as a loading control. Membranes were developed using the LI-COR Odyssey XF and quantitation of relative protein levels was performed in Empiria Studio Software (LI-COR Biosciences, Lincoln, NE).

Lambda protein phosphatase treatment

Three dissected *Mef2>NUAK OE* larvae reared at 25 °C were dissected and lysed into 100uL Protein MetalloPhosphatases (PMP) buffer with a pestle. The resulting lysates were spun down at 13000 x g at 4°C for 10 min. The samples were split into untreated (45 µL, 5 µL $MnCl_2$, 1 µL ultra-pure water) and treated (45 µL, 5 µL $MnCl_2$, 1 µL lambda-phosphatase P0753S (New England Biolabs, Ipswich, MA) groups. Both samples were incubated for 1 hr at 30 °C followed by overnight at room temperature. After incubation, 50 µL of 3x SDS sample buffer was added before boiling and SDS-PAGE as described above.

Yeast Two-Hybrid (Y2H)

Y2H assays were carried out by Hybrigenics Services (Gard, FR). The coding sequence of the full-length *D. melanogaster* NUAK/CG43143 (GenBank accession number NM_206469.3) was PCR-amplified and cloned in frame with the Gal4 DNA binding domain (DBD) into plasmid pB66 as a

C-terminal fusion to Gal4 (Gal4-bait fusion). Prey fragments of Prm (AA 588-867) or CryAB (AA 78-156) corresponding to the smallest region that interacts with NUAK were cloned in-frame with the Gal4 activation domain (AD) into plasmid pP6. Bait and prey constructs were transformed in the yeast haploid cells CG1945 (mata) and YHGX13 (Y187ade2-101::loxP-kanMX-loxP, matα) and diploid yeast cells were obtained using a mating protocol with both yeast strains. The interaction between SMAD and SMURF is used as positive control [30]. As negative controls, all prey plasmids were tested with the empty bait vector pB66. Streaks were plated for three independent yeast clones for each control and interaction. Medium lacking tryptophan and leucine was used as a growth control and to verify the presence of the bait and prey plasmids. The selective medium without tryptophan, leucine, and histidine selected for the interaction between bait and prey.

Lethal stage analysis

For each of the analyzed genotypes, 50 embryos/replicate were placed in a grid pattern on apple juice-agar plates with yeast paste at 25 °C. Embryos that hatched were transferred onto new apple juice-agar plates supplemented with yeast paste and analyzed at ~24 hr intervals for lethality or transferred to new plates. The number of dead, missing, or living individuals were counted and recorded for each stage. The survival plot curve in Prism was used to display the data. N≥3 biological replicates.

Proximity Ligation Assay (PLA)

Wandering L3 larvae of the genotypes *Mef2>lacZ, Mef2>CryAB::3xHA*, or *Mef2>NUAK OE; CryAB-3xHA* were heat-killed, dissected, fixed in 4% formaldehyde and washed in PBT before

following instructions for the Duolink® In Situ Red Starter Kit Mouse/Rabbit (Sigma-Aldrich, St. Louis, MO). Tissues were blocked for 1 h at 37 °C in the Duolink® blocking solution, incubated with primary antibody diluted in the Duolink® antibody diluent overnight at 4 °C. Primary antibodies used were mouse anti-HA 6E2 (1:400, Cell Signaling Technology, Danvers, MA); anti-NUAK DZ41105 (1:400, Boster Bio, Pleasanton, CA). Tissues were washed twice for 5 min in wash buffer A and then incubated in 40 µl PLA probe solution (8 µl PLUS probe, 8 µl MINUS probe, 24 µl antibody diluent) for 1 h at 37 °C. Tissues were washed twice for 5 min in wash buffer A and then incubated for 30 min at 37 °C in 40 µl ligation solution (8 µl ligation buffer, 31 µl ddH_2O, 1 µl ligase). Tissues were again washed twice for 5 min in wash buffer A and incubated for 100 min at 37 °C in 40 µl amplification solution (8 µl amplification buffer, 31.5 µl ddH_2O, 0.5 µl polymerase). Tissues were washed twice for 10 min in wash buffer B, then rinsed for 1 min with 0.01× wash buffer B and Phalloidin 488 to label F-actin (1:400, Molecular Probes, Eugene, OR). Tissues were mounted in PLA mounting medium.

Determination of CryAB phosphosites

Wandering L3 larvae of the genotype *Mef2>NUAK OE; CryAB::3xHA* were used for the determination of phosphorylated residues via MS. Larvae were raised in cages at 31° C and rinsed with PBS. Larvae equivalent to ~3 ml volume were transferred into a 15mL dounce tissue grinder (Wheaton, USA) with 2 mL lysis buffer (50 mM Tris-HCl pH 7.5, 150 mM NaCl, 1% Triton X-100, 10% glycerol) plus inhibitors (1x Halt protease inhibitor cocktail, 1x Halt phosphatase inhibitor cocktail; 1 mM Na_3VO_4, 1 mM NaF, 1 mM PMSF, 10 µM MG132, 0.001% PTU, 5 mM NPPS). The lysates were spun at 15,000 rpm for 10 min at 4° C to harvest the supernatant. The resulting lysate was incubated with pre-washed (in 0.05% TBS-T buffer) Pierce anti-HA

conjugated magnetic beads #88837 (ThermoFisher Scientific, Waltham, MA) for 2 hours at room temperature. The beads with bound proteins were washed twice with 0.05% TBS-T and eluted with SDS sample buffer. Samples were boiled at 95 °C for 10 mins before running on a 15% SDS-page gel. After Coomassie blue staining, bands corresponding to the predicted molecular weight of CryAB-3xHA were cut out of the gel, placed into a sterile 1.5 mL microcentrifuge tube and sent to the Taplin Biological Mass Spectrometry Facility at Harvard University for phosphosite identification.

Protein structure overlay

The Alphafold structures for *D. melanogaster* l(2)efl/CryAB (UniProt: A0A0B4KEY5) and *H. sapiens* Alpha-crystallin B chain/CryAB (UniProt: P02511) were superimposed in PyMol.

Cell culture

Cell maintenance

Mouse myogenic C2C12 cells (ATCC, Manassas, VA) were used up to passage number 12. Myoblasts were grown on plastic cell culture dishes in Dulbecco's modified Eagle's medium (DMEM) supplemented with 10% fetal bovine serum and 1% penicillin-streptomycin in a humidified incubator at 37 °C and 5% CO_2. When the cells reached 70% confluency, they were detached and plated on a fresh plastic cell culture dish at 1.5 x 10^5 cells/ml in a 35 mm dish. Once cells were confluent, they were serum limited with differentiation media (DMEM, 2% horse serum, 1% penicillin-streptomycin) and allowed to differentiate. The media for growth or differentiation was replaced daily.

In vitro phosphorylation assay

C2C12 cells were seeded in a 60 mm cell dish at 1.5 x 10^5 cells/ml. The cells were differentiated to day 3 and treated for 24 hours with WZ4003 at a final concentration of either 4 μM or 6 μM in fresh differentiation media. After 24 hours, the cells were collected into *in vitro* phosphorylation lysis buffer [400 mM Tris-HCl (pH 7.5), 10 mM $MgCl_2$, 200 μM $CaCl_2$, 1 mM DTT, 1% Triton-100] and homogenized with a tissue homogenizer. The resulting cell lysates were incubated in an ice bath for 20 minutes and centrifuged for 15 minutes at 4°C before removing the supernatant to a new tube. A Bicinchoninic acid (BCA) assay was used to determine the total protein concentration and equal amounts of each cell lysate were split into two groups: without ATP or to a final concentration of 5mM. After incubation for 30 mins at 30 °C, SDS sample buffer was added before Western blotting. Membranes were probed with anti-NUAK1/ARK5 22723-1-AP (ThermoFisher Scientific, Waltham, MA), anti-CryAB ab13497 (Abcam, Waltham, MA), or anti-pCryAB ADI-SPA-227 (Enzo, Farmingdale, NY). Secondary antibody and total protein stain is described above.

Quantitation and statistical analysis

Pupal case muscle contraction

Pupae of the indicated genotype were adhered to a glass slide with a drop of nail polish. All pupae were oriented with dorsal side up and imaged on a Leica M165FC stereoscope. Image J was used to measure the length (l) and width (w) of each pupae and the axial ratio (l/w) was calculated in Excel. All data was imported into Prism to generate a box and whiskers plot. N≥20 for each genotype.

Muscle abnormalities

Embryos from parents of the genotype *Mef2>NUAK RNAi, Mef2>NUAK K99R, Mef2>NUAK E197K,* or *Mef2>NUAK T226A* were collected at 25 °C and transferred to 31 °C at the L1 stage. Wandering L3 larvae were dissected in PBS. The resulting muscle carcasses were fixed in 4% methanol-free formaldehyde (Polysciences, Warrington, PA) for 15 minutes at room temperature and washed three times in PBST before incubating with phalloidin 488 (1:400) and Hoechst (1:400). For each muscle carcass, seven distinct muscle fibers (VL1, VL2, VL3, VL4, LO1, LL1, and SBM) from eight randomly selected abdominal hemisegments were examined under the Zeiss 700 confocal microscope. The number of normal or defective muscles for each larvae were divided by the total number of muscles to calculate the percentage of muscle defects. N≥17 for each genotype.

2.6 References

1. Xue, L. and W.A. Tao, *Current technologies to identify protein kinase substrates in high throughput.* Front Biol (Beijing), 2013. **8**(2): p. 216-227.
2. Chen, C. and B.E. Turk, *Analysis of serine-threonine kinase specificity using arrayed positional scanning peptide libraries.* Curr Protoc Mol Biol, 2010. **Chapter 18**: p. Unit 18.14.
3. Dente, L., et al., *Modified phage peptide libraries as a tool to study specificity of phosphorylation and recognition of tyrosine containing peptides.* J Mol Biol, 1997. **269**(5): p. 694-703.
4. Breitkopf, S.B. and J.M. Asara, *Determining in vivo phosphorylation sites using mass spectrometry.* Curr Protoc Mol Biol, 2012. **Chapter 18**: p. Unit18.19.1-27.
5. Hastie, C.J., H.J. McLauchlan, and P. Cohen, *Assay of protein kinases using radiolabeled ATP: a protocol.* Nat Protoc, 2006. **1**(2): p. 968-71.
6. Li, Y., W. Xie, and G. Fang, *Fluorescence detection techniques for protein kinase assay.* Anal Bioanal Chem, 2008. **390**(8): p. 2049-57.
7. Hardie, D.G., *AMP-activated protein kinase: an energy sensor that regulates all aspects of cell function.* Genes Dev, 2011. **25**(18): p. 1895-908.
8. Herzig, S. and R.J. Shaw, *AMPK: guardian of metabolism and mitochondrial homeostasis.* Nat Rev Mol Cell Biol, 2018. **19**(2): p. 121-135.
9. Steinberg, G.R. and D.G. Hardie, *New insights into activation and function of the AMPK.* Nat Rev Mol Cell Biol, 2023. **24**(4): p. 255-272.
10. Bright, N.J., C. Thornton, and D. Carling, *The regulation and function of mammalian AMPK-related kinases.* Acta Physiol (Oxf), 2009. **196**(1): p. 15-26.
11. Sun, X., et al., *The regulation and function of the NUAK family.* J Mol Endocrinol, 2013. **51**(2): p. R15-22.
12. Lizcano, J.M., et al., *LKB1 is a master kinase that activates 13 kinases of the AMPK subfamily, including MARK/PAR-1.* EMBO J, 2004. **23**(4): p. 833-43.
13. Alessi, D.R., K. Sakamoto, and J.R. Bayascas, *LKB1-dependent signaling pathways.* Annu Rev Biochem, 2006. **75**: p. 137-63.
14. Bennison, S.A., X. Liu, and K. Toyo-Oka, *Nuak kinase signaling in development and disease of the central nervous system.* Cell Signal, 2022. **100**: p. 110472.
15. Molina, E., L. Hong, and I. Chefetz, *NUAK Kinases: Brain-Ovary Axis.* Cells, 2021. **10**(10).
16. van de Vis, R.A.J., A. Moustakas, and L.P. van der Heide, *NUAK1 and NUAK2 Fine-Tune TGF-β Signaling.* Cancers (Basel), 2021. **13**(13).
17. Inazuka, F., et al., *Muscle-specific knock-out of NUAK family SNF1-like kinase 1 (NUAK1) prevents high fat diet-induced glucose intolerance.* J Biol Chem, 2012. **287**(20): p. 16379-89.
18. Koh, H.J., et al., *Sucrose nonfermenting AMPK-related kinase (SNARK) mediates contraction-stimulated glucose transport in mouse skeletal muscle.* Proc Natl Acad Sci U S A, 2010. **107**(35): p. 15541-6.
19. Bonnard, C., et al., *A loss-of-function NUAK2 mutation in humans causes anencephaly due to impaired Hippo-YAP signaling.* J Exp Med, 2020. **217**(12).
20. Zagórska, A., et al., *New roles for the LKB1-NUAK pathway in controlling myosin phosphatase complexes and cell adhesion.* Sci Signal, 2010. **3**(115): p. ra25.

21. Yamamoto, H., et al., *Identification of a novel substrate for TNFalpha-induced kinase NUAK2.* Biochem Biophys Res Commun, 2008. **365**(3): p. 541-7.
22. Suzuki, A., et al., *Identification of a novel protein kinase mediating Akt survival signaling to the ATM protein.* J Biol Chem, 2003. **278**(1): p. 48-53.
23. Hou, X., et al., *A new role of NUAK1: directly phosphorylating p53 and regulating cell proliferation.* Oncogene, 2011. **30**(26): p. 2933-42.
24. Brooks, D., et al., *Drosophila NUAK functions with Starvin/BAG3 in autophagic protein turnover.* PLoS Genet, 2020. **16**(4): p. e1008700.
25. Brooks, D., et al., *Independent pathways control muscle tissue size and sarcomere remodeling.* Dev Biol, 2022. **490**: p. 1-12.
26. Hudson, A.M., et al., *Mononuclear muscle cells in Drosophila ovaries revealed by GFP protein traps.* Dev Biol, 2008. **314**(2): p. 329-40.
27. Bischof, J., et al., *A versatile platform for creating a comprehensive UAS-ORFeome library in Drosophila.* Development, 2013. **140**(11): p. 2434-42.
28. Kondo, S. and R. Ueda, *Highly improved gene targeting by germline-specific Cas9 expression in Drosophila.* Genetics, 2013. **195**(3): p. 715-21.
29. Reece-Hoyes, J.S. and A.J.M. Walhout, *Gateway Recombinational Cloning.* Cold Spring Harb Protoc, 2018. **2018**(1): p. pdb.top094912.
30. Colland, F., et al., *Functional proteomics mapping of a human signaling pathway.* Genome Res, 2004. **14**(7): p. 1324-32.
31. Carrera, A.C., K. Alexandrov, and T.M. Roberts, *The conserved lysine of the catalytic domain of protein kinases is actively involved in the phosphotransfer reaction and not required for anchoring ATP.* Proc Natl Acad Sci U S A, 1993. **90**(2): p. 442-6.
32. Meharena, H.S., et al., *Decoding the Interactions Regulating the Active State Mechanics of Eukaryotic Protein Kinases.* PLoS Biol, 2016. **14**(11): p. e2000127.
33. Hoppe, P.E., et al., *Caenorhabditis elegans unc-82 encodes a serine/threonine kinase important for myosin filament organization in muscle during growth.* Genetics, 2010. **184**(1): p. 79-90.
34. Yeh, Y.Y., K. Wrasman, and P.K. Herman, *Autophosphorylation within the Atg1 activation loop is required for both kinase activity and the induction of autophagy in Saccharomyces cerevisiae.* Genetics, 2010. **185**(3): p. 871-82.
35. LaBeau-DiMenna, E.M., et al., *Thin, a Trim32 ortholog, is essential for myofibril stability and is required for the integrity of the costamere in Drosophila.* Proc Natl Acad Sci U S A, 2012. **109**(44): p. 17983-8.
36. Ranganayakulu, G., R.A. Schulz, and E.N. Olson, *Wingless signaling induces nautilus expression in the ventral mesoderm of the Drosophila embryo.* Dev Biol, 1996. **176**(1): p. 143-8.
37. Schiller, N.R., et al., *The Role of the UNC-82 Protein Kinase in Organizing Myosin Filaments in Striated Muscle of.* Genetics, 2017. **205**(3): p. 1195-1213.
38. Wójtowicz, I., et al., *Drosophila small heat shock protein CryAB ensures structural integrity of developing muscles, and proper muscle and heart performance.* Development, 2015. **142**(5): p. 994-1005.
39. Dimauro, I. and D. Caporossi, *Alpha B-Crystallin in Muscle Disease Prevention: The Role of Physical Activity.* Molecules, 2022. **27**(3).
40. Bakthisaran, R., et al., *Phosphorylation of αB-crystallin: Role in stress, aging and patho-physiological conditions.* Biochim Biophys Acta, 2016. **1860**(1 Pt B): p. 167-82.

41. Batonnet-Pichon, S., et al., *Myofibrillar Myopathies: New Perspectives from Animal Models to Potential Therapeutic Approaches.* J Neuromuscul Dis, 2017. **4**(1): p. 1-15.
42. Béhin, A., et al., *Myofibrillar myopathies: State of the art, present and future challenges.* Rev Neurol (Paris), 2015. **171**(10): p. 715-29.
43. Fichna, J.P., A. Maruszak, and C. Żekanowski, *Myofibrillar myopathy in the genomic context.* J Appl Genet, 2018. **59**(4): p. 431-439.
44. Guglielmi, V., G. Tomelleri, and G. Vattemi, *Myofibrillar myopathies through the microscope: From diagnosis to molecular pathogenesis*. 2018: M icroscopie.
45. Kato, K., et al., *Phosphorylation of alphaB-crystallin in mitotic cells and identification of enzymatic activities responsible for phosphorylation.* J Biol Chem, 1998. **273**(43): p. 28346-54.
46. Jacko, D., et al., *Coordinated alpha-crystallin B phosphorylation and desmin expression indicate adaptation and deadaptation to resistance exercise-induced loading in human skeletal muscle.* Am J Physiol Cell Physiol, 2020. **319**(2): p. C300-C312.
47. Reimann, L., et al., *Myofibrillar Z-discs Are a Protein Phosphorylation Hot Spot with Protein Kinase C (PKCα) Modulating Protein Dynamics.* Mol Cell Proteomics, 2017. **16**(3): p. 346-367.
48. Singh, B.N., K.S. Rao, and C.M. Rao, *Ubiquitin-proteasome-mediated degradation and synthesis of MyoD is modulated by alphaB-crystallin, a small heat shock protein, during muscle differentiation.* Biochim Biophys Acta, 2010. **1803**(2): p. 288-99.
49. Dimauro, I., et al., *The role of αB-crystallin in skeletal and cardiac muscle tissues.* Cell Stress Chaperones, 2018. **23**(4): p. 491-505.
50. Wang, X., et al., *AlphaB-crystallin modulates protein aggregation of abnormal desmin.* Circ Res, 2003. **93**(10): p. 998-1005.
51. Bagnéris, C., et al., *Crystal structures of alpha-crystallin domain dimers of alphaB-crystallin and Hsp20.* J Mol Biol, 2009. **392**(5): p. 1242-52.
52. Jehle, S., et al., *Solid-state NMR and SAXS studies provide a structural basis for the activation of alphaB-crystallin oligomers.* Nat Struct Mol Biol, 2010. **17**(9): p. 1037-42.
53. Baranova, E.V., et al., *Three-dimensional structure of α-crystallin domain dimers of human small heat shock proteins HSPB1 and HSPB6.* J Mol Biol, 2011. **411**(1): p. 110-22.
54. Braun, N., et al., *Multiple molecular architectures of the eye lens chaperone αB-crystallin elucidated by a triple hybrid approach.* Proc Natl Acad Sci U S A, 2011. **108**(51): p. 20491-6.
55. Jehle, S., et al., *N-terminal domain of alphaB-crystallin provides a conformational switch for multimerization and structural heterogeneity.* Proc Natl Acad Sci U S A, 2011. **108**(16): p. 6409-14.
56. Peschek, J., et al., *The eye lens chaperone alpha-crystallin forms defined globular assemblies.* Proc Natl Acad Sci U S A, 2009. **106**(32): p. 13272-7.
57. Ito, H., et al., *Phosphorylation-induced change of the oligomerization state of alpha B-crystallin.* J Biol Chem, 2001. **276**(7): p. 5346-52.
58. Ahmad, M.F., et al., *Effect of phosphorylation on alpha B-crystallin: differences in stability, subunit exchange and chaperone activity of homo and mixed oligomers of alpha B-crystallin and its phosphorylation-mimicking mutant.* J Mol Biol, 2008. **375**(4): p. 1040-51.
59. Yamaguchi, T., et al., *Age-related increase of insoluble, phosphorylated small heat shock proteins in human skeletal muscle.* J Gerontol A Biol Sci Med Sci, 2007. **62**(5): p. 481-9.

60. Kato, K., et al., *Innervation-dependent phosphorylation and accumulation of alphaB-crystallin and Hsp27 as insoluble complexes in disused muscle.* FASEB J, 2002. **16**(11): p. 1432-4.
61. Huang, C.H., et al., *Phosphoproteomics characterization of novel phosphorylated sites of lens proteins from normal and cataractous human eye lenses.* Mol Vis, 2011. **17**: p. 186-98.
62. Ueda, Y., M.K. Duncan, and L.L. David, *Lens proteomics: the accumulation of crystallin modifications in the mouse lens with age.* Invest Ophthalmol Vis Sci, 2002. **43**(1): p. 205-15.

Chapter 3 - Stage-specific modulation of *Drosophila* gene expression with muscle GAL4 promoters

This chapter has been published as a journal article in the *Fly*.

Ziwei Zhao[a] and Erika Geisbrecht[a]

[a]Department of Biochemistry and Molecular Biophysics, Kansas State University, Manhattan, KS 66506, USA

*Corresponding author

E-mail: geisbrechte@ksu.edu

3.1 Abstract

The bipartite GAL4/UAS system is the most widely used method for targeted gene expression in *Drosophila melanogaster* and facilitates rapid *in vivo* genetic experimentation. Defining precise gene expression patterns for tissues and/or cell types under GAL4 control will continue to evolve to suit experimental needs. However, the precise spatial and temporal expression patterns for some commonly used muscle tissue promoters is still unclear. This missing information limits the precise timing of experiments during development. Here we focus on three muscle-enriched GAL4 drivers (*Mef2*-GAL4, *C57*-GAL4 and *G7*-GAL4) to better inform selection of the most appropriate muscle promoter for experimental needs. Specifically, *C57*-GAL4 and *G7*-GAL4 turn on in the first or second instar larval stages, respectively, and can be used to bypass myogenesis for studies of muscle function after development.

3.2 Introduction

Drosophila melanogaster is an excellent experimental model for *in vivo* genetics experiments due to its highly conserved protein sequences, short growth cycles, ease of laboratory culture, and well-established genetic expression systems [1]. Most laboratories employing *Drosophila* as a model use and benefit from the GAL4/UAS system to knockdown gene expression, rescue loss-of-function mutations, and express mutated proteins, namely human disease alleles [2]. These tools together make *Drosophila* an unparalleled model in understanding gene function.

In 1988, the Ptashne lab showed that the *Saccharomyces cerevisiae* yeast GAL4 protein can stimulate transcription of reporter genes in multiple cell types, including mammalian cells, plant cells, and *Drosophila* larvae [3-5]. In 1993, Andrea Bread and Norbert Perrimon extended

this GAL4/UAS technique to manipulate *Drosophila* gene expression in a cell- or tissue-specific manner [6]. This bipartite approach makes use of the transcription factor GAL4 and a 'responder' element under the control of a cis-acting regulatory sequence called the upstream activating sequence (UAS). The binding of GAL4 to these engineered UAS sites activates transcription of downstream components, which may include expression of wild-type or mutated genes, RNAi sequences, and reporter constructs, among others [2,7]. Implementation of this technique is still widely utilized to study the impact of genes during *Drosophila* development and growth.

With the need to regulate gene expression in independent tissues and at different stages, numerous tissue- and/or cell-specific promoters have been constructed to allow for precise gene control. For example, collections of GAL4 drivers exist for targeting specific cell types in the *Drosophila* intestine [8] or to manipulate specific motor neuron types, such as the glutamatergic motor neurons Ib or Is [9]. Alternatively, the development of Split-GAL4 allows for single cell resolution based upon the overlapping expression of two independent enhancers [10]. Additional temporal control of gene expression may be necessary if alteration of gene function (e.g., overexpression, dominant-negative, RNAi knockdown) causes lethality or altered phenotypes prior to the desired stage of analysis. While methods such as temperature-sensitive GAL80 (GAL80ts), tetracycline-inducible GAL80 (Tet-off GAL80), Gene-switch, and auxin-inducible gene expression systems (AGES) have been developed [11-14], these expression systems have limitations and may complicate experimental design. Thus, it is valuable to continue developing new and further characterizing existing GAL4 lines that can be used for more precise spatial and temporal control.

The focus of this paper is to characterize the developmental gene expression patterns of three muscle driver lines: *Mef2*-GAL4, *C57*-GAL4, and *G7*-GAL4. Myocyte enhancer factor-2

(*Mef2*) is one of the earliest identified and well-studied transcription factors in both *Drosophila* and mammalian muscles [15,16]. Since *Drosophila* Mef2 protein is present in the developing mesoderm and persists throughout somatic, visceral, and cardiac cells spanning embryogenesis into adulthood [17], the *Mef2*-GAL4 driver provides a well characterized control to compare muscle expression during development. However, there is lack of primary data describing the exact timing of target gene expression by the widely used *C57*-GAL4 and *G7*-GAL4 muscle promoters [18-28]. *C57*-GAL4 was first published as *BG57*-GAL4 and expression was reported in all larval muscles from the first instar (1^{st}) to the third (3^{rd}) instar stage as well as two sensory cell bodies in the body wall and in mesodermally-derived gut tissues [18]. However, unpublished reports suggested possible expression in late embryogenesis. In 2008, while *G7*-GAL4 was described as having expression in all muscles beginning from the second instar larval stage [27], the supporting references did not include primary data to support this conclusion. To clarify these discrepancies, in this study we pinpoint this spatial and temporal expression of these muscle GAL4 drivers using UAS-mCherry.NLS (mCh) as a fluorescence readout.

3.3 Results and Discussion

Only *Mef2*-GAL4 is detected in stage 13 to 16 embryos

The well characterized *Mef2*-GAL4 driver promotes expression in embryonic mesodermal cells from stage 7 onwards and subsequently in the cardiac, visceral, and somatic musculature [29]. The goal of this study is to clarify the exact stage at which *C57*-GAL4 or *G7*-GAL4 turn on compared to *Mef2*-GAL4 in terms of target gene expression during development. Even though Mef2 is expressed earlier, we only documented embryos at key stages in myogenesis: stage 13 (myoblast fusion ongoing), stage 14 (the peak of myoblast fusion), stage 15 (individual muscle

fibers are recognizable), and stage 16 (mature muscle pattern completed) [30,31]. Tropomyosin (Tm) was used to stain the developing body wall muscles and to confirm staging by assessing development of the midgut. Consistent with published literature [29] and summarized in **Table 3.1**, the *Mef2*-GAL4 driver robustly expressed mCh from stage 13 to stage 16 **(Figure 3.1 A)**. This fluorescence signal intensified during muscle development as fusing muscles increased the number of mCh-expressing nuclei. We could not detect *C57*-GAL4 **(Figure 3.1 B)** or *G7*-GAL4 **(Figure 3.1 C)** mCh expression in embryo stages 13 to 16 using this approach. In summary, *Mef2*-GAL4, but not *C57*-GAL4 or *G7*-GAL4, initiate target gene expression during embryogenesis.

Table 3.1 Summary of GAL expression patterns compiled from the literature and data in this paper.

	***Mef2*-GAL4**	***C57*-GAL4**	***G7*-GAL4**
Stages of somatic muscle expression	Embryo - adult	1st - 3rd instar larvae	2nd - 3rd instar larvae
Reported expression pattern	Mesoderm expression at stage 7 onwards, then expressed in somatic muscle, visceral muscle and cardiac cells. (Ranganayakulu, et al, 1998)	All larval body wall muscles, two sensory cell bodies in the body wall, and mesodermal-derived tissues, including the gut. (Budnik, et al., 1996)	Expression in all muscles beginning from the second instar larval stage. (Cauchi, et al., 2008)
Expression pattern using mCh reporter (this study)	We only documented stage 13 – 16 expression in the somatic muscle, visceral muscle and cardiac cells.	All larval body wall muscles, strong expression in salivary gland, and weak midgut expression.	All larval body wall muscles, weak expression in salivary gland
Gene expression and/or gene insertion	Mef2	Likely inserted into the upstream coding region of neuromusculin (80C2-80C4) based on plasmid rescue experiments (personal communication from Ulrich Thomas)	Possibly inserted into U2SNRP probably means snRNA:U2, a small nuclear ribonucleoprotein gene on the 2nd at 34A-B or 38A4 (personal communication from Kendal Broadie)

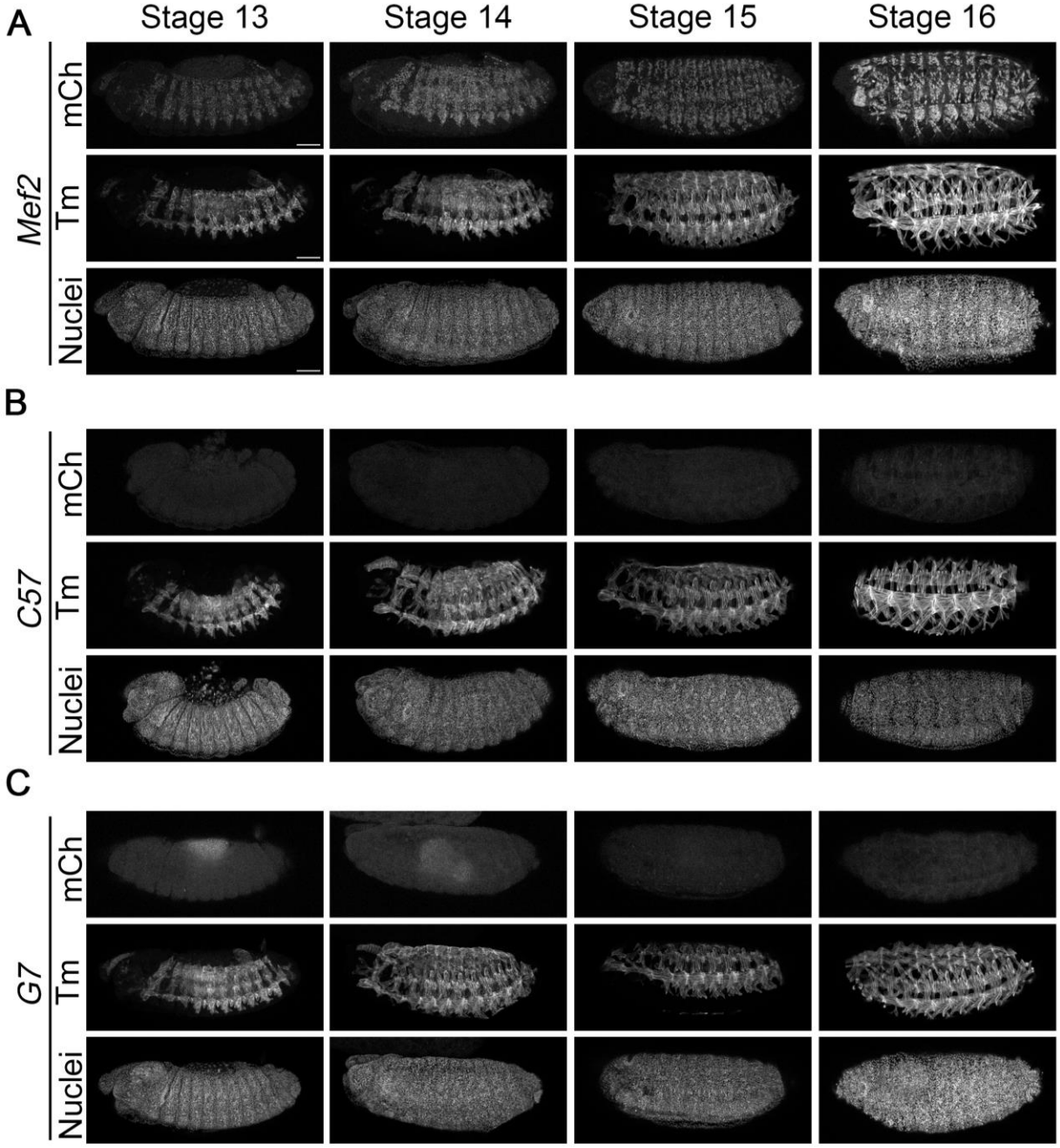

Figure 3.1 Differentmuscle-specific promoters show different target gene pattern of expression during embryonic muscle development.

A-D. Tropomyosin staining in muscle tissue confirms the different stages of muscle growth morphology. *UAS-NLS-mCherry* was used as a target gene to demonstrate the timing of gene expression. *Mef2*-Gal4 begins to express *UAS-NLS-mcherry* from the early to late stages of the embryo. The *C57*, *C7*, and *ApME*-Gal4 drivers do not express the target gene in the embryo stage13-16. Scale Bar: 50μm.

Muscle tissue promoters show variable spatial distribution in larval development

To confirm the reported gene expression patterns for the chosen muscle-GAL4 drivers, we investigated larval development spanning from the 1st to the 3rd instar stages. As expected, *Mef2*-GAL4 showed strong expression of mCh in all somatic body wall muscles throughout larval development **(Figure 3.2 A, left panels)**. In contrast, weak expression of mCh was first observed in the body wall muscles of 1st instar larvae using *C57*-GAL4 **(Figure 3.2 B, middle panels)** and not observed until the 2nd instar larval stage with *G7*-GAL4 **(Figure 3.2 C, right panels)**. Though enriched in somatic muscles, the *C57* and *G7* promoters also expressed mCh in salivary glands (white arrowheads). Together these results confirm that each GAL4 driver shows a unique pattern of spatial and temporal target gene expression. To our knowledge, this salivary gland expression has not been reported and if not taken into account, could confound studies involving inter-tissue communication.

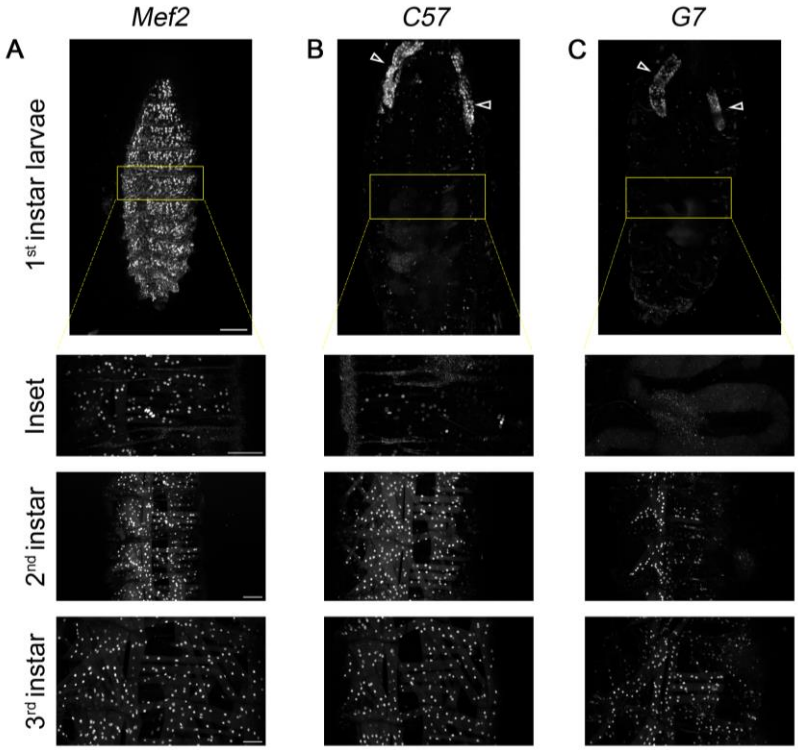

Figure 3.2 Variable spatial distribution and periods of target protein expression in larvae stage under different muscle tissue promoters.

A. 1st instar larvae stage images shows NLS-mCherry start to express Under *C57*-Gal4 and *ApME*-Gal4 promoter, not *G7*-Gal4. B & C. All drivers start to express the target gene in 2nd instar larvae through 3rd instar larvae. White arrow: Salivary gland. Scale Bar: 50μm.

Comparison of mCh protein expression levels throughout *Drosophila* development.

We next employed Western blotting to determine protein expression levels of mCh throughout embryonic and larval muscle development. During myogenesis, only the *Mef2*-GAL4 driver produced strong mCh signal, consistent with our confocal microscopy images **(Figure 3.3 A)**. Weak mCh expression was evident in 1st instar larvae using *C57*-GAL4 and *G7*-GAL4 **(Figure 3.3 B)**. Expression in the salivary glands likely accounts for some of this signal. 2nd instar larvae showed higher levels of mCh protein under control of the *C57* and *G7* promoters, albeit still lower compared to the *Mef2*-GAL4 promoter **(Figure 3.3 C)**. In the 3rd instar larvae stage, *C57*-GAL4 and *G7*-GAL4 both expressed at least 50% more of the mCh target protein than the *Mef2*-GAL4 driver **(Figure 3.3 D)**. Quantitation of GAL4 driver strength over time shows that *Mef2*-GAL4 expression was high throughout the embryonic and larval stages and decreased in 3rd instar larvae compared to *C57*-GAL4 or *G7*-GAL4 **(Figure 3.3 E)**.

A comprehensive and precise understanding of temporal and spatial expression patterns is informative for selecting the most appropriate muscle GAL4 driver in answering specific biological questions. Using two independent methods, our results confirm that *C57*-GAL4 expression is initiated in 1st instar larvae, while *G7*-GAL4 induction begins in 2nd instar larvae **(Figure 3.4 and Table 3.1)**. Based upon these results, the *C57* and *G7* drivers are useful for understanding how gene manipulation post-embryogenesis affects muscle structure, function, and/or growth. Importantly, these larval muscle promoters can be used to bypass embryonic lethality resulting from the use of *Mef2*-GAL4. Altering gene expression after the completion of

embryonic sarcomerogenesis also allows for distinguishing between sarcomere formation or sarcomere addition during larval muscle growth. Finally, the use of *G7*-GAL4 in 2nd instar larvae also eliminates using dual expression systems such as GAL4/GAL80ts or drug-inducible gene expression whereby temperature or drug toxicity may show leaky expression or behavioral changes [14].

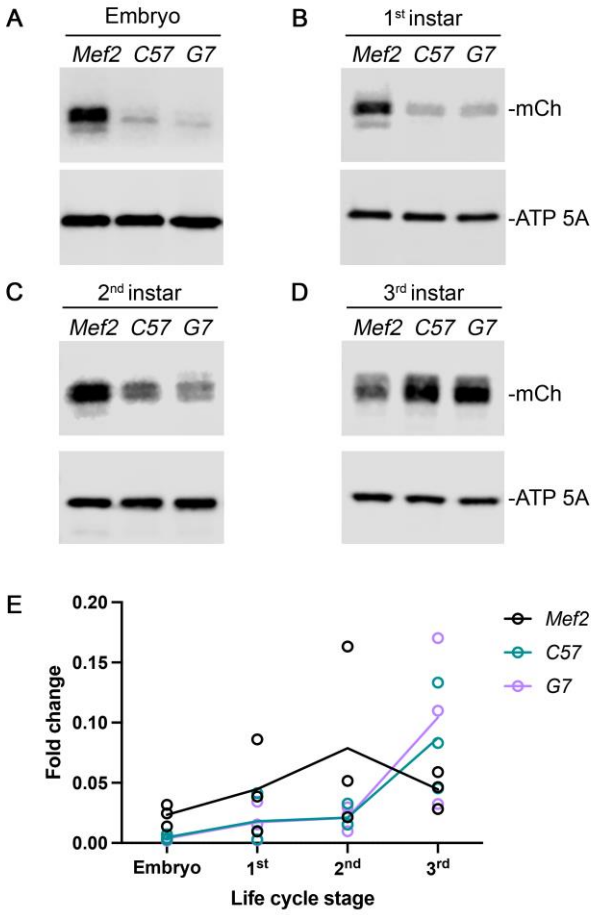

Figure 3.3 Variable spatial distribution and periods of target protein expression in larvae stage under different muscle tissue promoters.

A. Western blot analysis of mCherry protein expression levels in different drosophila life stages (embryo; L1; L2; L3 stages) of samples reveals diverse drivers. ATP5A is responsible for controlling load. B. Quantification of mCherry protein expression. N≥3

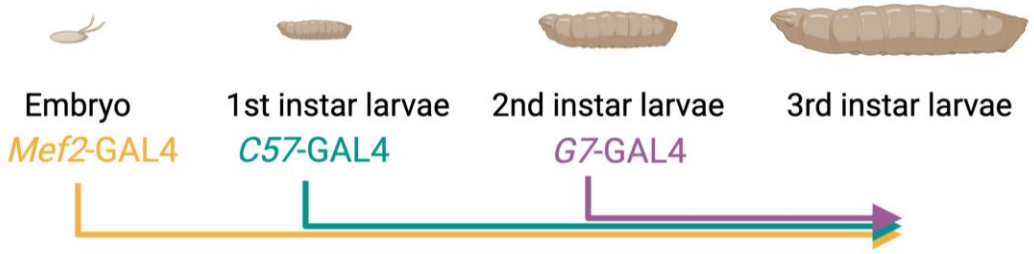

Figure 3.4 Schematic representationof muscle-specific drivers that express target genes at different stages of Drosophila development.

The *Mef2*-Gal4 driver begins to express the target gene from the early embryo stage and continues throughout the lifespan of *Drosophila*. *C57* and *ApME*-Gal4 enhance the target gene during the first instar larvae stage. *G7*-gal4 expresses the target gene beginning in the second instar larvae stage.

Therefore, we provided comprehensive data to support the spatial patterning, as well as the timing of these three drivers to express target gene in muscle tissue. Because we use the NLS-mCh to monitor target gene expression, not surprisingly, we did not observe any florescence in neuromuscular junction in *C57*-Gal4 and *G7*-Gal4 promoters. However, it needs the further experiments to verified whether *C57*-Gal4 is a proper driver for the neuromuscular junctions. To working on the genetics, the same gene in different tissue may play diverse function. Choosing the suitable driver is essential to correct understand the lethal samples caused by the target gene's abnormal function or the driver-associated lethality. For example, to understand the effect of gemin3 in mesodermal and larval muscle on *Drosophila* survival, there are several drivers are used to verify the gemin3's function, excluded the driver associated lethality [26]. Another example is to recognize whether target protein is essential for the post-embryonic larval, *G7*-Gal4 was used to prove that [17]. Existing research recognized the critical role of chose appropriate drivers. This publication will provide the basic facts for future studies of muscle regions in order to select the appropriate promoter according to the research objectives.

3.4 Material and methods

Drosophila stocks and husbandry

All stocks were reared at 25 °C on standard cornmeal-molasses-yeast media. Stocks obtained from the Bloomington *Drosophila* Stock Center (BDSC) are indicated with BL followed by the stock number. The following Gal4 drivers were used to direct expression UAS-*mCherry.NLS* (BL38424) in muscle tissue: *Mef2*-Gal4 (BL27390), *C57*-Gal4 (L. Wallrath), *G7*-Gal4 (M. Baylies).

Visualizing of muscle tissue

Embryo fixation

Crosses of the desired genotypes were set up in FlyStuff embryo collection cages (#59-105; Genesee Scientific, San Diego, CA) and inverted onto 35 mm petri dishes containing apple juice-agar with fresh yeast paste. The pots were placed in an incubator at a defined temperature (25 °C) and humidity (60%) where flies were allowed to lay eggs. After 2-3 hours, the collection plate was further staged for ~ 15 hours and a new plate was used to collect the next batch of embryos. Using a wet paintbrush, the embryos were collected into a mesh basket filled with 1x PBS and rinsed to remove yeast paste. Embryos were dechorionated in freshly diluted 50% bleach and rinsed with a solution of 0.7% NaCl/0.04% Triton X-100 before transferring to small glass vial containing a 1:1 fixative solution of heptane and 4% formaldehyde in PEM (0.1 M Pipes, pH 8.0; 2 mM $MgSO_4$; 1 mM EGTA). The embryos were shaken vigorously for 12 minutes on a platform shaker to ensure penetration of the fixative solution. The bottom layer of fixative was removed, and an equal volume of methanol was added. The settled embryos were transferred to a microcentrifuge tube, washed three times with methanol, followed by three washes with PBT. Embryos were blocked in PBT with 5% normal goat serum for 30 min before incubating in rat anti-Tropomyosin (TM)

MAC141 (1:50; Babraham Institute, Cambridge, UK) in PBT and 5% normal goat serum at 4°C overnight or at room temperature for 2 hours. Embryos were washed three times for 10 minutes each in PBT and reblocked in PBT with 5% normal goat serum for 30 minutes. Fluorescent anti-rat Alexa Fluor 488 (1:400, ThermoFisher Scientific, Waltham, MA) were added for 1 hour at room temperature. The embryos were again washed three times for 10 minutes each in PBT. After washing, the embryos were mounted onto glass slides, and imaged with a Zeiss 700.

Live larval muscle imaging

Larval stages were collected in a similar as above on apple juice plates. A new plate was used to collect the next batch of embryos. The old embryo plates were kept at 25 °C with 24 hours interval to collect correlated stage larvae from 1st instar larvae, 2nd instar larvae to 3rd instar larvae. Live larvae were transferred using a needle pole and placed onto a Sylgard plate. The sylgard plate with live larvae was incubated into -20 °C for 10 mins to slow down muscle movements. Larvae were transferred on the glass slide with clear nail polish. A coverslip was added over the embryo with small pieces of clay at the corners for support. A Zeiss 700 confocal microscope was used to capture the images of each stage of larva under the laser power 2.

Western blotting

Embryo sample preparation

Embryo samples were homogenized in the 50µl lysis buffer (50 mM Tris-HCl pH 7.5, 150 mM NaCl, 1% Triton X-100, 10% glycerol) plus inhibitors (1x Halt protease inhibitor cocktail, 1x Halt phosphatase inhibitor cocktail; 1 mM Na_3VO_4, 1 mM NaF, 1 mM PMSF, 10 µM MG132, 0.001% PTU, 5 mM NPPS). To load equal amounts of total protein, we performed bicinchoninic acid

assay (BCA) experiments on embryo samples (Pierce BCA Protein Assay Kit 23225; ThermoFisher). Proteins were evenly loaded.

Larval sample preparation

Dissected muscle carcasses were placed into 3x SDS sample buffer [188 mM Tris-HCl (pH 6.8), 3% (w/v) SDS, 30% (v/v) glycerol, 0.01% (w/v) bromophenol-blue, and 15% (v/v) β-mercaptoethanol], boiled at 95 °C for 3 min, homogenized, boiled for an additional 10 min at 95 °C, and centrifuged at 20,000 x g for 1 min to pellet debris.

Western blot

The resulting protein samples were separated by sodium dodecyl sulfate polyacrylamide gel electrophoresis (SDS-PAGE) and transferred to the nitrocellulose blotting membrane (pore size o.45 μm, Cytiva, Marlborough, MA) using the Trans-Blot® TurboTM Transfer System (Bio-Rad, Hercules, CA). Membranes were probed with the following primary antibodies: rabbit anti-mCherry ab167453 (1:1000, Abcam, Waltham, MA) mouse anti-ATP5A ab14748 (1:10000, Abcam, Waltham, MA). IRDye 800CW secondary antibodies (LI-COR Biosciences, Lincoln, NE) were used at 1:10000 and Revert 700 Total Protein Stain (LI-COR Biosciences, Lincoln, NE) or anti-ATP5α was used as a loading control. Membranes were developed using the LI-COR Odyssey XF and quantitation of relative protein levels was performed in Empiria Studio Software (LI-COR Biosciences, Lincoln, NE).

Image processing

Image processing and analysis was performed using a combination of Zen Black (Zeiss), ImageJ (NIH), and Adobe Photoshop.

3.5 References

1. Roote, J. and A. Prokop, *How to Design a Genetic Mating Scheme: A Basic Training Package for Genetics.* G3-Genes Genomes Genetics, 2013. **3**(2): p. 353-358.
2. Brand, A.H. and N. Perrimon, *Targeted gene expression as a means of altering cell fates and generating dominant phenotypes.* development, 1993. **118**(2): p. 401-415.
3. Fischer, J.A., et al., *GAL4 activates transcription in Drosophila.* Nature, 1988. **332**(6167): p. 853-856.
4. Lilly, B., et al., *D-MEF2: a MADS box transcription factor expressed in differentiating mesoderm and muscle cell lineages during Drosophila embryogenesis.* Proceedings of the national academy of sciences, 1994. **91**(12): p. 5662-5666.
5. Bour, B.A., et al., *Drosophila MEF2, a transcription factor that is essential for myogenesis.* Genes & development, 1995. **9**(6): p. 730-741.
6. Bryantsev, A.L., et al., *Differential requirements for Myocyte Enhancer Factor-2 during adult myogenesis in Drosophila.* Developmental biology, 2012. **361**(2): p. 191-207.
7. Fischer, J.A. and T. Maniatis, *Drosophila Adh: a promoter element expands the tissue specificity of an enhancer.* Cell, 1988. **53**(3): p. 451-61.
8. Lim, S.Y., et al., *Identification and characterization of GAL4 drivers that mark distinct cell types and regions in the adult gut.* Journal of Neurogenetics, 2021. **35**(1): p. 33-44.
9. Pérez-Moreno, J.J. and C.J. O'Kane, *GAL4 drivers specific for type Ib and type Is motor neurons in Drosophila.* G3: Genes, Genomes, Genetics, 2019. **9**(2): p. 453-462.
10. Brand, N.J., *Myocyte enhancer factor 2 (MEF2).* The international journal of biochemistry & cell biology, 1997. **29**(12): p. 1467-1470.
11. Webster, N., et al., *The Yeast Uasg Is a Transcriptional Enhancer in Human Hela-Cells in the Presence of the Gal4 Trans-Activator.* Cell, 1988. **52**(2): p. 169-178.
12. Pon, J.R. and M.A. Marra, *MEF2 transcription factors: developmental regulators and emerging cancer genes.* Oncotarget, 2016. **7**(3): p. 2297-312.
13. Budnik, V., et al., *Regulation of synapse structure and function by the Drosophila tumor suppressor gene dlg.* Neuron, 1996. **17**(4): p. 627-640.
14. Zhang, Y.Q., et al., *Drosophila fragile X-related gene regulates the MAP1B homolog Futsch to control synaptic structure and function.* Cell, 2001. **107**(5): p. 591-603.
15. Shaw, N.M., et al., *Effects of mutant lamins on nucleo-cytoskeletal coupling in Drosophila models of LMNA muscular dystrophy.* Frontiers in cell and developmental biology, 2022. **10**: p. 934586.
16. Coombs, G.S., et al., *Modulation of muscle redox and protein aggregation rescues lethality caused by mutant lamins.* Redox biology, 2021. **48**: p. 102196.
17. Zhao, Z., et al., *Identification of CryAB as a target of NUAK kinase activity in Drosophila muscle tissue.* Genetics, 2023. **225**(3): p. iyad167.
18. Renden, R.B. and K. Broadie, *Mutation and activation of Gαs similarly alters pre-and postsynaptic mechanisms modulating neurotransmission.* Journal of neurophysiology, 2003. **89**(5): p. 2620-2638.
19. Gorczyca, D., et al., *Postsynaptic membrane addition depends on the Discs-Large-interacting t-SNARE Gtaxin.* J Neurosci, 2007. **27**(5): p. 1033-44.
20. Viquez, N.M., et al., *The B′ protein phosphatase 2A regulatory subunit regulates synaptic growth and cytoskeletal stability at the neuromuscular junction.* Journal of Neuroscience, 2006. **26**(36): p. 9293-9303.

21. Lawrence, P.A. and P. Johnston, *The Genetic Specification of Pattern in a Drosophila Muscle.* Cell, 1984. **36**(3): p. 775-782.
22. Ruiz-Gomez, M., *Muscle patterning and specification in Drosophila.* International Journal of Developmental Biology, 1998. **42**(3): p. 283-290.
23. Johansen, J., M.E. Halpern, and H. Keshishian, *Axonal guidance and the development of muscle fiber-specific innervation in Drosophila embryos.* J Neurosci, 1989. **9**(12): p. 4318-32.
24. Potthoff, M.J. and E.N. Olson, *MEF2: a central regulator of diverse developmental programs.* 2007.
25. Poovathumkadavil, P. and K. Jagla, *Genetic control of muscle diversification and homeostasis: Insights from Drosophila.* Cells, 2020. **9**(6): p. 1543.
26. Cauchi, R.J., K.E. Davies, and J.L. Liu, *A Motor Function for the DEAD-Box RNA Helicase, Gemin3, in.* Plos Genetics, 2008. **4**(11).

Chapter 4 - Pathogenic CryAB Mutations in Muscle Suggest a Novel Mechanism for Amyloid Secretion via Extracellular Vesicles

This chapter will be published as a journal article in the *iScience*.

Zhao Z[a], Lim HY[b], Cannone E[c], Marchetto G[d], Schiavone M[c], Vattemi G[d],

Guo Y[a], Wang Z[e], Glancy B[e], and Geisbrecht ER[a,*].

[a]Department of Biochemistry and Molecular Biophysics, Kansas State University, Manhattan, KS, 66506

[b]Department of Genetics, University of Alabama at Birmingham, Birmingham, AL 35294

[c]Department of Molecular and Translational Medicine, Zebrafish Facility, University of Brescia, Brescia, Italy 25123

[d]Department of Neurosciences, Biomedicine and Movement Sciences, University of Verona, Verona, Italy 37129

[e]National Institute of Arthritis and Musculoskeletal and Skin Diseases, National Institutes of Health, Bethesda, MD 20892

*Corresponding author: Erika R Geisbrecht, 141 Chalmers Hall, Kansas State University, Manhattan, KS, 66506, geisbrechte@ksu.edu

4.1 Abstract

Amyloid fibrils are insoluble protein aggregates commonly associated with neurodegenerative disorders such as Alzheimer's and Parkinson's disease. Although predominantly studied in the brain, amyloid deposition in skeletal muscle is poorly understood. Mutations in the small heat shock protein αB-crystallin (CryAB) result in cataracts, cardiomyopathies, and myofibrillar myopathies (MFMs), all of which are marked by intracellular protein aggregation. To investigate the pathological mechanisms of CryAB mutations in muscle tissue, we expressed four human CryAB alleles in *Drosophila melanogaster* (*D. melanogaster*) cardiac and skeletal muscle. All variants disrupted autophagic flux, resulting in the accumulation of protein aggregates labeled by ubiquitin and p62/SQSTM1. Notably, mutations within the conserved α-crystallin domain (ACD) led to the formation of distinctive CryAB-positive inclusions that colocalized with an amyloidogenic form of human Desmin. Transmission electron microscopy and Congo red staining confirmed that these CryAB inclusions exhibited amyloid-like architecture. The presence of amyloid was not limited to mutations in *D. melanogaster* CryAB as amyloid deposits are also evident in other mutant genes causative for MFM in the zebrafish musculature or in human MFM muscle biopsy samples. Strikingly, these CryAB aggregates were also associated with markers of extracellular vesicle (EV) pathways. Modulating EV proteins - either through overexpression or RNAi - altered the size and number of CryAB inclusions. Furthermore, secreted inclusions were detectable in the hemolymph, suggesting an EV-mediated export mechanism. This work sheds new light on the pathological basis of myofibrillar myopathies and broadens the understanding of amyloid dynamics beyond the nervous system.

4.2 Introduction

Protein homeostasis, or proteostasis, is an equilibrium system that ensures proper protein folding and degradation. When proteostasis fails, protein aggregates with pathological roles may form, as seen with tau in Alzheimer's disease and alpha-synuclein in Parkinson's disease [1-4]. A hallmark of Alzheimer's and Parkinson's diseases is amyloid fiber formation in the brain [5-7]. However, this fibrillar-like protein aggregation, also known as amyloidosis, extends beyond neurodegenerative diseases—it can occur in the lungs, kidneys, muscles, and other organs [8-11]. However, it is yet unclear if other types of protein aggregates that form in non-neuronal tissues are linked to the formation of amyloid fibers.

Myofibrillar myopathies (MFMs) are a type of protein aggregate disease characterized by muscle fiber degeneration and progressive muscle weakness - typically in distal limb muscles [12-15]. Although MFMs can onset in early childhood, symptoms most commonly appear later in life [16]. A subset of muscle proteins, including the Z-disk-associated proteins Desmin, Myotilin, Filamin C, α-Crystallin B (CryAB), and Bag3 are overrepresented and abnormally accumulate in biopsies from MFM patients [17-19]. Due to the diversity of mutations in MFM-causing genes and the lack of understanding in the underlying pathogenicity of disease initiation and progression, there are no effective treatments.

To date, over 15 different mutations in CryAB have been linked to MFMs and/or cardiomyopathies [20-25]. CryAB, also known as heat shock protein 5 (HSPB5), is widely expressed across various tissues [26]. As a chaperone protein, CryAB aids in protein refolding and preventing aggregation. This approximately 20 kDa monomer forms highly ordered hetero-oligomeric complexes in response to intracellular stresses (heat, aging, oxidative or reductive stress) to sequester damaged or misfolded proteins, thereby maintaining proteostasis [27, 28].

Mutations in CryAB lead to structural and functional changes that impair its interactions with client proteins, with distinct mutations producing varying effects on CryAB function. For instance, the D109A and R157H mutations differentially decrease or enhance chaperone activity *in vitro*, respectively [29, 30]. Previous studies suggest that CryAB helps protect cytoskeletal myofibrils [31], implying that mutant CryAB may play a pathological role in muscle and cardiac tissue.

Intercellular communication is essential for maintaining tissue homeostasis and coordinating physiological processes between tissues. One key mechanism by which cells communicate is through extracellular vesicles (EVs), which transport molecular signals - including proteins, lipids, and RNA - between cells [32-35]. Beyond their secretory role in normal physiology, EVs are also widely implicated in pathological contexts, particularly in cancer, where they contribute to tumor growth, survival, and metastasis [36-39]. EV biogenesis involves a tightly regulated series of intracellular trafficking events. Early endosomes mature into multivesicular bodies (MVBs), which package selected cargos for eventual secretion. Once formed, MVBs can fuse with the plasma membrane, releasing their contents as EVs into the extracellular space using two primary routes: endosomal sorting complexed required for transport (ESCRT)-dependent and ESCRT-independent pathways [40, 41]. While the role of EVs in cancer has been extensively studied, their involvement in muscle disorders, particularly in myofibrillar myopathies (MFMs), remains largely unexplored. Given the progressive and sometimes systemic nature of MFM pathologies [13, 42], understanding the potential for EV-mediated propagation of disease-related proteins could reveal novel mechanisms of pathogenesis.

Despite decades of research, the pathogenicity of CryAB mutations remains incompletely understood. Although numerous CryAB mutations have been identified, most research has focused on the R120G mutation, limiting a broader genotype-phenotype correlation [20, 43-49]. To fill this

scientific gap, we selected independent human CryAB mutations, including R120G (linked to Desmin-related cardiomyopathy), D109A (implicated in MFM or Desmin-related myopathy), and D109H and R157H (both associated with dilated cardiomyopathy) for further analysis using *Drosophila melanogaster (D. melanogaster)* as a cell biological model. First, we show that CryAB mutations disrupt protein homeostasis via impaired molecular chaperone activity, resulting in the accumulation of misfolded proteins marked by Ubiquitin (Ubi) and the autophagy adaptor protein p62/SQSTM1. Second, we identify novel CryAB intracellular structures that are amyloidgenic in nature, colocalize with EV markers, and are secreted, thereby linking amyloid-inclusions to vesicle trafficking. Third, these CryAB inclusions exhibit amyloid-like properties not only in *Drosophila* muscle but also in zebrafish and human MFM muscle biopsies, indicating a conserved and clinically relevant pathogenic feature. In summary, this study establishes a mechanistic link between CryAB mutations, amyloid formation, and secretion from muscle tissue, possibly as a protective mechanism to limit tissue damage. Our findings extend the role of CryAB beyond protein quality control, highlighting its broader impact on cytoskeletal dynamics, vesicle trafficking, and disease progression.

4.3 Results

CryAB is comprised of an alpha-crystallin domain (ACD) common to heat shock family proteins and less conserved flexible N- and C-terminal regions that are responsible for oligomerization and the binding of client proteins **(Figure 4.1 A)** [26, 28]. Primary amino acid sequence alignments shows that the location of the dominant human CryAB mutations D109, R120, and R157 are conserved in *Drosophila* (D113, R124, and R163), although we will continue to use the human amino acid numbering here **(Appendix Figure E1 A)**. Mutations D109 and R120

reside within the ACD, while R157 is positioned near the C-terminus **(Figure 4.1 A)**. *In vitro* studies demonstrate that the CryAB mutations D109A and R120G induce oligomerization, while R157H does not, suggesting that the location of each mutation distinctly influences CryAB's structural and functional properties [25, 26].

To investigate the *in vivo* effects of these CryAB mutations, we generated transgenic *Drosophila* lines expressing four conserved human mutations (D109A, D109H, R120G, R157H) and wildtype CryAB under the control of upstream activating sequences (UAS). Each of these CryAB pathogenic alleles was independently expressed under control of the *Myocyte enhancer factor 2* (*Mef2*) promoter [50, 51]. For phenotypic analysis, we first examined wandering third instar larvae (L3), whose larger size facilitates muscle dissection and imaging. L3 carcasses were stained with anti-CryAB and phalloidin to assess protein distribution and muscle structure, respectively. While F-actin striations appeared normal, the sarcomeric CryAB protein pattern was disrupted, instead forming distinct circular or oval structures upon expression of ACD mutations (D109A, D109H, and R120G) **(Figure 4.1 B, open white triangles)**. We previously identified two novel residues in CryAB (S68 and S70) that are phosphorylated by the serine/threonine (S/T) protein NUAK kinase [52]. The location of these phosphorylated residues is conserved in the human CryAB sequence **(Appendix Figure E.1 A)**, but as of yet no human mutations are linked to disease. Only the S70A or S70E mutations displayed a CryAB phenotype similar to the ACD variants **(Figure 4.1 B and Appendix Figure E.1 B)**. Since S70 is located within the ACD **(Figure 4.1 A)**, we collectively refer to D109A, D109H, R120G, and S70E as "ACD domain mutations."

Aging is characterized by the accumulation of cellular damage, contributing to functional decline and heightened disease susceptibility [53]. Human mutations in CryAB promote protein accumulation with age in specific tissues, namely the eye, brain, and heart [26, 54, 55]. To

investigate if human CryAB mutations affect *Drosophila* lifespan, we monitored the longevity of transgenic flies at 31 °C. As shown in **Figure 4.1 C**, overexpression of either wildtype or mutant CryAB significantly shortened lifespan compared to *mCh RNAi* controls ($p<0.0001$), with wildtype CryAB exhibiting 50% lethality around Day 15. Increased lethality was also observed in the pupal stage, except in lines expressing R157H and S70E **(Appendix Figure E.1 C)**. These findings demonstrate that increased temperature exacerbates CryAB-associated toxicity and accelerates mortality in *Drosophila*.

Since CryAB mutations can cause dilated cardiomyopathies (DCM) [26, 27, 30, 56], we next investigated how CryAB mutations affect cardiac function in 2.5 week-old flies at 25 °C. First, we verified that all CryAB insertion lines driven by *Mef2*-Gal4 expressed similar amounts of CryAB protein since they were all inserted into the same attB site on chromosome 2 **(Appendix Figure E.1D and E)**. Again, using *Mef2*-Gal4 to express CryAB mutations in the *Drosophila* heart tube, we observed a significant reduction in both diastolic and systolic intervals **(Figure 1D and E; Figure S1F and G)**, indicating impaired cardiac function. Further analysis revealed that heart tube contractility was markedly increased in flies expressing the CryAB D109A, R120G, or R157H mutations, with the exception of D109H which showed no significant change **(Figure 4.1 F; Appendix Figure E.1 H)**. To examine potential protein aggregation and structural abnormalities in this tissue, we selected D109A and R120G for heart tube staining. Immunostaining revealed excess or irregular CryAB distribution **(Figure 4.1 G, open arrowheads)** compared to normal Z-disc localization **(Figure 4.1 G, open arrows)**. We also detected numerous Ubiquitin (Ubi)-positive puncta, suggesting the formation of protein aggregates within the heart tube **(Figure 4.1G, solid arrowheads)**. Due to the small size and limited resolution of the heart tube, these phenotypes were difficult to assess in detail. To overcome this

limitation, we shifted our focus to the indirect flight muscles (IFMs), which offer the advantage of larger tissue size and more muscle fibers for clearer observations of morphological and pathological changes.

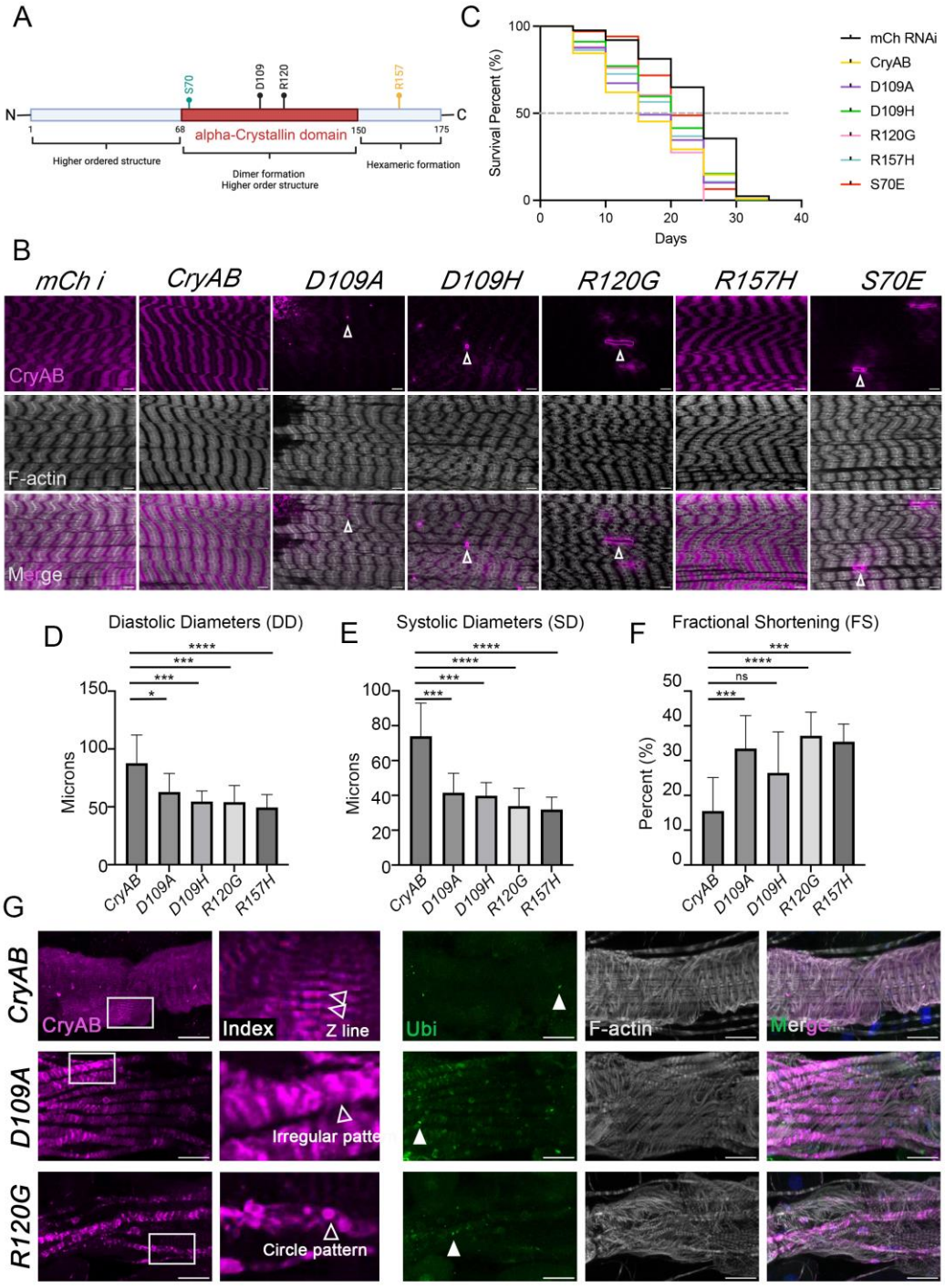

Figure 4.1 Impacts of CryAB mutations on protein localization and cardiac function in Drosophila

(A) Schematic of CryAB domains. The flexible N-terminal domain is involved in oligomer assembly, the conserved alpha-crystallin domain (ACD) is required or dimer formation, and the C-terminal domain is associated with hexamer formation. The location of mutations being analyzed are shown.
(B) Confocal images of L3 muscles expressing the *mCh RNAi* (*mCh i*) and wild-type *CryAB* (*CryAB*) controls along with the indicated CryAB point mutations. All UAS constructs are driven using *Mef2*-Gal4. F-actin is shown in gray and CryAB in magenta. Aberrant CryAB localization is indicated by the open white arrowheads. Scale bar: 5 μm.
(C) Survival curves of adult flies expressing CryAB variants. While *mCh RNAi* controls show extended longevity, expression of CryAB wildtype and mutants significantly reduces lifespan, with over 50% mortality in the WT group by Day 15 (N>140).
(D-F) CryAB variants expressed in adult cardiac tube and assessed via semi-automated optical heartbeat analysis. (D) Diastolic diameter (DD) measurements result in reduced heart tube relaxation compared to CryAB WT. (N > 5 per genotype; one-way ANOVA, Kruskal-Wallis test). (E) Systolic diameter (SD) measurements reveal that CryAB mutations cause a pronounced decrease in heart tube contraction relative to WT. (N>5 per genotype; One-way ANOVA, Kruskal-Wallis test). **(F)** Fractional shortening (FS), an indicator of cardiac contractility, is significantly impaired in CryAB mutants (N>5 per genotype; One-way ANOVA, Kruskal-Wallis test).
(G) Confocal images of adult Day 2 fly hearts expressing CryAB constructs with *Mef2*-Gal4. Localization of CryAB (magenta), F-actin (gray), and ubiquitin (green) are shown. Insets highlight CryAB protein distribution. *CryAB WT* localizes along regular Z-discs, while *D109A* and *R120G* mutants exhibit disorganized Z-line accumulation and ring-like aggregates (open white arrowheads). Solid white arrowheads indicate Ubi-labeled protein aggregates. Scale bar: 20 μm.

CryAB mutations promote insoluble aggregates

Given the role of CryAB mutations in cardiomyopathies, which often involve disrupted protein turnover, we investigated if these pathogenic alleles lead to protein aggregation in the IFMs. Based upon our lifespan analysis (**Figure 4.1 B**) we selected Day 2 and Day 10 females flies to assure we had enough viable adults for experiments to assess the impact of CryAB mutations during this 8-Day period of aging. Confocal microscopy revealed two distinct phenotypes in the IFMs: aggregates and inclusions **(Figure 4.2 A; Appendix Figure E.2 A;** movie do not provide in this thesis**)**. CryAB aggregates, defined as solid CryAB immunostaining that overlapped with Ubi signal, were present in all genotypes tested. All CryAB ACD domain mutations, but not CryAB WT or R157H, also revealed hollow, circular structures that stain

positive for CryAB which we have termed CryAB inclusions. Below, we present evidence supporting each of these phenotypes.

We first used Ubi to label misfolded and/or aggregated proteins that fail to undergo degradation. Co-staining with CryAB antibodies confirmed more Ubi accumulation in IFMs expressing CryAB ACD domain mutations at Day 2 (**Figure 4.2 B**). Quantitative analysis of Ubi aggregates using ImageJ confirmed that D109A, R120G, and S70E exhibited a significant increase in Ubi aggregates - at least two-fold higher than CryAB or R157H at Day 2 **(Figure 4.2 C)**. However, by Day 10, aggregates marked by Ubi were observed in all genotypes, with the largest increase in D109H and R120G **(Figure 4.2 D; Appendix Figure E.2 B)**. Co-localization analysis revealed that CryAB ACD domain mutations exhibited more than a 60% increase in CryAB/Ubi overlap compared to CryAB or R157H at Day 2, with a continuous increase in aggregation of all genotypes by Day 10 **(Figure 4.2 E)**. The observed accumulation of CryAB aggregates in muscle tissue is characteristic of protein aggregation and predicts that these complexes may lead to protein insolubility. To confirm the presence of insoluble CryAB, we performed Western blot analysis. ACD domain mutations led to a 50 to 70-fold increase of insoluble CryAB protein compared to CryAB or R157H which remained largely in the soluble fraction at Day2 **(Figure 4.2 F-H)** or Day 10 **(Appendix Figure E.2 C-E)**.

Proteins destined for degradation in the lysosome via autophagy or by the proteasome can both be tagged with Ubi [57]. To establish which aspect(s) of proteostasis may be altered by CryAB mutations, we next examined the localization and levels of the autophagy adaptor protein p62/SQSTM1 (Sequestosome 1) which marks ubiquitinated cargo proteins [58]. Immunostaining showed co-localization of Ubi aggregates with p62 **(Figure 4.2 I, solid arrowhead)** and a general increase in the levels of both soluble and insoluble p62 in all CryAB lines except for R157H and

S70E **(Appendix Figure E.3 A-F)**. This accumulation of p62 indicates that autophagic flux is compromised by CryAB mutations. Day 2 and Day 10 IFMs expressing mutant CryAB proteins also showed a reduction in proteasome activity **(Appendix Figure E.3 G, H)**. These data together show that loss of autophagic turnover due to CryAB mutations fails to upregulate proteasome function, further promoting the progressive accumulation of aggregates with age in muscle tissue.

Since the BAG-domain-containing co-chaperone protein Starvin (Stv) also marks aggregates [59] and is involved in the autophagy pathway [60, 61], we next examined Stv localization. Indeed, Stv labeled Ubi aggregates in the IFMs **(Appendix Figure E.4, solid arrowheads)**. Note that not all aggregates may be degraded via Bag3-related autophagy since some Ubi aggregates did not co-localize with Stv **(Appendix Figure E.4, asterisks)**. Here we conclude that protein aggregates, marked by CryAB, Ubi, p62, and Stv, accumulate with age in *Drosophila* IFMs coincident with decreased autophagic protein turnover upon expression of CryAB mutant proteins.

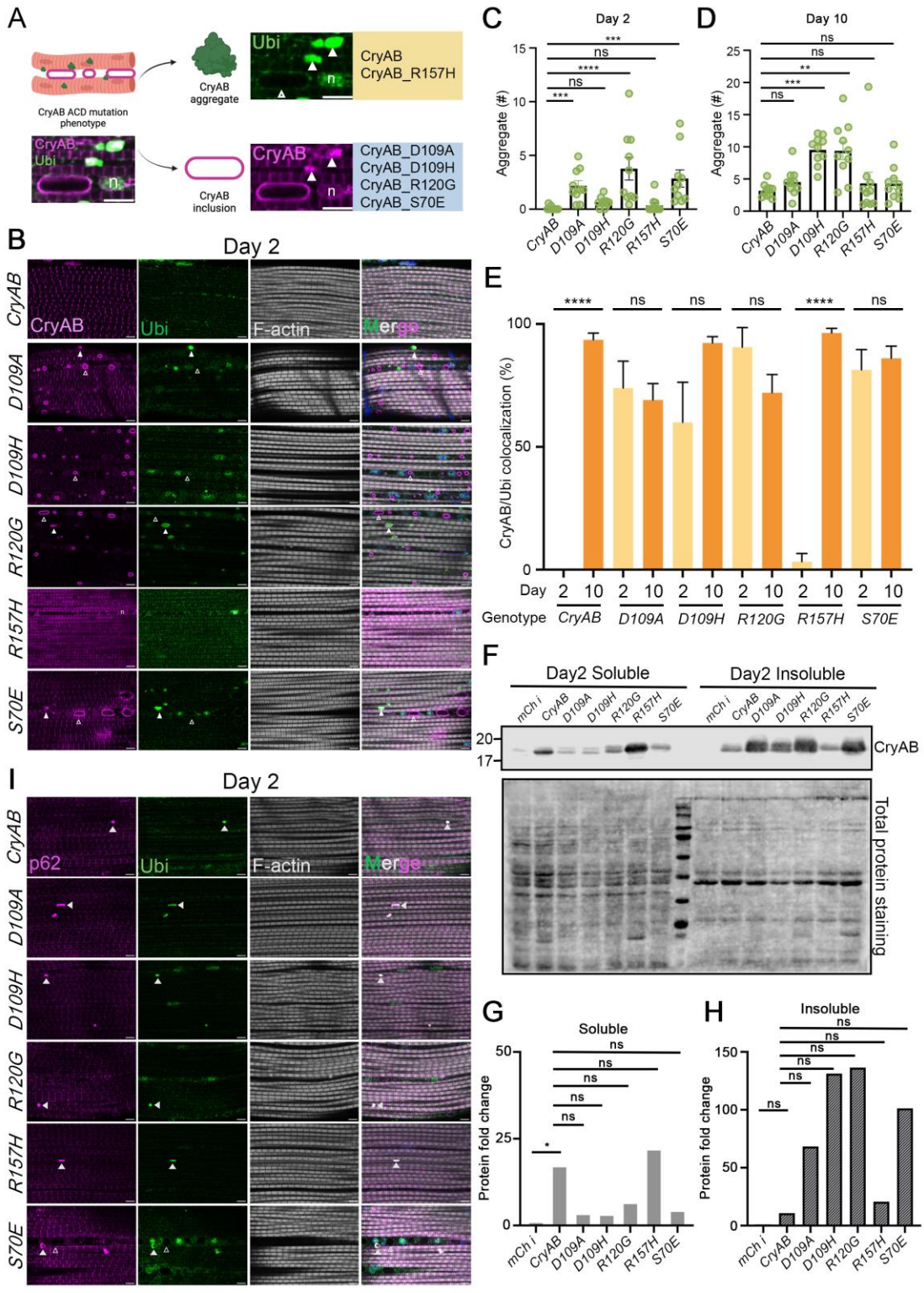

Figure 4.2 CryAB mutations disrupt proteostasis and promote insoluble aggregates

(A) Schematic summarizing the two phenotypes observed in adult IFMs: aggregation (CryAB colocalized with Ubi, solid white triangles) and inclusions (CryAB staining without Ubi, open

white triangles). CryAB inclusions are associated with mutations in the ACD domain (*D109A, D109H, R120G, S70E*). Scale bar: 5 μm.
(B) Representative single-slice images of Day 2 adult IFMs showing F-actin (gray), CryAB (magenta), and Ubi (green). *CryAB WT* and *R157H* exhibit Z-disc localization, while ACD mutations display aggregates and inclusions. Nuclei are counterstained with DAPI (blue). Scale bar: 5 μm.
(C, D) Quantification of Ubi-positive aggregates in Day 2 and Day 10 flies represented as a scatter-bar plot. Data are mean ± SD (N=10 per genotype, One-way ANOVA, Kruskal-Wallis test). ns = not significant, *p>0.05, **p<0.05, ***p<0.01, ****p<0.001.
(E) Percentage of CryAB/Ubi colocalization in aggregates of Day 2 and Day 10 IFMs. Data are mean ± SD (N=10 per genotype, Unpaired student t-test, Mann-Whitney test). ns = not significant, *p>0.05, **p<0.05, ***p<0.01, ****p<0.001.
(F) Western blot showing soluble and insoluble CryAB levels in Day 2 adult samples. ACD mutations result in increased insoluble CryAB compared to Cry WT and R157H. Total protein staining serves as a loading control. N≥3.
(G, H) Bar graph shows quantification of soluble and insoluble CryAB protein from (F). Data are mean ± SD (N=3).
(I) Immunostaining of 2-Day-old IFMs for p62 (magenta), Ubi (green), and F-actin (gray). Nuclei are counterstained with DAPI (blue). Solid white triangle highlights the aggregation phenotype. Scale bar: 5 μm.

CryAB ACD mutations promote inclusion formation

As previously mentioned, we observed a novel phenotype characterized by hollow circular or oval structures outlined by CryAB staining prevalent in both L3 larval muscles **(Figure 4.1 B, open arrowheads)** and adult IFMs **(Figure 4.2 B, open arrowheads)**. The lack of co-localization with Ubi or p62 indicated that CryAB inclusions were not associated with canonical proteasome or autophagy protein degradation pathways. To further characterize these CryAB inclusions, we conducted statistical analyses on the number and size of these structures across different mutations and ages. All CryAB ACD mutations (S70E, D109A, D109H, and R120G), but not CryAB or R157H, showed significantly more inclusions in both Day 2 and Day 10 IFMs **(Figure 4.3 A and B)**. We also observed size variation, leading to the hypothesis that inclusion size would increase with age. Indeed, while only the increase in size of D109A inclusions was statistically significantly

from Day 2 to Day 10, other ACD mutations exhibited a strong trend of inclusion size growth **(Figure 4.3 C)**.

To gain further insight into the composition of CryAB inclusions, we performed Transmission Electron Microscopy (TEM) on two CryAB ACD mutations (D109A and S70E) to analyze the IFM ultrastructure. Low-magnification micrographs (1500x) revealed the embedding of mutant CryAB inclusions between muscle fibers without significantly disrupting fiber structure **(Figure 4.3 D-F)**. Higher magnification TEM images (5000x) surprisingly showed inclusions as large structures surrounding multiple smaller inclusions in D109A **(Figure 4.3 E)** or S70E **(Figure 4.3 F, top panel)** muscles. This internal structural complexity was only occasionally visible, likely due to limited antibody penetration. Notably, fibril-like structures were also observed in S70E **(Figure 4.3 F, bottom panel)**. Increased magnification (8000x) detailed irregular ribbon-like formations that eventually looped to form protofilament-like structures, resembling amyloid fibrils. These findings provide the first *in vivo* evidence that CryAB mutations promote amyloid formation.

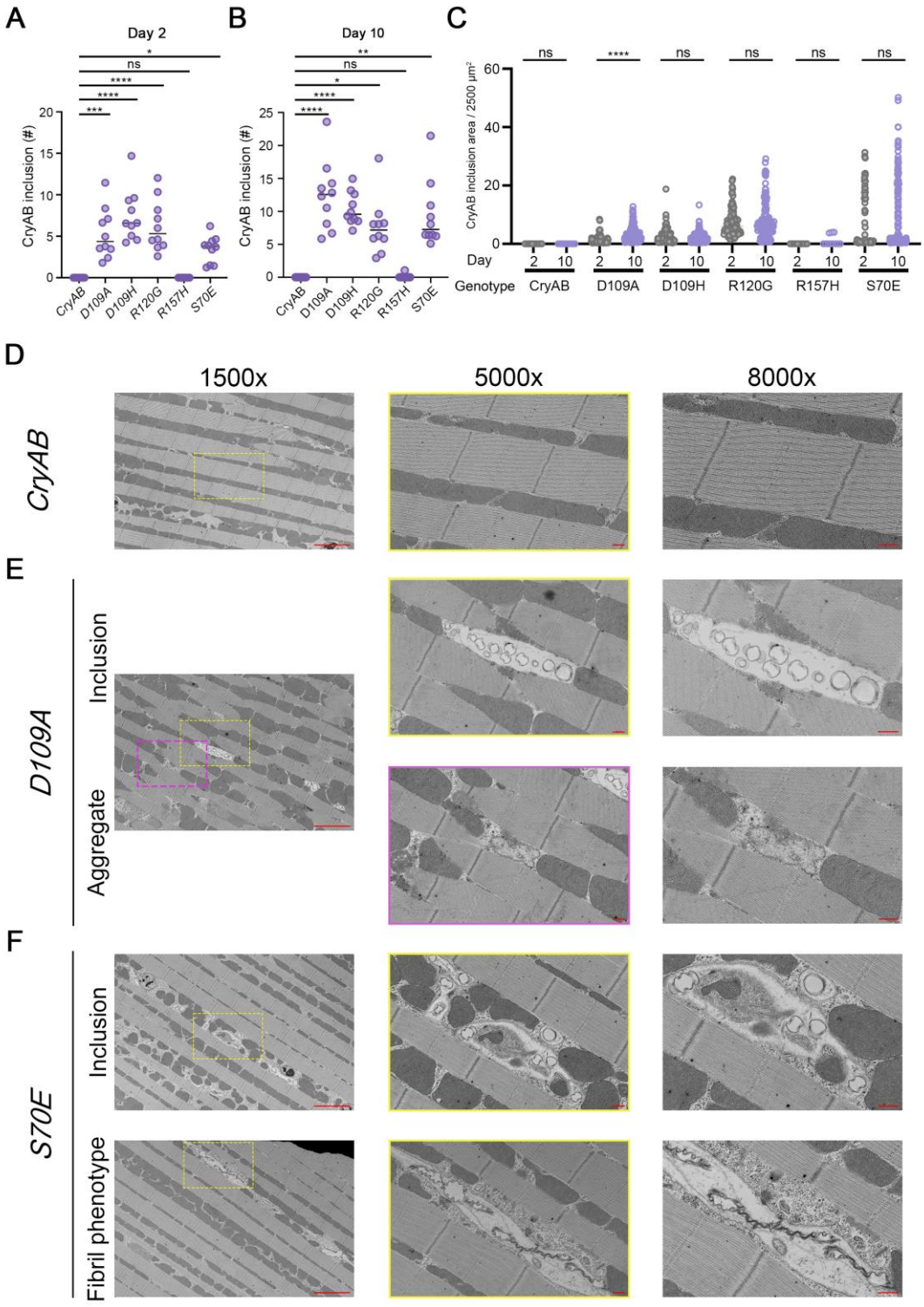

Figure 4.3 Overexpression of CryAB ACD mutations promotes inclusion formation

(A, B) Quantification of CryAB inclusions per genotype in Day 2 IFMs. Data are mean ± SD (N=10 per genotype, One-way ANOVA, Kruskal-Wallis test). ns = not significant, *p>0.05, **p<0.05, ***p<0.01, ****p<0.001.

(C) Inclusion area per 2500 μm² for Day 2 and Day 10 IFMs. Data are mean ± SD (N=10 per genotype, Unpaired student t-test, Mann-Whitney post hoc analysis).
(D-F) TEM analysis of Day 10 IFMs across genotypes. D109A shows aggregates and inclusions; S70E exhibits aggregate-inclusion transitions and fibril-like structures. Magnifications: 1500x, Scale bar: 5 μm, 5000x, Scale bar: 500 nm, and 8000x, Scale bar: 500 nm.

CryAB inclusions co-localize with amyloidogenic Desmin

Desmin-related myopathy (DRM), a sub-type of MFM, is characterized by myofibrillar dissolution and the accumulation of the intermediate filament protein Desmin [62]. Moreover, *in vitro* studies showed that CryAB R120G can induce Desmin aggregation [63, 64]. To test if an amyloidogenic region (aa 117-348) of Desmin [65] possesses *in vivo* amyloid-like features similar to CryAB, we developed a humanized model of DRM **(Figure 4.4 A)**. Expression of amyloidogenic human Desmin revealed Desmin-positive inclusions that co-localized with CryAB **(Figure 4.4 B, open arrowheads)**. Co-expression of CryAB ACD mutations also localized with amyloidgenic Desmin **(Figure 4.4 C, open arrowheads)**, supporting the amyloid-like nature of CryAB inclusions. Occasionally small inclusions were also present with CryAB alone or R157H when co-expressed with hDesmin, suggesting that normal or heightened chaperone activity was insufficient to prevent the amyloid phenotype induced by human Desmin. Quantitative analysis confirmed that inclusion numbers in flies co-expressing amyloidgenic Desmin with CryAB mutations were not significantly different from those with Desmin alone at Day 2 or Day 10 **(Appendix Figure E.5 B and C)**.

To further substantiate the presence of amyloid-like structures, we isolated CryAB inclusions from muscle tissue and stained them with the amyloid marker Congo red. Extracted inclusions from muscles expressing D109A, R120G, or S70E all stained positive stained for Congo red and CryAB (**Figure 4.4 D**). Isolation of these structures allowed for improved reagent penetration as we were able to detect smaller circular inclusions inside the typical CryAB(+)

staining **(Appendix Figure E.5 D)**, similar to those seen by TEM **(Figure 4.3 E and F)**. These double-labeling experiments confirm that the CryAB inclusions indeed consist of amyloid-like fibers.

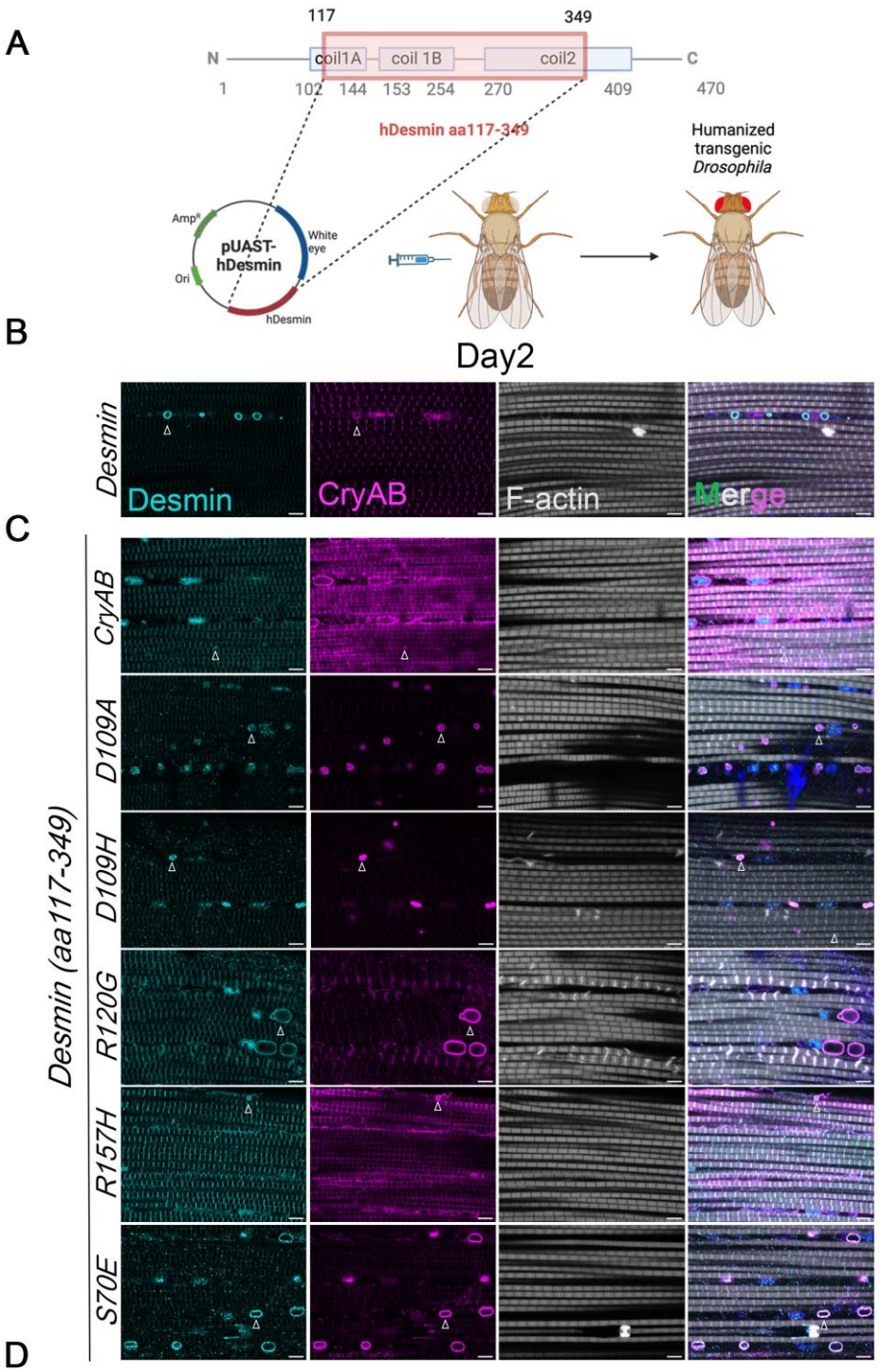
A
117
349
N
coil1A
coil 1B
coil2
C
1
102
144
153
254
270
409
470
hDesmin aa117-349
Humanized transgenic Drosophila
Amp^R
pUAST-hDesmin
White eye
Ori
hDesmin
B
Day2
Desmin
Desmin
CryAB
F-actin
Merge
C
Desmin (aa117-349)
CryAB
D109A
D109H
R120G
R157H
S70E
D
Inclusion extraction from muscle tissue
D109A
R120G
Congo Red
CryAB

Figure 4.4 CryAB inclusions phenocopy Desmin accumulation and form amyloid fibrils

(A) Schematic of amyloidogenic region of Desmin (AA 117-349) used to generate humanized Desmin transgenic fly lines.
(B,C) Immunostaining of IFMs with *Mef2*-Gal4 expressing human Desmin (AA 117–349) alone (B) or with CryAB mutants (C). Desmin (cyan) forms structures similar to CryAB inclusions (open white triangles) in Day 2 IFMs. F-actin is labeled in grey and nuclei are stained with DAPI (blue). Scale bar: 5 μm.
(D) CryAB inclusions isolated from adult IFMs stained with Congo red. Co-localization of CryAB antibody (green) with Congo red-positive structures (red) confirms amyloid fibrils. Scale bar: 5 μm.

CryAB amyloid-like inclusions are present in zebrafish and human muscle

Next we wanted to test if amyloid-like inclusions can form in muscle tissue from other species expressing human mutations. We first assessed hCryAB G154S since this mutation causes MFM, but not cataracts or cardiomyopathy [66, 67]. Compared to hCryAB WT, hCryAB G154S expression resulted in approximately a 40% increase in Congo red–positive aggregates **(Figure 4.5 A and B)**, confirming the presence of amyloid-like inclusions in zebrafish muscle. Next, we investigated whether similar amyloid features could be observed with other proteins implicated in myofibrillar myopathies (MFMs). We focused on human *Myotilin* (*MYOT*), another gene commonly mutated in MFM patients [68]. Zebrafish embryos injected with the hMYOT S95I mutant displayed a 50% occurrence of Congo red–positive aggregates, approximately 20% higher than hMYOT WT **(Figure 4.5 C and D)**. These results demonstrate that amyloid accumulation is not restricted to CryAB mutations in *Drosophila*, but is a broader pathological feature in vertebrate muscles.

To extend these findings to human pathology, we analyzed muscle biopsy samples from MFM patients carrying mutations in *CryAB* (G154S), *MYOT* (S60F), or *Desmin* (R454W). In all cases, histological examination revealed features characteristic of MFMs, including variable fiber size and fatty replacement assessed by hematoxylin and eosin (H&E) and NADH–tetrazolium

reductase (NADH-TR) staining **(Figure 4.5 E-G)**. Importantly, these patient tissues also showed positive Congo red staining, reinforcing the presence of amyloid-like structures. Collectively, these data suggest that amyloid accumulation is a shared pathological feature across multiple MFM-related genes and model systems. This supports a broader hypothesis that amyloidogenesis is not limited to neurodegenerative conditions but is also a central mechanism in muscle diseases such as MFMs.

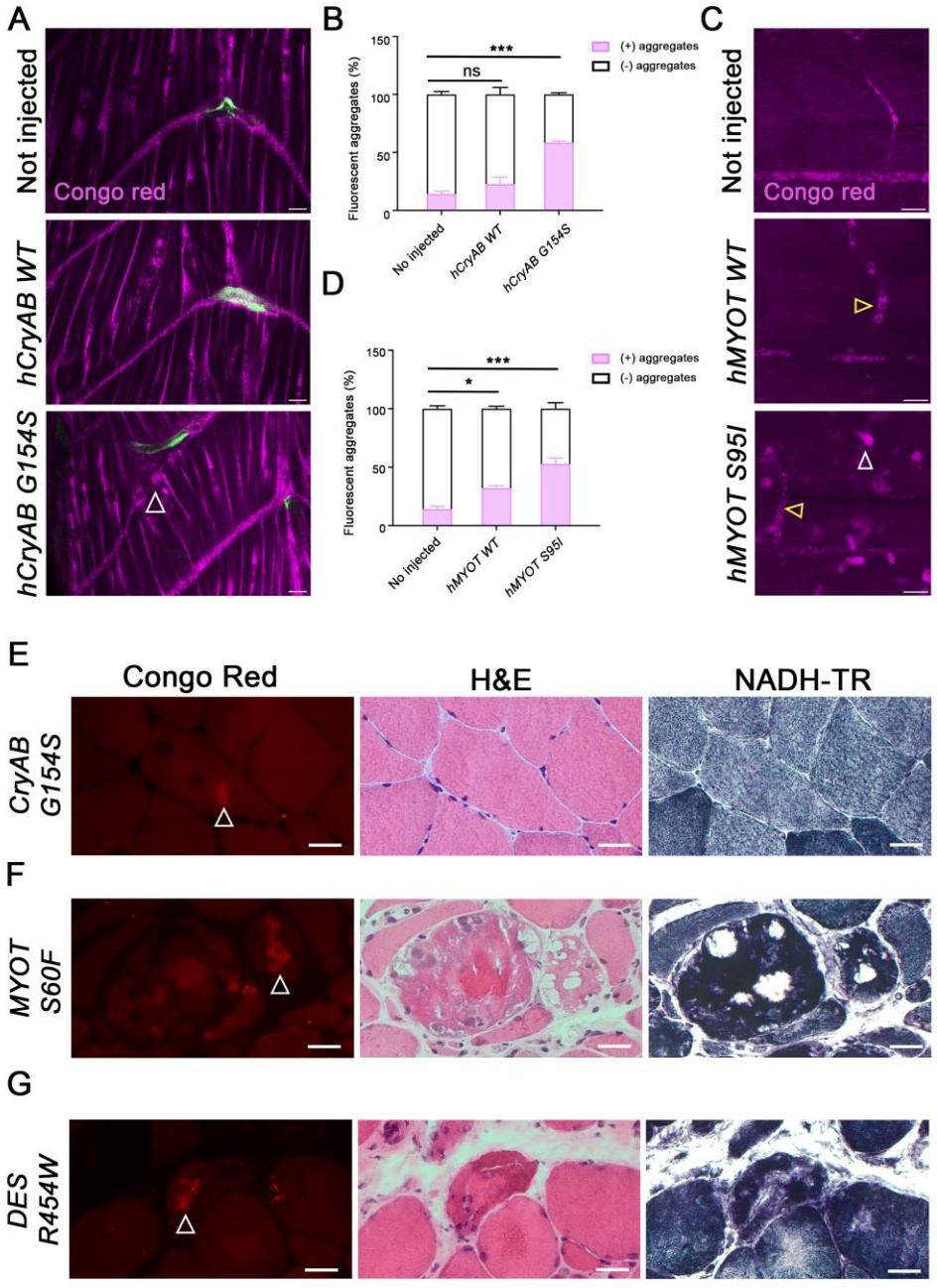

Figure 4.5 ACD domain mutations induce amyloid deposition in zebrafish and are associated with congophilic inclusions in human MFMs

(A) Representative images of whole-mount Congo red staining in zebrafish embryos at 120 hours post-fertilization (hpf). Embryos were either uninjected, injected with human wild-type *CRYAB* (*hCRYAB WT*), or with the G154S mutant (*hCRYAB G154S*). Merged images show Congo red staining (magenta) and vasculature labeled by the tg(*kdrl:EGFP*) transgene (green). Open white arrows highlight congophilic aggregates in trunk muscle fibers. N=3 independent experiments. Scale bar: 5 μm.
(B) Bar graph quantification of embryos exhibiting Congo red-positive aggregates. Not injected (5/35), *hCRYAB WT* (7/29), *hCRYAB G154S* (31/53). Mean ± SEM. (***p < 0.001, One-way ANOVA with Bonferroni correction).
(C) Congo red staining of zebrafish embryos injected with human *MYOT* constructs. Embryos were either uninjected, or injected with wild-type (*hMYOT WT*) or mutant (*hMYOT S95I*) forms. White arrows indicate Congo red-positive deposits in muscle fibers. Open yellow arrows indicate intersomitic blood vessels. N=3 independent experiments. Scale bar: 20 μm.
(D) Bar graph quantification of embryos with Congo red-positive aggregates. Not injected (5/35), *hMYOT WT* (10/31), *hMYOT S95I* (11/21). Mean ± SEM. (*p < 0.05, ***p < 0.001, One-way ANOVA with Bonferroni correction).
(E–G) Histological analysis of skeletal muscle from patients with MFM. Congo red staining (left panels) reveals fluorescent amyloid deposits (red) in muscle fibers from (E) a patient with the *CRYAB* p.Gly154Ser mutation, (F) a patient with the *MYOT* p.Ser60Phe mutation, and (G) a patient with the *DES* p.Arg454Trp mutation. Corresponding H&E (middle panels) and NADH (right panels) stains highlight structural abnormalities. Images were captured using a 40× objective. Scale bar: 100 μm.

CryAB inclusions hijack mechanisms of extracellular vesicle (EV) secretion

Transmission electron microscopy (TEM) revealed CryAB inclusions located on the surface of muscle fibers **(Figure 4.6 A)**. Notably, one inclusion was observed outside the muscle boundary, suggesting the possibility that EV pathways may contribute to the formation and/or transport of these CryAB inclusions **(Figure 4.6 B, open yellow arrowhead;** Movie do not provide in this thesis**)**. Mechanisms of EV secretion varies depending on cargos and can be classified into endosomal sorting complexes required for transport (ESCRT)-independent or dependent pathways [40, 69, 70]. First, we focused on a protein required for ESCRT-independent cargos. Tetraspanin 96F (Tsp96F) is the *Drosophila* homolog of the mammalian EV marker CD81 [71]. Expression of Tsp96F tagged with mCherry (mCh-Tsp96F) in the IFMs shows a diffuse pattern while CryAB maintained its normal Z-disc location **(Figure 4.6 C)**. To assess the effect of

Tsp96F on CryAB inclusion dynamics, we co-expressed Tsp96F-mCh with either D109A or R120G at 25 °C. In both cases, Tsp96F co-localized with CryAB inclusions **(Figure 4.6 C, open arrowheads; Appendix Figure E.6 A)**. Quantitative analysis showed that overexpression of Tsp96F significantly increased the size of CryAB inclusions **(Figure 4.6 D)**, while the number of inclusions increased only for D109A **(Figure 4.6 E)**. Conversely, RNAi-mediated knockdown of Tsp96F led to a marked reduction in inclusion size for both D109A and R120G at 31 °C **(Figure 4.6 F and G; Appendix Figure E.6B)**. However, only D109A showed a decrease in inclusion number **(Figure 4.6 H)**. In addition to Tsp96F, we also tested the Rab GTPase protein Rab27, the ortholog of mammalian Rab27A/B, which is implicated in EV biogenesis and secretion [72]. Rab27-GFP also colocalized with CryAB inclusions **(Appendix Figure E.6 C)**. Statistical analysis revealed a significant increase in both the size and number of CryAB inclusions **(Appendix Figure E.6 D and E)**, whereas Rab27 knockdown led to a reduction in inclusion size but not in number **(Appendix Figure E.6 F-H)**. These data together cement a role for Tsp96F and Rab27 in the EV secretion pathway and indicate that modulation of protein levels is sufficient to increase or decrease EV dynamics.

We next investigated whether components of the ESCRT pathway contribute to CryAB inclusion biogenesis. We focused on the ESCRT accessory protein Alix (ALG-2-interacting protein X) and TSG101, a core component of the ESCRT-I complex [70, 72]. Alix-HA and TSG101-HA both co-localized with CryAB inclusions **(Appendix Figure E.7 A and E)**. Moreover, Alix significantly increased both inclusion area and number when co-expressed with the CryAB mutants D109A and R120G **(Appendix Figure E.7 B and C)**. Quantification revealed

no significant change in inclusion area with TSG101-HA expression and led to a reduction in inclusion size in only the D109A mutant **(Appendix Figure E.7 F and G)**.

To further examine the specificity of EV markers with CryAB, we tested additional proteins for possible overlap with CryAB inclusions. However, none of the proteins examined, including the human EV marker CD63, the early endosome marker Rab5, or the neurodegenerative disease-associated protein alpha-synuclein (SNCA), co-localized with CryAB inclusions **(Appendix Figure E.8)**. Combined with yeast two-hybrid data whereby mutant CryAB exhibited stronger binding to its interacting protein NUAK than to CryAB WT **(Appendix Figure E.9)**, it is clear that mutant CryAB does not simply associate with any abundant protein. Instead, our results support the selective association between CryAB inclusions and specific EV proteins, highlighting a targeted mechanism for their trafficking and potential extracellular release.

To confirm that CryAB inclusions are secreted from muscle tissue, we extracted hemolymph from thoraces containing IFMs. CryAB inclusions were detectable in the hemolymph and showed positive staining with Congo red, indicating amyloid-like properties. To ensure that these structures were not derived from hemocytes or other nucleated cells, we included a DAPI stain. The absence of DAPI signal confirmed that the extracted structures were indeed cell-free amyloid inclusions **(Figure 4.6 I)**. These results support the conclusion that CryAB inclusions can be secreted from muscle tissue into the extracellular space.

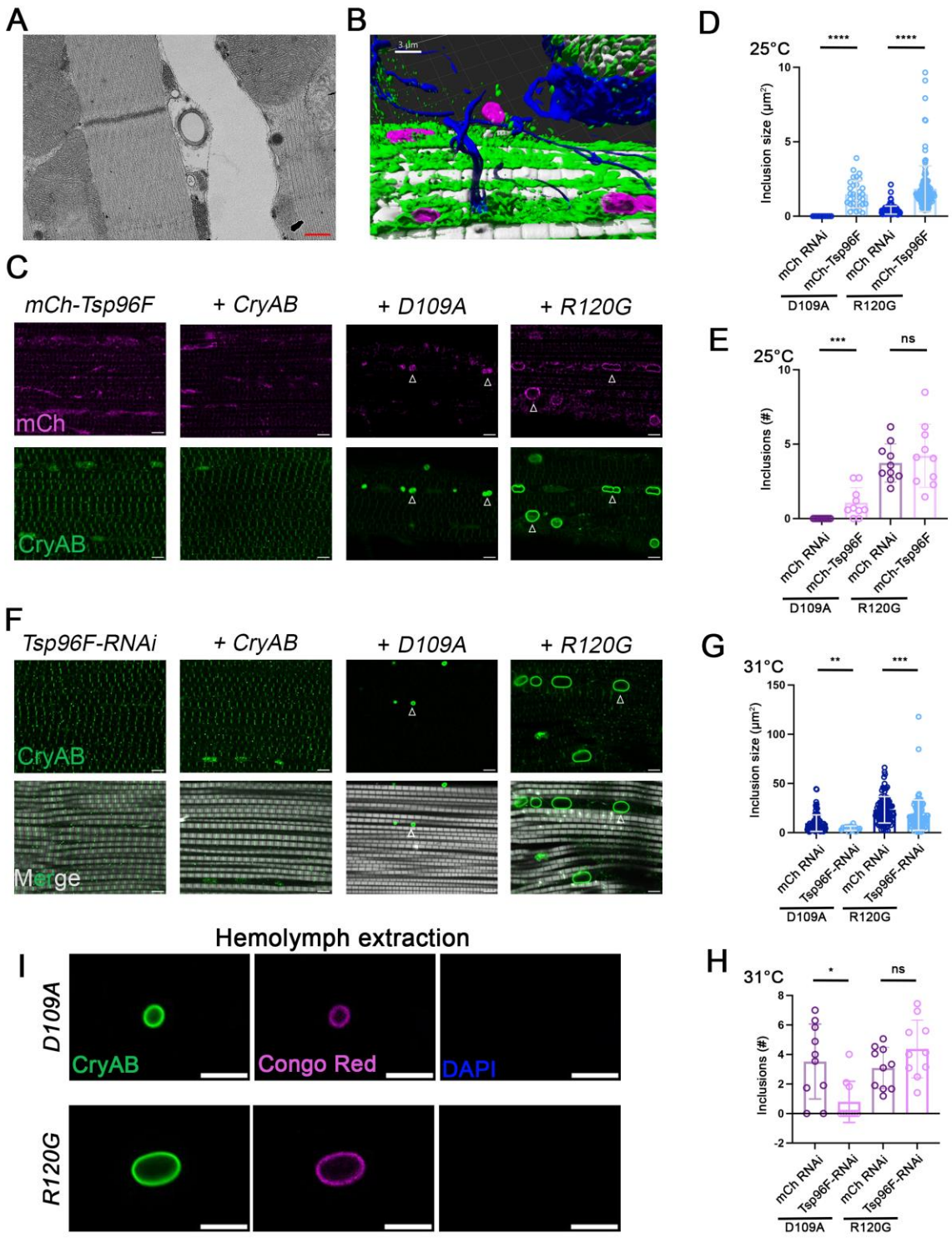

Figure 4.6 CryAB inclusions exploit the EV pathway to mediate pathogenicity

(A) TEM) images of Day 10 IFMs expressing the D109A mutation reveals intracellular inclusions. Scale bar: 500 nm (magnification: 5000×).

(B) Three-dimensional rendering of IFMs expressing R120G. Mitochondria are labeled with ATP5A (green), CryAB inclusions are shown in magenta, F-actin in gray, and nuclei with DAPI (blue). Non-specific DAPI signal marks tracheal tissue. Arrows indicate CryAB inclusions located outside of muscle fibers. Scale bar: 3 μm.
(C) Colocalization analysis of CryAB inclusions with the EV marker Tsp96F/CD81. Flies co-expressing mCherry-tagged Tsp96F (Tsp96F-mCh) and mutant CryAB proteins under control of the *Mef2* driver were raised at 25°C and dissected at Day 2. CryAB (green) colocalizes with Tsp96F (magenta) in IFMs. Scale bar: 5 μm.
(D,E) Scatter bar plot quantification of CryAB inclusion size (D) and number (E) in IFMs co-expressing Tsp96F at Day 2. Data are presented as mean ± SD. (N=10 per genotype, Unpaired student *t*-tests followed by Mann–Whitney). ns = not significant, *p>0.05, **p<0.05, ***p<0.01, ****p<0.001.
(F) Representative single-plane images of IFMs from Day 2 adult flies following *Tsp96F RNAi* knockdown at 31°C. CryAB is shown in green and F-actin in gray. Scale bar: 5 μm.
(G,H) Scatter bar plot quantification of CryAB inclusion size (G) and number (H) following induction of *Tsp96F RNAi*. Data are mean ± SD (n = 10 per genotype). Statistical significance as in (D, E).
(I) CryAB inclusions detected in hemolymph extracted from muscle tissue. CryAB is shown in green, Congo red-stained amyloid in magenta, and DAPI in blue to identify nuclei and exclude hemocytes. Scale bar: 5 μm.

4.4 Discussion

This study investigated the functional characteristics of CryAB mutations to clarify their role in the development of cardiomyopathies and MFMs. We focused on four human CryAB disease alleles, D109A (Desmin-related myopathy), D109H and R157H (dilated cardiomyopathy), and R120G (Desmin-related cardiomyopathy), using a *Drosophila* model to explore their pathological effects on muscle tissue. Our findings confirmed that all CryAB mutations impacted protein degradation and autophagy. Notably, mutations in different regions of CryAB formed distinct subcellular complexes. Mutations in the ACD domain retained the ability to form amyloid fibers, consistent with previous observations that D109 mutations possess amyloid-forming properties *in vitro* [29, 56]. Mutation of the ACD region, primarily composed of beta-sheet secondary structures, is crucial to this process. Each CryAB monomer interacts via antiparallel beta strands 6 and 7 located in the ACD, where both D109 and R120 are positioned and interact through ionic bonds for dimerization [29, 73]. These mutations decrease the stability of oligomers

and may lead to unfolding of normally stable beta sheets. Such destabilization would predict a higher propensity to spuriously interact with other proteins to form aggregates and/or amyloidogenic structures, this leading to a more stable oligomeric structure that resists degradation by autophagy or proteases.

There was a definitive increase in inclusion number and a trend of larger inclusion size upon expression of CryAB mutations. Maybe CryAB inclusions reach a maximal attainable size due to constraints of space within the tissue. Another possibility is that inclusion size might increase with age, which we could not fully assess in this model due to a shortened lifespan upon expression of CryAB mutations. While both WT CryAB or the R157H mutations were associated with age-related lethality similar to those in the ACD domain (possibly due to altered cardiac function), these alleles did not promote amyloid fiber formation *in vivo*. *In vitro*, the R157H mutation enhances the chaperone activity of CryAB [30], which is also observed in patients undergoing chemotherapy where CryAB expression is elevated [74]. This suggests that heightened chaperone function, while cytoprotective, may actually be harmful under certain conditions.

Our research on CryAB originated from its identification as a substrate for the serine/threonine kinase NUAK in muscle tissue where we identified two conserved, novel phosphorylation sites (S68 and S70) [75]. The pseudo-phosphomimetic S70E mutation shows an amyloid-like phenotype similar to the ACD mutations D109 and R120. However, other phosphorylation site mutations (S68A, S68E, S70A) did not affect CryAB distribution or F-actin stability in larval muscles. Despite literature that CryAB phosphorylation regulates extracellular secretion [76], the lack of differences between phospho-null and phospho-mimetic changes at amino acid S70 suggest that its location within the ACD domain, and not its phosphorylation status, promote amyloid formation. To further explore how CryAB may impact other aspects of

NUAK-mediated signaling, we conducted immunoprecipitation experiments with 3x-HA-tagged CryAB transgenic flies to identify downstream CryAB-interacting proteins. Unfortunately, cell lysis resulted in the pulldown of hundreds of interacting proteins, suggesting that CryAB is a promiscuous binding protein in non-cellular contexts. Switching to yeast two-hybrid assays, we confirmed that CryAB mutants exhibit higher binding affinity with NUAK under selective pressure (0.5 to 3 mM 3-AT), supporting previous findings that mutant CryAB forms stable complexes with client proteins, hindering degradation.

Although amyloid fibrils are predominantly studied in the brain, amyloid deposition in skeletal muscle is poorly understood. The presence of CryAB inclusions containing protofibril-like features in muscle tissue was suggested by TEM images and confirmed by positive Congo red fluorescence and the presence of the amyloidogenic protein Desmin. Observing such clear protofibril structures was unexpected, as *in vivo* amyloid deposition is challenging to detect. Since amyloid fibrils are typically markers of a progressive disease [6, 7], the shorter longevity of our animal model may have precluded observations of fibril accumulation. To our benefit, the Gal4-mediated *in vivo* expression system 'enriched' for aggregates and amyloid inclusions, likely due to higher expression levels of mutant CryAB proteins. The ability to modulate CryAB mutant expression by raising the temperature to increase output of the Gal4/UAS system at the same time may have introduced *in vivo* heat stress to further promote amyloid formation. These inherent advantages likely promoted CryAB amyloid formation compared to the normal intracellular environment which prevents spontaneous fibril formation.

While *in vitro* studies provide valuable insights into amyloid microstructures, they lack a comprehensive understanding of amyloid macroscopic architecture in living organisms. A meaningful example of this is the presence of circular amyloid structures in muscle, likely forming

due to space and tension constraints implicit in a contractile tissue such as muscle. The mechanical properties of these fibrils, which exhibit both bending and stretching abilities, align with previous reports on amyloid flexibility [77]. In addition to our findings in *Drosophila*, we validated the presence of amyloid fibrils in both zebrafish and human patient CryAB muscle samples. These results confirm that CryAB-related aggregation/inclusion is not species-specific and likely represents a conserved mechanism of muscle pathology [67]. The consistent detection of amyloid-like inclusions across models in our work and others [14, 78] suggests that amyloid-specific staining, such as Congo red, holds promise as a diagnostic tool in muscle diseases, particularly in myofibrillar myopathies.

Importantly, we identified a link between CryAB inclusions and extracellular vesicle (EV) pathways, suggesting that CryAB amyloids are secreted as a protective mechanism since they cannot be degraded via normal degradation pathways. This expands the scope of amyloid biology beyond the nervous system to include muscle tissue. In the future, small-molecule drugs targeting CryAB mutations could potentially prevent amyloid fibril formation by disrupting these stable oligomeric structures. Our ongoing research will focus on identifying the precise molecular mechanisms and protein interactions that facilitate CryAB amyloid fibril formation *in vivo*. Understanding these pathways could shed light on amyloid deposition processes in muscle tissue and their parallels with neurodegenerative diseases.

4.5 Material and methods

Drosophila stocks and husbandry

All stocks were reared at 25 °C on standard cornmeal-molasses-yeast media. *Drosophila* stocks obtained from the Bloomington *Drosophila* Stock Center (BDSC) are indicated with BL followed

by the stock number. *Mef2*-Gal4 (BL27390) was used to direct expression in larval muscles and the IFMs. UAS-*mCherry RNAi* (BL35785) was used as a control for Gal4-mediated experiments. BDSC stocks used for the analysis of EV markers: UAS-TSG101-HA (BL77977), UAS-Alix-Flag-HA (BL95213), and UAS-YFP-Rab27 (BL9810). UAS-SCNA served as a negative control (BL51376). RNAi lines from BDSC: UAS-Tsp6F-RNAi (BL40901) and UAS-Rab27-RNAi (BL31887). The UAS-mCh-Tsp96F flies were a gift from Julia Groß [71] and the UAS-hCD63-GFP flies were obtained from Dr. Young Kwon.

Creation of transgenic flies

CryAB

UAS-CryAB (wild-type) and UAS-mediated phosphosite mutations (*S68A*, *S68E, S70, S70E, S68/70A*) were previously published [52]. To generate UAS-human CryAB mutations (*D109A, D109H, R120G* or *R157H*), cDNA corresponding to the coding region of wild-type *CryAB-RC* was synthesized by Genscript, subcloned into the pUAST_attB vector using EcoRI/XbaI sites, and subjected to site-directed mutagenesis. Plasmid DNA was verified by sequencing and purified using the Qiagen Maxi kit (Hilden, Germany). Constructs were sent to Rainbow Transgenic Flies, Inc. (Camarillo, CA) for injection into line # 9736 for integration at the PhiC31landing site (53B2). All resulting transgenic lines were balanced over the w; ScO/Cyo,Tb balancer (BL36335). Each CryAB line was then recombined with the *Mef*-Gal4 driver and maintained at 18 °C.

hDesmin

cDNA corresponding to the amyloidogenic region of human *Desmin* (aa 117-348) [65] was synthesized by Genscript and subcloned into the pUAST vector using EcoRI/XbaI sites. Plasmid DNA was verified by sequencing, purified using the Qiagen Maxi kit (Hilden, Germany), and

Rainbow Transgenic Flies, Inc. (Camarillo, CA) for injection into *y+* embryos. The resulting *w+* fly lines were balanced over the w; ScO/Cyo,Tb (BL36335) or w; TM3,Sb/TM6b,Tb (Geisbrecht lab) balancers. Experiments in this paper used an insertion on chromosome 2.

Visualization of muscle tissue

Larval muscle staining

Wandering L3 larvae were placed onto a Sylgard plate, pinned near the mouth hooks at the anterior end, and the internal organs were removed. Muscle carcasses were fixed in 4% formaldehyde, rinsed 3x in PBT and blocked for 30 min in 5% normal goat serum (NGS). Primary antibodies were incubated overnight at 4 °C in PBT, washed 3x in PBT followed by secondary antibody incubation for 2 hours at room temperature. Samples were then washed 3x in PBT and mounted in glycerol + 0.5% n-propyl gallate (anti-fade reagent with 10% 20mM Tris buffer, pH=8.0). Tissues were stained with rabbit anti-CryAB (1:200, #DZ33926, Boster Bio, Pleasanton, California) followed by Alexa Fluor anti-rabbit 488 (1:400; A11001, Invitrogen, Waltham, MA) and phalloidin 594 to label F-actin (1:400, A12381 Molecular Probes, Invitrogen, Waltham, MA).

Adult IFM staining

Day 2 or Day 10 female adult flies were anaesthetized on a CO_2 plate and the head, wings and abdomen were removed. The remaining whole thoraces were fixed in 4% methanol-free formaldehyde (Polysciences, Warrington, PA) for 30 minutes at room temperature and washed three times in PBST (phosphate buffered saline + 0.5% Tween) before bissection using a sharp blade. Immunostaining was performed as described above using the following primary antibodies: rabbit anti-CryAB (1:200, #DZ33926, Boster Bio, Pleasanton, California), mouse anti-Ubi UBCJ2 (1:200, ENZ-ABS840, Enzo Life Sciences, Farmingdale, NY); rabbit anti-p62 (1:200, ab178440,

Abcam, Cambridge, MA), rabbit anti-Stv (1:200) [79]; rabbit anti-hDesmin (1:200, AB_11000611, Invitrogen, Waltham, MA), mouse anti-HA 6E2 (1:400, #2367, Cell Signaling, Danvers, MA), anti-Rab5 (1:200, ab31261, Abcam, Cambridge, United Kingdom), and anti-SNCA (1:200, sc-12767, Santa Cruz Biotechnology, Dallas, TX). Secondary antibodies were either Alexa Fluor anti-rabbit 488 (1:400, A11034, Invitrogen, Waltham, MA), Alexa Fluor anti-rabbit 594 (1:400, A21207, Invitrogen, Waltham, MA), Alexa Fluor anti-mouse 488 (1:400, A11001, Invitrogen, Waltham, MA), Alexa Fluor anti-mouse 594 (1:400, A-11005, Invitrogen, Waltham, MA). Alexa Fluor Phalloidin 647 were used to label F-actin (1:400, A22287, Invitrogen, Waltham, MA)

Adult heart tube staining

Day 2 female adult flies were anaesthetized on a CO_2 plate. Whole flies were fixed in 4% formaldehyde overnight at room temperature, dissected to reveal heart tube, and immunostained as described above with rabbit anti-CryAB (1:200, #DZ33926, Boster Bio, Pleasanton, California) and mouse anti-Ubi UBCJ2 (1:200, ENZ-ABS840, Enzo Life Sciences, Farmingdale, NY). Alexa Fluor anti-rabbit 488 (1:400, A11034, Invitrogen, Waltham, MA), Alexa Fluor rabbit 594 (1:400, A21207, Invitrogen, Waltham, MA), Alexa Fluor anti-mouse 488 (1:400, A11001, Invitrogen, Waltham, MA), Alexa Fluor mouse 594 (1:400, A-11005, Invitrogen, Waltham, MA). Phalloidin 647 were used to label F-actin (1:400, A22287, Invitrogen, Waltham, MA).

Zeiss image processing

Images were captured using a Zeiss 700 confocal microscope. Image processing and analysis were performed using a combination of Zen Black (Zeiss), ImageJ (NIH), and Adobe Photoshop. All fly muscle images taken at 63x are displayed as a single plane confocal microscope.

3D morphological analysis of fly muscles

Z-stack images were opened with Imaris (version 10.2, Oxford Instruments). Four fluorescence channels of cellular structures in each Z-stack image were assigned different colors using the 'Display Adjustment' tool. The intensity and contrast of each channel were adjusted individually. The 'Volume' tool was used to generate a 3D volume view of each channel. In the 'Volume Settings' stub, the 'Normal Shading' mode was chosen to display the volume view and 'Opacity' was set to 0.39. The 'Min' and 'Max' parameters were adjusted to ensure that the fluorescence signal channel in each channel was accurately represented within the corresponding volume rendering. 3D animations of cellular structures were created using the horizontal and vertical rotation functions, and 3D images were captured with the 'Snapshot' tool.

Semi-intact *Drosophila* heart preparation and heartbeat analysis

Cardiac contractility measurements on semi-intact preparations of fly hearts were performed as described previously [80]. Briefly, adult females of the indicated genotypes were pinned down in the anterior and posterior regions on a Sylgard dissecting dish and carefully dissected to reveal the beating hearts in an artificial hemolymph buffer. High-speed 30 s movies were recorded at a rate of > 150 frames per second using a Hamamatsu CCD camera on a Nikon 80i upright microscope with a 10x dipping immersion lens. The images were processed using Simple PCI imaging software (Compix Inc.). M-modes and quantitative data were generated using a MATLAB-based image analysis program. To generate the M-mode, a single pixel-wide column was selected from the most posterior portion of the adult heart at the abdominal A3 segment that encompassed both edges of the heart tube. The corresponding columns were cut from all movie frames and aligned horizontally according to time. Heart periods (HP) or heartbeat lengths were defined as the time

between the ends of two consecutive diastolic intervals. The arrhythmia index (AI) was defined as the standard deviation of all recorded HPs for an individual fly, normalized to the median HP to compensate for variability between flies [81]. Diastolic and systolic diameters represent the relaxed and contracted state of the heart tube, respectively. Measurements were made in the exact same location in abdominal segment A3. High-speed 30 s movies were recorded at a rate of > 150 frames per second using a Hamamatsu CCD camera on a Nikon 80i upright microscope with a 10x dipping immersion lens. The images were processed using Simple PCI imaging software (Compix Inc.). Quantitative data were generated using a MATLAB-based image analysis program [80].

Western blotting to assess soluble and Insoluble fractions

Day 2 or Day 10 adult female flies were anaesthetized on a CO_2 plate and the head, wings and abdomen were removed and prepared as described with minor modifications [82]. Three thoraces for each genotype were homogenized in 50 µl of freshly prepared TritonX-100 cell lysis buffer: 1% TritonX-100 cell in PBS, 1x Halt Phosphatase inhibitor cocktail (#1862495, Thermo Scientific, Waltham, MA), 1x Halt Protease inhibitor cocktail (#1861278, Thermo Scientific, Waltham, MA) on ice with the aid of a tissue homogenizer (Kimble). Homogenates were then centrifuged at 21,000 x g at 4 °C for 10 min and the supernatant (soluble fraction) was collected in 3x SDS sample buffer: 188 mM Tris-HCl (pH 6.8), 3% (w/v) SDS, 30% (v/v) glycerol, 0.01% (w/v) bromophenol-blue, and 15% (v/v) β-mercaptoethanol, and boiled at 95 °C for 5 min before gel loading. The remaining pellet (insoluble fraction) was washed with Triton X-100 buffer 3x and the samples were centrifuged at 21,000 x g for 5 mins at 4 °C. The supernatant was discarded and the pellet was resuspended with 50uL freshly prepared Urea/SDS buffer (Urea and SDS solubilization buffer

10mL: 8M Urea, 2.5mL 20% SDS, 1mL 10X RIPA buffer, 1x Halt Phosphatase inhibitor cocktail, and 1x Halt Protease inhibitor cocktail with homogenization. The sample was centrifuged at 21,000 x g at 4 °C for 10 mins and the resulting insoluble supernatant was transferred to a new tube. 50uL 3x SDS sample buffer was added and the sample was boiled at 95 °C for 5 min before gel loading. The soluble or insoluble protein samples were separated by sodium dodecyl sulfate polyacrylamide gel electrophoresis (SDS-PAGE) and transferred to the nitrocellulose blotting membrane (pore size 0.45 μm, Cytiva, Marlborough, MA) using the Trans-Blot® TurboTM Transfer System (Bio-Rad, Hercules, CA). Membranes were probed with rabbit anti-CryAB (1:1000, #DZ33926, Boster Bio, Pleasanton, CA), or rabbit anti-Ref(2)p/p62 (ab178440, 1:2000, Abcam, Cambridge, UK). IRDye 800CW secondary antibodies (LI-COR Biosciences, Lincoln, NE) were used at 1:10000 and Revert 700 Total Protein Stain (LI-COR Biosciences, Lincoln, NE) or anti-ATP5α (1:20000, ab14748, Abcam, Cambridge, United Kingdom) was used as a loading control. Membranes were developed using the LI-COR Odyssey XF and quantitation of relative protein levels was performed in Empiria Studio Software (LI-COR Biosciences, Lincoln, NE).

Lethal stage analysis

Adult survival

Lifespan measurements for adult flies was performed at 31 °C in an incubator with 60% humidity. For each of the analyzed genotypes, virgin female flies were collected at Day 1 and transferred to fresh media each day. The number of dead flies was recorded at 24 hr intervals until the end of lifespan. N≥3 biological replicates.

Pupal lethality

To measure the stage of pupal lethality for each genotype, the F1 generation was shifted to the 31°C incubator at the embryo stage. After the flies eclosed as adults, the remaining empty pupa cases or dead pupa in each vial were recorded (N≥3 biological replicates).

Quantification of CryAB aggregates or inclusions

For each muscle thorax, 10 randomly selected confocal images were selected for quantification. Ubi was used as a marker for aggregates in double labeling experiments with CryAB. Either CryAB alone or CryAB and hDesmin were used to label inclusions. For quantification, the number of Ubi(+)/CryAB(+) aggregates or CryAB(+) and/or hDesmin(+) structures were manually counted and divided by the total area of muscles per picture to calculate the average number/2500 μm^2 in each image. Measurements of CryAB inclusion body area was analyzed using the Wand tool of Image J. N≥10 for each genotype. See also **Table S2**.

Transmission Electron Microscopy (TEM)

Adult female flies were reared at 31 °C until Day 10, anaesthetized on a CO_2 plate and the head, wings and abdomen were removed. Each fly thorax was dissected in 0.1 M cacodylate buffer and fixed in 1% glutaraldehyde/4% paraformaldehyde in 0.1 M cacodylate buffer overnight at 4 °C followed by three washes with 0.1 M cacodylate buffer. The samples were treated with 1% OsO4 for 1 h at 4 °C. After washing with ddH2O, the samples were dehydrated in a gradient series using 30%, 50%, 70%, 95%, and 100% ethanol solutions at room temperature. The samples were then infiltrated using series epoxy resin at room temperature and mounted in pure resin. After polymerization at 60 °C for 2 Days, 90 nm semi-thin sections were cut and stained with toluidine

blue stain to determine orientation. Ultrathin sections were stained with uranyl acetate and lead citrate for observation under a JEOL JEM 1400 electron microscope.

Inclusion extraction and Congo red staining

Muscle inclusion extraction

Adult *Drosophila* were anesthetized on a CO_2 pad, and thoraces were carefully dissected and transferred into 50 µL of phosphate-buffered saline (PBS) containing protease and phosphatase inhibitors, along with 1-phenyl 2-thiourea (PTU) to prevent melanization. Samples were processed on ice to preserve protein integrity. Thoracic tissue was homogenized thoroughly and centrifuged at 1,000 × g for 3–5 minutes at 4 °C. The resulting supernatant was collected and applied to L-lysine-coated slides to allow inclusions to settle for 5 minutes at 4 °C. Samples were then fixed with 1 mL of 4% formaldehyde in PBS for 30 minutes in the dark. After fixation, the slides were rinsed twice with PBS containing 0.3% Triton X-100 (PBT) before proceeding to Congo red and CryAB staining.

Hemolymph inclusion extraction

Adult *Drosophila* were anesthetized on a CO_2 pad, and thoraces were dissected and transferred into 500 µL microcentrifuge tubes containing 50 µL of phosphate-buffered saline (PBS) supplemented with protease and phosphatase inhibitors, and 1-phenyl 2-thiourea (PTU). A small hole was pierced at the bottom of a 500 µL tube, which was then placed inside a 1 mL collection tube to allow hemolymph to drain during centrifugation. Samples were centrifuged at 1,000 × g for 5 minutes at 4 °C. The resulting hemolymph was collected in the 1 mL tube was carefully transferred onto L-lysine-coated glass slides for downstream Congo red and CryAB staining.

Congo red and CryAB staining

Slides with isolated inclusions from either muscle or hemolymph were incubated in Solution A (NaCl-saturated 80% ethanol with 0.01% NaOH) for 20 mins. This was followed by a 20 min incubation in Solution B (2.5 g Congo red and 1 g potassium hydroxide dissolved in 500 mL of 80% ethanol) at room temperature. Samples were then sequentially rinsed in absolute ethanol and xylene before immunofluorescence staining. Following Congo red staining, slides were washed 2–3 times with PBT. To prevent disruption of Congo red signals during antibody staining, blocking was performed using PBS supplemented with 5% normal goat serum (NGS) for 30 minutes (PBT was avoided at this step). Primary antibodies were diluted in the same PBS blocking buffer and incubated with samples overnight at 4 °C. The following day, slides were washed twice in PBT for 5 minutes each. Samples were re-blocked in PBS + 5% NGS for 30 minutes before incubation with fluorescently labeled secondary antibodies Alexa Fluor anti rabbit 488 (1:400, A11034, Invitrogen, Waltham, MA) for 2 hours at room temperature. Finally, slides were washed twice in PBT and mounted for imaging.

Proteasome activity assay

Drosophila 20S proteasome activity was determined using the 20S Proteasome Assay Kit (#10008041, Cayman Chemical, Ann Arbor, MI). Crosses were reared at 25 °C and transferred to 31 °C after eclosion. For each genotype, 5 adult female flies at either Day 2 or Day 10 were dissected to remove the head, wings, and abdomen. The thorax was transferred to a 1.5 ml microcentrifuge tube containing 200 µl of ice-cold 20S Proteasome Lysis Buffer. After homogenization on ice, the tube was centrifuged at 12000 x g for 5 minutes at 4 ºC, and the

supernatant was transferred to a new tube and kept on ice. 5 wells were used for each genotype in a 96-well plate. 10 µl of 20S Proteasome Assay Buffer was added to each well with increasing amounts of supernatant (0, 5, 10, 20, and 50 µl in wells 1-5, respectively). 20S Proteasome Lysis Buffer was added to each well to bring the total volume up to 100 µl. For samples treated with the 20S Proteasome Inhibitor (EGCG), 10 µl of inhibitor was added instead of Assay buffer. Finally, 10 µl of the 20S Proteasome Substrate (SUC-LLVY-AMC) was added to each well. The plate was incubated at 37 ˚C for 1 hour. After 1 hour the fluorescence intensity for each well was read using a Biotek Synergy HI plate reader (excitation = 360 nm, emission 480 nm).

Yeast Two-Hybrid (Y2H)

Y2H assays were carried out by Hybrigenics Services. The coding sequence of the full-length *D. melanogaster* NUAK/CG43143 (GenBank accession number NM_206469.3) was PCR-amplified and cloned in frame with the Gal4 DNA binding domain (DBD) into plasmid pB66 as a C-terminal fusion to Gal4 (Gal4-bait fusion). Prey fragments of full length CryAB, CryAB D109A, CryAB D109H, CryAB R120G, and CryAB R157H were cloned in-frame with the Gal4 activation domain (AD) into plasmid pP7. Bait and prey constructs were transformed in the yeast haploid cells CG1945 (mata) and YHGX13 (Y187ade2-101::loxP-kanMX-loxP, matα) and diploid yeast cells were obtained using a mating protocol with both yeast strains. The interaction between SMAD and SMURF was used as positive control. As negative controls, all prey plasmids were tested with the empty vector (EV) pB66. Controls and interactions were tested in the form of streaks of three independent yeast clones for each control and interaction. Medium lacking tryptophan and leucine was used as a growth control and to verify the presence of the bait and prey plasmids. The selective

medium without tryptophan, leucine, and histidine selected for the interaction between bait and prey and 0.05 mM 3-AT was added to select for interaction between bait and prey.

Zebrafish maintenance

AB Zebrafish wildtype and the previously generated transgenic reported line *tg(Kdrl:EGFP)* were kindly provided by the Zebrafish Facility of the University of Padova [83]. Zebrafish manipulation and experiments have been performed according to the formal Italian Ministry of Health Authorization n. 60/2023 and followed all standard Animal Care Standard Operating Procedures (ARRIVE guidelines 2.0). All lines have been maintained at 28.5°C, with a 14-10 light-dark cycle in aerated saline water, in the Zebrafish Facility at the University of Brescia according to standard protocols [84]. To allow animal breeding, egg deposition and fertilization, male and female animals were separated in the late afternoon and free to start courtship the next morning to allow mating events. Embryos were then injected at 1 cell stage with 25 ng/uL of each plasmid (hCRYAB WT, hCRYAB G154S, hMYOT WT and hMYOT S95I) as previously described [67, 85]. Embryos were collected and maintained at 28.5°C in embryo medium (0.19 g/L CaSO4, 0.1 g/L Instant Ocean Salt e 0.1 g/L NaHCO3). All manipulation and experiments were performed within 120 h post-fertilization (hpf) and thus did not require formal authorization according to Standard Operating Procedures of the Animal Care, the Use Committee of the University of Brescia and Italian Ministry of Health directives.

Zebrafish Congo red staining

Zebrafish embryos at 120 hpf from each condition were fixed for 3 h in 4% PFA (Merck KGaA, Darmastadt, Germany) and washed in PBS. Successively, embryos were permeabilized for 60 min

with 10 µg/mL proteinase K in PBS and briefly re-fixed in 4% PFA in PBS for 20 min. After 3 PBS and 2 Milli-Q water washes, samples were incubated 1 hour in Congo red, followed by a Milli-Q wash of 10 min, a brief wash in a 0.036 M/L KOH solution in ETOH followed by 2 Milli-Q water washes. Samples were then analyzed using an Axiozoom.V16 fluorescence stereomicroscope equipped with Axiocamera 506 (Zeiss International, Oberkochen, Germany). The representative images were kindly taken by Prof A. Vettori's group at the CPT of the University of Verona with a confocal-Multiphoton Leica TCS SP5 AOBS with 20x objective (Leica Microsystem, Wetzlar, Germany).

Human biopsy histochemistry

The study was conducted in accordance with the Declaration of Helsinki, and approved by the Ethics Committee of Azienda Ospedaliera Universitaria Integrata di Verona (BIOB-NEU-DNA-2014, prog. 430CESC). All patients underwent open muscle biopsy at the Neuromuscular Center of Clinical Neurology, Department of Neurosciences, Biomedicine and Movement Sciences, University of Verona, Verona, Italy. Muscle biopsies were performed for diagnostic purpose after written informed consent. For conventional histological and histochemical studies, consecutive or nonconsecutive 8-µm-thick cryosections were stained with haematoxylin and eosin (H&E), modified Gomori trichrome, adenosine triphosphatase (ATPase, pre-incubation at pH 4.3, 4.6 and 10.4), succinate dehydrogenase (SDH), cytochrome c oxidase (COX), reduced nicotinamide adenine dinucleotide (NADH), periodic acid-Schiff (PAS) with diastase digestion and Sudan black. Congo red staining was performed by 1h incubation at room temperature in Congo red followed by consecutive washes in water, KOH solution (0.036 M/L) in 90% Ethanol, water and PBS. Congo red-stained sections were viewed under rhodamine fluorescence. Image acquisition was

performed on Axioscope 5 equipped with Axiocam 208 color (Zeiss) and Axiolab fluorescence microscope equipped with AxioCam HRm (Zeiss).

4.6 References

1. Almeida, C.G., Takahashi, R.H., and Gouras, G.K. (2006). β-amyloid accumulation impairs multivesicular body sorting by inhibiting the ubiquitin-proteasome system. Journal of Neuroscience *26*, 4277-4288.
2. Freer, R., Sormanni, P., Vecchi, G., Ciryam, P., Dobson, C.M., and Vendruscolo, M. (2016). A protein homeostasis signature in healthy brains recapitulates tissue vulnerability to Alzheimer's disease. Science advances *2*, e1600947.
3. Cheng, J., North, B.J., Zhang, T., Dai, X., Tao, K., Guo, J., and Wei, W. (2018). The emerging roles of protein homeostasis-governing pathways in Alzheimer's disease. Aging cell *17*, e12801.
4. Xilouri, M., Brekk, O.R., and Stefanis, L. (2013). Alpha-synuclein and protein degradation systems: a reciprocal relationship. Molecular neurobiology *47*, 537-551.
5. Braak, H., and Braak, E. (1991). Demonstration of amyloid deposits and neurofibrillary changes in whole brain sections. Brain pathology *1*, 213-216.
6. Hayashi, H., Kimura, N., Yamaguchi, H., Hasegawa, K., Yokoseki, T., Shibata, M., Yamamoto, N., Michikawa, M., Yoshikawa, Y., and Terao, K. (2004). A seed for Alzheimer amyloid in the brain. Journal of Neuroscience *24*, 4894-4902.
7. Rodrigue, K.M., Kennedy, K.M., and Park, D.C. (2009). Beta-amyloid deposition and the aging brain. Neuropsychology review *19*, 436-450.
8. Kyle, K.A., and BAYED, K.D. (1975). Amyloidosis: review op 236 cases. Medicine *54*, 271-299.
9. Hazenberg, B.P. (2013). Amyloidosis: a clinical overview. Rheumatic Disease Clinics *39*, 323-345.
10. Wechalekar, A.D., Gillmore, J.D., and Hawkins, P.N. (2016). Systemic amyloidosis. The Lancet *387*, 2641-2654.
11. Benson, M.D., Buxbaum, J.N., Eisenberg, D.S., Merlini, G., Saraiva, M.J.M., Sekijima, Y., Sipe, J.D., and Westermark, P. (2020). Amyloid nomenclature 2020: update and recommendations by the International Society of Amyloidosis (ISA) nomenclature committee. Amyloid *27*, 217-222. 10.1080/13506129.2020.1835263.
12. Nakano, S., Engel, A.G., Waclawik, A.J., Emslie-Smith, A.M., and Busis, N.A. (1996). Myofibrillar myopathy with abnormal foci of desmin positivity. I. Light and electron microscopy analysis of 10 cases. Journal of Neuropathology & Experimental Neurology *55*, 549-562.
13. Schröder, R., and Schoser, B. (2009). Myofibrillar myopathies: a clinical and myopathological guide. Brain pathology *19*, 483-492.
14. Selcen, D., and Engel, A.G. (2011). Myofibrillar myopathies. Handbook of clinical neurology *101*, 143-154.
15. Claeys, K.G., and Fardeau, M. (2013). Myofibrillar myopathies. Handbook of clinical neurology *113*, 1337-1342.
16. Olivé, M., Odgerel, Z., Martínez, A., Poza, J.J., Bragado, F.G., Zabalza, R.J., Jericó, I., Gonzalez-Mera, L., Shatunov, A., and Lee, H.S. (2011). Clinical and myopathological evaluation of early-and late-onset subtypes of myofibrillar myopathy. Neuromuscular Disorders *21*, 533-542.
17. Kley, R.A., Maerkens, A., Leber, Y., Theis, V., Schreiner, A., van der Ven, P.F., Uszkoreit, J., Stephan, C., Eulitz, S., Euler, N., et al. (2013). A combined laser microdissection and

mass spectrometry approach reveals new disease relevant proteins accumulating in aggregates of filaminopathy patients. Mol Cell Proteomics *12*, 215-227. 10.1074/mcp.M112.023176.

18. Maerkens, A., Olivé, M., Schreiner, A., Feldkirchner, S., Schessl, J., Uszkoreit, J., Barkovits, K., Güttsches, A.K., Theis, V., Eisenacher, M., et al. (2016). New insights into the protein aggregation pathology in myotilinopathy by combined proteomic and immunolocalization analyses. Acta Neuropathol Commun *4*, 8. 10.1186/s40478-016-0280-0.
19. Maerkens, A., Kley, R.A., Olivé, M., Theis, V., van der Ven, P.F., Reimann, J., Milting, H., Schreiner, A., Uszkoreit, J., Eisenacher, M., et al. (2013). Differential proteomic analysis of abnormal intramyoplasmic aggregates in desminopathy. J Proteomics *90*, 14-27. 10.1016/j.jprot.2013.04.026.
20. Vicart, P., Caron, A., Guicheney, P., Li, Z., Prévost, M.C., Faure, A., Chateau, D., Chapon, F., Tomé, F., Dupret, J.M., et al. (1998). A missense mutation in the alphaB-crystallin chaperone gene causes a desmin-related myopathy. Nat Genet *20*, 92-95. 10.1038/1765.
21. Sacconi, S., Féasson, L., Antoine, J.C., Pécheux, C., Bernard, R., Cobo, A.M., Casarin, A., Salviati, L., Desnuelle, C., and Urtizberea, A. (2012). A novel CRYAB mutation resulting in multisystemic disease. Neuromuscul Disord *22*, 66-72. 10.1016/j.nmd.2011.07.004.
22. Fichna, J.P., Potulska-Chromik, A., Miszta, P., Redowicz, M.J., Kaminska, A.M., Zekanowski, C., and Filipek, S. (2017). A novel dominant D109A CRYAB mutation in a family with myofibrillar myopathy affects αB-crystallin structure. BBA Clin *7*, 1-7. 10.1016/j.bbacli.2016.11.004.
23. Inagaki, N., Hayashi, T., Arimura, T., Koga, Y., Takahashi, M., Shibata, H., Teraoka, K., Chikamori, T., Yamashina, A., and Kimura, A. (2006). αB-crystallin mutation in dilated cardiomyopathy. Biochemical and biophysical research communications *342*, 379-386.
24. Pilotto, A., Marziliano, N., Pasotti, M., Grasso, M., Costante, A.M., and Arbustini, E. (2006). alphaB-crystallin mutation in dilated cardiomyopathies: low prevalence in a consecutive series of 200 unrelated probands. Biochem Biophys Res Commun *346*, 1115-1117. 10.1016/j.bbrc.2006.05.203.
25. Thorkelsson, A., and Chin, M.T. (2024). Role of the Alpha-B-crystallin protein in cardiomyopathic disease. International Journal of Molecular Sciences *25*, 2826.
26. Dimauro, I., Antonioni, A., Mercatelli, N., and Caporossi, D. (2018). The role of αB-crystallin in skeletal and cardiac muscle tissues. Cell Stress Chaperones *23*, 491-505. 10.1007/s12192-017-0866-x.
27. Bakthisaran, R., Akula, K.K., Tangirala, R., and Rao, C.M. (2016). Phosphorylation of αB-crystallin: Role in stress, aging and patho-physiological conditions. Biochim Biophys Acta *1860*, 167-182. 10.1016/j.bbagen.2015.09.017.
28. Dimauro, I., and Caporossi, D. (2022). Alpha B-Crystallin in Muscle Disease Prevention: The Role of Physical Activity. Molecules *27*. 10.3390/molecules27031147.
29. Fichna, J.P., Potulska-Chromik, A., Miszta, P., Redowicz, M.J., Kaminska, A.M., Zekanowski, C., and Filipek, S. (2017). A novel dominant D109A CRYAB mutation in a family with myofibrillar myopathy affects αB-crystallin structure. BBA clinical *7*, 1-7.
30. Nasiri, P., Ghahramani, M., Tavaf, Z., Niazi, A., Moosavi-Movahedi, A.A., Kurganov, B.I., and Yousefi, R. (2021). The biochemical association between R157H mutation in human αB-crystallin and development of cardiomyopathy: Structural and functional analyses of the mutant protein. Biochimie *190*, 36-49.

31. Yin, B., Tang, S., Xu, J., Sun, J., Zhang, X., Li, Y., and Bao, E. (2019). CRYAB protects cardiomyocytes against heat stress by preventing caspase-mediated apoptosis and reducing F-actin aggregation. Cell Stress and Chaperones *24*, 59-68.
32. Yáñez-Mó, M., Siljander, P.R., Andreu, Z., Zavec, A.B., Borràs, F.E., Buzas, E.I., Buzas, K., Casal, E., Cappello, F., Carvalho, J., et al. (2015). Biological properties of extracellular vesicles and their physiological functions. J Extracell Vesicles *4*, 27066. 10.3402/jev.v4.27066.
33. Yáñez-Mó, M., Siljander, P.R.-M., Andreu, Z., Bedina Zavec, A., Borràs, F.E., Buzas, E.I., Buzas, K., Casal, E., Cappello, F., and Carvalho, J. (2015). Biological properties of extracellular vesicles and their physiological functions. Journal of extracellular vesicles *4*, 27066.
34. Tkach, M., and Théry, C. (2016). Communication by extracellular vesicles: where we are and where we need to go. Cell *164*, 1226-1232.
35. Van Niel, G., d'Angelo, G., and Raposo, G. (2018). Shedding light on the cell biology of extracellular vesicles. Nature reviews Molecular cell biology *19*, 213-228.
36. El Andaloussi, S., Mäger, I., Breakefield, X.O., and Wood, M.J. (2013). Extracellular vesicles: biology and emerging therapeutic opportunities. Nature reviews Drug discovery *12*, 347-357.
37. Yamamoto, S., Azuma, E., Muramatsu, M., Hamashima, T., Ishii, Y., and Sasahara, M. (2016). Significance of extracellular vesicles: pathobiological roles in disease. Cell Structure and Function *41*, 137-143.
38. Xu, R., Rai, A., Chen, M., Suwakulsiri, W., Greening, D.W., and Simpson, R.J. (2018). Extracellular vesicles in cancer—implications for future improvements in cancer care. Nature reviews Clinical oncology *15*, 617-638.
39. Kalluri, R., and McAndrews, K.M. (2023). The role of extracellular vesicles in cancer. Cell *186*, 1610-1626.
40. Juan, T., and Fürthauer, M. (2018). Biogenesis and function of ESCRT-dependent extracellular vesicles. (Elsevier), pp. 66-77.
41. Vietri, M., Radulovic, M., and Stenmark, H. (2020). The many functions of ESCRTs. Nat Rev Mol Cell Biol *21*, 25-42. 10.1038/s41580-019-0177-4.
42. Luo, Y.B., Peng, Y., Lu, Y., Li, Q., Duan, H., Bi, F., and Yang, H. (2020). Expanding the Clinico-Genetic Spectrum of Myofibrillar Myopathy: Experience From a Chinese Neuromuscular Center. Front Neurol *11*, 1014. 10.3389/fneur.2020.01014.
43. Bova, M.P., Yaron, O., Huang, Q., Ding, L., Haley, D.A., Stewart, P.L., and Horwitz, J. (1999). Mutation R120G in alphaB-crystallin, which is linked to a desmin-related myopathy, results in an irregular structure and defective chaperone-like function. Proc Natl Acad Sci U S A *96*, 6137-6142.
44. Wang, X., Osinska, H., Klevitsky, R., Gerdes, A.M., Nieman, M., Lorenz, J., Hewett, T., and Robbins, J. (2001). Expression of R120G–αB-crystallin causes aberrant desmin and αB-crystallin aggregation and cardiomyopathy in mice. Circulation research *89*, 84-91.
45. Perng, M.D., Wen, S.F., van den IJssel, P., Prescott, A.R., and Quinlan, R.A. (2004). Desmin aggregate formation by R120G alphaB-crystallin is caused by altered filament interactions and is dependent upon network status in cells. Mol Biol Cell *15*, 2335-2346. 10.1091/mbc.e03-12-0893.

46. Sanbe, A., Osinska, H., Saffitz, J.E., Glabe, C.G., Kayed, R., Maloyan, A., and Robbins, J. (2004). Desmin-related cardiomyopathy in transgenic mice: a cardiac amyloidosis. Proc Natl Acad Sci U S A *101*, 10132-10136. 10.1073/pnas.0401900101.
47. den Engelsman, J., Gerrits, D., de Jong, W.W., Robbins, J., Kato, K., and Boelens, W.C. (2005). Nuclear import of αB-crystallin is phosphorylation-dependent and hampered by hyperphosphorylation of the myopathy-related mutant R120G. Journal of Biological Chemistry *280*, 37139-37148.
48. Maloyan, A., Sanbe, A., Osinska, H., Westfall, M., Robinson, D., Imahashi, K., Murphy, E., and Robbins, J. (2005). Mitochondrial dysfunction and apoptosis underlie the pathogenic process in alpha-B-crystallin desmin-related cardiomyopathy. Circulation *112*, 3451-3461. 10.1161/CIRCULATIONAHA.105.572552.
49. Andley, U.P., Hamilton, P.D., Ravi, N., and Weihl, C.C. (2011). A knock-in mouse model for the R120G mutation of αB-crystallin recapitulates human hereditary myopathy and cataracts. PloS one *6*, e17671.
50. Lilly, B., Galewsky, S., Firulli, A.B., Schulz, R.A., and Olson, E.N. (1994). D-MEF2: a MADS box transcription factor expressed in differentiating mesoderm and muscle cell lineages during Drosophila embryogenesis. Proc Natl Acad Sci U S A *91*, 5662-5666. 10.1073/pnas.91.12.5662.
51. Bour, B.A., O'Brien, M.A., Lockwood, W.L., Goldstein, E.S., Bodmer, R., Taghert, P.H., Abmayr, S.M., and Nguyen, H.T. (1995). Drosophila MEF2, a transcription factor that is essential for myogenesis. Genes Dev *9*, 730-741. 10.1101/gad.9.6.730.
52. Zhao, Z., Brooks, D., Guo, Y., and Geisbrecht, E.R. (2023). Identification of CryAB as a target of NUAK kinase activity in Drosophila muscle tissue. Genetics *225*, iyad167.
53. Guo, J., Huang, X., Dou, L., Yan, M., Shen, T., Tang, W., and Li, J. (2022). Aging and aging-related diseases: from molecular mechanisms to interventions and treatments. Signal Transduct Target Ther *7*, 391. 10.1038/s41392-022-01251-0.
54. Graw, J. (2009). Genetics of crystallins: cataract and beyond. Exp Eye Res *88*, 173-189. 10.1016/j.exer.2008.10.011.
55. Sadeh, M., Rahat, D., Meiner, V., Fellig, Y., Arad, M., Schueler-Furman, O., Hu, Y., Li, Y., Bönnemann, C.G., and Lossos, A. (2021). Multi-system neurological disorder associated with a CRYAB variant. neurogenetics *22*, 117-125.
56. Hafizi, M., Chebotareva, N.A., Ghahramani, M., Moosavi-Movahedi, F., Khaleghinejad, S.H., Kurganov, B.I., Moosavi-Movahedi, A.A., and Yousefi, R. (2021). Structural and functional studies of D109A human αB-crystallin contributing to the development of cataract and cardiomyopathy diseases. PloS one *16*, e0260306.
57. Li, Y., Li, S., and Wu, H. (2022). Ubiquitination-Proteasome System (UPS) and Autophagy Two Main Protein Degradation Machineries in Response to Cell Stress. Cells *11*. 10.3390/cells11050851.
58. Kumar, A.V., Mills, J., and Lapierre, L.R. (2022). Selective autophagy receptor p62/SQSTM1, a pivotal player in stress and aging. Frontiers in cell and developmental biology *10*, 793328.
59. Ryan, S.M., Almassey, M., Burch, A.M., Ngo, G., Martin, J.M., Myers, D., Compton, D., Archie, S., Cross, M., Naeger, L., et al. (2021). Drosophila p38 MAPK interacts with BAG-3/starvin to regulate age-dependent protein homeostasis. Aging Cell *20*, e13481. 10.1111/acel.13481.

60. Arndt, V., Dick, N., Tawo, R., Dreiseidler, M., Wenzel, D., Hesse, M., Fürst, D.O., Saftig, P., Saint, R., Fleischmann, B.K., et al. (2010). Chaperone-assisted selective autophagy is essential for muscle maintenance. Curr Biol *20*, 143-148. 10.1016/j.cub.2009.11.022.
61. Brooks, D., Naeem, F., Stetsiv, M., Goetting, S.C., Bawa, S., Green, N., Clark, C., Bashirullah, A., and Geisbrecht, E.R. (2020). Drosophila NUAK functions with Starvin/BAG3 in autophagic protein turnover. PLoS Genet *16*, e1008700. 10.1371/journal.pgen.1008700.
62. Clemen, C.S., Herrmann, H., Strelkov, S.V., and Schröder, R. (2013). Desminopathies: pathology and mechanisms. Acta Neuropathol *125*, 47-75. 10.1007/s00401-012-1057-6.
63. Sharma, S., Conover, G.M., Elliott, J.L., Der Perng, M., Herrmann, H., and Quinlan, R.A. (2017). αB-crystallin is a sensor for assembly intermediates and for the subunit topology of desmin intermediate filaments. Cell Stress Chaperones *22*, 613-626. 10.1007/s12192-017-0788-7.
64. Houck, S.A., Landsbury, A., Clark, J.I., and Quinlan, R.A. (2011). Multiple sites in αB-crystallin modulate its interactions with desmin filaments assembled *in vitro*. PLoS One *6*, e25859. 10.1371/journal.pone.0025859.
65. Kedia, N., Arhzaouy, K., Pittman, S.K., Sun, Y., Batchelor, M., Weihl, C.C., and Bieschke, J. (2019). Desmin forms toxic, seeding-competent amyloid aggregates that persist in muscle fibers. Proc Natl Acad Sci U S A *116*, 16835-16840. 10.1073/pnas.1908263116.
66. Pilotto, A., Marziliano, N., Pasotti, M., Grasso, M., Costante, A.M., and Arbustini, E. (2006). alphaB-crystallin mutation in dilated cardiomyopathies: low prevalence in a consecutive series of 200 unrelated probands. Biochemical and biophysical research communications *346*, 1115-1117.
67. Cannone, E., Guglielmi, V., Marchetto, G., Tobia, C., Gnutti, B., Cisterna, B., Tonin, P., Barbon, A., Vattemi, G., and Schiavone, M. (2023). Human Mutated MYOT and CRYAB Genes Cause a Myopathic Phenotype in Zebrafish. International Journal of Molecular Sciences *24*, 11483.
68. Batonnet-Pichon, S., Behin, A., Cabet, E., Delort, F., Vicart, P., and Lilienbaum, A. (2017). Myofibrillar Myopathies: New Perspectives from Animal Models to Potential Therapeutic Approaches. J Neuromuscul Dis *4*, 1-15. 10.3233/JND-160203.
69. Babst, M. (2011). MVB vesicle formation: ESCRT-dependent, ESCRT-independent and everything in between. Current opinion in cell biology *23*, 452-457.
70. van Niel, G., D'Angelo, G., and Raposo, G. (2018). Shedding light on the cell biology of extracellular vesicles. Nat Rev Mol Cell Biol *19*, 213-228. 10.1038/nrm.2017.125.
71. Linnemannstöns, K., Karuna M, P., Witte, L., Choezom, D., Honemann-Capito, M., Lagurin, A.S., Schmidt, C.V., Shrikhande, S., Steinmetz, L.K., Wiebke, M., et al. (2022). Microscopic and biochemical monitoring of endosomal trafficking and extracellular vesicle secretion in an endogenous *in vivo* model. J Extracell Vesicles *11*, e12263. 10.1002/jev2.12263.
72. Xu, M., Ji, J., Jin, D., Wu, Y., Wu, T., Lin, R., Zhu, S., Jiang, F., Ji, Y., Bao, B., et al. (2023). The biogenesis and secretion of exosomes and multivesicular bodies (MVBs): Intercellular shuttles and implications in human diseases. Genes Dis *10*, 1894-1907. 10.1016/j.gendis.2022.03.021.
73. Sacconi, S., Féasson, L., Antoine, J.C., Pécheux, C., Bernard, R., Cobo, A.M., Casarin, A., Salviati, L., Desnuelle, C., and Urtizberea, A. (2012). A novel CRYAB mutation resulting in multisystemic disease. Neuromuscular Disorders *22*, 66-72.

74. Kim, H.S., Lee, Y., Lim, Y.A., Kang, H.J., and Kim, L.S. (2011). αB-Crystallin is a Novel Oncoprotein Associated with Poor Prognosis in Breast Cancer. J Breast Cancer *14*, 14-19. 10.4048/jbc.2011.14.1.14.
75. Zhao, Z.W., Brooks, D., Guo, Y.G., and Geisbrecht, E.R. (2023). Identification of CryAB as a target of NUAK kinase activity in Drosophila muscle tissue. Genetics *225*. 10.1093/genetics/iyad167.
76. Kore, R.A., and Abraham, E.C. (2016). Phosphorylation negatively regulates exosome mediated secretion of cryAB in glioma cells. Biochimica et Biophysica Acta (BBA)-Molecular Cell Research *1863*, 368-377.
77. Xu, Z., Paparcone, R., and Buehler, M.J. (2010). Alzheimer's abeta(1-40) amyloid fibrils feature size-dependent mechanical properties. Biophys J *98*, 2053-2062. 10.1016/j.bpj.2009.12.4317.
78. Béhin, A., Salort-Campana, E., Wahbi, K., Richard, P., Carlier, R.-Y., Carlier, P., Laforêt, P., Stojkovic, T., Maisonobe, T., and Verschueren, A. (2015). Myofibrillar myopathies: state of the art, present and future challenges. Revue neurologique *171*, 715-729.
79. Arndt, V., Dick, N., Tawo, R., Dreiseidler, M., Wenzel, D., Hesse, M., Fürst, D.O., Saftig, P., Saint, R., and Fleischmann, B.K. (2010). Chaperone-assisted selective autophagy is essential for muscle maintenance. Current Biology *20*, 143-148.
80. Fink, M., Callol-Massot, C., Chu, A., Ruiz-Lozano, P., Izpisua Belmonte, J.C., Giles, W., Bodmer, R., and Ocorr, K. (2009). A new method for detection and quantification of heartbeat parameters in Drosophila, zebrafish, and embryonic mouse hearts. Biotechniques *46*, 101-113. 10.2144/000113078.
81. Ocorr, K., Reeves, N.L., Wessells, R.J., Fink, M., Chen, H.S., Akasaka, T., Yasuda, S., Metzger, J.M., Giles, W., Posakony, J.W., and Bodmer, R. (2007). KCNQ potassium channel mutations cause cardiac arrhythmias in Drosophila that mimic the effects of aging. Proc Natl Acad Sci U S A *104*, 3943-3948. 10.1073/pnas.0609278104.
82. Rai, M., Curley, M., Coleman, Z., Nityanandam, A., Jiao, J., Graca, F.A., Hunt, L.C., and Demontis, F. (2021). Analysis of proteostasis during aging with western blot of detergent-soluble and insoluble protein fractions. STAR Protoc *2*, 100628. 10.1016/j.xpro.2021.100628.
83. Moro, E., Vettori, A., Porazzi, P., Schiavone, M., Rampazzo, E., Casari, A., Ek, O., Facchinello, N., Astone, M., Zancan, I., et al. (2013). Generation and application of signaling pathway reporter lines in zebrafish. Mol Genet Genomics *288*, 231-242. 10.1007/s00438-013-0750-z.
84. Kimmel, C.B., Ballard, W.W., Kimmel, S.R., Ullmann, B., and Schilling, T.F. (1995). Stages of embryonic development of the zebrafish. Dev Dyn *203*, 253-310. 10.1002/aja.1002030302.
85. Guglielmi, V., Pancheri, E., Cannone, E., Nigro, V., Malatesta, M., Vettori, A., Giorgetti, A., Torella, A., Aurino, S., Cisterna, B., et al. (2023). A novel in-frame deletion in MYOT causes an early adult onset distal myopathy. Clin Genet *104*, 705-710. 10.1111/cge.14413.

Chapter 5 - Conclusions and future directions

5.1 Conclusions

Our findings demonstrate that the catalytic activity of NUAK is essential for maintaining muscle integrity and preventing degeneration. We identified a direct physical interaction between NUAK and CryAB and showed that NUAK promotes CryAB phosphorylation at serine residues 68 and 70. Given that mutations in FLNC, BAG3, and CRYAB are linked to protein aggregation disorders, our results highlight the importance of NUAK-mediated phosphorylation in safeguarding muscle tissue from abnormal protein accumulation.

Mechanistic insights suggest that kinase-dead variants of NUAK can interfere with phosphorylation through several routes. They may preferentially bind CryAB and outcompete endogenous NUAK, disrupt potential dimerization required for kinase activity, or sequester substrates within inactive catalytic pockets. These dominant-negative effects reduce the pool of phosphorylated CryAB, emphasizing how tightly regulated NUAK activity must be for normal muscle function. Moreover, although phosphorylation at the conserved T226 site contributes to activity, our results indicate that additional regulatory sites may exist, and the upstream kinases responsible for NUAK activation remain to be identified.

Evidence also supports a conserved role for NUAK in CryAB phosphorylation across species. Overexpression of wild-type or activated NUAK enhances CryAB phosphorylation, while kinase-dead or inactive mutants reduce it. Although we cannot yet confirm whether NUAK directly phosphorylates CryAB or acts through intermediate kinases, related studies in mammalian

systems point toward a broader NUAK–CryAB signaling axis. This conservation is particularly significant given that CryAB mutations are associated with diverse pathologies, including cardiomyopathies, cataracts, and skeletal myopathies.

CryAB functions as a molecular chaperone, preventing protein aggregation and maintaining proteostasis. However, its broad range of binding partners complicates efforts to define its precise molecular role. Our pulldown experiments support the idea that CryAB's interactions are highly regulated *in vivo* but become promiscuous under experimental conditions, suggesting that cellular context is key to its specificity. Importantly, the oligomerization state of CryAB strongly influences its chaperone activity, with smaller oligomers exhibiting higher substrate-binding capacity. Phosphorylation shifts CryAB toward smaller oligomers, yet the biological consequences of this redistribution vary depending on the cellular context, age, and stress conditions.

Taken together, our study reveals that NUAK-mediated regulation of CryAB is critical for muscle health. NUAK likely acts as a protective factor by enabling CryAB to counteract protein aggregation, potentially linking its kinase activity to autophagy and stress resilience. While phosphorylation of CryAB can be either protective or harmful depending on context, our results suggest that, within muscle tissue, it plays a key role in maintaining proteostasis and preventing degeneration. Future research should focus on clarifying whether NUAK directly phosphorylates CryAB, identifying additional upstream regulators of NUAK, and determining how CryAB's phosphorylation state integrates with cellular mechanisms of stress response and protein quality control.

5.2 Future directions

A key priority for future work will be to resolve the structural basis of NUAK regulation and its interaction with CryAB. Understanding how NUAK adopts active and inactive conformations, and how CryAB engages its client proteins, will provide critical insight into how phosphorylation governs proteostasis in muscle tissue. Particular attention should be given to the ring-like amyloid assemblies of CryAB observed in disease, as these circular oligomers may represent an important intermediate in aggregate formation. Future studies should also explore whether wild-type and mutant CryAB subunits co-assemble into the same complexes and how such heterogeneity affects chaperone function and disease progression. While current structural approaches face limitations due to the size and complexity of these assemblies, advancing imaging and modeling techniques will help overcome these challenges.

Another promising avenue involves translating these molecular insights into therapeutic design. Targeting CryAB to prevent its pathological transition into amyloid assemblies could yield novel anti-amyloid therapies. Strategies may include stabilizing its protective oligomeric forms, blocking pathological assembly interfaces, or modulating NUAK activity to favor phosphorylation states that maintain proteostasis. The development of such therapies will not only shed light on CryAB's role in muscle disorders but may also extend to other conditions where protein aggregation is a hallmark.

Finally, the role of CryAB-positive vesicles in disease offers intriguing opportunities. These vesicles carry diverse protein and molecular cargo, yet their precise content and functional impact remain poorly understood. Future work should aim to define how these vesicles select their cargo, how they transfer material between cells, and whether certain components can cross

physiological barriers such as the blood–brain barrier. This line of research may reveal how CryAB vesicles contribute to disease spread, while also opening possibilities for harnessing them as vehicles for targeted drug delivery.

Together, these directions highlight the importance of connecting structural biology with therapeutic innovation and cellular biology. By bridging these perspectives, future research has the potential to not only clarify the mechanisms of NUAK–CryAB regulation but also uncover new strategies to combat muscle degeneration and related protein aggregation disorders.

Appendix A Myopalldin (MYPN) function in *Drosophila* muscle tissue

This section forms part of a larger manuscript that has been submitted for publication, where we explore broader aspects of myopalladin function across model systems.

Material and Method

Drosophila stocks and husbandry

All stocks were reared at 31 °C on standard cornmeal-molasses-yeast media. w^{1118} was used as the *WT* control in Appendix Figure A.1 B. The *Mef2*-GAL4 (Bloomington *Drosophila* Stock Center; RRID:BDSC_27390) driver was used to direct expression in muscle tissue.

Creation of transgenic flies

All UAS-*MYPN* lines (*hMYPN WT, hMYPN R955W, hMYPN P961L, hMYPN WT-GFP, hMYPN R955W-GFP,* and *hMYPN P961L-GFP*) were created using gene synthesis by Genscript and subcloned into the pUAST vector using EcoRI and HpaI restriction sites. Plasmid DNA from all constructs were purified with a Qiagen Maxi Kit (Hilden, Germany), sequence verified, and sent to Rainbow Trangenics for the creation of transgenic flies. The insertions were balanced on their respective chromosomes. All lines were balanced over the *Cyo, tb* (BL36335), or *TM6/TM6, tb* balancers.

Larval muscle staining

Wandering L3 larvae were placed onto a Sylgard plate, pinned near the mouth hooks at the anterior end and the internal organs were removed. The muscle carcasses were fixed in 4% formaldehyde and immunostained using standard immunostaining protocols, with normal goat serum used as a blocking agent in PBT. Tissues were stained with the following primary antibodies: rabbit anti-

MYPN (1:200; kindly provided by Marie-Louise Bang) or secondary antibodies: Alexa Fluor anti-Rabbit 488 or 594 (1:400, Molecular Probes, Eugene, OR). Phalloidin 488 or 594 were used to label F-actin (1:400, Molecular Probes, Eugene, OR). A Zeiss 700 confocal microscope was used to capture the images. Image processing and analysis was performed using a combination of Zen Black (Zeiss), ImageJ (NIH), and Adobe Photoshop. Images taken at 5x are displayed as maximum intensity projections. Data acquisition at increased magnifications (63x) are presented as single plane confocal images.

Western blotting

Three whole L3 larvae were placed into 3x SDS sample buffer [188 mM Tris-HCl (pH 6.8), 3% (w/v) SDS, 30% (v/v) glycerol, 0.01% (w/v) bromophenol-blue, and 15% (v/v) β-mercaptoethanol], boiled at 95 °C for 3 min, homogenized, boiled for an additional 10 min at 95 °C, and centrifuged at 20,000 x g for 1 min to pellet debris. The resulting protein samples were separated by sodium dodecyl sulfate polyacrylamide gel electrophoresis (SDS-PAGE) and transferred to the nitrocellulose blotting membrane (pore size 0.45 μm, Cytiva, Marlborough, MA) using the Trans-Blot® TurboTM Transfer System (Bio-Rad, Hercules, CA). Membranes were stained with the Revert 700 Total Protein Stain (LI-COR Biosciences, Lincoln, NE) as a loading control. Membranes were probed with the rabbit anti-MYPN (1:1000; kindly provided by Marie-Louise Bang). IRDye 800CW secondary antibodies (LI-COR Biosciences, Lincoln, NE) were used at 1:10000. Membranes were developed using the LI-COR Odyssey XF and quantitation of protein levels was performed in Empiria Studio Software (LI-COR Biosciences, Lincoln, NE).

Result

MYPN function in *Drosophila* muscle tissues

To investigate the impact of MYPN mutations *in vivo*, we generated humanized *Drosophila* models to analyze MYPN protein localization in larval heart and muscle tissues. The *Drosophila* genome does not encode for MYPN, so we expressed wild-type and mutant versions in transgenic fly lines utilizing the GAL4-UAS binary expression system (PMID: 8223268). The *Mef2* promoter drives expression of the transactivator GAL4 protein in heart and skeletal muscle throughout the *Drosophila* life cycle (PMID: 9671578). GAL4 binds to upstream activating sequences (UAS) to induce expression of MYPN proteins.

Immunostaining of the larvae heart tube revealed localization of human MYPN to the Z-disc of cardiac tissue using our GAL4-mediated expression system *Mef2*-GAL4>UAS-*MYPN WT* **(Appendix Figure A.1 A)**. This result nicely validates the *Drosophila* musculature as an evolutionary conserved model to study mammalian muscle structure and function as human MYPN is also located at the Z-disc. The *Drosophila* larval body wall muscles are larger than the heart tube and the organization of sarcomeres in series within each muscle cell are ideal for studying sarcomeric protein localization. As expected due to the lack of MYPN in *Drosophila*, there was no MYPN signal in w^{1118} control muscles **(Appendix Figure A.1 B)**. Expression of human WT MYPN is located at the Z-disc **(Appendix Figure A.1 B, open white triangle)** in larval muscles. To verify our immunostaining results, we also generated transgenic flies containing GFP-tagged versions of MYPN and found that MYPN-GFP showed the same Z-disc localization as the untagged protein **(Appendix Figure A.2 A and B)**. Importantly, the overall pattern of larval muscles was not altered upon expression of MYPN or MYPN mutant proteins appended with GFP **(Appendix Figure A.2 A and B)**.

Appendix Figure A.1 MYPN is located at the Z-disc and Ig domain mutations cause aberrant MYPN accumulation.

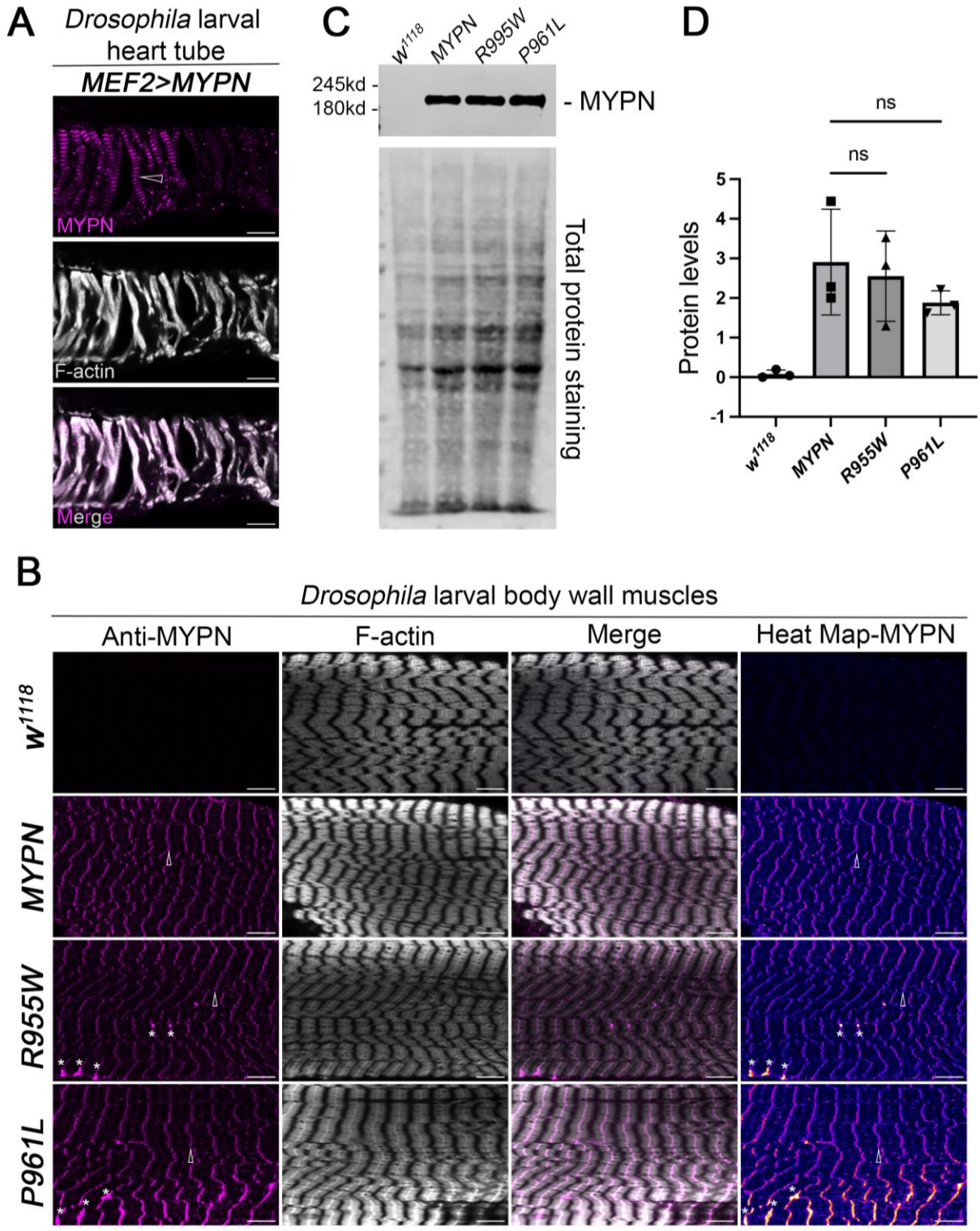

(A). Immunostaining of *Drosophila* larval heart tube expressing *Mef2>MYPN WT*. MYPN protein is localized to the Z-disc (magenta, open white triangle). F-actin is shown in grey. Scale bar: 10μM.

(B). L3 larval muscles stained with phalloidin to visualize F-actin or with an antibody against MYPN. F-actin and MYPN co-localize at the Z-disc (open white triangle), in in *Mef2>MYPN WT* muscles. *MYPN R955W* and *MYPN P961L* Ig domain mutations show abnormal accumulation of MYPN (white asterisk). Scale bar: 10μM.
(C). Western blot showing the expression levels of MYPN in the indicated genotypes. Total protein staining serves as a loading control. One-way ANOVA. N = 3.
(D). Quantification of MYPN expression levels.

In *MYPN R955W* and *P961L* mutants, we discovered that MYPN was largely present at its expected location **(Appendix Figure A.1 B, open white triangle)**, but also accumulated abnormally in clusters away from the Z-disc or appeared as widened Z-discs **(Appendix Figure A.1 B, asterisks)**. Similar phenotypes were observed for GFP-tagged MYPN mutants, where R955W-GFP signal extended into the thin filament **(Appendix Figure A.2 B, arrow)** and P961L-GFP resulted in larger aggregates **(Appendix Figure A.2 B, asterisks)**. Overexpression of all MYPN-GFP proteins resulted in substantial accumulation near the nuclei **(Appendix Figure A.2 C)**. Western blotting was used to confirm expression levels of all MYPN proteins and confirmed that the differences in subcellular localization were not due to differences in expression levels **(Appendix Figure A.1 C and D; Appendix Figure A.2 D and E)**.

Appendix Figure A.2 GFP-tagged versions of MYPN show similar phenotypes to untagged versions.

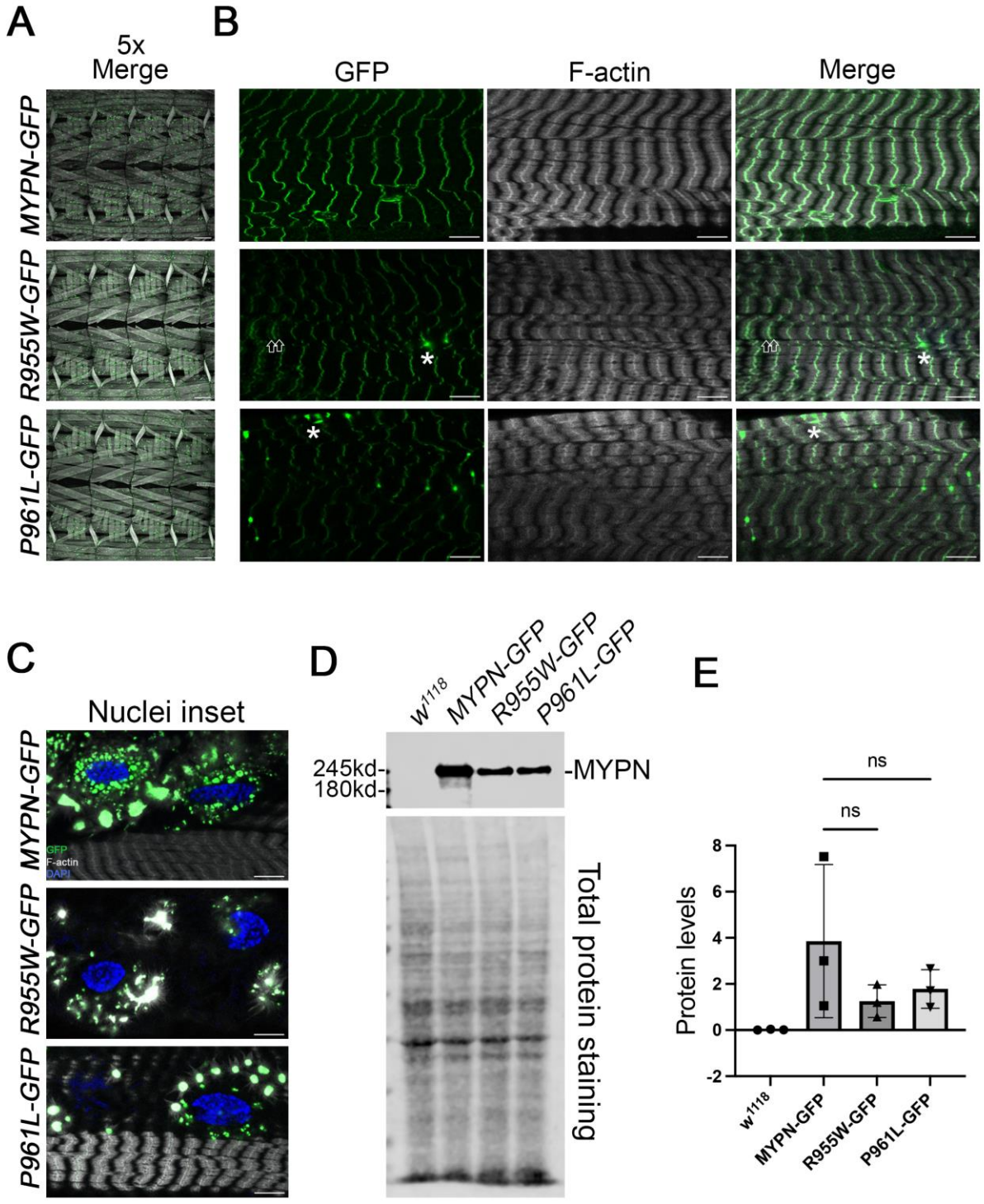

(A). Maximum intensity projections of *Mef2>MYPN_WT-GFP*, *R955W-GFP* and *P961L-GFP*

(green) co-stained for F-actin (gray) at low magnification to visualize muscle pattern. Scale bar: 200μM.
(B). GFP tagged MYPN in L3 larval muscles (green). To visualize F-actin, larval muscle was stained with phalloidin (grey). MYPN_R955W-GFP Ig domain mutation resulting in a mislocalization (open white arrow) and MYPN accumulation (asterisk). MYPN_P961L-GFP showed accumulation outside of the Z-disc (asterisk). Scale bar: 10μM.
(C). Inset of nuclei at the surface of L3 larval muscles. The merged images show F-actin (grey) abnormally accumulates with MYPN-GFP proteins (green) near the nuclei (blue) in *MYPN WT-GFP* the Ig domain mutations (*MYPN-R955W* and *MYPN-P961L*). Scale bar: 10μM.
(D). Western blot illustrating the expression levels of MYPN-GFP tagged proteins. Total protein staining serves as a loading control.
(E)**.** Quantification of MYPN expression levels of GFP-tagged lines. One-way ANOVA. N = 3.

Appendix B Transglutaminase function in *Drosophila* muscle tissue

Results and Summary

Muscle contraction is only one component of coordinated muscle function; tendons also play a critical role in maintaining muscle homeostasis and preventing injury. Tendons are primarily composed of extracellular matrix (ECM), with collagen type I as the major structural component. The myotendinous junction (MTJ), which serves as the interface between muscle termini and tendon, represents an excellent model for investigating how ECM responds to mechanical stress. However, the molecular mechanisms underlying ECM adaptation to force remain incompletely understood.

In our laboratory, a genetic screen in *Drosophila* was initiated by Dylan Feist to identify ECM proteins required for stable muscle–tendon adhesion. This screen, based on RNAi-mediated knockdown, identified Transglutaminase (Tg)—a protein crosslinking enzyme—as a candidate regulator. Tg is a known component of the MTJ in mammals, with established roles in blood coagulation and skin barrier formation in humans, as well as cuticle morphogenesis in *Drosophila*.

To assess the role of Tg at the MTJ, we utilized two independent Tg RNAi lines. Knockdown of Tg led to muscle detachment and loss phenotypes when driven ubiquitously (*da*-Gal4) or in genetic backgrounds sensitized by mutations in key ECM proteins such as Fondue (Fon) and Tiggrin (Tig). To examine Tg localization during embryonic muscle development, we generated a Tg-specific antibody for immunostaining. Co-staining with the integrin subunit βPS, a marker of muscle attachment sites, revealed that Tg is enriched at MTJs in wild-type embryos.

Further phenotypic analyses using the tendon-specific driver *sr*-Gal4 (with and without Dicer-2 to enhance RNAi efficacy) demonstrated that Tg knockdown results in severe larval

muscle defects, including missing or detached muscles at the L3 stage. Control experiments with *sr*-Gal4>UAS-CD8-GFP confirmed tendon-specific expression and validated Tg localization in tendon cells and cuticle regions **(Appendix Figure B.1)**. In adult flies, Tg depletion resulted in reduced F-actin organization and loss of MTJ-specific Tg staining **(Appendix Figure B.2)**.

Appendix Figure B.1 Tg protein is found in both the cuticle and tendon cells.

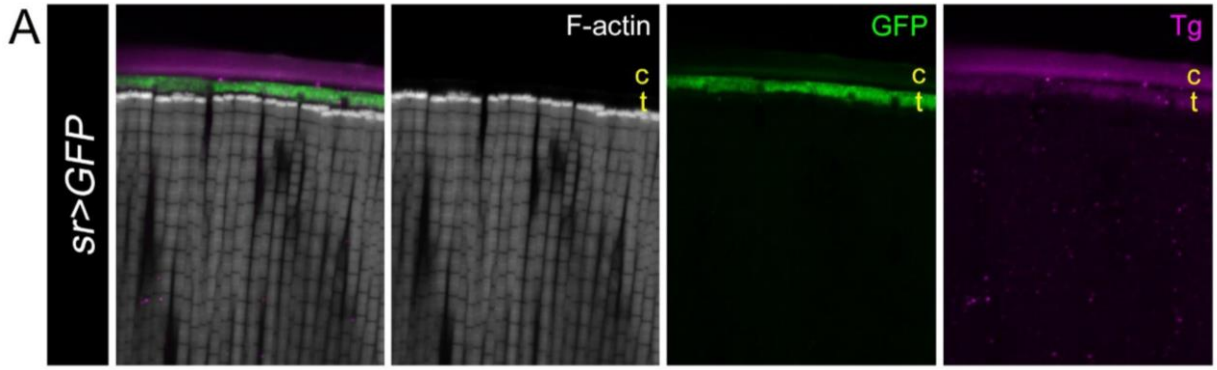

(A) *sr*-Gal4 is driving CD8-GFP to mark the tendon cells in 2 day old adult IFMs where muscles are labeled with phalloidin (gray). Anti-Tg immunostaining shows labeling in tendon cells (t) and the cuticle (c).

To probe Tg function under mechanical stress, we combined Tg knockdown with a hypertensive allele of myosin heavy chain (Mhc). Under these conditions, flies displayed thoracic indentations, degeneration of indirect flight muscles (IFMs), and increased incidence of muscle detachment, underscoring Tg's role in maintaining MTJ stability under tension **(Appendix Figure B.3)**. Since the muscle tension mainly foamed during the pupa stage, these data suggest that Tg play the essential role during the myogenesis during the pupa stage. The mechanical tension test for the Tg-RNAi using the optogenetic approach to generate muscle force under the LexA/LexAop system. I helped to dissect the adult fly thoraces after the optogenetic force. IFMs with the detached muscle phenotype when induce the muscle tension under the light in adult stage **(Appendix Figure B.4)**. Collectively, these findings demonstrate that Tg is required for proper muscle–tendon

attachment in *Drosophila*, particularly under conditions of mechanical load, and provide a genetic framework for studying conserved Tg functions at the MTJ.

Appendix Figure B.2 Mild muscle phenotype in Tg RNAi knockdown.

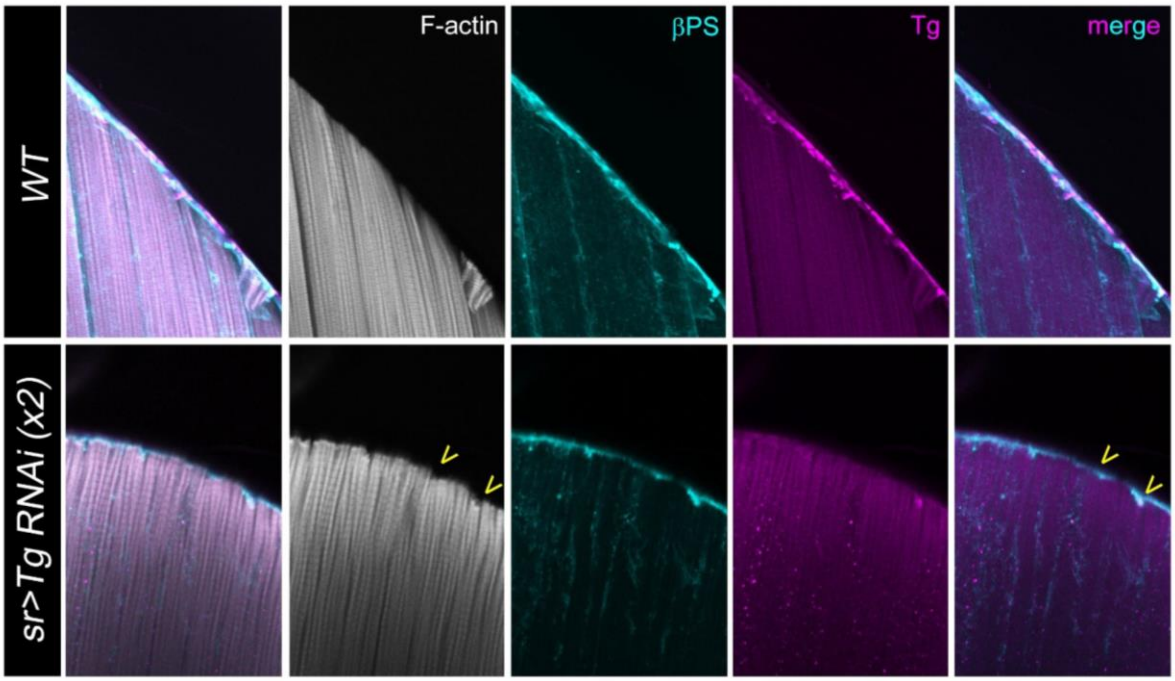

(A) 2 day old adult IFMs from either control or *sr*-Gal4 driving two copies of *>Tg RNAi.* Muscles are labeled with phalloidin (gray). βPS integrin marks the MTJ (cyan) and Tg is in magenta. Note that Tg protein is reduced in *sr>Tg RNAi* and muscles are slightly pulled away from the MTJ (yellow carets).

Appendix Figure B.3 Tg crosslinking activity affects IFM muscle attachment.

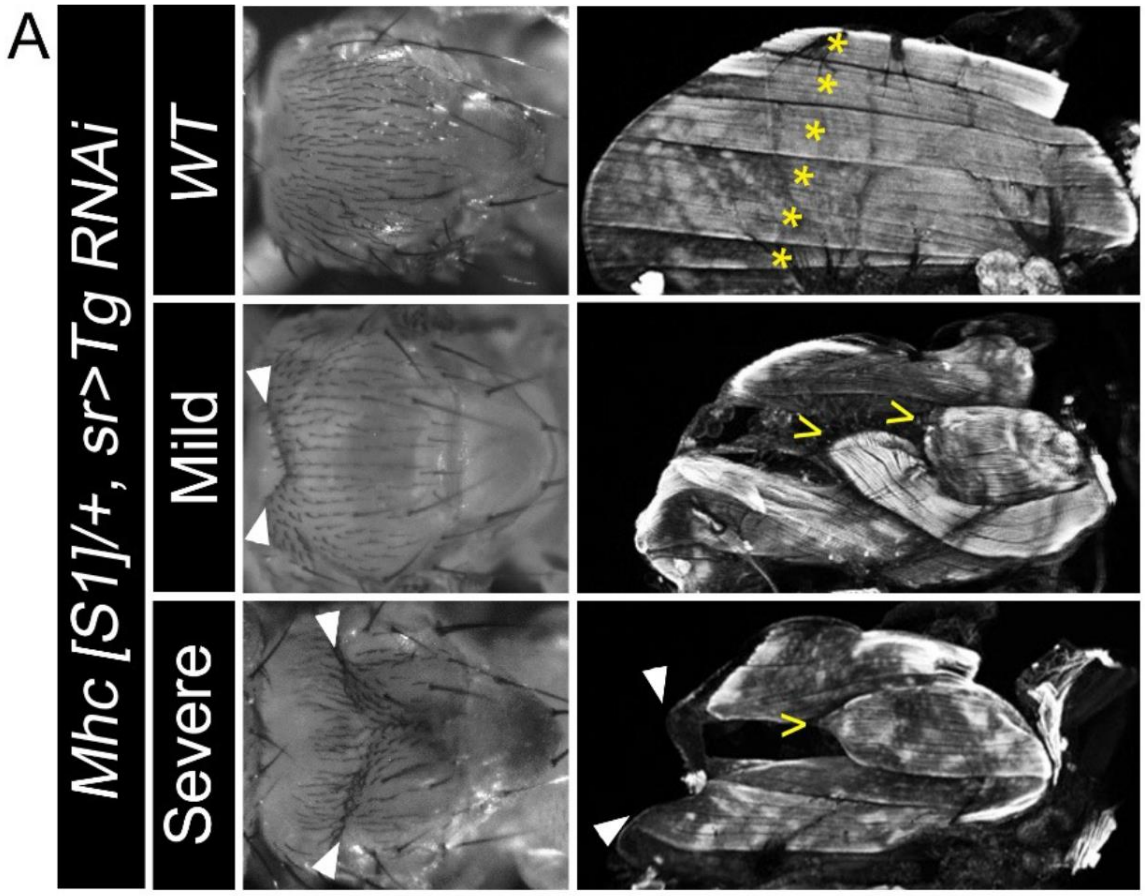

(A) Thoracic phenotypic classes present in *Mhc[S1]/+, sr>Tg RNAi* adult flies. Anterior is to the left. Compared to a '*WT*' notum, small and V-like indentations (white arrows) are seen in phenotypes classified as 'Mild.' These are larger and wider in the 'Severe' category. Phalloidin staining reveals the normal compliment of 6 IFM fibers (*) in *WT* samples. Mild or Severe phenotypes show degenerated or detached IFMs (yellow carets).

Appendix Figure B.4 Increased mechanical tension weakens IFM attachment.

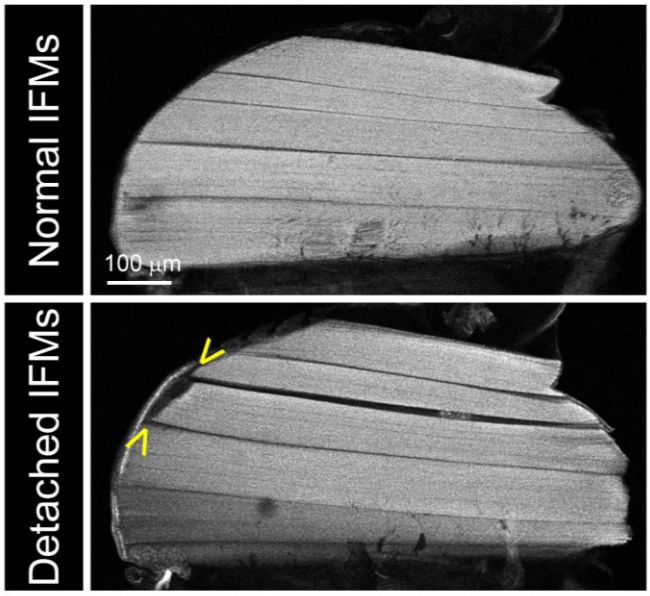

Representative confocal single plane images of either attached (upper panel) or detached (lower panel) IFMs (F-actin, gray).

Appendix C Loss of nuclear envelope bud formation leads to mitophagy initiation in *Drosophila* muscles

Summary

Autophagosome transport and fusion with lysosomes depend on microtubule-based trafficking, yet the molecular machinery coordinating this process in muscle tissue remains incompletely defined. To investigate the requirement of intracellular transport for autophagy, we performed a targeted RNAi screen in Drosophila larval muscle, monitoring accumulation of the autophagy substrate p62/Ref(2)p. Knockdown of the microtubule-associated protein Pavarotti (Pav/Kif23) resulted in robust p62 aggregation, indicative of defective autophagic flux. Depletion of Tumbleweed (Tum), the binding partner of Pav in the centralspindlin complex, produced a similar phenotype. Immunostaining revealed colocalization of p62 aggregates with the autophagosome marker Atg8a/LC3, supporting a failure of autophagosome trafficking. Pav and Tum were further implicated in nuclear envelope (NE) budding, a nuclear export pathway essential for macromolecule clearance. Consistently, RNAi-mediated loss of Pav or Tum impaired NE budding, linking defective nuclear export to cytoplasmic accumulation of autophagic cargo. Moreover, p62 aggregates in mutant muscles colocalized with mitochondria, suggesting clustering of autophagosomes and mitochondria under disrupted transport conditions. Together, these findings establish Pav and Tum as critical regulators of autophagy in muscle, coordinating nuclear export and microtubule-based trafficking to maintain proteostasis. I assisted Yungui with the NE budding quantification **(Appendix Figure C.1)**.

Appendix Figure C.1 Scatter plot quantifying the number of NE buds per nucleus.

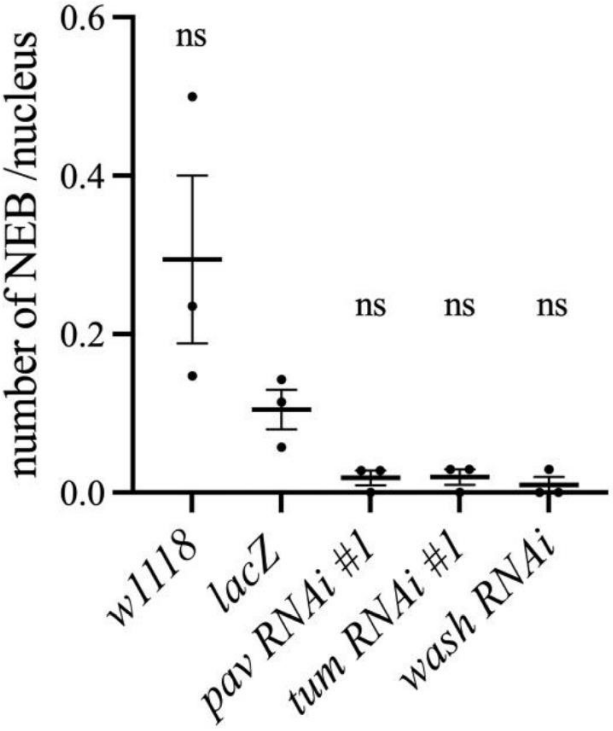

Appendix D Chapter 2 Supplementary Figures

Appendix Figure D.1 Confirmation of muscle morphology phenotypes with the C57-Gal4 driver.

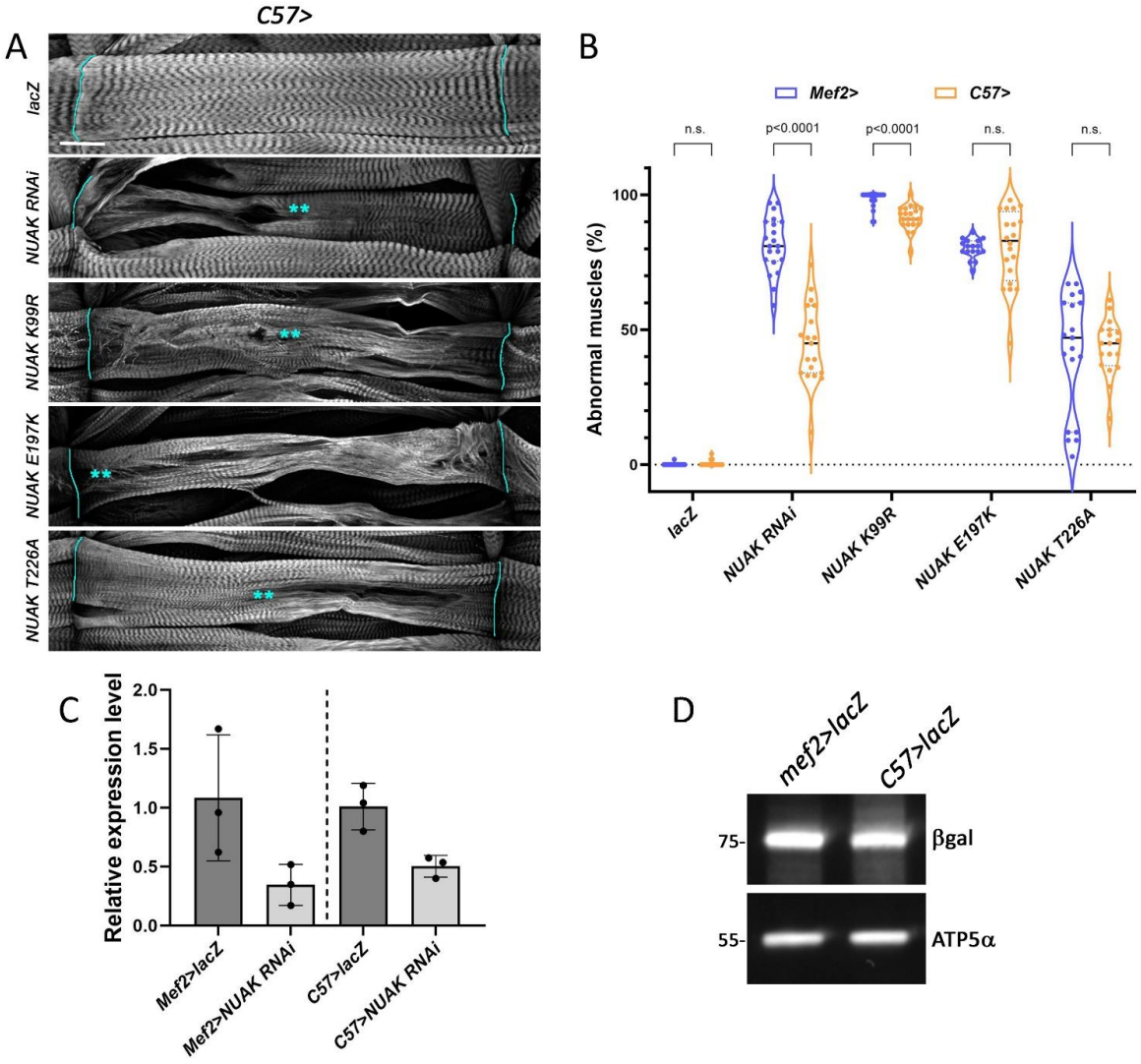

(A) Maximum intensity projections of L3 muscles expressing *NUAK RNAi* or *NUAK* kinase domain mutations. Asterisks indicate muscle morphology defects and solid lines demarcate muscle attachment sites. Scale bar, 25 µm. (B) Quantitation of muscle abnormalities shown by violin plots with individual data points. Mann-Whitney tests were used for statistical analysis and the indicated p-values represent pair-wise comparisons between the *Mef2*-Gal4 and *C57*-Gal4 drivers for each genotype. N ≥ 17. (C) Quantitative RT-PCR reveals knockdown of *NUAK mRNA* transcripts in *Mef2>NUAK RNAi* or *C57>NUAK RNAi* dissected muscle carcasses compared to *Mef2>lacZ* controls. N = 3 biological replicates. (D) β-galactosidase protein levels are relatively similar when driving expression of the *lacZ* gene with either the *Mef2* or *C57* promoters. ATP5α is used as a loading control.

Appendix Figure D.2 Specificity of the CryAB antibody.

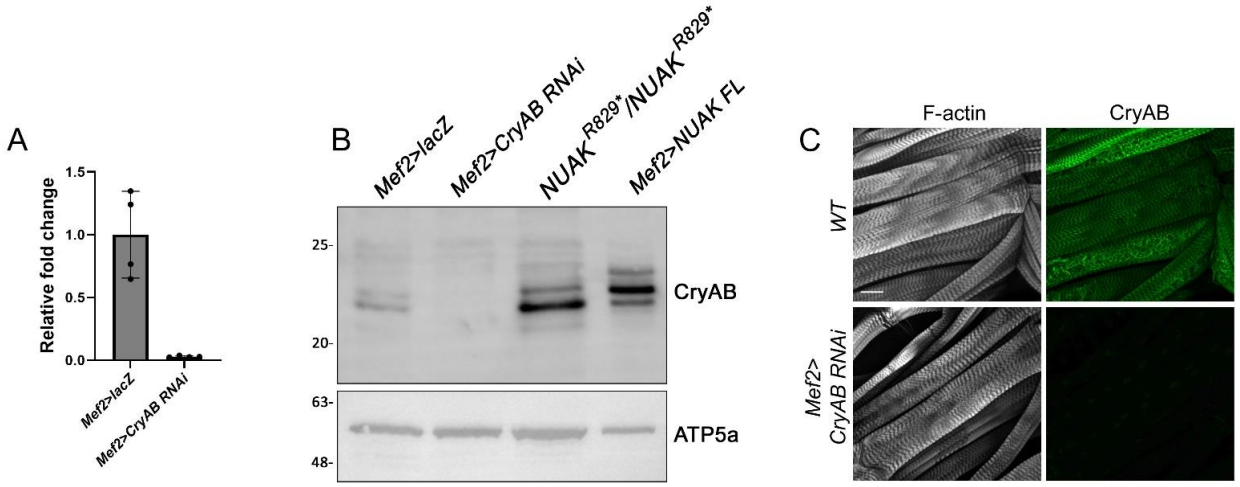

(A) Quantitative RT-PCR shows that *CryAB RNAi* induced by the *Mef2* promoter knocks down *CryAB mRNA* transcripts in dissected muscle carcasses. N = 3 biological replicates. (B) Western blot showing that CryAB protein levels are reduced upon induction of *CryAB RNAi* in muscle tissue. ATP5α is used as a loading control. (C) Immunostaining of L3 muscles confirms loss of CryAB immunoreactivity in *Mef2>CryAB* RNAi muscles. Scale bar, 50 μm.

Appendix Figure D.3 Prm does not accumulate in regions that lack F-actin in NUAK RNAi muscles.

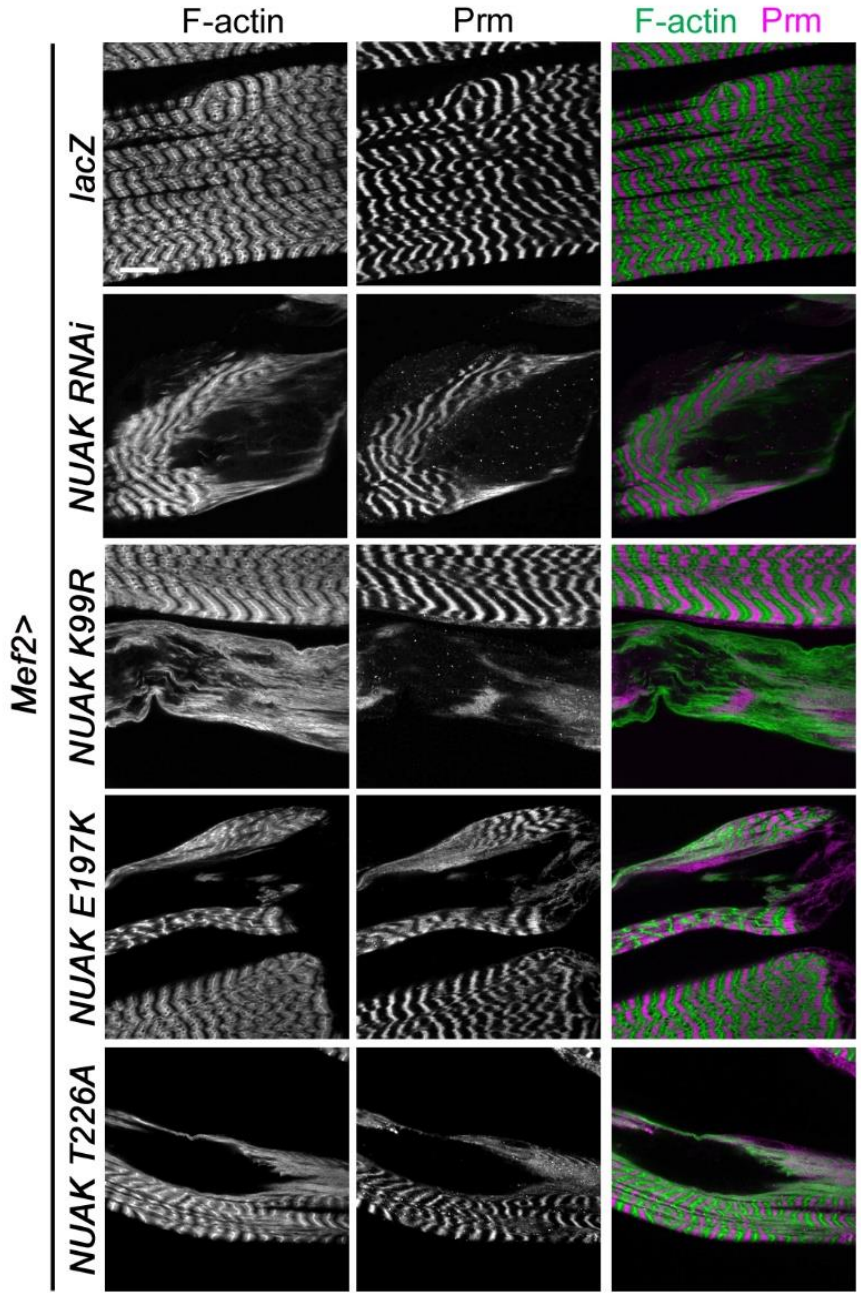

(A) Single slice confocal images of F-actin (green) and Prm (magenta) in muscles expressing *lacZ*, *NUAK RNAi* or NUAK kinase domain mutations. Prm is absent from regions lacking F-actin. Scale bar, 20 μm.

Appendix Figure D.4 Western blot confirms specificity of the pT211 antibody.

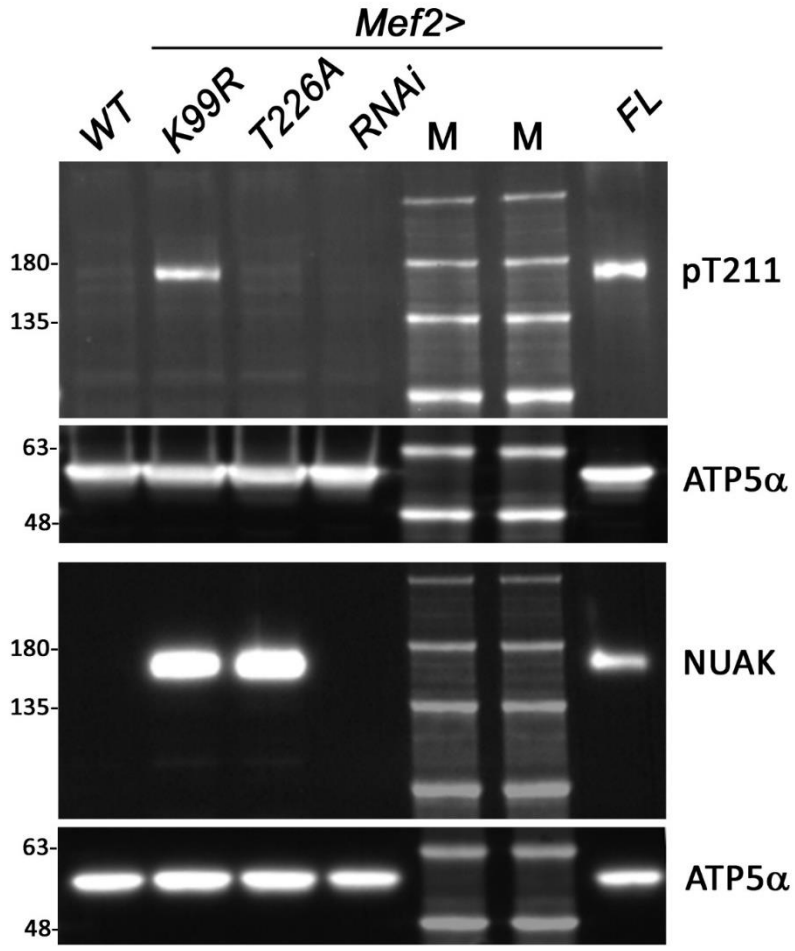

Immunoblotting with an antibody generated against NUAK confirms overexpression of the NUAK K99R or NUAK T226A transgenes. The phospho pT211 antibody recognizes NUAK K99R, but not the T226A protein where the epitope has been mutated. ATP5α is used as a loading control.

Appendix Figure D.5 Inhibition of mammalian NUAK1 causes a reduction in pCryAB levels in C2C12 cells.

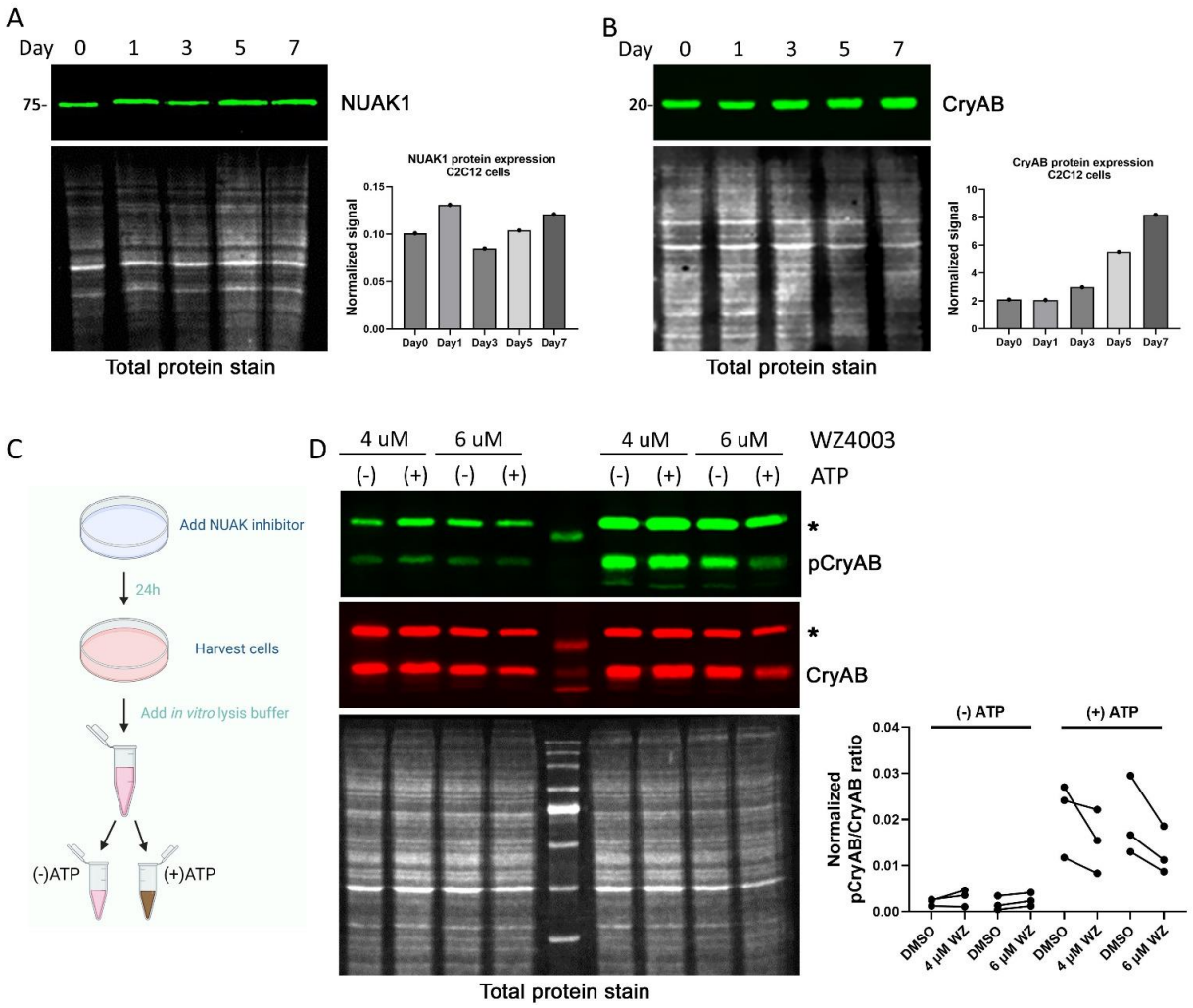

(A,B) Western blots (left panel) and bar graph quantification (right panel) of mouse NUAK1 or mouse CryAB expression during C2C12 cell differentiation. (A) NUAK1 is detected at similar levels throughout C2C12 differentiation. (B) CryAB expression is present in C2C12 myoblasts (day 0) and increases during days 1-7. (C) Schematic of the *in vitro* phosphorylation assay used to enhance pCryAB levels. C2C12 cells were differentiated for 3 days and treated with the NUAK inhibitor WZ4003 for 24 hours (h). The WZ4003-treated cells were divided into two groups, one without ATP and the other with ATP to enhance cellular phosphorylation levels. (D) pCryAB (top panel) and total CryAB protein levels (middle panel) were detected by Western blotting. Total protein stain (bottom panel) shows loading for each lane. * denotes non-specific band. Quantification of the pCryAB/total CryAB ratio reveals a reduction in pCryAB upon inhibition of NUAK kinase activity. N = 3 biological replicates.

Appendix E Chapter 4 Supplementary Figures

Appendix Figure E.1 CryAB sequence alignment, mutated phosphosites, and cardiac phenotypes, related to Figure 1.

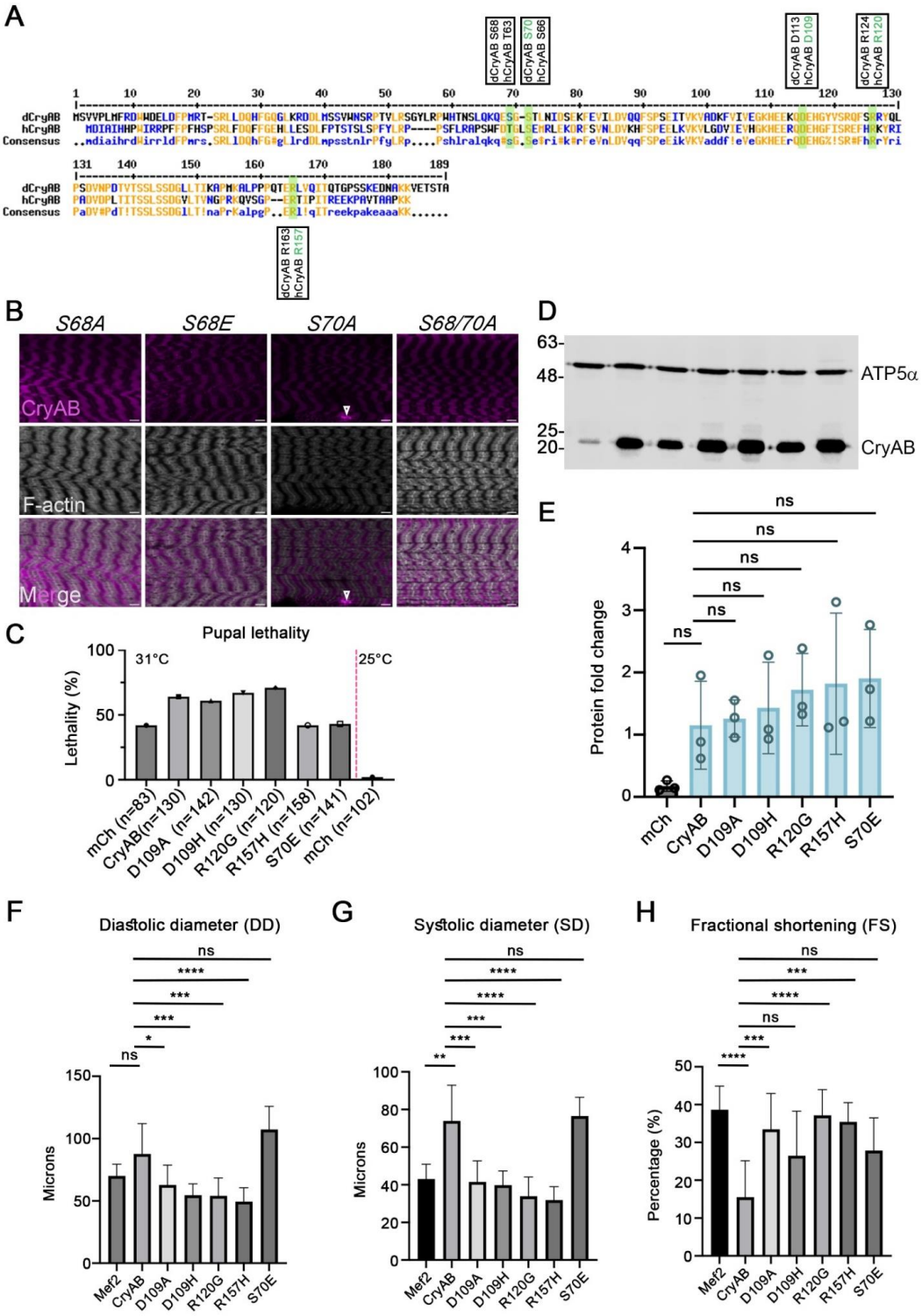

(A) Sequence alignment of human and *Drosophila* CryAB proteins using MultAlin. Highly conserved or identical amino acids are shown in orange. The location of mutated amino acids used for the creation of transgenic flies in this study are highlighted by black boxes. Green font denotes the amino acid numbering nomenclature. **(B)** Representative images of L3 muscles immunostained with anti-CryAB (magenta) or phalloidin to mark F-actin (gray). Open white arrow marks CryAB inclusion. Scale bar: 5 μm. **(C)** Quantification of pupal lethality at 31 °C. Due to high lethality, *mCh RNAi (mCh)* flies were incubated at 25 °C as an additional control. **(D,E)** Western blot analysis of CryAB expression levels Day 2 IFMs. ATP5α was used as a loading control. **(C-F)** Quantification of CryAB WT and mutant proteins from panel DData are presented as the mean of N=3. **(F-G)** Quantitative assessment of adult fly hearts expressing CryAB variants using semi-automated optical heartbeat analysis. (F) Diastolic diameter (DD) measurements shows reduced heart tube relaxation compared to *Mef2*-Gal4 controls and CryAB wildtype. (N>5 per genotype; One-way ANOVA, Kruskal-Wallis test). **(G)** Systolic diameter (SD) measurements reveal that CryAB mutations cause a pronounced decrease in heart tube contraction relative to controls. (N>5 per genotype; One-way ANOVA, Kruskal-Wallis test). **(H)** Fractional shortening (FS), an indicator of cardiac contractility, is significantly impaired in CryAB mutants (N>5 per genotype; One-way ANOVA, Kruskal-Wallis test). ns = not significant, *$p>0.05$, **$p<0.05$, ***$p<0.01$, ****$p<0.001$.

Appendix Figure E.2 CryAB aggregates and insolubility in Day 10 IFMs, related to Figure 2.

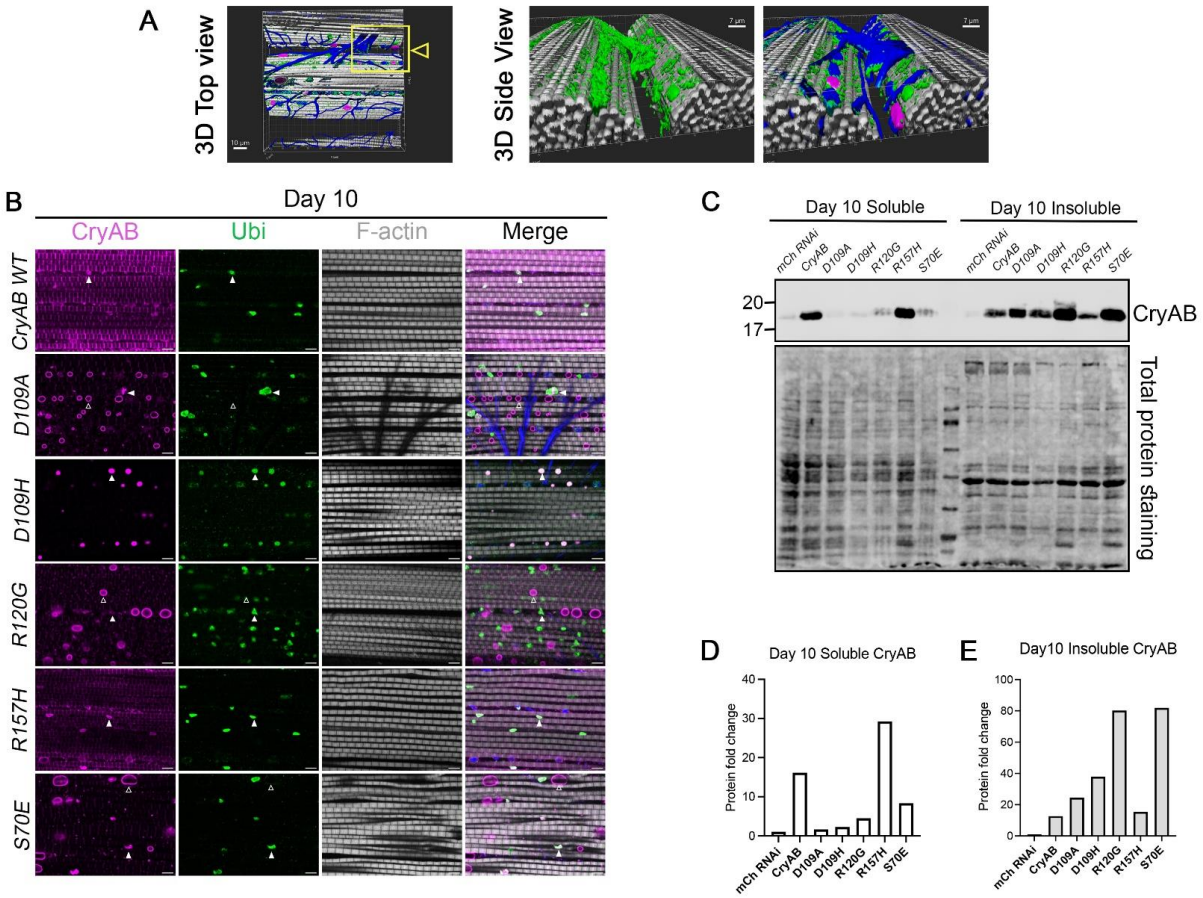

(A) Three-dimensional confocal rendering of IFMs expressing R120G. IFMs are labeled for F-actin (gray), Ubi (green), CryAB (magenta) and nuclei with DAPI (blue). The yellow box in the top view image (left panel) was used to generate side views (right panels). Non-specific DAPI signal marks tracheal tissue. Scale bar: 10 µm for top view image and 7µm for side view images. **(B)** Day 10 IFMs stained for CryAB (magenta), Ubi (green), and phalloidin to label F-actin (gray). Nuclei are counterstained with DAPI (blue). Aggregates are marked with solid triangles, and inclusions with empty triangles. Scale bar: 5 µm. **(C)** Western blot analysis of soluble and insoluble CryAB fractions in Day 10 IFMs. Total protein staining was used as a loading control. **(D, E)** Quantitative analysis of CryAB levels from the soluble and insoluble fractions in panel C. Data are presented as the mean of N=3.

Appendix Figure E.3 CryAB mutants impair autophagic protein degradation and proteasome activity, related to Figure 2.

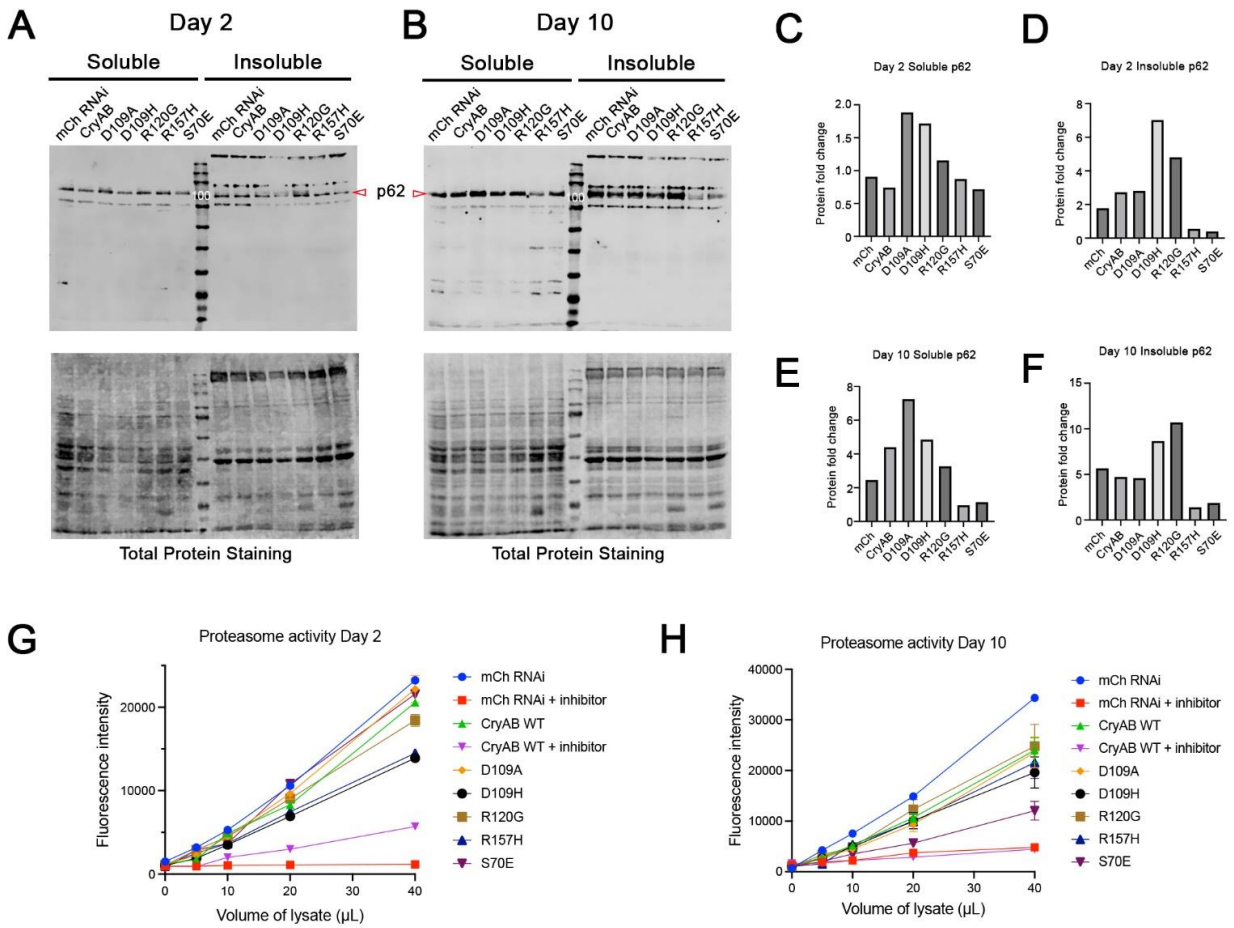

(A, B) Western blot analysis of soluble and insoluble p62 in Day 2 (A) and Day 10 (B) IFMs. Total protein staining was used as a loading control. N≥3. **(C-F)** Quantification of soluble and insoluble p62 from panel A for Day 2 or panel B for Day 10 IFMs. Data are presented as the mean of N=3. **(G, H)** Linear plots of proteasome activity in Day 2 (G) and Day 10 (H) IFMs. *CryAB WT* and mutants exhibit lower proteosome activity compared to *mCh RNAi*. Data are presented as the mean of N=3.

Appendix Figure E.4 Additional markers confirm aggregates in Day 2 IFMs, related to Figure 2.

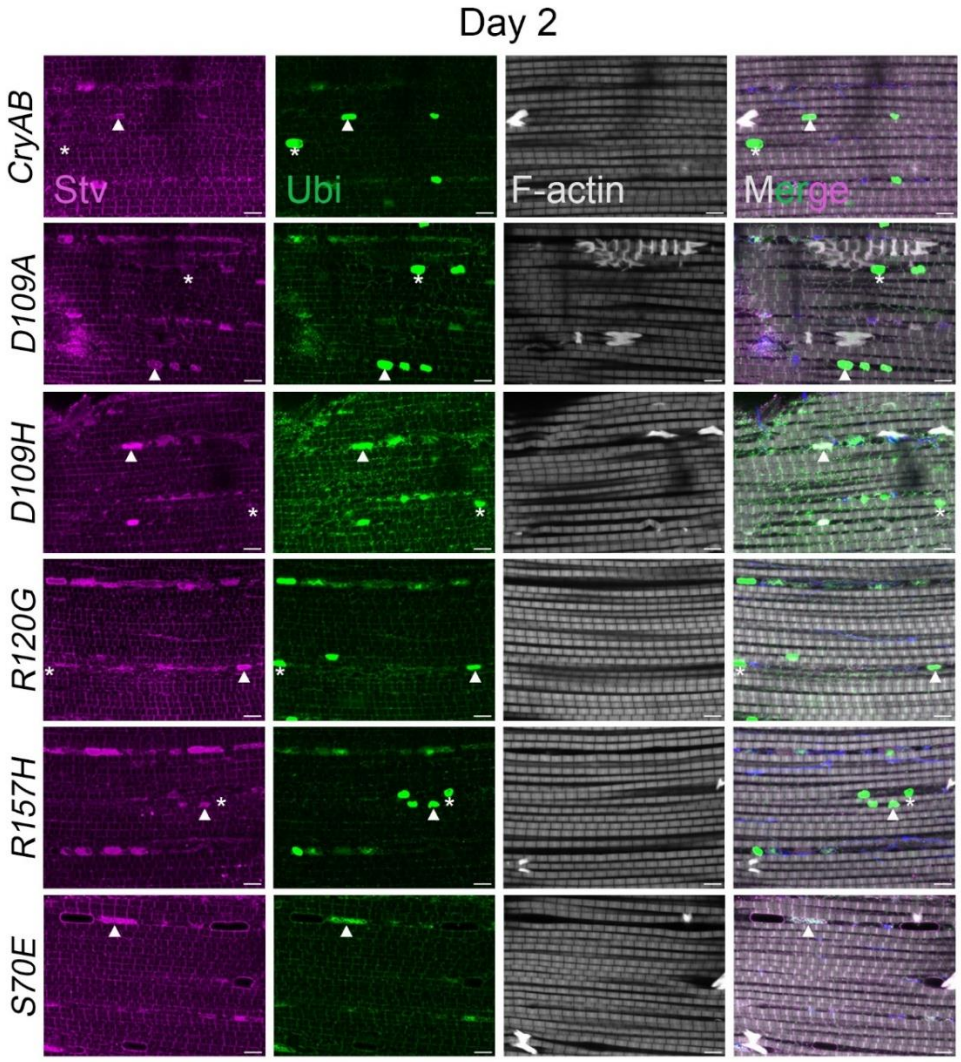

IFMs from 2-day-old *Drosophila* adults stained with anti-Stv (magenta) and anti-Ubi (green) to detect CryAB aggregates. F-actin is visualized with phalloidin (gray) and nuclei are counterstained with DAPI (blue). Scale bar: 5 μm.

Appendix Figure E.5 Desmin colocalizes with CryAB inclusions, related to Figure 4.

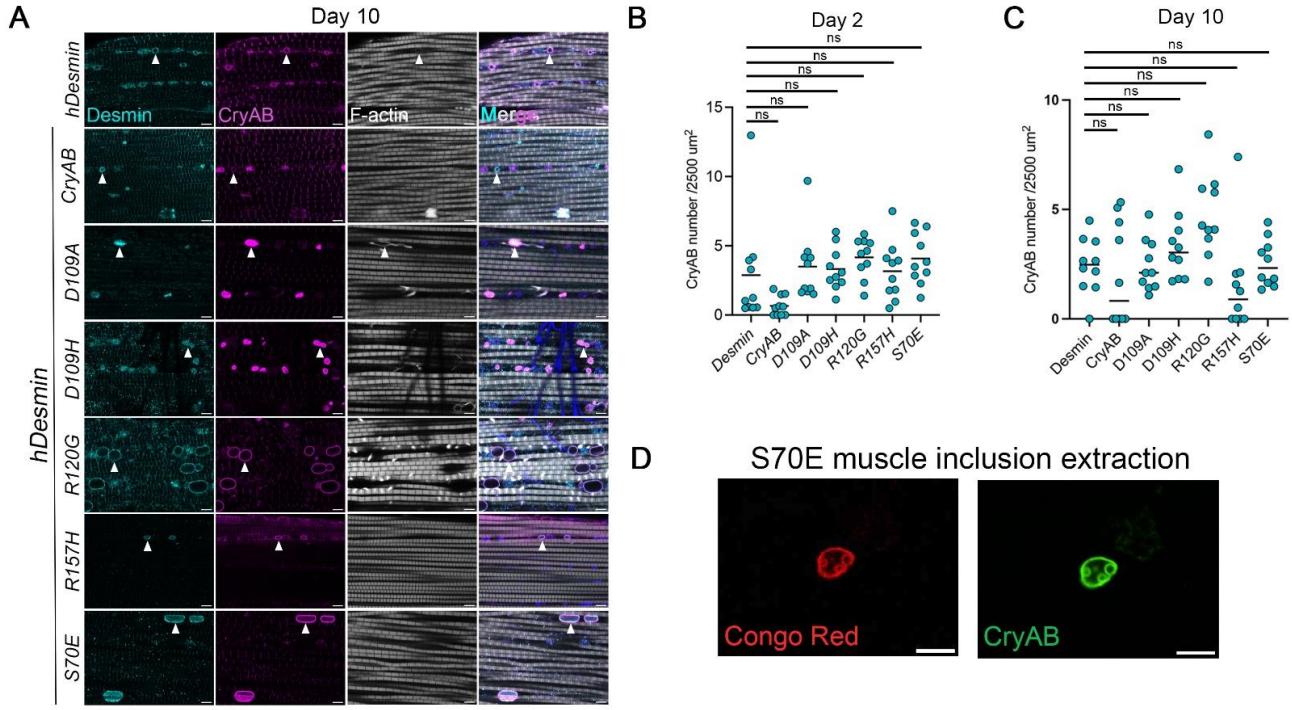

(A) Fluorescent images of Day 10 IFMs stained for human Desmin (cyan), CryAB (magenta), and F-actin (gray). Nuclei are counterstained with DAPI (blue). Inclusion structures are marked with solid triangles. Scale bar: 5 μm. **(B, C)** Quantification of inclusion structures in IFMs at Days 2 and 10. **(D)** Isolated CryAB inclusions from S70E IFMs were stained with Congo red. Co-localization of CryAB antibody (green) with Congo red-positive structures confirms amyloid fibrils. Scale bar: 5 μm.

Appendix Figure E.6 Manipulation of Rab27 affects the number and size of CryAB inclusions, related to Figure 6.

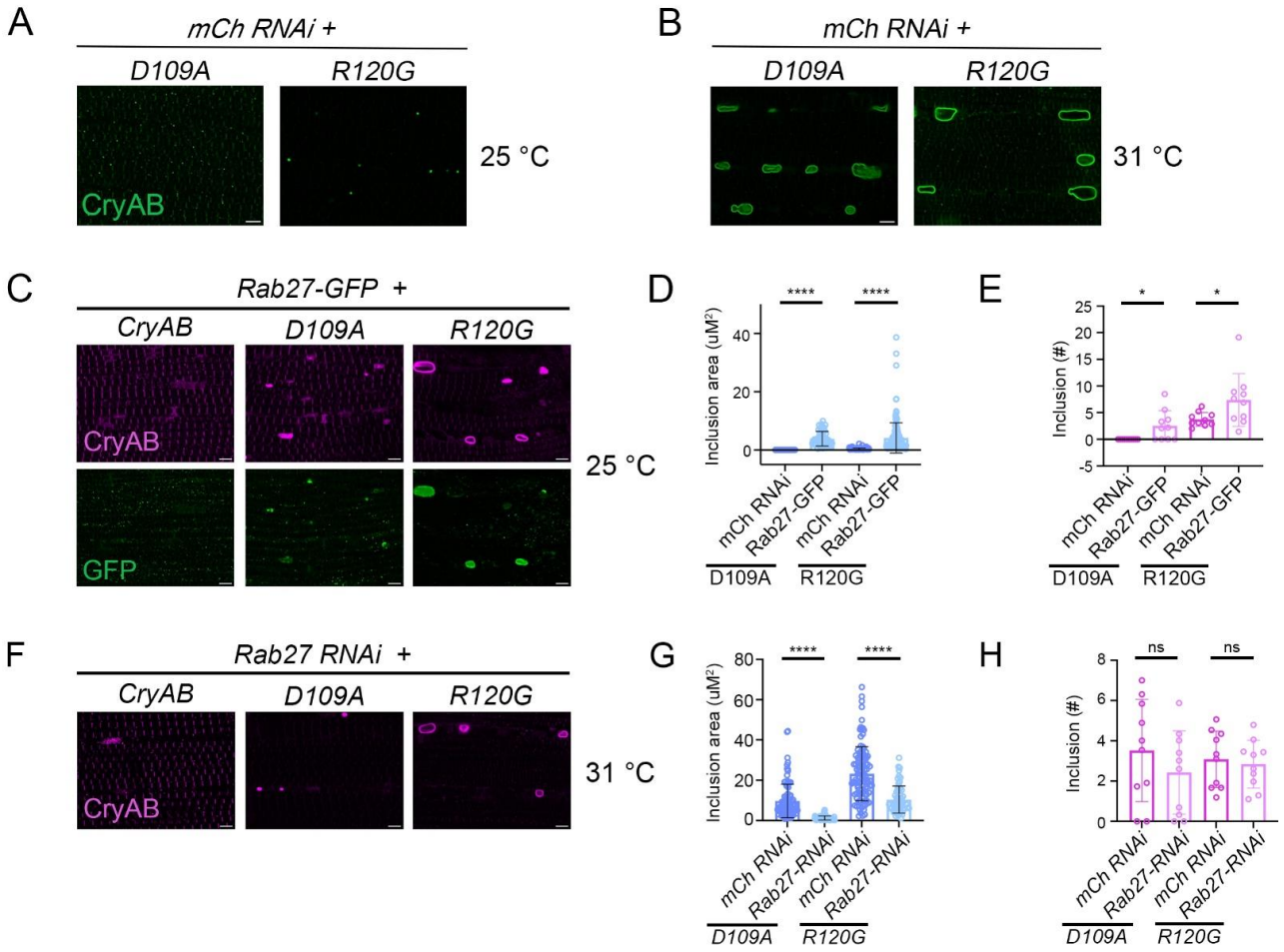

(A, B) Fluorescent images of CryAB inlcusions (green) in D109A and R120G Day 2 IFMs co-expressed with *mCh RNAi* as a baseline for EV formation at either 25 °C or 31 °C. Scale bar: 5 µm. **(C)** Confocal images of Rab27-GFP (green) in Day2 IFMs expressed under control of the *Mef2*-gal4 driver with either wild-type CryAB or CryAB mutants (magenta). CryAB. Scale bar: 5 µm. **(D, E)** Quantification of CryAB inclusion size and number following expression of *Rab27-GFP with CryAB D109A or R120G. (*N=10 per genotype, Unpaired student *t*-test, Mann–Whitney,). *p>0.05, ****p<0.001. **(F)** Fluorescent images of Day 2 IFMs stained for CryAB (magenta) in Mef2>*Rab27 RNAi* expressed with either wild-type CryAB or CryAB mutants (magenta). Scale bar: 5 µm. **(G, H)** Quantification of CryAB inclusion size and number after induction of *Rab27 RNAi with CryAB D109A or R120G. (*N=10 per genotype, Unpaired student *t*-test, Mann–Whitney,). ns = not significant, ****p<0.001.

Appendix Figure E.7 ESCRT-dependent pathway proteins are associated with CryAB inclusions, related to Figure 6.

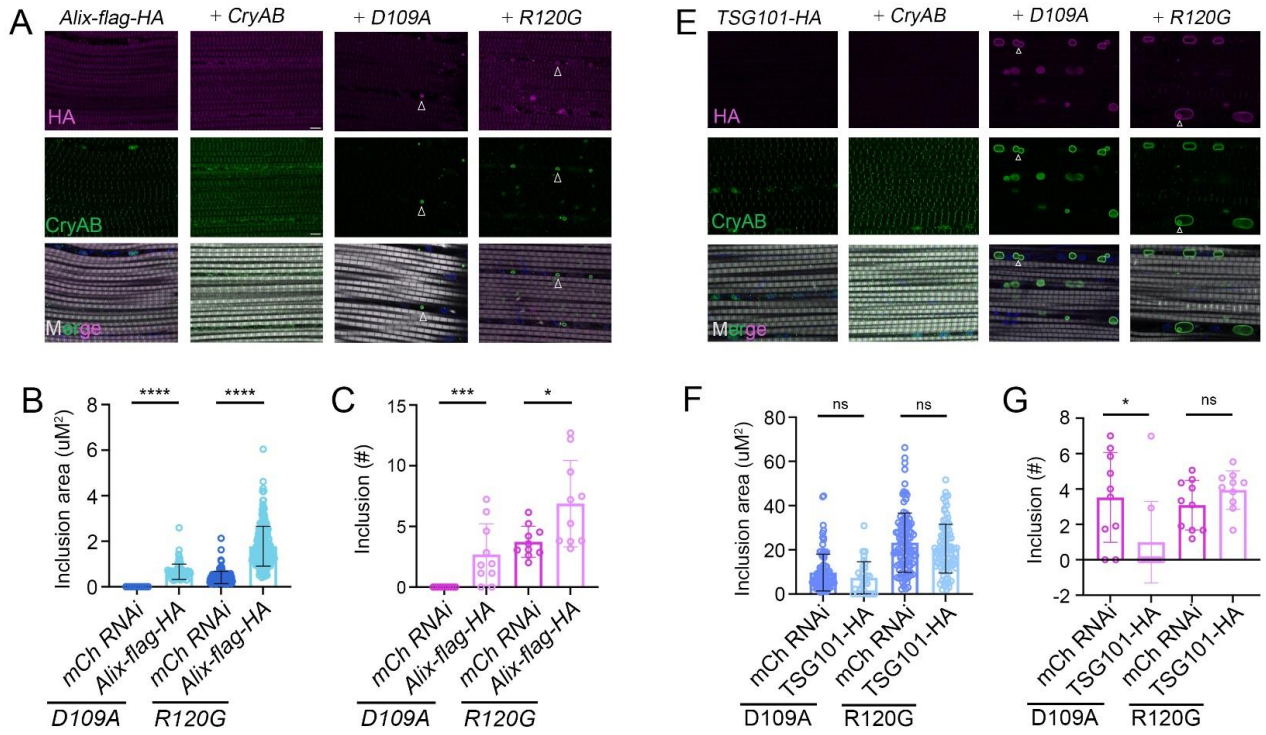

(A, E) Fluorescent images of Alix-flag-HA (A) or TSG101-HA (E) expressed with the *Mef2*-gal4 driver alone or with CryAB variants. Day 2 IFMs are stained with anti-HA (magenta), anti-CryAB (green), and phalloidin (F-actin, gray). Scale bar: 5 µm. **(B-C, F-G)** Quantification of CryAB inclusion size and number following *Alix-flag-HA (B, C) or* TSG101-HA (F,G) expression. Mean ± SD (N=10 per genotype, Unpaired student *t*-test, Mann–Whitney). *p>0.05, ***p<0.05, ****p<0.001.).

Appendix Figure E.8 Trafficking or amyloidogenic proteins that are not associated with CryAB inclusions, related to Figure 6.

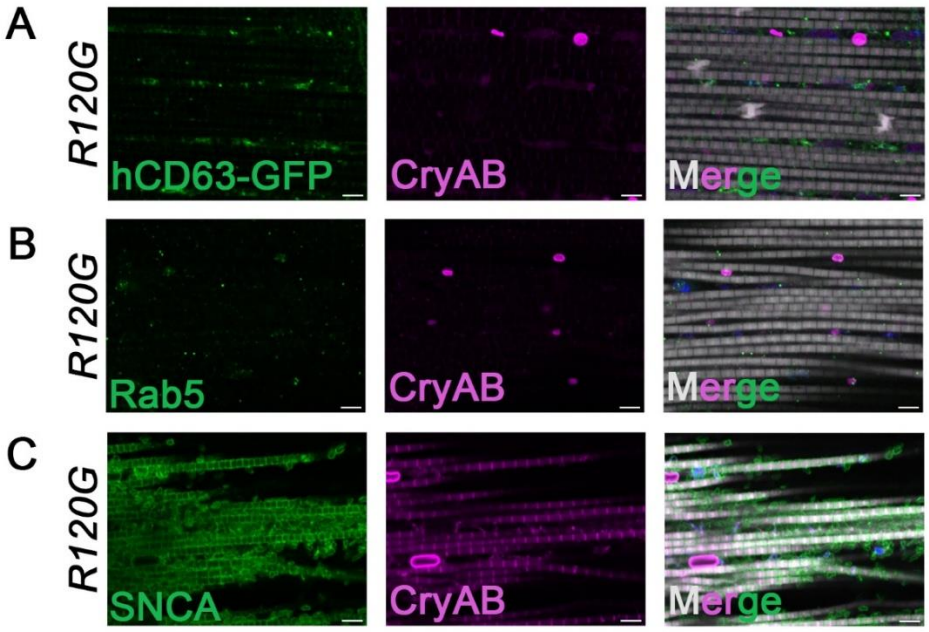

(A-C) Representative confocal images of CryAB 120G (magenta) co-stained for hCD63-GFP (A), Rab5 (B), or alpha-synuclein (SNCA) (C) expressed in Day 2 IFMs with *Mef2*-gal4. Phalloidin labels F-actin (gray) and nuclei are counterstained with DAPI (blue). Scale bar: 5 μm.

Appendix Figure E.9 CryAB mutants preferentially bind NUAK compared to wild-type CryAB, related to Figure 6.

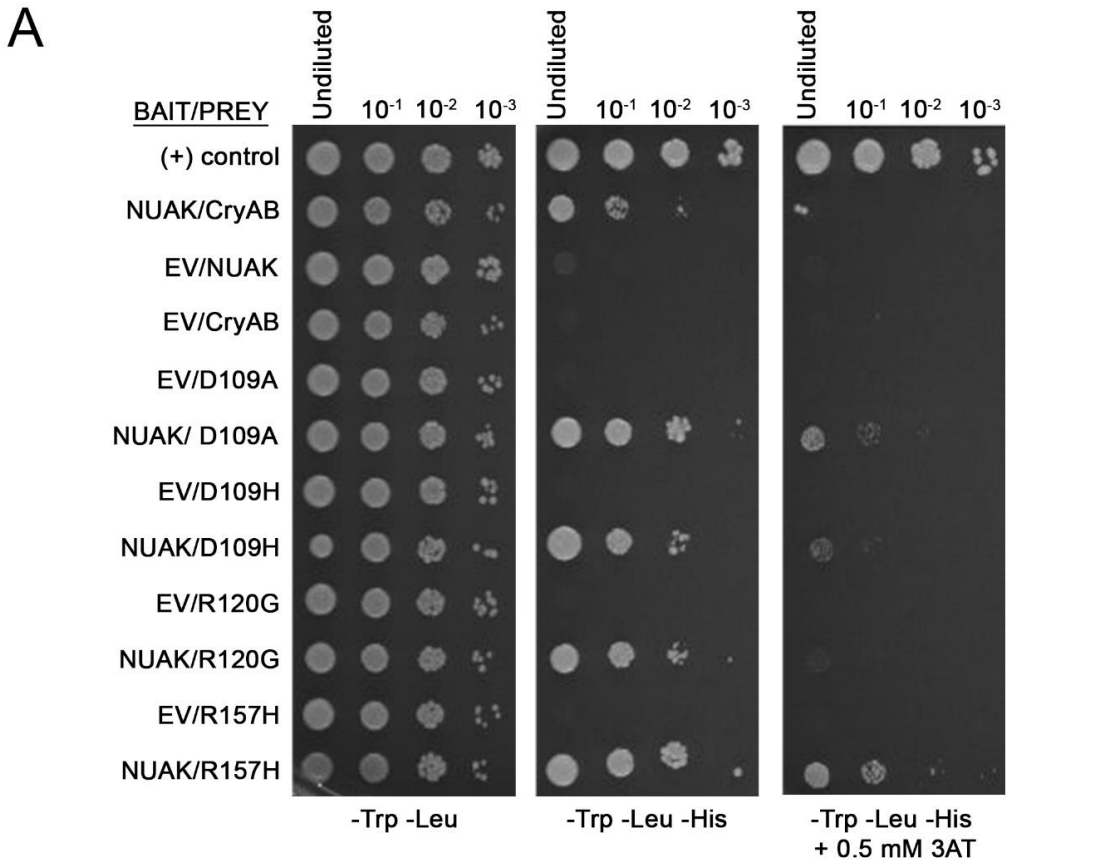

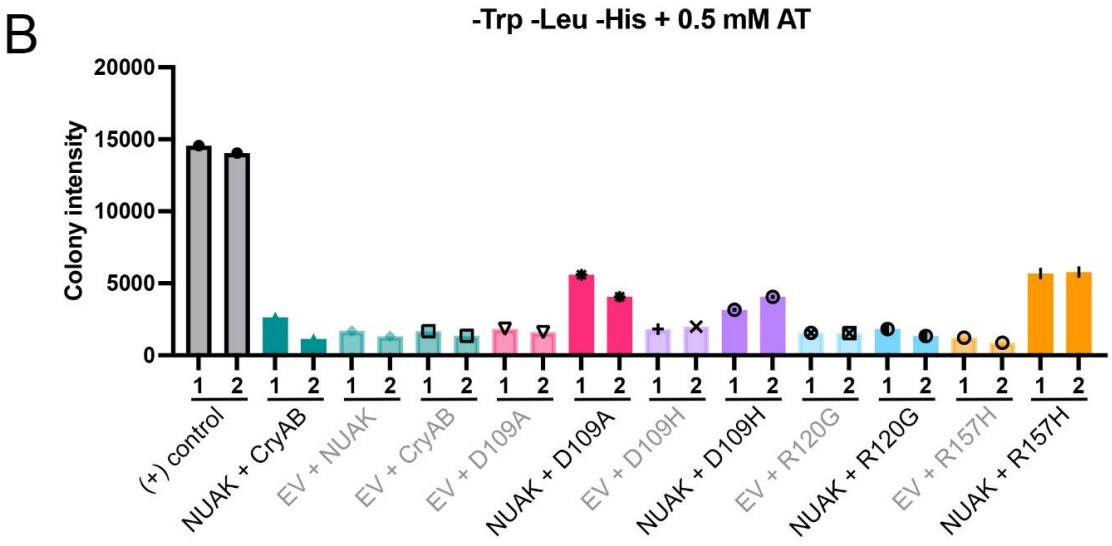

(A) Yeast two-hybrid (Y2H) assays for interactions between the indicated bait and prey proteins. Growth on media lacking tryptophan and leucine (-Trp -Leu) confirms the presence of the bait and prey plasmids. Colony growth on selective media (-Trp, -Leu, -His) indicates interactions between the (+) control (SMAD-SMURF) and NUAK-CryAB pairs. Stronger interactions on media with higher selectivity (-Trp, -Leu, -His + 0.5 mM 3-AT) were observed for NUAK-CryAB mutants compared to controls. No growth was detected for empty bait vectors with NUAK or CryAB mutants. Three independent yeast clones were tested for each bait-prey pair. **(B)** Bar graph quantifying colony intensity (growth) on selective media (-Trp, -Leu, -His + 0.5 mM 3-AT). Clones 1 and 2 are shown for each genotype.

Appendix F Copyright Permission

Chapter 2: Identification of CryAB as a target of NUAK kinase activity in Drosophila muscle tissue

This chapter (or section) is based on the article "Identification of CryAB as a target of NUAK kinase activity in Drosophila muscle tissue", authored by Ziwei Zhao et al., published in *Genetics*, Oxford University Press, 2023.

The material is reused here with permission under the author's rights policy of Oxford University Press. The reuse is for non-commercial academic purposes, and full credit is given to the original publication.

Chapter 3: Stage-specific modulation of Drosophila gene expression with muscle GAL4 promoters

Chapter 4: Pathogenic CryAB Mutations in Muscle Suggest a Novel Mechanism for Amyloid Secretion via Extracellular Vesicles

This chapter is based on the manuscript entitled "Pathogenic CryAB Mutations in Muscle Suggest a Novel Mechanism for Amyloid Secretion via Extracellular Vesicles", authored by Ziwei Zhao et al., which is currently under review in iScience (Cell Press, Elsevier).

Appendix A: Myopalldin (MYPN) function in *Drosophila* muscle tissue

This chapter (or section) includes material from the manuscript entitled "Cardiomyopathy-Associated and Basic Residue Mutations in Myopalladin Alter Actin Binding, Bundling, and Structural Stability", authored by Asha Rankoth Arachchige , Julie Tran , Ziwei Zhao, and colleagues.

Appendix B: Transglutaminase function in *Drosophila* muscle tissue

This chapter includes material from the manuscript entitled "Drosophila Transglutaminase crosslinking activity preserves the integrity of muscle attachments under mechanical strain", authored by Dylan Feist; David Brooks; Ziwei Zhao, and colleagues. The manuscript is currently under review in the *Journal of Cell Science* (The Company of Biologists).

Appendix C: Loss of nuclear envelope bud formation leads to mitophagy initiation in Drosophila muscles